Origami-Inspired Kinematic Morphing Surfaces



Chenying Liu

St Hugh's College (2019 - 2021)
Wolfson College (2021 - 2023)

University of Oxford

A thesis submitted for the degree of

Doctor of Philosophy in Engineering Science

Michaelmas Term 2023

To my family

Acknowledgements

I extend my deepest gratitude to Prof. Zhong You, my supervisor, whose unwavering support has been instrumental throughout my doctoral journey. Working with Prof. You was an immensely fulfilling experience. He not only introduced me to the fascinating realm of origami but also inspired me through enthusiasm and patience with research, shaping me into a more independent researcher. He motivated me to delve into diverse subjects beyond origami and generously supported the project financially. I feel extremely fortunate to have worked under Prof. You's guidance.

Additionally, I owe a tremendous debt of gratitude to Prof. Perla Maiolino, who joined me at the beginning of my research and quickly became my co-supervisor. Perla's expertise in soft robotics has been pivotal in expanding the applications of origami designs to versatile robotic domains. Without Perla's constant involvement, I would not have been able to refine my research questions to the degree of clarity they possess now. Her passion and encouragement have been a guiding light through the ebbs and flows of my research.

Furthermore, I would acknowledge the invaluable support from mentors, collaborators, and engineers: Prof. Liang He's generosity in dedicating time to refine my experiment plans and provide feedback on my manuscripts, Prof. Fufu Yang's insightful suggestions on morphing unit categorisation, Dr. Alessandro Albini's assistance in setting up the robot arm, Mr. Albert Williams' immense patience with the laboratory work, as well as Dr. Peter Walters and Mr. Cleveland Williams's enormous invaluable assistance in fabricating all the origami structures I need. Heartfelt thanks to Profs. Sinan Acikgoz and Barbara Rossi

for serving as examiners during transfer and confirmation, and for their critical comments to make the thesis better.

In the past four years, St. Hugh's College and Wolfson College have been my home, providing an inclusive environment and generous support for study, research, and social engagement. I was also lucky to get involved in undergraduate tutorials at New College and Christ Church, an enriching opportunity made possible by Profs. Barbara Rossi and Laurence Brassart. They are inspiring female role models, urging me to grow not only as a researcher but also a person.

The journey would have been solitary without the presence of companions. I appreciate the help from the current and past members of the Special Structures Group and Soft Robotics Lab, including but not limited to Dr. Jingyi Yang, Dr. Yunlan Zhang, Dr. David Xing, Dr. Leo de Waal, Dr. Mateusz Portka, Dr. Xiao Zhang, Miss Elenor Naraidoo, Mr. Shaohong Zhong, and Dr. Yunfang Yang. Gratitude also extends to friends and colleagues from the university, department, colleges, and Room 11, with whom I've shared so many delightful moments - from hanging out to playing poker and Avalon, as well as fun activities such as swimming, fishing, and punting. To name a few: Miss Yuan Zhang, Mr. Zhan Huang, Miss Zheni Fei, Ms. Yue Chen, Dr. Clare Rees-Zimmerman, Ms. Subin Park, Miss Jiayao Meng, Mr. Guosheng Ji, Ms. Misha Patel, Mr. Andrew Kirby, Mr. George Taylor, Mr. Jiawei Zhang, Ms. Yuanyuan Su, and many many more. A special mention to my two flatmates, Miss Anqi Li and Miss Jessica Rahardjo, who are close companions sharing life's daily adventures, as well as Dr. Sihan Wang, for his unwavering encouragement and companion.

Lastly, I would like to express my gratitude to my parents, Feichao Liu and Yongchun Chen, for their unconditional love, and to my extended family for their continuous support. This thesis is also a tribute to my grandfather, Xiusan Chen, who passed away in 2018. Your approach to life is always close to my heart.

Statement of Originality

I hereby declare that the work presented in this thesis is my own. Where information is derived from other studies, the sources are indicated in the text and appropriately referenced.

Chenying Liu

December 2023

Abstract

In the past decades, an emerging technology has tried to build robots from soft materials to mimic living organisms in nature. Despite the flexibility and adaptability offered by such robots, the soft materials introduce very high or even infinite degrees of freedom (DoFs). It is thus challenging to achieve controllable shape changes on soft materials, which are essential for robots to carry out their functions.

Many material-based approaches have been attempted to constrain the excessive DoFs of soft materials, so that they can bend, stretch, or twist as desired. In most applications, considering that only limited mobility is required to perform certain tasks, it would also be feasible to employ mechanical coupling to remove unwanted motions. To achieve this, engineers resort to origami techniques to design predictable and controllable robotic structures.

However, most origami-inspired robots are built from existing patterns, where the material thickness is always neglected. Using zero-thickness sheets restricts the modelling accuracy, fabrication flexibility, and motion possibility. A recent study reveals that considering material thickness can further reduce the overall DoFs of origami, since its mechanical model is often overconstrained and differs significantly from that of the zero-thickness one. The novel structures with thickness, known as thick-panel origami, were originally developed for space use and are not accessible to roboticists. Hence, a thorough investigation is needed to develop thick-panel origami targeting robotic applications.

This thesis is thus centred on two aspects. The first is to systematically design thick-panel origami for shape-changing, namely morphing surfaces. The second part extends selected surfaces into the design

of intelligent robots, with the aim of simplified design, actuation, and control. The main achievements of this research are as follows.

Firstly, a systematic design methodology is proposed to map thick-panel origami with 6R spatial overconstrained linkages. A library of morphing units whose thicknesses are uniform and not negligible is thus uncovered. Morphing surfaces, which are the tessellations or assemblies of morphing units, are then demonstrated to achieve common soft material behaviours, including bending, expanding, and twisting. Complex motions such as wrapping and curling are also presented. The mobility of these surfaces is restricted to one, while bifurcations may exist for extra motion possibilities.

Secondly, a robotic gripper is designed from the wrapping surface. By exploiting the bifurcation and compliance of the surface, the proposed gripper has achieved a balance between motion dexterity and control complexity, aiming to solve the control challenges of grasping and manipulation. More specifically, the gripper can grasp objects of various shapes with one motor and conduct manipulations with only two control inputs, as opposed to many current end effectors that can only grasp or need around 20 actuators for manipulation tasks. On top of this, the gripper can be 3D-printed with ease, largely streamlining the mechanical design and fabrication process.

Lastly, a reconfigurable robot is demonstrated on the curling surface to mimic a millipede's morphology. The robot can not only morph into a coil but also reconfigure into wave-like and triangular shapes. The reconfigurability is achieved by utilising the kinematic bifurcations of the surface without increasing the system's overall DoF. The design is also free from module disconnection and reconnection for new configurations, making the system more robust. The proof-of-concept robotic study has showcased the potential of maintaining reconfigurability with a relatively straightforward control strategy.

Keywords: origami design, overconstrained linkages, kinematic analysis, robotics, grasping, manipulation, reconfigurability.

Abbreviations

2D	Two-dimensional
3D	Three-dimensional
4R	Four-bar
5R	Five-bar
6R	Six-bar
8R	Eight-bar
ACW	Anticlockwise
CAD	Computer-aided-design
CW	Clockwise
DH	Denavit-Hartenberg
DoFs	Degrees of freedom
F_1	Finger 1
F_2	Finger 2
F_3	Finger 3
F_4	Finger 4
FSR	Force resistive sensor
M_1	Motor 1
M_2	Motor 2
ME	Maximum error
MGW	Maximum grasping weight

MPE	Maximum position error
PLA	Polylactic acid
PneuNets	Pneumatic networks
QVP	Quadrilateral-void pattern
RMSE	Root-mean-square error
S_1	Segment 1
S_2	Segment 2
S_3	Segment 3
S_4	Segment 4
S_5	Segment 5
S_6	Segment 6
SFAs	Soft fluidic actuators
SMAs	Shape memory alloys
SPAs	Soft pneumatic actuators
SSP	Single-slit pattern
SVP	Single-vertex pattern
T_1	Tendon 1
T_2	Tendon 2
T_3	Tendon 3
T_4	Tendon 4
TPU	Thermoplastic polyurethane
TVP	Triangular-void pattern

Contents

1 Introduction **1**

1.1 Background and Significance 1

1.2 Aim and scope 4

1.3 Thesis layout 5

2 Literature Review **8**

2.1 Soft robotics 8

2.1.1 Definitions and applications 8

2.1.2 Bending, expanding, and twisting of soft materials for soft robotic applications 9

2.1.3 Advantages and limitations 12

2.2 Origami robots 13

2.2.1 Definitions and applications 14

2.2.2 Bending, expanding, and twisting of origami structures for origami robots 15

2.2.3 Advantages and limitations 17

2.3 Functional robots 19

2.3.1 End effectors for grasping and manipulation 19

2.3.2 Reconfigurable robots . . . 22
2.4 Shape-changing structures with thickness . . . 25
2.4.1 Rigid origami and thick-panel origami . . . 25
2.4.2 Shape-changing structures inspired by thick-panel origami . . . 27
2.4.3 Shape-changing structures inspired by kirigami . . . 31
2.4.4 Shape-changing structures by assembling linkages . . . 33
2.4.5 Summary and discussions . . . 34
2.5 Related theories in rigid origami . . . 35
2.5.1 Kinematic modelling of rigid origami . . . 35
2.5.2 Overconstrained spatial linkages . . . 38
2.5.3 Tilings and patterns to produce origami tessellations . . . 42

3 Thick-Panel Morphing Units Inspired by Origami 45

3.1 Design methodology . . . 45
3.1.1 2D patterns and geometric features . . . 45
3.1.2 Evaluation process and selection criteria . . . 51
3.2 Morphing units . . . 53
3.2.1 Units based on the plane-symmetric Bricard linkage: type 1 53
3.2.2 Units based on the plane-symmetric Bricard linkage: type 2 58
3.2.3 Units based on the line-symmetric Bricard linkage . . . 63
3.2.4 Units based on other 6R overconstrained linkages . . . 67
3.3 Immobile cases . . . 70
3.3.1 Extended Myard 6R linkage . . . 71
3.3.2 Altmann linkage and Schatz linkage . . . 72
3.3.3 Bennett 6R hybrid linkage . . . 72

3.3.4 Wohlhart 6R linkage 74
3.4 Summary and discussions 74

4 Construction of Morphing Surfaces from Individual Units 76

4.1 Tessellations of morphing units 76
4.1.1 Bending behaviours 77
4.1.2 Expanding behaviours 81
4.1.3 Twisting behaviours 82
4.1.4 Summary and discussions 86
4.2 Assemblies of morphing units 88
4.2.1 Wrapping surface 88
4.2.2 Curling surface 88

5 Wrapping Surface: a Robotic Gripper Enabled by a Single Motor 91

5.1 Gripper design from the wrapping surface 91
5.1.1 Motivation statement 92
5.1.2 Kinematic modelling of the wrapping surface 92
5.1.3 Actuation of the wrapping motion 94
5.1.4 Gripper design and modelling 95
5.1.5 Calculation of grasping range 97
5.2 Experimental procedure 98
5.2.1 Gripper prototype fabrication 98
5.2.2 Characterization of the gripper's performance 100
5.3 Results and discussions 102
5.3.1 Motion trajectories of the gripper 102
5.3.2 Contact force generated on objects 106

5.3.3 Grasping performance . . . 107
5.4 Summary . . . 110

6 A Two-Motor-Controlled Gripper for Object Manipulation 111
6.1 Gripper platform design and analysis . . . 111
6.1.1 Motivation statement . . . 112
6.1.2 Motion paths of a single finger . . . 112
6.1.3 Motion mode analysis of the gripper . . . 115
6.1.4 A differential mechanism for minimal actuators . . . 118
6.1.5 Analysis of gripper compliance via a kinematic model . . . 121
6.2 Experimental procedure . . . 127
6.2.1 Gripper platform fabrication . . . 127
6.2.2 Characterisation of the gripper . . . 128
6.3 Results and discussions . . . 131
6.3.1 Basic motion paths . . . 131
6.3.2 Motion switch at non-bifurcations . . . 134
6.3.3 Object manipulation . . . 135
6.4 Summary . . . 138

7 Curling Surface: a Millipede-Like Reconfigurable Robot 140
7.1 Design and analysis of a curling surface . . . 140
7.1.1 Motivation statement . . . 141
7.1.2 Millipede and its morphologies . . . 142
7.1.3 The curling surface and its constituent units . . . 143
7.1.4 Combined kinematics, segmentation, and bifurcation . . . 146
7.1.5 Analysis of curling profile . . . 148

7.2 Experimental procedure . . . 151
7.2.1 Actuation of the curling surface . . . 151
7.2.2 Fabrication trials . . . 153
7.2.3 Characterisation of the actuated prototypes . . . 155
7.3 Results and discussions . . . 158
7.3.1 Single segment behaviour . . . 158
7.3.2 Double segment behaviour . . . 158
7.3.3 Configurations of the six-segment robot . . . 162
7.3.4 Potential of the robotic prototype and its segments . . . 162
7.4 Summary . . . 165

8 Final Remarks **166**
8.1 Summary of achievements . . . 166
8.1.1 Design of morphing units and surfaces . . . 166
8.1.2 Wrapping surface: grasping and manipulation with limited control inputs . . . 167
8.1.3 Curling surface: a low-DoF reconfigurable robot free from module reconnection . . . 168
8.2 Future work . . . 169

A Additional Morphing Units **171**

B Supplementary Videos **173**

C Kinematic Model for Compliance Analysis **174**

References **179**

List of Figures

1.1 Origami of zero-thickness and thick panels (Chen et al., 2015). (a) A four-crease zero-thickness origami and its thick-panel version based on the Bennett linkage, and (b) their folding processes to create a flat or compact volume. 3

2.1 Controllable shape changes on soft materials. **(a)** A PneuNets actuator for bending (Mosadegh et al., 2014). **(b)** Fiber-reinforced actuators that extend, twist, expand, and bend (Connolly et al., 2017). **(c)** Tendon-based actuation to bend a finger (Zaidi et al., 2021). **(d)** Complex shape changing achieved via shape memory alloys (Han and Ahn, 2017). 11

2.2 Origami robots. **(a)** A shape-morphing structure based on the Miura-ori fold (Li and Wang, 2015). **(b)** A robotic arm based on a bellow-like Yoshimura pattern that is extensible and bendable (Zhang et al., 2022). **(c)** A robotic arm based on the Kresling origami (Kresling, 2020) that can extend and twist (Wu et al., 2021). **(d)** A robotic gripper whose fingers are based on the origami twisted tower (Lee et al., 2020). **(e)** An expandable wheel based on the tessellation of six-crease waterbomb origami (Lee et al., 2017). **(f)** A pneumatic origami platform based on the six-crease waterbomb unit cell. (Robertson et al., 2021) 16

2.3 End effectors for grasping and manipulation. **(a)** A rigid hand, Shadow Dexterous Hand (Andrychowicz et al., 2020) and **(b)** its soft counterpart, RBO Hand 3 (Puhlmann et al., 2022), both of which can grasp and manipulate objects. **(c)** A soft gripper with three fingers for grasping only (Truby et al., 2018). **(d)** A three-finger gripper with reconfigurable palm, known as the RUTH gripper, for in-hand manipulation with only three fingers (Lu et al., 2021). . . . 20

2.4 Modular reconfigurable robots such as **(a)** the PolyBot (Yim et al., 2000), a chain-type mechanism and its four configurations, and **(b)** the StarBlocks (Zhao et al., 2023) based on lattice structures and its self-assembly process. 23

2.5 Other reconfigurable robots. **(a)** Mori, a modular origami robot that generates different configurations using different folds (Belke and Paik, 2017). **(b)** A chain robot based on the Kresling origami that can shrink and expand (Ze et al., 2022b). **(c)** A robot whose backbone is a 3-DoF planar linkage climbs up the slope (Liu et al., 2022b). **(d)** A soft robot that can crawl and roll (Gu et al., 2020). . 24

2.6 Thick-panel origami originating from **(a)** five-crease and **(b)** six-crease vertices. The former is modelled as the Myard linkage and the latter is a Bricard linkage (Chen et al., 2015). 27

2.7 Thick-panel origami tessellations based on **(a)** Miura-ori pattern (Zhang and Chen, 2018a), **(b)** extended Diamond pattern where sector angles are non-equal (Zhang and Chen, 2018b), **(c)** Water-bomb origami (Zhang and Chen, 2021), and **(d)** Triangular Ron Resch pattern (Yang et al., 2022a). Only the tessellation in **(b)** is flat on both top and bottom surfaces in the unfolded state. 29

2.8 Two motion paths of a thick-panel origami based on a reconfigurable linkage (Peng and Chirikjian, 2024). Each path is of single DoF. . . 31

2.9 Thick-panel kirigami design based on the Waldron hybrid linkage. (a) The zero-thickness pattern and its thick-panel counterpart (Wang et al., 2018b). (b) Tessellation of the thick-panel units with uniform thickness (Wang et al., 2022). 32

2.10 Shape-changing structures created by assembling linkages. **(a)** Planar 4R linkage for programmable shape morphing (Dudte et al., 2023). **(b)** 4R linkages with versatile motions and their assembly capable of bending (Ou et al., 2018). 33

2.11 DH notations of adjacent links connected by revolute joints. 36

2.12 The general plane-symmetric Bricard linkage by Feng et al. (2017). 42

2.13 Examples of tillings and patterns, where each tessellation is based on **(a)** equilateral triangles, **(b)** squares, **(c)** regular hexagons, **(d)** general triangles, **(e)** convex quadrilaterals, **(f)** hexagons with parallel and equal opposite sides, and **(g) - (f)** a combination of regular shapes. 43

3.1 Origami bases. **(a)** Single-vertex pattern. **(b)** Single-slit pattern. **(c)** Triangular-void pattern. **(d)** Quadrilateral-void pattern. **(e)** Possible fold locations at the top or bottom of adjacent panels and the associate dihedral angle. 46

3.2 Special cases of the QVP. **(a)** The QVP is equivalent to the SSP. **(b)** The QVP is equivalent to the TVP. 49

3.3 All possible fold arrangements on the origami bases. 50

3.4 Special fold arrangement. **(a)** and **(b)** Examples of intersecting folds to create zero joint offsets. **(c)** and **(d)** Examples of parallel folds to create zero joint offsets. 52

3.5 The origami bases of Units a_1 - a_3 based on the plane-symmetric Bricard linkage and their 3D models. 54

3.6 Path 1 of Units a_1 - a_3 and associated 3D models. 56

3.7 Path 1 (black) and path 3 (coloured) of Unit a_2 when $\alpha = \beta = 60°$. The 3D models depict the configurations along path 3. 58

3.8 The origami bases of Units b_1 - b_3 based on the plane-symmetric Bricard linkage and their 3D models. 59

3.9 Kinematic behaviour of Units b_1 - b_3 and associated 3D models. Path 1 of each unit is given at the top while path 2 is at the bottom. 62

3.10 The origami bases of Units c_1 - c_3 based on the line-symmetric Bricard linkage and their 3D models. 63

3.11 Path 1 of Units c_1 - c_3 and associated 3D models. 65

3.12 The origami base of Unit m_1 based on the Wohlhart 6R linkage and its 3D model. 67

3.13 Kinematic behaviours of Unit m_1 when all sector angels are 60°. 3D configurations of the two motion paths are also displayed. 68

3.14 The origami base of Unit m_2 based on the Sarrus linkage and its 3D model. Its kinematic motion paths when $\alpha = \beta = \gamma = \delta_1 = \delta_2 = 60°$ and $a = 3h$ are plotted by the side. 69

3.15 Evaluation of the extended Myard 6R linkage on a morphing unit. **(a)** and **(b)** Possible cases to meet certain geometric conditions on the SVP. **(c)** and **(d)** Possible cases to meet the zero joint offsets on the SSP and TVP. 72

3.16 Patterns that satisfy **(a)** the Bennet 6R hybrid linkage and **(b)** the line-symmetric Bricard linkage. The physical inference exists between P_2 and P_5. 73

4.1 Tessellations of Units a_1 - a_3 from Fig. 3.5 and their 3D models. **(a)**, **(b)**, and **(c)** Horizontal strips based on the connection of Units a_1 - a_3. **(d)** Vertical extension of a strip. 77

4.2 The general tessellation of Units a_1 - a_3 and its bending motion. **(a)** The fold pattern and its simulated model in the flat unfolded and semi-folded states. **(b)** The bending motion on a physical prototype made from 3D-printed prisms (serving as rigid panels) and glass fibre tapes (serving as folds). 79

4.3 Tessellations of identical panels to achieve regular bending shapes. The panels' bases include **(a)** general triangles, **(b)** isosceles triangles, and **(c)** isosceles trapezoids. Repeated individual units of each tessellation are highlighted. 80

4.4 Assemblies of Units b_1 from Fig. 3.8 for expanding behaviours. ω_1 of Unit $b_{1.2}$ is taken as input. 81

4.5 Expanding behaviours on the tessellations of Units b_1 where the two-layered surfaces are based on **(a)** general triangles with interior angles as 45°, 75°, and 60°, and **(b)** equilateral triangles. The latter has a more uniform expansion. 83

4.6 Tessellation of repeated Units c_1 from Fig. 3.10. The surface is based on identical triangle panels, where $\alpha = 60°$, $\beta = 45°$, and $\gamma = 75°$. The fold pattern, simulated model, and physical prototypes are all displayed. 84

4.7 Tessellation of repeated Units c_2 from Fig. 3.10. The surface is based on identical quadrilateral panels. Fold pattern where $\alpha = 60°$, $\beta = 45°$, $\gamma = 75°$, and $\delta = 15°$. The slit length d is set twice as the panel thickness h. **(b)** and **(c)** Physical prototype and its twisting process. 85

4.8 Tessellation of repeated Units c_3 from Fig. 3.10 and their modifications into an assembly of identical hexagon panels. **(a)** and **(b)** Single unit modification process and its tessellation pattern. **(c)** Folding process of the physical prototype. 86

4.9 Wrapping motions of **(a)** three-unit, **(b)** four-unit, and **(c)** five-unit assemblies. 89

4.10 Design of a curling surface. **(a)** Top view of the origami pattern. **(b)** and **(c)** Cross-sectional views of two curling configurations. . . 90

5.1 Origami pattern and corresponding 3D kinematic models of **(a)** a morphing unit and **(b)** its assembly that forms the gripper backbone. 92

5.2 The Cartesian coordinate system for the morphing unit. 93

5.3 Pulling the tendons enables the assembly to start from **(a)** the nearly unfolded state, pass through **(b)** the semi-folded state, and end up at **(c)** the near fully folded state. The process is reversible by loosening the tendons. 94

5.4 Kinematic model of the gripper and its fingers. **(a)** Proposed design of the origami gripper from its top view, where lengthened fingers, hemisphere fingertips, tendon channels, and folds' widths are all denoted. **(b)** Cross-sectional view of F_1 at two poses. Its rotation angle is represented by θ. The central top point of the fingertip is marked in red. 96

5.5 Cross-sectional view of the gripper holding an object. 97

5.6 CAD model of the gripper backbone and fingertip coat for 3D printing. 99

5.7 The gripper prototype. **(a)** Top view of the gripper with four fingers semi-closed. **(b)** Side view of the gripper holding an egg. 100

5.8 Experimental setup to measure the maximum contact force that the gripper is able to generate on objects of different sizes. 101

5.9 Motion trajectories and position errors of the gripper. **(a)** Experimental results of 3D fingertip positions in comparison with theoretical predictaions. Calculation of position error in **(b)** the xOy plane and **(c)** the xOz plane are illustrated by taking a random position of fingertip 2 in its opening motion. The unit is in mm. 103

5.10 Experimental 2D trajectories of all fingertips in the closing and opening motions. **(a)** and **(b)** Fingertip trajectories in the xOy plane. **(c)** and **(d)** Fingertip trajectories in the xOz plane. **(e)** and **(f)** Fingertip trajectories in the yOz plane. The unit is in mm. . . . 104

5.11 The contact forces generated on objects of different side lengths, ranging from 10 to 100 mm at a step of 10 mm. 106

5.12 Grasping daily objects, which include **(a)** a dice, **(b)** an orange, **(c)** a hand sanitiser, **(d)** an egg, **(e)** a marker pen, and **(f)** a mug with water. 108

5.13 Grasping capability evaluation. **(a)** Objects used for grasping whose bases are circle, square, hexagon, and triangle. **(b)** MGW of each object. 109

6.1 CAD model of the gripper reproduced from Fig. 5.6. The endpoints of each finger are marked in red for trajectory analysis. 113

6.2 Motion paths of a single finger. **(a)** 3D models that illustrate each motion path, where path 1 is a Bricard linkage motion. Paths 2 and 3 are symmetric to each other. **(b)** Plots of kinematic behaviours in each path. 114

6.3 Actuation scheme where the tendons can be pulled **(a)** individually or **(b)** in combination. F_1 and its associated tendon channels are taken as an example. For simplicity, lengthened fingers and fingertips are omitted in the assembly. 115

6.4 Five motion types of the gripper. The unit is in mm under actual fabrication parameters. They are the same as Table 5.1, except that the finger length L has increased to 45 mm for a wider motion range. In particular, motion type 5 is the grasping motion in Chapter 5. . 119

6.5 Design of a tendon-pulley-based differential mechanism where **(a)** four sets of tendons are controlled by two motors to achieve **(b)** eight motion modes. X indicates that the motor is immobile rather than pulling any tendons. 120

6.6 Origami pattern for a finger in its (a) original form and (b) new version with hinge width taken into account. The hinge body has zero thickness. 121

6.7 Dihedral angles among P_1 , P_6, and the hinge body. 123

6.8 Path 1, path 2, and their transition. Note that ω_2 and ω_3 can increase to 180° in paths 1 and 2 but only half of their motion range is indicated. 125

6.9 The relationship between ω_{12} and ω_2 when the transition angle ω_3 is fixed at **(a)** 45°, **(b)** 60°, and **(c)** 75°. The threshold value of w_2/h is indicated. 126

6.10 The gripper platform for object manipulation. Some small pulleys are used to guide the tendon sets so that they do not intertwine. . . 128

6.11 Key steps for ball manipulation by exploiting **(a)** motion type 5 and **(b)** a combination of motion types 2 and 5. Innate compliance is also required. 130

6.12 Experimental motions against theoretical models. Fingers are numbered for clarity. The unit is in mm. 132

6.13 Compliant motion switch from **(a)** motion 2a to motion 4a and **(b)** motion 2a to motion 5. The switch process occurs outside of the gripper's bifurcation. The unit is in mm. 134

6.14 Manipulation of cuboids under motion type 3. Each object's trajectory is roughly an arch whose size varies along with the cuboid thickness. The unit is in mm. The widest motion range is up to 52 mm. 136

6.15 Manipulation of balls under motion type 5. The smaller ball's trajectory is roughly a line while the bigger one still has a curvature. The unit is in mm. The widest motion range is up to 63 mm. . . . 137

6.16 Manipulation of **(a)** a cone under motion type 4 and **(b)** a ball using a variety of motion modes. The cone has a complex motion trajectory. The unit is in mm. The ball has the widest motion range of up to around 71 mm. 138

7.1 Morphologies of a millipede, including **(a)** coil, **(b)** wave-like, and **(c)** triangular shapes. Photos are adapted from Northwest Pest Control (2020); Innovative Pest Control (2020); Native Pest Management (2023). 142

7.2 Animals similar to the millipede. **(a)** A pill bug, **(a)** a lobster, and **(c)** the curling process of a pill bug toy, which is made by a Japanese company named Bandai Co., Ltd. The photos are adapted from Lanier (2017); Alois (2021). 143

7.3 (a) Origami pattern of the curling surface and its constituent units. The pattern is composed of identical equilateral triangles and isosceles trapezoids. (b) The curling process in SOLIDWORKS when all central and side units are in their respective path 1. 144

7.4 Unit combination and bifurcation. **(a)** Origami pattern of a central unit and a pair of side units, along with **(b)** its topological diagram. Two bifurcation paths are displayed, where the central unit is in path 1. The side units are in **(c)** path 1 and **(d)** path 2, respectively. 147

7.5 Cross-sectional view of selected surface configurations. Curling, wave-like, and triangular morphologies can be obtained from the kinematic bifurcations. Note that segments can look different even if they are in the same path as they may have different curvatures. This is exemplified by configurations 1 and 3 where path 1 of each looks distinctive. 149

7.6 Cross-sectional views of the curling configurations when all segments are in **(a)** path 1 and **(b)** path 2. Parameters for geometric analysis are denoted. 150

7.7 Actuation design of a single segment. **(a)** Top view of the segment with a rotating axle. Note that the panel connections are upside-down from the original one in Fig. 7.3. **(b)** Side view of the segment in a semi-closed state. The arrangements of closing and opening tendons are given in **(c)** and **(d)**, respectively. 152

7.8 Fabrication of an actuated surface. **(a)** Schematic design of the driving axle. **(b)** Fabrication of fold connections between panels. **(c)** Completed prototype of a six-segment millipede-like robot. . . . 154

7.9 Marker placement for (a) an actuated single segment which only has path 1, (b) an actuated segment with a passive one in path 1, and (c) an actuated segment with a passive one in path 2. 156

7.10 Experimental results of the single segment in path 1 compared with the theoretical model. Note that the range of the vertical axis differs for each distance, making some of the errors seemingly bigger than others but actually not. The same applies to Figures 7.11 and 7.12. 159

7.11 Experimental results of double segments compared with the theoretical model. The passive segment is in path 1. 160

7.12 Experimental results of double segments compared with the theoretical model. The passive segment is in path 2. 161

7.13 Eight configurations of the robot in comparison with simulations. . 163

7.14 Potential of the robotic prototype and its segments. **(a)** The curling and **(b)** triangular configurations roll down a slope. Crawling behaviours have been achieved on **(c)** a single segment, **(d)** double segments, and **(e)** four segments. 164

A.1 Morphing units with more than one DoF or physical collisions. **(a)** Unit based on the Waldron hybrid linkage. **(b)** Unit based on the line-symmetric Bricard linkage. Both start with two DoFs and then reduce to a single mobility. **(c)** and **(d)** Units based on Bennett 6R hybrid linkage. **(e)** and **(f)** Units based on the plane-symmetric and line-symmetric Bricard linkages, respectively. The collision occurs between P_2 and P_5 on these four units. **(e)** Unit based on the Sarrus linkage and the interference exists between P_2 and P_6. The interfered area of each unit is identified by the SOLIDWORKS simulation and marked in red. 172

List of Tables

2.1 Commonly used cylindrical origami for robotic structures 15

2.2 Thick-panel origami tessellations and their properties 28

2.3 Kinematic parameters of a joint 36

2.4 Geometric conditions of 6R overconstrained linkages whose joint offsets are all zero 39

2.5 Geometric conditions of 6R overconstrained linkages derived from Bennett linkage with non-zero offsets 40

2.6 Geometric conditions of 6R overconstrained linkages derived from Bricard linkage with non-zero offsets 41

3.1 Geometric constraints of 2D origami bases 48

3.2 Relationship between the revolute variable θ_i and dihedral angle ω_i of morphing units 55

3.3 Summary of morphing units and their kinematic properties 75

4.1 Basic shapes and their tessellation properties 87

5.1 Fabrication parameters of the gripper prototype (unit: mm) 99

5.2 MPE of fingertips in the 2D planes (unit: mm) 105

5.3 Displacement between the opening and closing motions (unit: mm) 105

5.4 Daily objects for grasping evaluation and the successful grasping rate 107

6.1 Gripper motion type, relevant tendon arrangements, and kinematic behaviours 117

6.2 New conversion between revolute variable and dihedral angle . . . 122

6.3 RMSE and ME of experimental motion paths (unit: mm) 133

Chapter 1

Introduction

1.1 Background and Significance

Conventional robots are usually constructed from rigid links connected by joints to achieve desirable motions that can be precisely modelled (Bauer et al., 2014). Despite their extensive industrial use, these robots have limited adaptability and are not intended to interact with humans. In contrast, soft robots, a new type of robot inspired by biological systems in nature, are made from soft or extensible materials similar to those found in living organisms (Rus and Tolley, 2015). The flexibility and adaptability of soft robots are ideal properties that could bridge the gap between humans and machines. However, such materials often come with very high or even infinite degrees of freedom (DoFs) (Majidi, 2019), making it harder to achieve controllable shape changes on soft materials.

There are various approaches to constraining the excessive DoFs of purely soft materials, such as soft fluidic actuators, tendon-driven design, and active materials (Pagoli et al., 2021b). For instance, pneumatic networks, a class of soft

actuators, can enable synchronised bending and twisting motions upon pressurization (Ilievski et al., 2011; Wang et al., 2018a). Loop-linked structures made of thermally responsive shape memory alloys (SMAs) can morph into various configurations when heated (Han and Ahn, 2017). All these approaches are highly dependent on material properties and may increase the complexity of modelling, fabrication, and control.

In most applications, only limited mobility is required to perform specific tasks. For instance, a surface only needs to bend, stretch, and twist. Instead of relying on the material-dependent actuation system, it is desirable to create morphable structures using mechanical coupling to remove unwanted motions. To achieve this, this thesis resorts to origami, whose mechanical coupling is realised through shared creases.

As the ancient art of paper folding, origami has been practised for centuries (Lang, 2007) and is already applied in diverse engineering fields from large deployable antennas (Georgakopoulos et al., 2021) to miniature medical devices (Kuribayashi et al., 2006). The in-build crease design also permits continuous motions and yields many soft-bodied properties, making it a promising candidate for robotic structures (Rus and Tolley, 2018).

To date, most origami robots are built from existing patterns based on flat sheet materials such as paper (Jeong and Lee, 2018) and polymer (Onal et al., 2012). In addition to basic folds on the two-dimensional (2D) sheets, some of them could also function in three-dimensional (3D) forms, such as a cylinder, to perform bending, expanding, or twisting (Kaufmann et al., 2022; Lee et al., 2017, 2020). Despite the substantial progress, few attempts have been reported to modify or change the commonly used patterns. In particular, material thickness is rarely considered

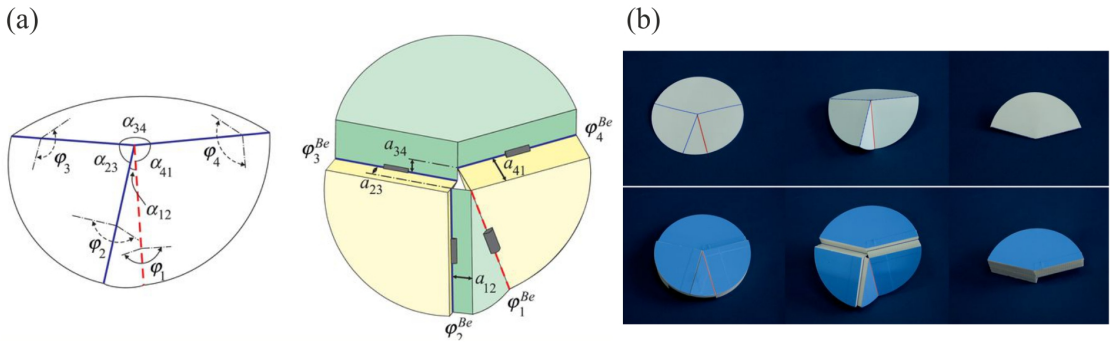


Figure 1.1: Origami of zero-thickness and thick panels (Chen et al., 2015). (a) A four-crease zero-thickness origami and its thick-panel version based on the Bennett linkage, and (b) their folding processes to create a flat or compact volume.

in the development of origami robots, which reduces the modelling accuracy and restricts the materials that could be used to make the robots. A more detailed investigation is needed to develop new origami for robotic applications.

Amongst many types of origami, there is a subset known as rigid origami. It is concerned with folding structures using flat rigid facets joined by hinges, without the need to stretch or twist the facets (Watanabe and Kawaguchi, 2009). Rigid origami based on a zero-thickness sheet is modelled as a spherical linkage, as shown in Fig. 1.1(a) left. Generally, a four-crease vertex has a single DoF and the number increases with the crease numbers (Tachi, 2009). A few years ago, a new approach was developed to accommodate material thickness by placing folds or hinges at the upper or lower surfaces of a panel with finite thickness (Chen et al., 2015), as shown in Fig. 1.1(a) right. This is known as thick-panel origami and the associated new mechanical model becomes a spatial linkage, e.g., the Bennett linkage. Thick-panel origami not only gives a more accurate description of the folding motions but also brings a stronger mechanical coupling to further reduce the overall DoFs (Chen et al., 2016). These features make it possible to achieve desirable motions with

simplified actuation and control. Whilst the thick-panel design has been exploited in aerospace applications (Zirbel et al., 2013) and metamaterials (Ye et al., 2023), it is not yet available in robots. The idea gives rise to this research.

1.2 Aim and scope

One key objective of this thesis is to utilise thick-panel origami for the development of kinematic morphing surfaces that are ready to be applied in robotics. The resultant surfaces will have the following features.

- The surfaces consist of rigid panels with uniform thickness joined by folds or hinges. When the surfaces are unfolded, they are as flat as a sheet of paper but the thickness cannot be neglected.
- The surfaces are constructed from tessellations or assemblies of single-DoF morphing units. The geometric parameters of these units can be tuned for tailored motions.
- The surfaces can bend, expand, and twist similar to soft materials, or undergo other complex motions. All these behaviours can be mathematically predicted with ease.
- The surfaces should have limited DoFs so that they can be controlled with a small number of actuators when they are developed into functional robots.
- The concept of morphing surfaces is independent of scale and domain materials, which allows them to be made at any reasonable scale and transferred to other applications requiring shape-changing.

Upon finishing the design of morphing surfaces, another key objective is to harness their distinctive features, such as predictable motions, single mobility, and bifurcations, to address various robotic challenges. In particular, the research will focus on striking a balance between motion dexterity and control intricacy. The intended robotic functions include grasping, manipulation, and reconfiguration.

1.3 Thesis layout

The thesis is structured into seven chapters. Apart from this introductory chapter, the others are outlined as follows.

Chapter 2 presents an extensive literature review relevant to the research. The first two sections cover key concepts in soft robots and origami robots, with a special focus on the controllable shape changes in soft or origami-inspired structures. Secondly, end effectors and reconfigurable robots are discussed respectively, which are relevant robotic functions to be achieved in this thesis. Thirdly, the design methodology of shape-changing structures with thickness is reviewed, which includes origami design, kirigami design, and linkage-inspired materials. Finally, the kinematic approach to modelling rigid origami and a summary of overconstrained spatial linkages are given, along with the mathematical tiling and pattern method for large-scale tessellations. All of them are the enabling techniques that are subsequently employed in the thesis.

Chapter 3 focuses on the development of kinematic morphing units. A systematic design methodology is given to map thick-panel origami units with 6R spatial overconstrained linkages, which yields a complete library of single-DoF morphing units with tunable geometries.

Chapter 4 deals with morphing surfaces, which are obtained by tessellating or assembling morphing units. Guided by tiling and pattern techniques, the units are combined into large-scale tessellations that can bend, expand, and twist. These surfaces are of single DoF whereas bifurcations may exist for additional motion possibilities. Two particular assemblies with complex behaviours, including a wrapping surface and a curling surface, are also presented. They will be leveraged for robotic studies in later chapters.

Chapter 5 presents a robotic gripper developed from the wrapping surface, whose grasping motion is controlled by a single motor. The gripper's design, modelling, actuation, and fabrication are detailed. Its grasping performance is experimentally characterised. It is found that even with a relatively simple design and actuation system, the gripper shows good adaptability to a variety of daily objects. Compliance, i.e., the ability to deform and conform to different shapes, is observed on the gripper. It is further validated by grasping objects that are asymmetric about the gripper's finger arrangements.

Chapter 6 further develops the gripper prototype into a platform for object manipulation. In addition to the wrapping motion, this chapter analyses the gripper's bifurcations and compliance in detail, which are then leveraged to produce various motions. Aided by a differential mechanism, only two motors are required to achieve eight motion modes and the compliant transitions among these motions. The gripper is then explored to manipulate cuboids, balls, and cones, which exhibit translational, rotational, and complex motion trajectories.

Chapter 7 switches to the curling surface, based on which a reconfigurable robot concept is developed to mimic a millipede. The surface can morph into a coil shape and also reconfigure into other morphologies such as waves and triangles. A

detailed kinematic study is given to analyse the surface's bifurcations and curling profiles. Suitable tendon-based actuation and fabrication methods are adopted to enable a six-segment millipede robot from the surface. Experiments are then carried out to validate the reconfigurability of the robot and explore its potential for different locomotion strategies such as rolling and crawling.

Finally, Chapter 8 provides a summary of the accomplishments within this thesis and reveals potential avenues for future research.

This thesis will resonate with individuals working on linkage mechanisms, origami design, and robotics. The author aims to provoke readers to reconsider the integration of origami into robot design from a kinematic perspective and explore how traditional linkages can be utilised for novel applications. Always remember, origami is more than just a pretty face.

Chapter 2

Literature Review

2.1 Soft robotics

Soft robotics is an emerging technology in the last few decades (Laschi et al., 2016). Made of soft materials akin to those in living organisms, soft robots have shown great adaptability and flexibility compared to traditional industrial robots, thereby bridging the gap between humans and machines (Rus and Tolley, 2015). This section gives a brief overview of soft robots, with a focus on how controllable shape changes are achieved on soft materials.

2.1.1 Definitions and applications

In structural terms, conventional robots are commonly composed of rigid links and joints (Bauer et al., 2014). They excel in precise control for extensive industrial use, but are in no way comparable to biological systems which function through continuously deformable bodies. Specifically, the rigidity within traditional robots results in a lack of compliance, making the robots less adaptable to interact with

the environment. To improve the performance of robots, compliant and soft materials are used to design fully or partially soft-bodied robots, known as soft robots (Rus and Tolley, 2015).

The soft bodies have taken the capabilities of a robot to a new level. Soft robots have demonstrated versatile functions including locomotion (Shepherd et al., 2011), grasping (Hughes et al., 2016), and manipulation (Puhlmann et al., 2022), as well as general interactions with humans and their surroundings (Arnold and Scheutz, 2017). For instance, rolling (Gu et al., 2020), crawling (Lu et al., 2018), walking (Drotman et al., 2021), jumping (Gorissen et al., 2020), and swimming (Li et al., 2021) have been achieved by a variety of bio-inspired soft robots, which can navigate through unstructured environments Calisti et al. (2017). Soft grippers also outperform their rigid counterparts when dealing with unknown or fragile objects, since the inherent compliance allows the grippers to conform to diverse shapes and sizes (Shintake et al., 2018). Additionally, soft robots have been employed in households and clinical scenarios (Rossiter and Hauser, 2016), with initial products already available in the market (Amend et al., 2016).

2.1.2 Bending, expanding, and twisting of soft materials for soft robotic applications

The compliant deformation of soft materials is essential for soft robots to achieve their functionalities (Gariya and Kumar, 2021). Purely soft materials cannot always be directly used as the robot body as they tend to possess large or even infinite degrees of freedom (DoFs), making it very challenging to model, actuate, and control (Iida and Laschi, 2011; Majidi, 2019). It is therefore very important

to realise controllable shape changes in soft materials so that they can achieve desirable motions for robots. Specifically, the high-DoF soft materials need to be actuated into pre-programmed configurations. In most cases, only limited mobility is required to perform specific functions, where bending, expanding, and twisting form the fundamental components for soft deformation (Liu et al., 2022a). This part reviews how the three basic motions and more complex behaviours are attained on soft materials for soft robotic applications.

Many actuated soft material motions are achieved via soft fluidic actuators (SFAs), which are either pneumatic or hydraulic (Pagoli et al., 2021a). The former is also known as soft pneumatic actuators (SPAs).

Among SFAs, pneumatic networks (PneuNets), originally developed by the Whitesides Research Group at Harvard (Ilievski et al., 2011), are one of the most widely employed. Figure 2.1(a) illustrates the working principle of a PneuNets actuator made up of interlinked chambers inside an elastomer. When the actuator is pressurised, expansion occurs at the most 'soft' or 'stretchy' area and the actuator bends towards the more 'rigid' part. The latter is also known as the strain limiting layer and usually appears in the form of a paper piece. By properly arranging the chamber directions, coupled bending and twisting motions can also be achieved on PneuNets (Wang et al., 2018a).

Fiber-reinforced actuators are also a commonly-used SFA (Galloway et al., 2013). As shown in Fig. 2.1(b), each actuator consists of an elastomeric chamber wrapped with inextensible reinforcements. Depending on how the reinforcements are arranged, the actuator can extend, expand, bend, or twist upon pressurisation (Connolly et al., 2017).

Other SFAs include but are not limited to the McKibben artificial muscle

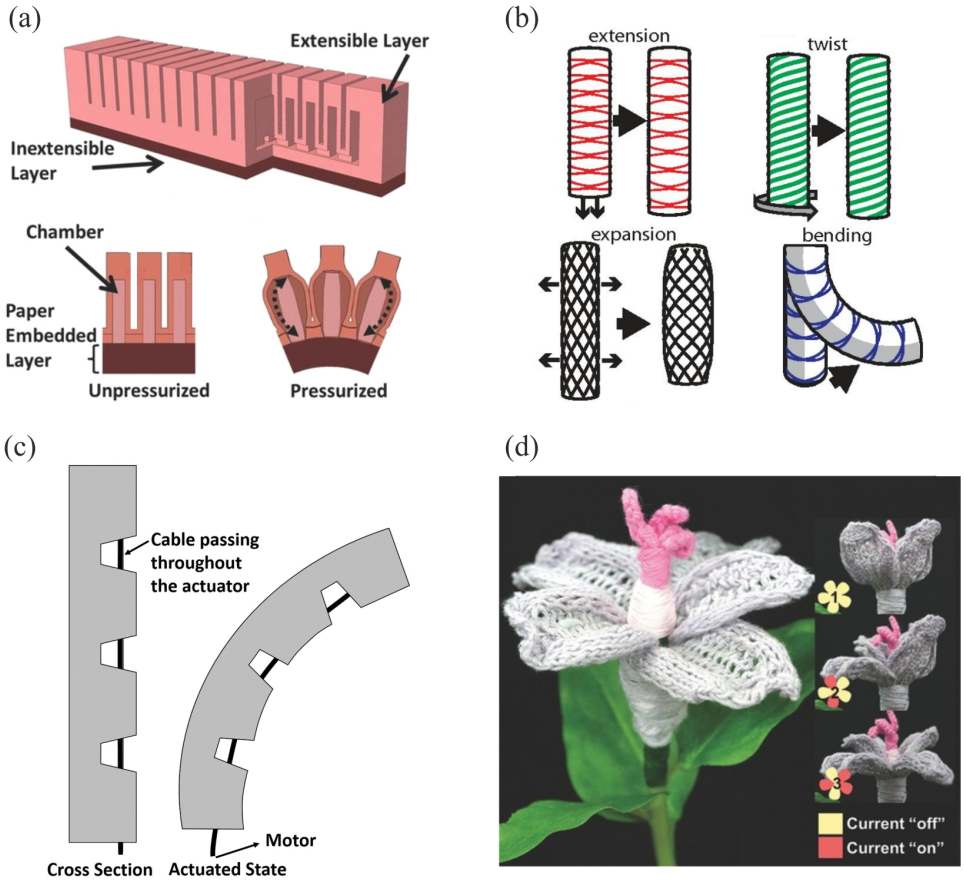


Figure 2.1: Controllable shape changes on soft materials. **(a)** A PneuNets actuator for bending (Mosadegh et al., 2014). **(b)** Fiber-reinforced actuators that extend, twist, expand, and bend (Connolly et al., 2017). **(c)** Tendon-based actuation to bend a finger (Zaidi et al., 2021). **(d)** Complex shape changing achieved via shape memory alloys (Han and Ahn, 2017).

(Tondu, 2012) and textile-based soft actuator (Cappello et al., 2018). The former is also known as the braided pneumatic muscle, which shrinks in length and expands radially when inflated (Doumit et al., 2009). The latter has a similar working principle to the fibre-reinforced actuator but is lighter with a lower operation pressure (Cappello et al., 2018).

In addition to SFAs, tendon-based actuation and active materials are exploited

for controllable shape changes in soft robots. The tendon-based mechanism, usually powered by electrical motors, is widely exploited in the bending of robotic fingers (Mishra et al., 2017; Hussain et al., 2020; Zaidi et al., 2021) or arms (Wockenfuß et al., 2022). An example of a bending finger is depicted in Fig. 2.1(c), which requires a certain level of material rigidity. The active materials allow the robots to morph into desired shapes as a response to environmental stimuli such as heat, electrical, and magnetic fields. The exact shape changes can be very complex as shown in Fig. 2.1(d) and are characterised by the material properties (Lee et al., 2019; Liu et al., 2021a), geometric design (Han and Ahn, 2017; Boley et al., 2019; Zhao et al., 2022a), imposed constraints (Digumarti et al., 2019), and the external stimuli (Kotikian et al., 2019; Guseinov et al., 2020).

2.1.3 Advantages and limitations

Each technique to achieve controllable shape changes on soft materials has its inherent advantages and limitations.

The SFAs and tendon-based designs can produce reliable and high force output (Pagoli et al., 2021a). However, both require external devices such as pumps or motors, whilst the former is especially heavy and bulky as a driving pressure of 10 - 100 kPa is normally required. The fabrication for both is at a low cost and relatively straightforward by casting or assembling commercially available products. Although the process used to be labour-intensive, laser cutting and 3D printing techniques have been adopted to facilitate the fabrication (Xavier et al., 2022; Jeong et al., 2021). It should be noted that for tendon-based actuation, the shape-changing possibilities are quite limited, most of which are purely bending.

The active soft materials have made it much easier to achieve fully untethered robots (Chen et al., 2018). Nonetheless, many of them have low output force and are thus not sufficient for robotic applications (Pagoli et al., 2021a). In addition, the materials are expensive, difficult to fabricate, and require rigorous operation of external stimuli.

Whatever the advantages and limitations, a common feature is that these methods are all highly dependent on material properties to achieve desired shape changes. As a result, many designs are based on trial and error to impose physical constraints on soft materials (Coevoet et al., 2017). It is also computationally expensive to achieve precise modelling and control on those materials for soft robotic applications (Fang et al., 2020; Yasa et al., 2023). Origami, the ancient art form of paper folding, has provided a promising alternative to purely soft materials. Its applications in robotics will be reviewed in the next section.

2.2 Origami robots

Origami has been extensively used from nanoscale to macroscale, such as DNA origami (Sarraf et al., 2023), biomedical devices (Kuribayashi et al., 2006), deployable shelters (Thrall and Quaglia, 2014), and foldable antennas (Georgakopoulos et al., 2021). The in-built crease structure of origami also has the potential to exhibit soft-bodied properties, making it a good candidate to replace purely soft materials (Rus and Tolley, 2018; Rus and Sung, 2018). Like the last section, here an overview of origami-inspired robots is provided and the shape changes achieved by a variety of origami patterns are discussed.

2.2.1 Definitions and applications

Origami, where 'ori' means fold and 'kami (gami)' means paper, is able to transform 2D paper sheets into intricate 3D configurations via folding along a set of creases (Hull, 1994). Composed of rigid facets and flexible folds, origami can exhibit inherent compliance no matter whether the facets are stretchable or not. As a geometric concept, the deformation of origami can be calculated with ease (Lang, 2007). The motions of origami are often coupled through in-built folds, leading to lower or more controllable DoFs while it is still able to achieve similar shape-changing behaviours like soft materials. These features make origami a promising candidate for robotic structures.

A robot, whose backbone is based on origami structures, can achieve the same functions to its soft material counterparts (Li et al., 2017). Potential applications include locomotion (Miyashita et al., 2015), grasping (Li et al., 2019), manipulation (Kan et al., 2020), and the general interaction with the environment (Zhakypov and Okamura, 2022). The use of paper folding techniques has not only simplified the modelling and control of robotic motions (Bhovad et al., 2019; Treml et al., 2018), but also reduced fabrication complexity to some extent as engineers are used to building 3D objects from 2D sheets (Onal et al., 2012). Kirigami ('kiri' means cut), a variation and less restrictive form of origami that incorporates slits in addition to folding, has also been exploited in robotics (Sareh and Rossiter, 2012; Tao et al., 2023). Recent examples include robotic crawlers (Tang et al., 2019), grippers (Yang et al., 2021), and stretchable skins (Khosravi et al., 2021), whose mechanical properties are improved via the kirigami design.

Table 2.1: Commonly used cylindrical origami for robotic structures

Origami	Motion 1	Motion 2	Motion 3	Example
Miura-ori pattern	Linear	– – –	– – –	Fig. 2.2(a)
Yoshimura origami Bellows fold	Linear	Bend	– – –	Fig. 2.2(b)
Kresling origami Diagonal fold Twisted tower	Rotational	Linear	Bend	Fig. 2.2(c) Fig. 2.2(d)
Waterbomb origami	Radial	Linear	– – –	Fig. 2.2(e)

2.2.2 Bending, expanding, and twisting of origami structures for origami robots

To date, most, or even all, origami robots are built from existing origami patterns (Rus and Tolley, 2018; Rus and Sung, 2018). Once folded, these patterns demonstrate different motion behaviours such as bending, expanding, or twisting with unique mechanical properties. This part summarises commonly used origami patterns for robots and their associated motions.

Whilst coming from flat sheets, many origami patterns are folded into cylindrical forms first and then used as robotic structures. Common patterns are given in Table 2.1 along with robotic prototypes in Fig. 2.2.

In Table 2.1, the linear motion refers to extending and contracting along the axial direction of the origami cylinder (Li and Wang, 2015). Upon contraction, the bending stiffness of the cylinder reduces dramatically and many applications are built on this feature to achieve bending with additional driving mechanisms (Lee et al., 2020). The rotational motion is actually the twist of the cylinder and is always coupled with its expansion or contraction. The radial motion indicates the

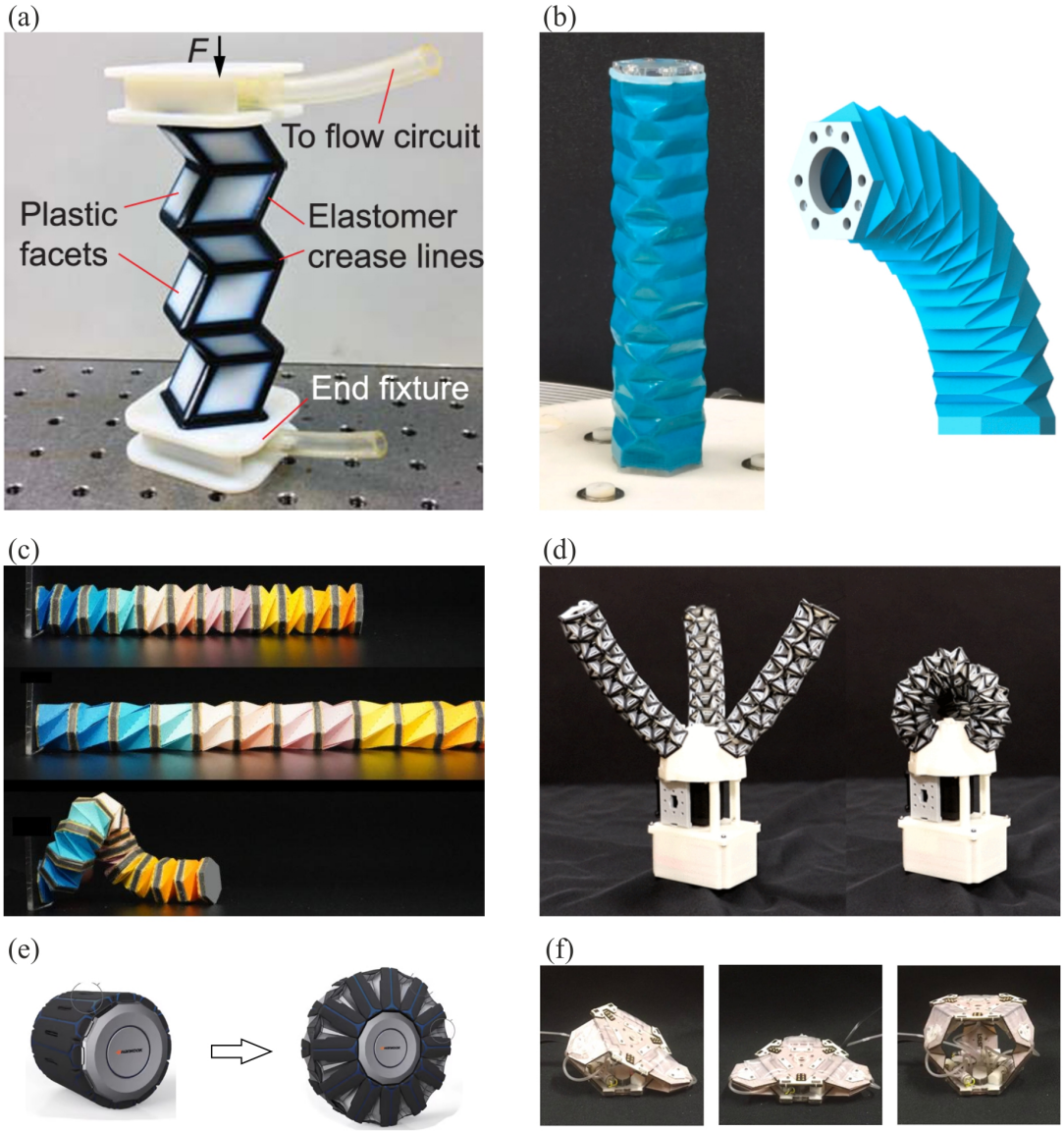


Figure 2.2: Origami robots. **(a)** A shape-morphing structure based on the Miura-ori fold (Li and Wang, 2015). **(b)** A robotic arm based on a bellow-like Yoshimura pattern that is extensible and bendable (Zhang et al., 2022). **(c)** A robotic arm based on the Kresling origami (Kresling, 2020) that can extend and twist (Wu et al., 2021). **(d)** A robotic gripper whose fingers are based on the origami twisted tower (Lee et al., 2020). **(e)** An expandable wheel based on the tessellation of six-crease waterbomb origami (Lee et al., 2017). **(f)** A pneumatic origami platform based on the six-crease waterbomb unit cell. (Robertson et al., 2021)

expansion along the waterbomb tube's radial direction. A not very evident twist has also been reported for the waterbomb origami while it has not been applied in robotics yet (Feng et al., 2018).

Other origami patterns include the square twist (Jiao et al., 2021), the Ron Resch origami (Liang et al., 2023), and unit cells from the cylindrical origami. Some have also been used in the design of robots (Li et al., 2019; Robertson et al., 2021), as shown in Fig. 2.1(f).

Origami has brought some interesting mechanical features, such as bistability and reconfigurability, thereby reducing the control complexity and increasing the motion dexterity. For the bistable feature, a special design of the Kresling origami has been used to program its crawling motions without digital controllers (Bhovad et al., 2019). Logic gates are also realised on the eight-crease waterbomb origami unit for onboard computation (Treml et al., 2018). The reconfigurable property has been exploited in origami grippers to change their grasping modes (Zhakypov et al., 2018; Liu et al., 2021b). Furthermore, the folding concept is explored on a few robotic platforms such as Mori3 by Belke et al. (2023), which can reconfigure itself and carry out various tasks.

2.2.3 Advantages and limitations

Origami can overcome some of the existing issues amongst soft materials. Compared to those robots based on fully soft materials, origami has been incorporated as a skeleton and enables a variety of controllable motions with a simpler design. As a geometric concept, the shape alteration of origami does not purely rely on the material property and can be more easily predicted (Lang, 2007), which is much

less computationally expensive compared to that of the soft ones. It also offers more flexibility within material selection, since only creases need to be soft and facets could be mainly rigid. 3D printing and laser cutting also make the fabrication of origami sheets more autonomous (Onal et al., 2014; Liu et al., 2017).

However, as mentioned earlier, most or even all origami robots rely on existing patterns, which are usually developed for zero-thickness sheets such as paper (Jeong and Lee, 2018), polymer films (Onal et al., 2012), or 3D-printed layers (Kan et al., 2019). The former two are prone to fatigue from repeated folding and unfolding. The latter neglects the material thickness, leading to the inaccuracy of motion predictions. In addition, many designs function in cylindrical configurations, which require a pre-folding process on the 2D sheets or need to be directly made into 3D tubular forms. The fabrication complexity is thus increased. Lastly, there is still a lack of flexibility in designing desirable motions, regardless of numerous origami patterns. For instance, the twisting behaviour of Kresling origami is coupled with axial extension and contraction, which cannot be separated.

With the emerging concept of thick-panel origami (Chen et al., 2015), it becomes possible to take material thickness into account when designing origami robots. However, the current thick-panel origami design mostly focuses on flat foldability and kinematic compatibility with the zero-thickness counterpart (Peng and Chirikjian, 2023), which will be reviewed later in detail. These concepts are more interesting to space engineers or mathematicians but less accessible to roboticists who care more about the exact motion behaviours. Some limited attempts are claimed to have designed origami grippers from thick materials (Liu et al., 2020a), whilst they are just a simple parallel mechanism. No insight has been provided regarding a generic design approach for thick-panel origami in robots.

Given the aforementioned limitations and research gaps, a more comprehensive method to develop robotic structures from thick materials is necessitated. These structures should stay as flat as paper sheets in the unfolded state whilst the thickness is not negligible. Their folding process will generate a variety of tailored motions that can be readily used in the design of functional robots. All these aspects will be addressed in this thesis.

2.3 Functional robots

Before moving into the design of origami structures, it is necessary to review some robots from a functional perspective. This section looks at challenges in end effectors for grasping and manipulation, as well as reconfigurable robots. The review not only serves as the background information for the robots to be developed in Chapters 5 - 7, but also specifies the requirements for shape-changing structures to overcome the challenges.

2.3.1 End effectors for grasping and manipulation

The adaptability and versatility of human hands enable grasping and manipulating objects as daily tasks (Cobos et al., 2008; Wei et al., 2022). Significant effort has been devoted to developing end effectors, i.e., robotic hands and grippers, to replicate these functions (Zhang et al., 2020; Mason, 2018). In general, robotic hands are often engineered with multiple fingers to emulate the intricacy and precision of human hand articulations. One example is the Shadow Dexterous Hand as shown in Fig. 2.3(a), which possesses 20 actuated DoFs for grasping and manipulation tasks (Andrychowicz et al., 2020). Its soft material counterpart,

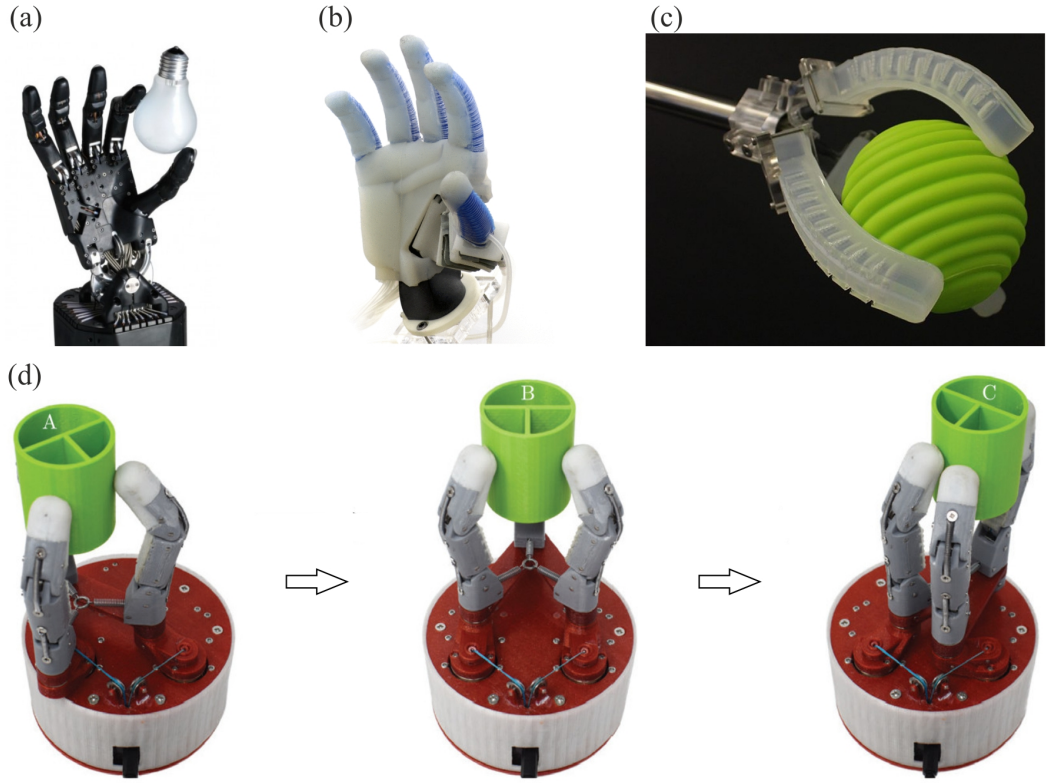


Figure 2.3: End effectors for grasping and manipulation. **(a)** A rigid hand, Shadow Dexterous Hand (Andrychowicz et al., 2020) and **(b)** its soft counterpart, RBO Hand 3 (Puhlmann et al., 2022), both of which can grasp and manipulate objects. **(c)** A soft gripper with three fingers for grasping only (Truby et al., 2018). **(d)** A three-finger gripper with reconfigurable palm, known as the RUTH gripper, for in-hand manipulation with only three fingers (Lu et al., 2021).

for instance, the RBO Hand 3 shown in Fig. 2.3(b), possesses 16 independent degrees of actuation for 33 grasp postures (Puhlmann et al., 2022). Similar five-fingered hands include but are not limited to the PISA Hand (Della Santina et al., 2015) and the BeBionic Hand (Medynski and Rattray, 2011). While these designs offer enhanced dexterity to mimic human hand movements, their high DoFs also necessitate complex control strategies (Andrychowicz et al., 2020). Additionally, the increased DoFs can lead to reduced system robustness (Yim et al., 2007).

In this respect, researchers have explored various approaches to simplify the design of end effectors while preserving their functions to the largest extent. One intuitive approach is to develop end effectors with a reduced number of fingers such as the SDM Hand (Dollar and Howe, 2010) and the GR2 gripper (Rojas et al., 2016). The former is a four-finger design with compliant materials, controlled by a single motor for adaptable grasping. The latter has two fingers with elastic joints. Each finger, controlled by a servo motor, contributes to object grasping and manipulation on the 2D plane.

It should be noted that grasping and manipulation are two distinctive functions. Manipulation occurs when an end effector applies forces to purposefully change the state of a grasped object, which is more than just holding it (Lynch and Park, 2017). Hence, a successful grip could not guarantee that the end effector can manipulate objects, where additional motions are required. Hence, due to a lack of motion dexterity, many grippers, such as the SDM Hand and the three-finger gripper shown in Fig. 2.3(c), are not suitable for manipulation tasks.

To address the challenge, a significant interest emerges in mechanically reconfigurable grippers to achieve dexterous motions for object manipulation. Fingers with adjustable lengths or stiffness are used to expand the gripper's motion range and generate multiple grasping modes (Yoon et al., 2022; Pagoli et al., 2021b). The arrangement of finger positions has also been proven to impact the manipulation capability (Teeple et al., 2021), and thus, a reconfigurable palm has been introduced in the RUTH gripper depicted in Fig. 2.3(d) (Lu et al., 2021). Made from a 5R planar linkage, the palm can shift finger positions to facilitate interaction with objects. With relatively complicated designs, these grippers have achieved manipulation tasks in 3D space with a smaller number of actuators.

To summarise, for end effectors with both grasping and manipulation functions, it is important but also challenging to strike a balance between motion dexterity and control complexity, with the need for a simplified mechanical design. If the end effector itself is seen as a shape-changing mechanism, it is desired to meet the following requirements.

- The mechanism can wrap around objects to perform grasping. Compliance for shape adaptation is preferable.
- The mechanism possesses a good variety of motion modes, which can facilitate the manipulation of objects.
- The mechanism should have relatively low DoFs, which can be controlled with a small number of actuation inputs.
- The mechanism is easy to model and fabricate wherever possible, as a complex mechanical system is not undesirable.

2.3.2 Reconfigurable robots

Reconfiguration refers to the process where a system is arranged into different configurations (Brunete et al., 2017). In terms of robots, reconfigurability makes it possible for them to change shapes and thus better adapt to the environment (Støy, 2015). In addition to aiding object manipulation, reconfigurable robots play a significant role in locomotion tasks. For instance, a variable-size wheel, as previously shown in Fig. 2.2(e), can traverse different terrains (Lee et al., 2017).

Many reconfigurable robots come with a modular design (Seo et al., 2019; Castano et al., 2002), where the mechatronic modules can be disassembled and

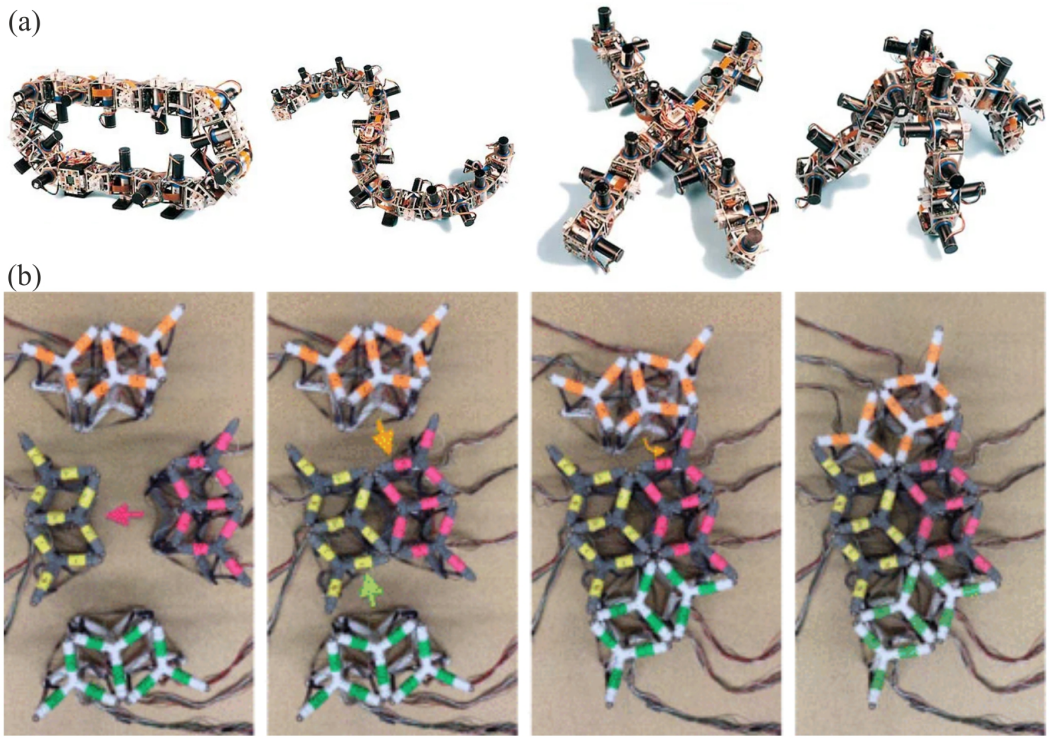


Figure 2.4: Modular reconfigurable robots such as **(a)** the PolyBot (Yim et al., 2000), a chain-type mechanism and its four configurations, and **(b)** the StarBlocks (Zhao et al., 2023) based on lattice structures and its self-assembly process.

then reconnected to produce task-specific morphologies, like chains (Yim et al., 2000; Bansal et al., 2023) or lattice structures (Zhao et al., 2022b, 2023), as shown in Fig. 2.4.

The reconnection of individual modules can sometimes cause misalignment, leading to system failure (Yao et al., 2019). Hence, researchers have also explored alternative approaches to changing the morphology of the overall robotic structure. The Mori robot series, inspired by origami folding, can produce diverse 3D structures from the same surface of 2D polygons (Belke and Paik, 2017; Belke et al., 2023), as shown in Fig. 2.5(a). Another origami robot, based on connected Kresling modules, can change its morphologies to navigate through confined space (Ze

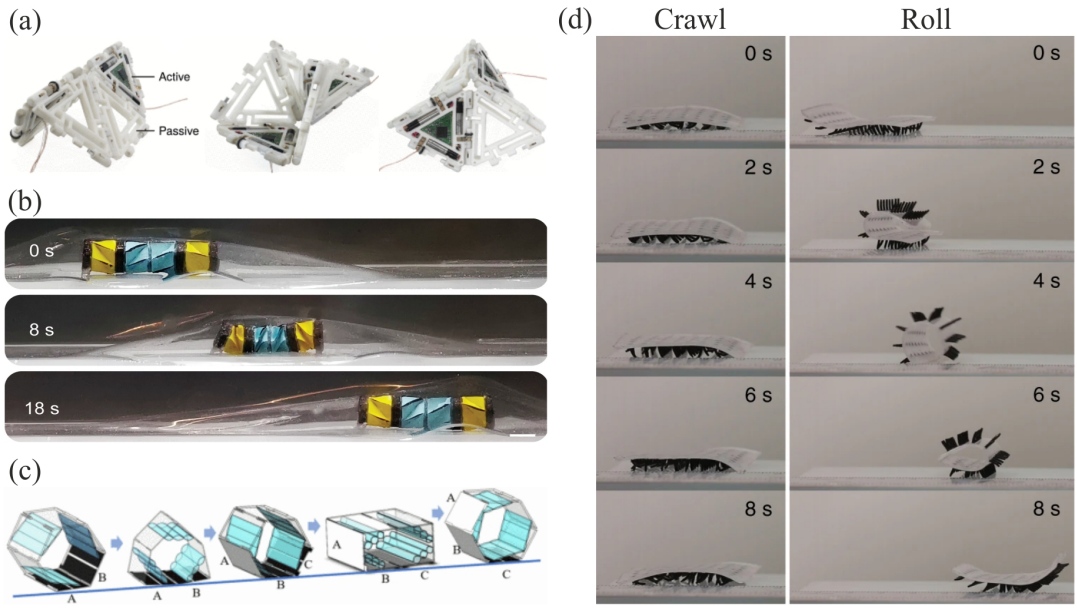


Figure 2.5: Other reconfigurable robots. **(a)** Mori, a modular origami robot that generates different configurations using different folds (Belke and Paik, 2017). **(b)** A chain robot based on the Kresling origami that can shrink and expand (Ze et al., 2022b). **(c)** A robot whose backbone is a 3-DoF planar linkage climbs up the slope (Liu et al., 2022b). **(d)** A soft robot that can crawl and roll (Gu et al., 2020).

et al., 2022b), as exemplified in Fig. 2.5(b). Additionally, multi-DoF mechanisms, which naturally possess multiple configurations, are exploited (Liu et al., 2022b). As illustrated in Fig. 2.5(c), a robot can roll up a rising slope by changing its cross-sectional shapes. Furthermore, malleable materials are employed in robots so that they can alter their locomotion modes (Shah et al., 2021; Baines et al., 2022; Gu et al., 2020), as evidenced by a soft-material robot in Fig. 2.5(d).

In general, more module reconnections and higher DoFs of a robot indicate better reconfigurability, making it more suitable to adapt to the environment and complete various tasks. However, the connectivity changes make the system less robust and the excessive DoFs would also complicate the mechanical, electrical, and control design of the robot Brunete et al. (2017). It is highly challenging to

achieve a good variety of configurations with reduced module reconnections and system mobilities. Hence, if a structure or mechanism is developed for reconfigurable robots, the following aspects should be considered.

- The structure or mechanism can generate multiple configurations as desired.
- When realising the required configurations, the number of reconnection activities should be minimised.
- When realising the required configurations, the number of overall DoFs in the system should be as low as possible for good controllability.

It should be noted that reconfigurable robots can be further categorised into manually reconfigurable and self-reconfigurable systems (Brunete et al., 2017), for which the latter is more desired. However, the thesis will only focus on the design of shape-changing structures for multiple configurations and their associated mobility. The means of reconfiguration is beyond the research scope.

2.4 Shape-changing structures with thickness

Jumping out of the robotics community, this section reviews the design of origami-inspired shape-morphing structures and relevant mechanisms. As mentioned in Section 2.2, robotic structures from thick materials are desired. Hence, the scope here is limited to those considering material thickness.

2.4.1 Rigid origami and thick-panel origami

Rigid origami is a branch of origami concerned with folding structures using flat rigid sheets joined by creases (Dai and Rees Jones, 1999). That is, the panels of

the sheet cannot be bent or twisted during the folding process and must remain flat at all times.

Rigid origami has an inbuilt connection with linkages. Each crease is treated as a revolute joint. Rigid origami of zero-thickness sheets can thus be modelled as an assembly of linkages. Each vertex, where creases intersect, is kinematically equivalent to a spherical linkage in a closed loop chain (O'Rourke, 2011). According to the Kutzbach criterion, the DoFs of a single vertex depend on the number of creases meeting there, which goes as

$$M = n - 3 \tag{2.1}$$

where M is the number of DoFs and n is the number of creases.

For instance, a four-crease vertex, whose configuration was previously shown in Fig. 1.1(a) left, has a single DoF. The mobility rises when more creases intersect at the vertex. In general, a five-crease vertex yields two DoFs and M rises to three when six creases meet, both of which are illustrated in Fig. 2.6. The total DoFs of an origami pattern consisting of many vertices can be calculated topologically (Tachi, 2009). For example, the Miura-ori pattern, a tessellation of four-crease origami, is a single-DoF mechanism no matter how many vertices exist.

A few years ago, a new method was proposed to design origami with thickness where creases are replaced by folding lines (folds) at either the top or bottom surfaces of a thick panel (Chen et al., 2015). The new mechanical model is known as thick-panel origami. Since the folds no longer meet at a vertex, the model becomes a spatial linkage, which is a closed chain consisting of n links and n revolute joints if the number of folds is n. According to the Kutzbach criterion,

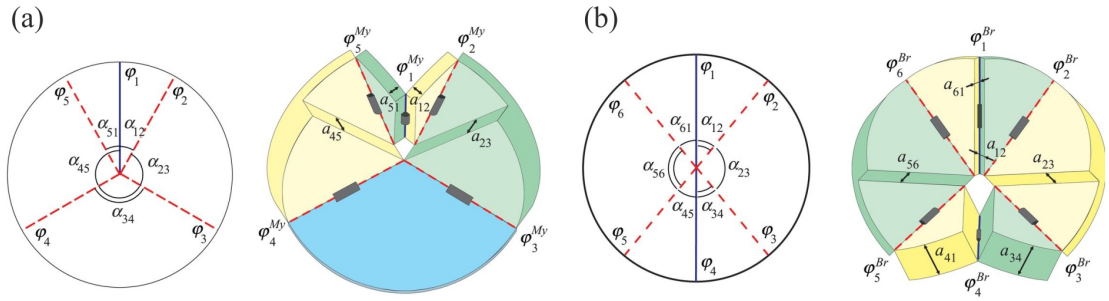


Figure 2.6: Thick-panel origami originating from **(a)** five-crease and **(b)** six-crease vertices. The former is modelled as the Myard linkage and the latter is a Bricard linkage (Chen et al., 2015).

the mobility of the thick-panel origami is

$$M = n - 6 \tag{2.2}$$

In general, n should be 7 so that the thick-panel origami has a single DoF, indicating a stronger mechanical coupling compared to the zero-thickness one. However, some linkages are mobile without satisfying $n \geq 7$, which are known as overconstrained spatial linkages. As shown in Figs. 1.1 and 2.6, the thick-panel versions of the four-crease, five-crease, and six-crease vertices are kinematically equivalent to the Bennett linkage, the Myard linkage, and the Bricard linkage, respectively. All these linkages yield single mobility.

2.4.2 Shape-changing structures inspired by thick-panel origami

Many scholars design thick-panel origami from existing zero-thickness sheets by adjusting the panel thickness and mapping them with spatial overconstrained linkages. Large-scale origami tessellations, i.e., repeated patterns consisting of multiple

Table 2.2: Thick-panel origami tessellations and their properties

Thick-panel tessellation	**Equivalent linkage**	**Unfolded state***	**Folded state****
Miura-ori pattern (Zhang and Chen, 2018a)	Bennett linkage	Non-flat***	Compact
Diamond pattern**** (Zhang and Chen, 2018b)	Plane-symmetric Bricard linkage	Non-flat*****	Compact
Waterbomb origami (Chen et al., 2016) (Zhang and Chen, 2021)	Plane-symmetric Bricard linkage	Non-flat	Compact
Triangular Resch pattern (Yang et al., 2022a)	Plane-symmetric Bricard linkage	Non-flat	Non-compact

* The tessellation is deployed into a surface-like profile, as exemplified in Fig. 2.7 left. If all constituent panels are of uniform thickness, the surface is flat. Otherwise, it is non-flat.
** The tessellation is fully folded when some panels collide with each other, as shown in Fig. 2.7 right. If there is no gap between adjacent panels, the folded configuration is compact. The concept is usually referred to as flat foldability for zero-thickness origami sheets.
*** Some uniform-thickness cases have been reported by Zhang and Chen (2023). However, the study incorporates a tap spring hinge that cannot be treated as a revolute joint.
**** The pattern is the same as the Yoshimura origami (Pratapa and Bellamkonda, 2022).
***** Special cases occur where all panels have a uniform thickness, as shown in Fig. 2.7(b).

vertices, are thus developed into thick-panel versions. Each thick-panel tessellation can be modelled as an assembly of spatial linkages. The commonly studied ones are summarised in Table 2.2, with examples illustrated in Fig. 2.7. Due to mechanical coupling, these thick-panel tessellations remain single-DoF as their constituent linkages.

Despite the extensive work, all the tessellations listed in Table 2.2 are based on the Bennett linkage (Bennett, 1903) or the plane-symmetric Bricard linkage (Bricard, 1926). It is unclear whether other spatial overconstrained linkages, such as the line-symmetric Bricard linkage (Mavroidis and Roth, 1995) and the Wolhart

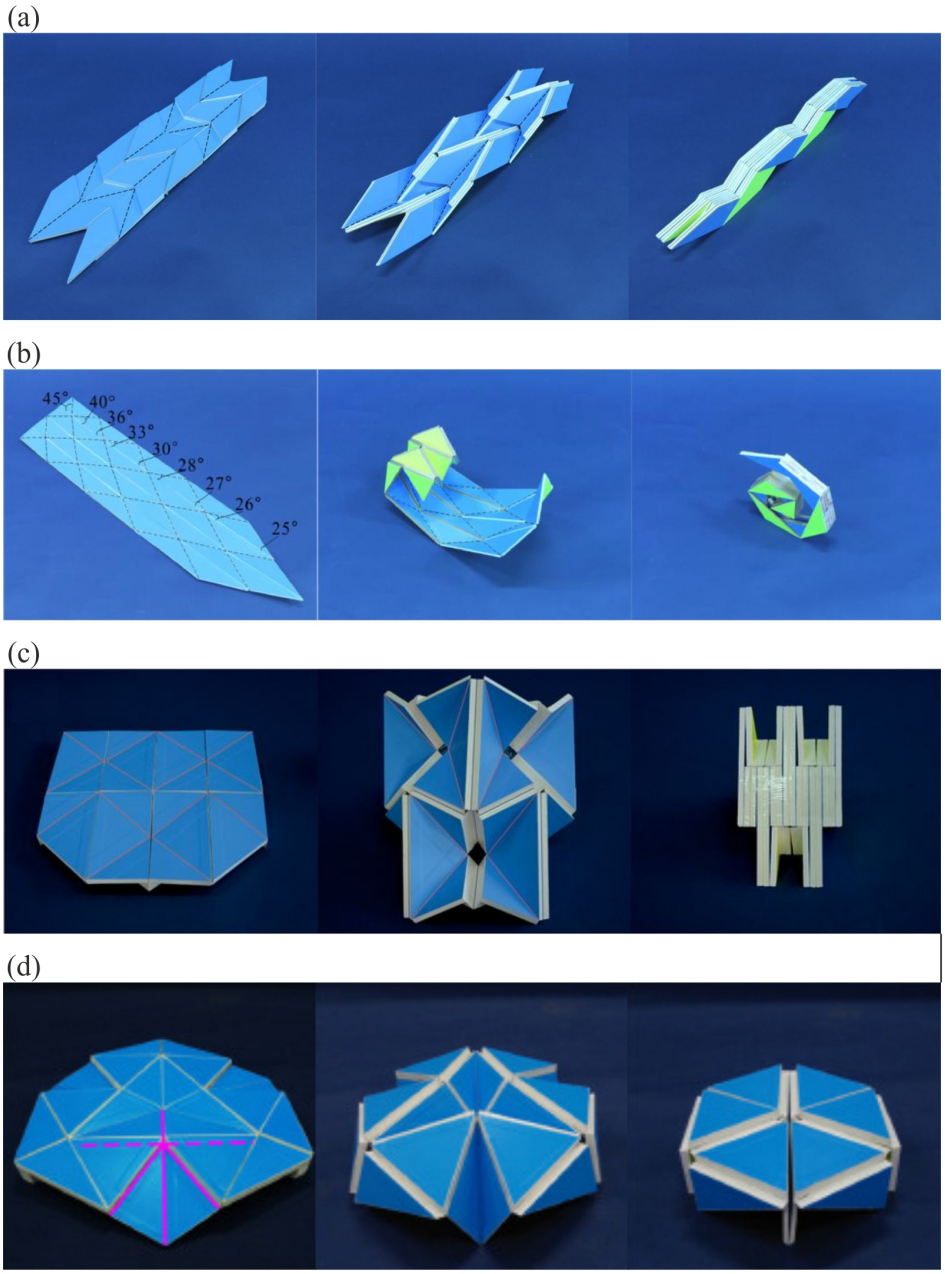


Figure 2.7: Thick-panel origami tessellations based on **(a)** Miura-ori pattern (Zhang and Chen, 2018a), **(b)** extended Diamond pattern where sector angles are non-equal (Zhang and Chen, 2018b), **(c)** Waterbomb origami (Zhang and Chen, 2021), and **(d)** Triangular Ron Resch pattern (Yang et al., 2022a). Only the tessellation in **(b)** is flat on both top and bottom surfaces in the unfolded state.

6R linkage (Wohlhart, 1987), can used in thick-panel origami tessellations.

In addition, since the concept of thick-panel origami was originally developed for space solar panels (Chen et al., 2015), engineers care more about whether the tessellations can be compactly folded to save up space. Researchers have also investigated whether the motions of thick-panel origami is identical to its zero-thickness counterpart, known as kinematic equivalence (Gu et al., 2021; Peng and Chirikjian, 2023). However, these properties are less appealing to roboticists, for whom the motion behaviours such as bending or twisting are more interesting. Recently, Peng and Chirikjian (2024) has reported a reconfigurable thick-panel origami design with the potential for multiple tasks, but it has not been put into practice. A knowledge gap clearly exists between origami engineers and roboticists.

Lastly, because the researchers put much emphasis on compact folding and kinematic equivalence, many of the thick-panel tessellations have to end up with uneven surfaces at the unfolded state, as summarised in Table 2.2. This is sometimes not desirable for robotic applications since such tessellations cannot be flat fabricated. As far as the author is aware, only the thick-panel Diamond pattern and its modified version can be turned into a flat surface (Zhang and Chen, 2018b; Pratapa and Bellamkonda, 2022), as illustrated in Fig. 2.7(b).

Although the current designs of thick-panel origami are not ready for robotic applications, they have some properties that can be exploited to tackle robotic challenges. For instance, the thick-panel origami could have multiple single-DoF motion paths (Peng and Chirikjian, 2024) as shown in Fig. 2.8. This is known as kinematic bifurcations (Kumar and Pellegrino, 2000). More specifically, an instantaneous increase of mobility exists at a certain state of the origami, where it can switch into different paths for various configurations. This feature improves

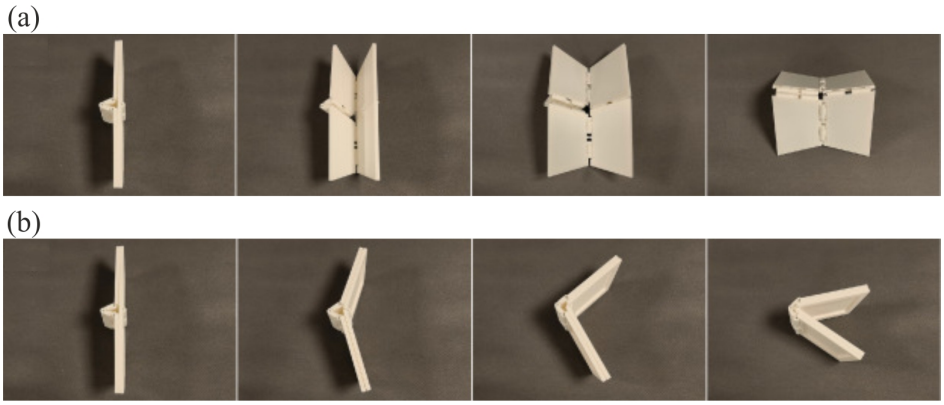


Figure 2.8: Two motion paths of a thick-panel origami based on a reconfigurable linkage (Peng and Chirikjian, 2024). Each path is of single DoF.

the reconfigurability of the origami without increasing its overall DoFs. Hence, it is promising to implement a simpler actuation and control strategy.

2.4.3 Shape-changing structures inspired by kirigami

The kirigami concept, a variation of origami, is also exploited to design shape-changing structures with thickness. As shown in Fig. 2.9(a), one example is a unit with a cut or slit in the middle (Wang et al., 2018b). The zero-thickness unit is an assembly of two 4R spherical linkages whilst the thick-panel one is based on the Waldron hybrid linkage (Waldron, 1968), another 6R spatial overconstrained linkage. The thick-panel unit is found to have panels of the same thickness when certain symmetric conditions are met, producing a flat tessellation in Fig. 2.9(b).

The cutting technique also inspires a few other designs with a uniform thickness, which go beyond the 4R, 5R, and 6R overconstrained linkages. For instance, Yang et al. (2022b) and Yang and You (2023) have reported two types of kirigami units composed of triangular prisms and parallelepiped. Each unit is modelled as an 8R linkage of two DoFs but its tessellation constrains its motion to single mobility. Li

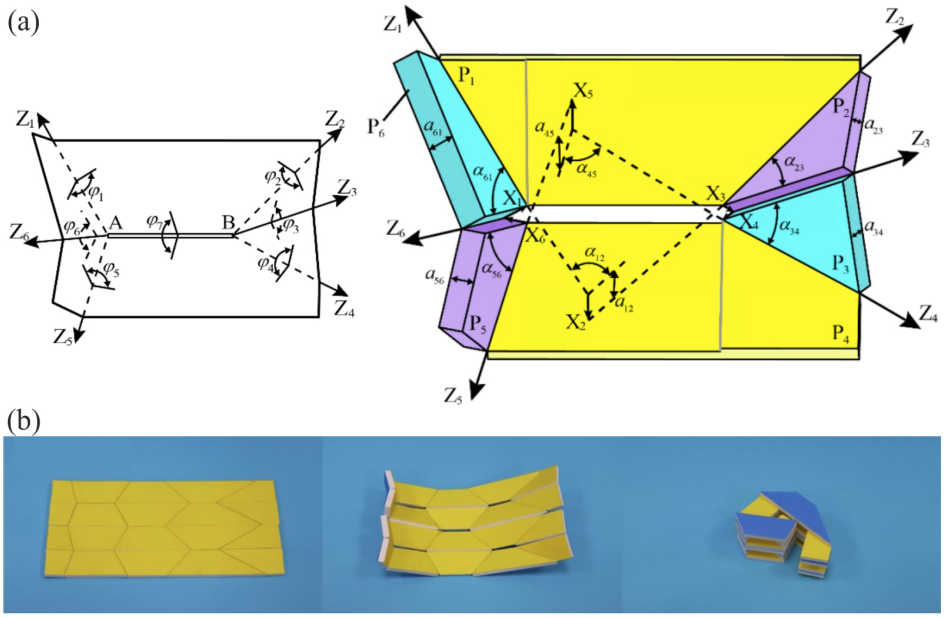


Figure 2.9: Thick-panel kirigami design based on the Waldron hybrid linkage. (a) The zero-thickness pattern and its thick-panel counterpart (Wang et al., 2018b). (b) Tessellation of the thick-panel units with uniform thickness (Wang et al., 2022).

et al. (2022) has uncovered a new mechanism made from hexagonal prisms that can deform into a 3D polyhedron. Kinematically, the design is a combination of the Bennett linkage and 4R spherical linkage.

The use of cuts has opened up the design possibilities. However, the current thick-panel kirigami units are often discovered by adding slits on a trial-and-error basis. In addition, some kirigami designs are just a simple geometric extension of the origami without cuts. For instance, the tessellations based on the Waldron hybrid linkage shown in Fig. 2.9(b) could become the origami surface in Fig. 2.7(b), when the slit length is zero. A more explicit, systematic, and comprehensive design methodology is necessitated to develop a library of shape-changing units.

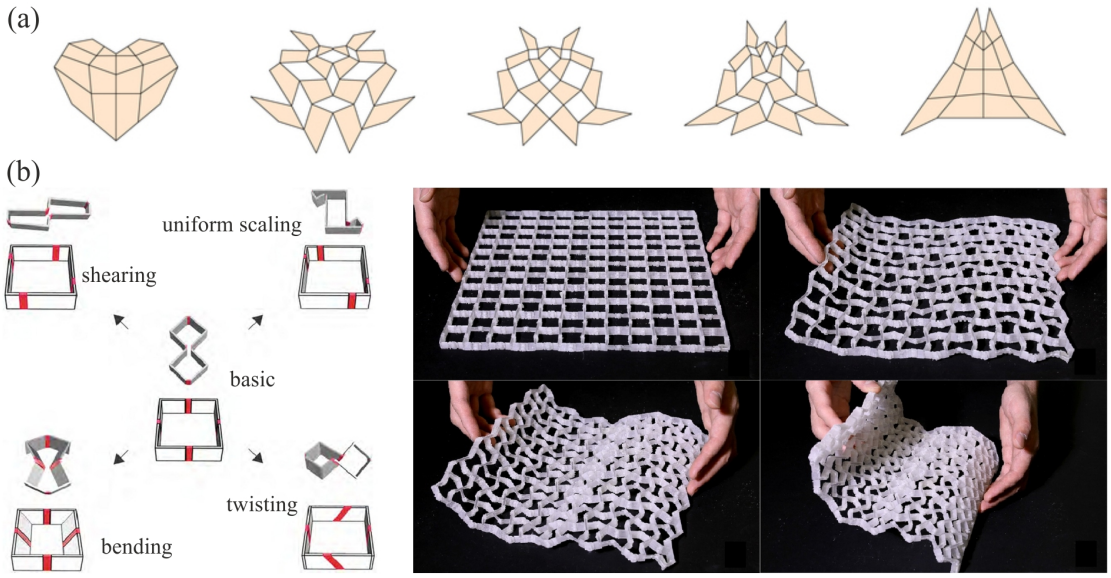


Figure 2.10: Shape-changing structures created by assembling linkages. **(a)** Planar 4R linkage for programmable shape morphing (Dudte et al., 2023). **(b)** 4R linkages with versatile motions and their assembly capable of bending (Ou et al., 2018).

2.4.4 Shape-changing structures by assembling linkages

Due to the intrinsic link between rigid origami and linkages, some scholars employ linkages directly to design shape-changing structures.

For instance, each void in the 2D kirigami design in Fig. 2.10(a) is based on a planar 4R linkage. With an algorithm-aided design framework, the flat surface can be transformed from a heart shape to a triangle (Dudte et al., 2023). The 4R linkage can also be modified into different units as shown in Fig. 2.10(b). Such units can be further assembled into large surfaces capable of complex deformations with single mobility (Ou et al., 2018).

Whilst the current research only employs 4R planar linkages, it is promising to look into more complex cases such as 6R spatial linkages and evaluate their shape-changing possibilities.

2.4.5 Summary and discussions

The shape-changing structures with thickness have two unique properties that are desired in robotic applications. They are listed as follows.

- All the shape-changing designs reviewed in this section can be programmed with single mobility, hence simplifying the actuation and control.
- Kinematic bifurcations improve some designs' reconfigurability without high DoFs, which could balance the motion dexterity and control complexity.

Yet, the designs are not ready for robotic use due to three obstacles.

- The motion possibilities are still limited.
  - The existing structures focus on the Bennett linkage, plane-symmetric Bricard linkage, Waldron hybrid linkage, and planar 4R linkage.
  - The current motions are usually bending-like. For more diverse motions, it is unclear whether other spatial overconstrained linkages can be used to develop thick-panel origami and its tessellations.
- Tessellations with uneven surfaces are not easy to fabricate.
  - Only a few uniform-thickness tessellations are obtained.
  - Whilst kirigami has the potential for uniform-thickness design, no systematic approach has been given so far.
- The values differ in the communities of origami engineers and roboticists.
  - Origami engineers are more interested in compactly folding origami or its kinematic equivalence with motions on the zero-thickness sheets.

– Roboticists prefer to use the dexterous motions of origami such as bending and twisting, or exploit their bifurcations for reconfigurability.

Addressing the above obstacles, this thesis will propose a systematic approach to designing thick-panel structures with uniform thickness, namely morphing surfaces. They are capable of a variety of motions, including bending, expanding, twisting, and even more complex behaviours. These surfaces will also be used to bridge the gaps between origami design and robotic applications. A series of robotic studies will be carried out on selected morphing surfaces, whose potential to balance motion dexterity and control complexity will be demonstrated.

2.5 Related theories in rigid origami

This section reviews enabling techniques for this thesis, which include the modelling of thick-panel origami, aspatial overconstrained linkages, as well as the tiling and pattern methods for tessellations. They are the foundation for the construction and analysis of morphing surfaces throughout the thesis.

2.5.1 Kinematic modelling of rigid origami

To model rigid origami, researchers often employ a matrix method using the Denavit-Hartenberg (DH) notations (Denavit and Hartenberg, 1955). The method standardises the setup of a coordinate system at each joint in a linkage presented in Fig. 2.11. The kinematic parameters that define the joint and the two links it connects are given in Table 2.3.

A vertex in rigid origami is modelled as a single-loop closed kinematic chain of

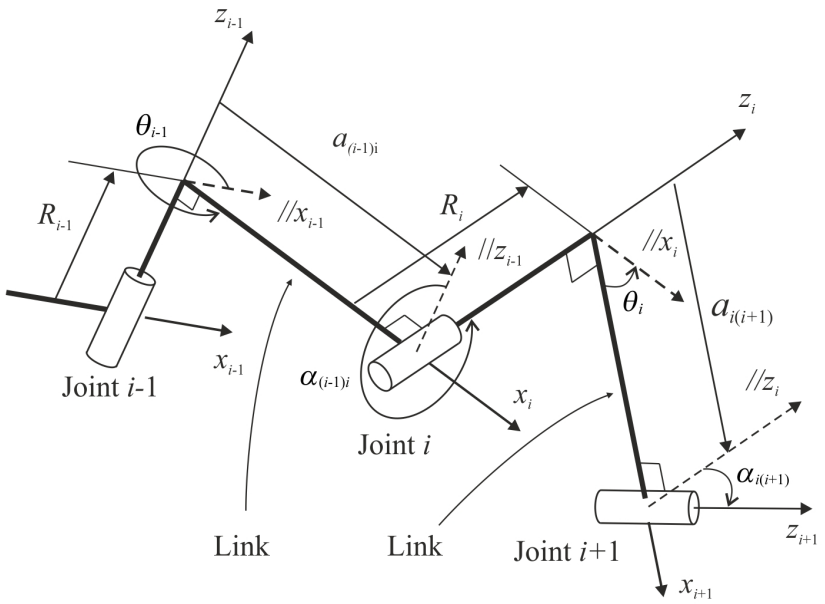


Figure 2.11: DH notations of adjacent links connected by revolute joints.

Table 2.3: Kinematic parameters of a joint

z_i	Coordinate axis along the revolute joint i
x_i	Coordinate axis common normal from z_{i-1} to z_i
y_i	Coordinate axis determined by the right-hand rule
θ_i	Rotation angle from x_i to x_{i+1} about z_i, revolute variable of joint i
$\alpha_{i(i+1)}$	Rotation angle from z_i to z_{i+1} about x_{i+1}, link twist of link$_{i(i+1)}$
$a_{i(i+1)}$	Distance between z_i and z_{i+1}, link length of link$_{i(i+1)}$
R_i	Distance between x_i and x_{i+1}, positive along z_i, offset of joint i

n links, whose closure equation is

$$T_{21}T_{32}...T_{1n} = I_4 \tag{2.3}$$

where I_4 is a 4×4 identity matrix.

The transformation matrix $T_{(i+1)i}$ is

$$T_{(i+1)i} = \begin{bmatrix} \cos\theta_i & -\cos\alpha_{i(i+1)}\sin\theta_i & \sin\alpha_{i(i+1)}\sin\theta_i & a_{i(i+1)}\cos\theta_i \\ \sin\theta_i & \cos\alpha_{i(i+1)}\sin\theta_i & -\sin\alpha_{i(i+1)}\sin\theta_i & a_{i(i+1)}\sin\theta_i \\ 0 & \sin\alpha_{i(i+1)} & \cos\alpha_{i(i+1)} & R_i \\ 0 & 0 & 0 & 1 \end{bmatrix} \tag{2.4}$$

When $i{+}1{>}n$, it is replaced by 1.

$T_{(i+1)i}$ transforms the expression in the $(i{+}1)$-th coordinate system to the i-th coordinate system. The inverse transformation matrix $T_{i(i+1)}$ is $T^{-1}_{(i+1)i}$.

For origami of zero-thickness sheets, the offsets and link lengths of each vertex are zero. For the origami of thick panels, these parameters need to be revised due to fold displacement. The kinematic behaviours of thick-panel origami discussed in this thesis will be based on the solutions of Eq. 2.3.

The focus of this thesis is on the thick-panel origami consisting of six panels, which are further modelled as a 6R linkage. Thus, Eq. 2.3 can be simplified as

$$E = T_{21}T_{32}T_{43} - T_{61}T_{56}T_{45} = 0_{4\times4} \tag{2.5}$$

where $0_{4\times4}$ is a null matrix.

A kinematic model will also be proposed to analyse the compliance of thick-panel origami, where two extra rigid panels are introduced to replace two revolute joints. The model thus becomes an 8R linkage, and in this case, Eq. 2.3 is

$$E = T_{21}T_{32}T_{43}T_{54} - T_{81}T_{78}T_{67}T_{56} = 0_{4\times4} \tag{2.6}$$

2.5.2 Overconstrained spatial linkages

As mentioned earlier, there are a group of spatial linkages that are overconstrained and do not need to satisfy Eq. 2.2 to be mobile (You and Chen, 2012). Examples discussed before include the Bennett linkage, the plane-symmetric Bricard linkage, and the Waldron hybrid linkage. They all show single mobility whilst some are reconfigurable as a result of kinematic bifurcations (Chai and Dai, 2019).

The number of spatial overconstrained linkages with only revolute joints is limited, which makes it feasible to exhaustively map all the linkages with thick-panel origami. One 4R linkage, i.e., the Bennett linkage, has been well studied (Zhang and Chen, 2018a, 2023). The two 5R linkages, i.e., the Myard linkage (Chen and You, 2008) and Goldberg 5R linkage (Goldberg, 1943), have less symmetry and are not desirable for tessellations. Thus, the thesis will only focus on 6R linkages. According to their geometric conditions, these linkages are categorised into three groups shown in Table 2.4, Table 2.5, and Table 2.6. Only two of these linkages are completely independent, i.e., the Bennett linkage and the Bricard linkage.

To better illustrate how these linkages look like and their DH representations, an example is taken for the plane-symmetric Bricard linkage as shown in Figure 2.12. A full list of each linkage's physical representation can be accessed in the thesis by Chen and Chen (2003) and the book by You and Chen (2012).

Notably, the first group, Table 2.4, includes the linkages whose joint offsets have to be all zero. The second group, Table 2.5, and the third group, Table 2.6, are the linkages derived from the Bennet linkage and the Bricard linkage, respectively. These cases also permit non-zero joint offsets. The three tables are the foundation for creating a mapping between overconstrained linkages and thick-panel origami.

Table 2.4: Geometric conditions of 6R overconstrained linkages whose joint offsets are all zero

Linkage	**Link length**	**Link twist**	**Other conditions**
Extended Myard 6R linkage (Chen and You, 2008)	$a_{12} = a_{34} = a_{45} = a_{61}$ $a_{23} = a_{56} = 0$	$\alpha_{12} = \alpha_{34} = \alpha_{45} = \alpha_{61}$ $\alpha_{23} + \alpha_{56} = 360^\circ$	—
Goldberg 6R linkage (series) (Goldberg, 1943)	$a_{12} = a_{34}$ $a_{23} = a_{45} + a_{45} + a_{61}$	$\alpha_{12} = \alpha_{34}$ $\alpha_{23} = \alpha_{45} + \alpha_{45} + \alpha_{61}$	$\frac{\sin \alpha_{i(i+1)}}{a_{i(i+1)}} = k_B \ (i = 1, 4, 5, 6)$
Goldberg 6R linkage (L-shaped) (Goldberg, 1943)	$a_{12} = a_{34} + a_{56}$ $a_{23} = a_{45} + a_{61}$	$\alpha_{12} = \alpha_{34} + \alpha_{56}$ $\alpha_{23} = \alpha_{45} + \alpha_{61}$	$\frac{\sin \alpha_{i(i+1)}}{a_{i(i+1)}} = k_B \ (i = 3, 4, 5, 6)$
Wohlhart double-Goldberg linkage (Wohlhart, 1991)	$a_{12} = a_{34}$ $a_{23} = a_{56} = b + c$ $a_{45} = a_{61}$	$\alpha_{12} = \alpha_{34}$ $\alpha_{23} = \alpha_{56} = \beta + \gamma$ $\alpha_{45} = \alpha_{61}$	$\frac{\sin \alpha_{i(i+1)}}{a_{i(i+1)}} = k_B \ (i = 1, 4)$ $\frac{\sin \beta}{b} = \frac{\sin \gamma}{c} = k_B$
Chen & You double-Goldberg linkage 1 (Chen and You, 2007)	$a_{12} = a_{45}$ $a_{23} = a_{56} = b - c$ $a_{34} = a_{61}$	$\alpha_{12} = \alpha_{45}$ $\alpha_{23} = \alpha_{56} = \beta - \gamma$ $\alpha_{34} = \alpha_{61}$	$\frac{\sin \alpha_{i(i+1)}}{a_{i(i+1)}} = k_B \ (i = 1, 4)$ $\frac{\sin \beta}{b} = \frac{\sin \gamma}{c} = k_B$ $\tan \frac{\alpha_{12}}{2} \tan \frac{\alpha_{61}}{2} = \tan \frac{\beta}{2} \tan \frac{\gamma}{2}$
Chen & You double-Goldberg linkage 2 (Chen and You, 2007)	$a_{12} = a_{34}$ $a_{23} = a_{56} = b - c$ $a_{45} = a_{61}$	$\alpha_{12} = \alpha_{34}$ $\alpha_{23} = \alpha_{56} = \beta - \gamma$ $\alpha_{45} = \alpha_{61}$	Same as Chen & You double-Goldberg linkage 1
Altmann linkage (Grodzinski and M'Ewen, 1954) (Baker, 1993)	$a_{12} = a_{45}, \ a_{34} = a_{61}$ $a_{23} = a_{56} = 0$	$\alpha_{12} = \alpha_{23} = 90^\circ$ $\alpha_{45} = \alpha_{56} = 90^\circ$ $\alpha_{34} = \alpha_{61} = 270^\circ$	—

Table 2.5: Geometric conditions of 6R overconstrained linkages derived from Bennett linkage with non-zero offsets

Linkage	**Link length**	**Link twist**	**Joint offset**
Dietmaier 6R linkage (Dietmaier, 1995)	$a_{23} = a_{56}$	$\alpha_{23} = \alpha_{56}$ $\frac{\sin\alpha_{12}}{a_{12}} = \frac{\sin\alpha_{61}}{a_{61}}, \quad \frac{\sin\alpha_{34}}{a_{34}} = \frac{\sin\alpha_{45}}{a_{45}}$ $\frac{\sin\alpha_{12}}{a_{12}}(\cos\alpha_{12} + \cos\alpha_{61})$ $= \frac{\sin\alpha_{34}}{a_{34}}(\cos\alpha_{34} + \cos\alpha_{45})$	$R_3 = R_6 = 0$ $R_1 = R_5$ $R_2 = R_4$
Bennett-joint 6R linkage (Mavroidis and Roth, 1994)	$a_{12} = a_{34}$ $a_{23} = a_{56}$ $a_{45} = a_{61}$	$\alpha_{12} = \alpha_{34}$ $\alpha_{23} = \alpha_{56}$ $\alpha_{34} = \alpha_{61}$ $\frac{\sin\alpha_{12}}{a_{12}} = \frac{\sin\alpha_{45}}{a_{45}}$	$R_1 = R_4 = 0$ $R_2 = R_5$ (R_6) $R_3 = R_6$ (R_5)
Bennett 6R hybrid linkage (Bennett, 1905)	$a_{12} = a_{34} = 0$ $a_{45} = a_{61} = 0$	—	$R_1 = R_4 = 0$
Double-Hooke's-joint linkage (Baker, 2002)	$a_{12} = a_{34} = 0$ $a_{45} = a_{61} = 0$	$\alpha_{12} = \alpha_{34} = \alpha_{45} = \alpha_{61} = 90^\circ$	$R_i = 0$ $(i = 1, ..., 4)$
Sarrus linkage (Sarrus, 1853; Bennett, 1905)	$a_{12} = a_{34}$ $a_{45} = a_{61}$ $a_{23} = a_{56} = 0$	$\alpha_{12} = \alpha_{34} = \alpha_{45} = \alpha_{61} = 0$ $\alpha_{23} = \alpha_{56} \neq 180^\circ$	—
Waldron hybrid linkage (Waldron, 1968)	—	$\alpha_{23} + \alpha_{61} = 180^\circ + \alpha_{45}$ $\alpha_{34} + \alpha_{56} = 180^\circ = +\alpha_{12}$ $\frac{a_{12}}{a_{61}} = -\frac{\sin\alpha_{12}}{\sin\alpha_{61}}, \quad \frac{a_{34}}{a_{45}} = -\frac{\sin\alpha_{34}}{\sin\alpha_{45}}$	$R_1 = R_4 = 0$ $\frac{R_2}{R_3} = \frac{\sin\alpha_{45}}{\sin\alpha_{61}}$ $\frac{R_5}{R_6} = \frac{\sin\alpha_{12}}{\sin\alpha_{34}}$

Table 2.6: Geometric conditions of 6R overconstrained linkages derived from Bricard linkage with non-zero offsets

Linkage	**Link length**	**Link twist**	**Joint offset**
Line-symmetric Bricard linkage (Bricard, 1926; Baker, 1980) (Mavroidis and Roth, 1995)	$a_{12} = a_{45}$ $a_{23} = a_{56}$ $a_{34} = a_{61}$	$\alpha_{12} = \alpha_{45}$ $\alpha_{23} = \alpha_{56}$ $\alpha_{34} = \alpha_{61}$	$R_1 = R_4$ $R_2 = R_5$ $R_3 = R_6$
Plane-symmetric Bricard linkage (Bricard, 1926; Baker, 1980) (Mavroidis and Roth, 1995)	$a_{12} = a_{61}$ $a_{23} = a_{56}$ $a_{34} = a_{45}$	$\alpha_{12} + \alpha_{61} = 360°$ $\alpha_{23} + \alpha_{56} = 360°$ $\alpha_{34} + \alpha_{45} = 360°$	$R_1 = R_4 = 0$ $R_2 = R_6$ $R_3 = R_5$
Schatz linkage (Phillips, 1984; Lee and Dai, 2003)	$a_{12} = a_{56}$ $a_{23} = a_{34} = a_{45}$ $a_{61} = \sqrt{3}a_{23}$	$\alpha_{12} = \alpha_{23} = \alpha_{34} = 90°$ $\alpha_{45} = \alpha_{56} = 90°$ $\alpha_{61} = 0$	$R_1 = -R_6$ $R_2 = R_3 = R_4 = R_5 = 0$
Wohlhart 6R linkage (Wohlhart, 1987)	$a_{12} = a_{23}$ $a_{34} = a_{45}$ $a_{56} = a_{61}$	$\alpha_{12} + \alpha_{23} = 360°$ $\alpha_{34} + \alpha_{45} = 360°$ $\alpha_{56} + \alpha_{61} = 360°$	$R_1 = R_3 = R_5 = 0$ $R_2 + R_4 + R_6 = 0$

Whilst some linkages are not included in Tables 2.4 - 2.6, such as the plano-spherical hybrid linkage (Zhang and Dai, 2015) as well as the Yu and Baker's syncopated linkage (Hon-Cheung and Baker, 1981), they can be regarded as special cases or derivatives of the ones summarised here.

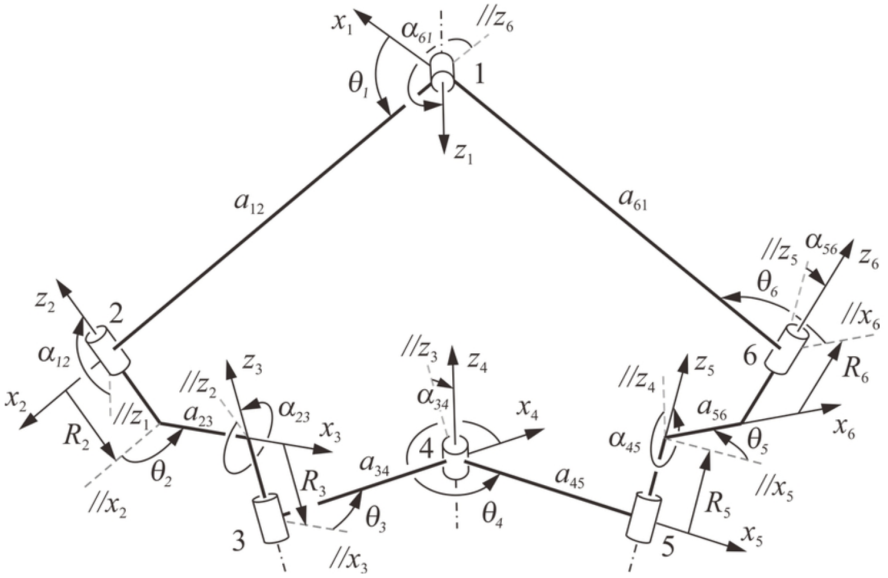


Figure 2.12: The general plane-symmetric Bricard linkage by Feng et al. (2017).

2.5.3 Tilings and patterns to produce origami tessellations

It is expected that the morphing surfaces are produced by tessellations or assemblies of individual origami units. Hence, a proper way to guide the tessellation is necessary. The mathematical tilings and patterns offer a useful tool to create origami tessellations (Grünbaum and Shephard, 1987).

A plane tiling is a countable family of closed sets that cover the plane without gaps or overlaps (Verrill, 1998). Tiling is also referred to as tessellation. A pattern is a design that repeats some motif in a more or less systematic manner.

Among all the tessellations, a regular tessellation involves only one type of regular polygon periodically covering the entire surface. Mathematically, there are only three ways to cover the plane with a regular polygon (Grünbaum et al., 1986). An equilateral triangle, a square, and a regular hexagon serve separately as the unit for tessellations as shown in Figs. 2.13(a) - (c). The triangular tiling

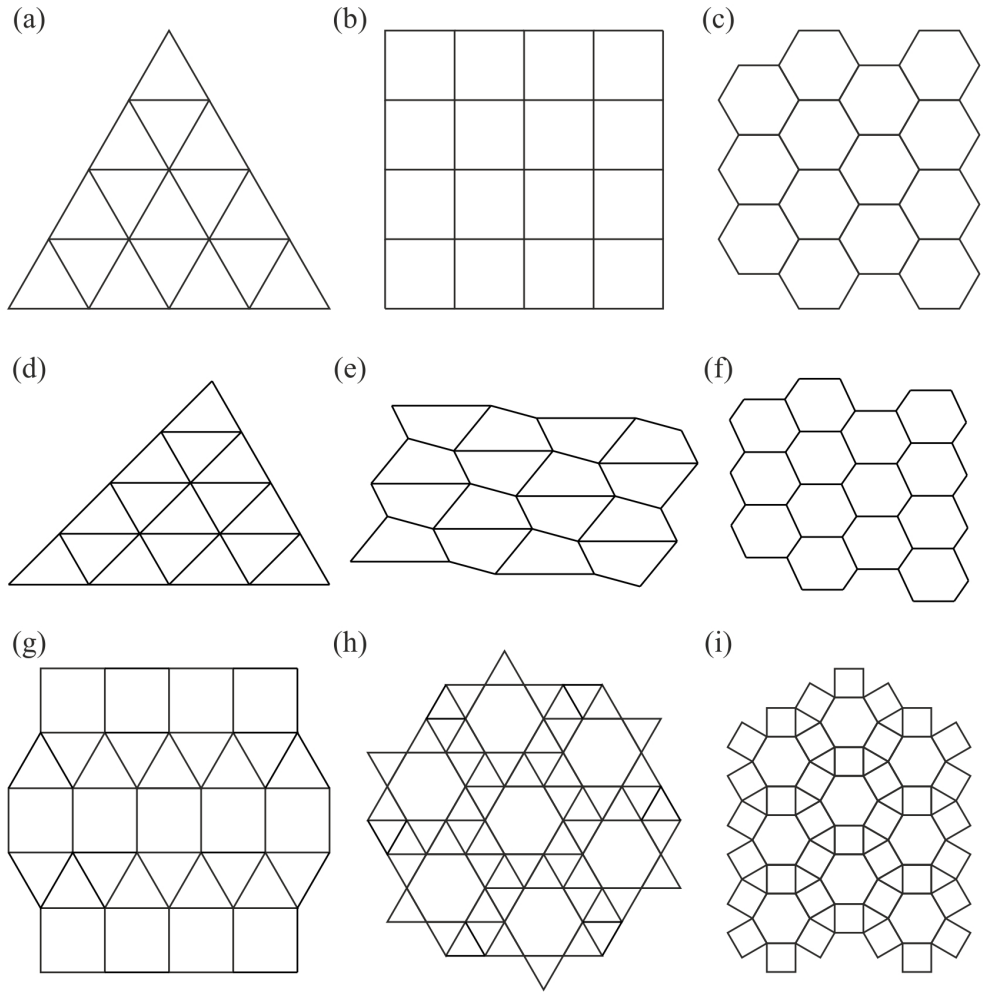


Figure 2.13: Examples of tillings and patterns, where each tessellation is based on **(a)** equilateral triangles, **(b)** squares, **(c)** regular hexagons, **(d)** general triangles, **(e)** convex quadrilaterals, **(f)** hexagons with parallel and equal opposite sides, and **(g) - (f)** a combination of regular shapes.

has the unit spread in six directions. The square tiling has the unit spread in four directions. The hexagonal tiling has the unit extend in three directions.

Modifications can be made to these regular shapes to create more monohedral tessellations. Figures 2.13(d) - (f) illustrate the examples based on a general triangle, a convex quadrilateral, and a hexagon. Note that the hexagon is a gen-

eralisation from the regular one but still requires opposite sides to be equal and parallel to each other. Different shapes can also be combined to produce more sophisticated tilings, as exemplified in Figs. 2.13(g) - (i). When certain geometric conditions are met with mountain and valley creases arranged properly, these tessellations are turned into foldable zero-thickness origami, with many of them reported by Evans et al. (2015), Siebrecht et al. (2018) and Hull and Tachi (2018).

With the literature review finishing up here, it is time to delve into the technical chapters focusing on origami design and its applications in robotics.

Chapter 3

Thick-Panel Morphing Units Inspired by Origami

A systematic approach is proposed in this chapter to design modular shape-changing structures with uniform thickness, namely morphing units. Inspired by origami, each unit is a closed chain of six rigid panels connected by top or bottom folds. A library of mobile units is derived, whose kinematic behaviours are detailed. The chapter lays the foundation for morphing surfaces in Chapter 4.

3.1 Design methodology

3.1.1 2D patterns and geometric features

In origami, a base is the simplest element whose tessellation forms the entire origami pattern. Figure 3.1 shows four origami bases which will be used to construct morphing units, including a single-vertex pattern (SVP), a single-slit pattern (SSP), a triangular-void pattern (TVP), and a quadrilateral-void pattern (QVP).

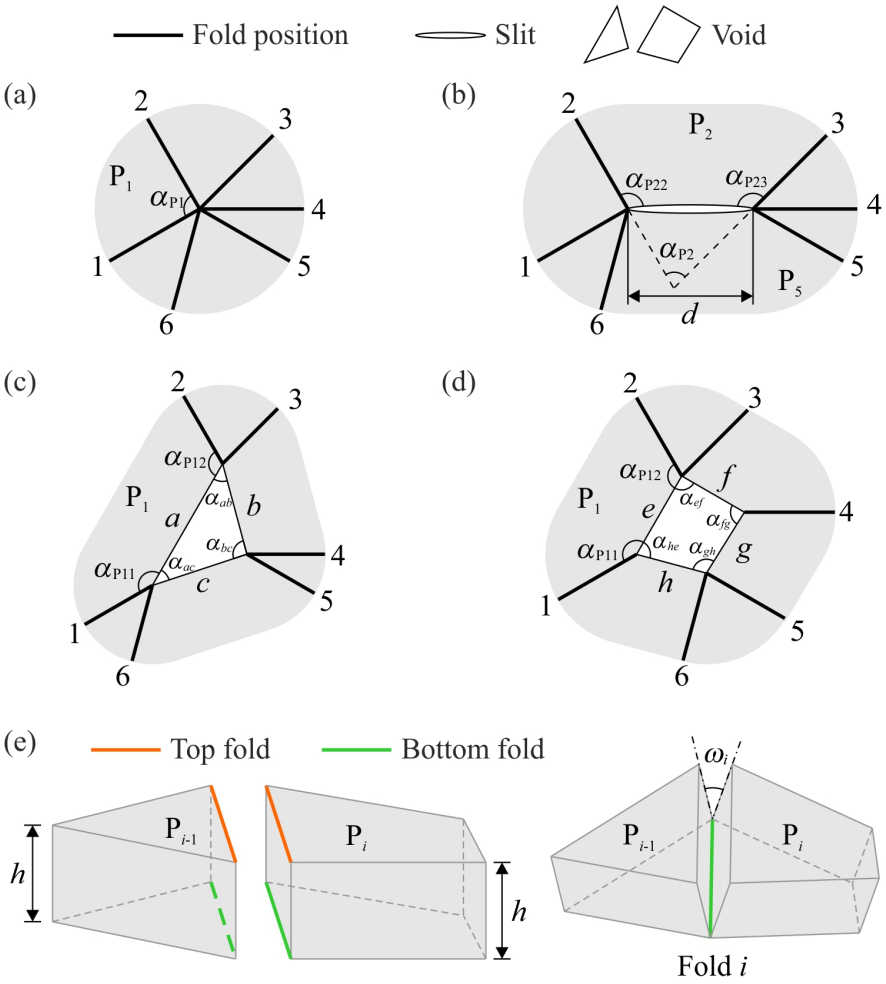


Figure 3.1: Origami bases. **(a)** Single-vertex pattern. **(b)** Single-slit pattern. **(c)** Triangular-void pattern. **(d)** Quadrilateral-void pattern. **(e)** Possible fold locations at the top or bottom of adjacent panels and the associate dihedral angle.

If we replace the sheet forming the base with panels of uniform thickness h, a unit is obtained. Each unit is composed of six rigid panels which are joined by folds at either the top or bottom of panels as shown in Fig. 3.1(e). These folds are numbered clockwise from 1 to 6 and P_i refers to the panel between folds i and $i+1$, where $i+1$ returns to 1 when $i=6$. The panels are connected to form a single closed loop. When no connection exists between two adjacent panels such

as P_2 and P_5 in the SSP, a slit is introduced. Multiple slits result in a void in the origami base, which yields the TVP and QVP.

For each base, the panels and their connecting folds are essentially a 6R closed chain if it can be folded. According to the Kutzbach criterion, its DoF is zero. To be mobile, the linkage must be overconstrained. We exclude the cases where:

- all folds are on the same surface of a unit, making it a spherical linkage or its assembly; or
- aligned folds exist on the same surface, leading to a hinge-like motion.

When a unit is modelled as a linkage under DH notations, fold i is a joint associated with coordinate z_i and revolute variable θ_i. Physically, the variable θ_i can be converted into the dihedral angle ω_i, namely the angle between the side walls of two connected panels, which is also illustrated in Fig. 3.1(e). Since the two panels cannot penetrate each other, ω_i must satisfy

$$0 \leq \omega_i \leq 180^\circ,\ i = 1, 2, ..., 6 \tag{3.1}$$

where each angle is continuous, starting from zero when the unit is fully unfolded. When one dihedral angle reaches its limit first, other angles cannot move forward, if the linkage has only one DoF.

For a mobile unit, its geometric conditions are characterised by its 2D base shape and fold arrangement. To understand the underlying mathematics, panel P_i is defined by a sector angle α_{Pi}, which is the angle between its two adjacent folds as shown in Fig. 3.1(a). If a base has a slit or void, the sector angle is decided

Table 3.1: Geometric constraints of 2D origami bases

2D base	**Geometric constraints**
SVP	$0 < \alpha_{\mathrm{P}i} < 360^\circ,\ i = 1, 2, ..., 6$
SSP	$\alpha_{\mathrm{P}2} = \alpha_{\mathrm{P}22} + \alpha_{\mathrm{P}23} - 180^\circ,\ \alpha_{\mathrm{P}5} = \alpha_{\mathrm{P}55} + \alpha_{\mathrm{P}56} - 180^\circ$ $\alpha_{\mathrm{P}1} + \alpha_{\mathrm{P}22} + \alpha_{\mathrm{P}56} + \alpha_{\mathrm{P}6} = 360^\circ,\ \alpha_{\mathrm{P}23} + \alpha_{\mathrm{P}3} + \alpha_{\mathrm{P}4} + \alpha_{\mathrm{P}55} = 360^\circ$ $0 < \alpha_{\mathrm{P}i} < 360^\circ,\ i = 1, 3, 4, 6;\ \ 0 < \alpha_{\mathrm{P}ii}, \alpha_{\mathrm{P}i(i+1)} < 360^\circ,\ i = 2, 5$
TVP	$\alpha_{\mathrm{P}i} = \alpha_{\mathrm{P}ii} + \alpha_{\mathrm{P}i(i+1)},\ i = 1, 3, 5$ $\alpha_{\mathrm{P}11} + \alpha_{ac} + \alpha_{\mathrm{P}56} + \alpha_{\mathrm{P}6} = 360^\circ,\ \alpha_{\mathrm{P}33} + \alpha_{ab} + \alpha_{\mathrm{P}12} + \alpha_{\mathrm{P}2} = 360^\circ$ $\alpha_{\mathrm{P}55} + \alpha_{bc} + \alpha_{\mathrm{P}34} + \alpha_{\mathrm{P}4} = 360^\circ$ $0 < \alpha_{\mathrm{P}i} < 360^\circ,\ i = 2, 4, 6;\ \ 0 < \alpha_{\mathrm{P}ii}, \alpha_{\mathrm{P}i(i+1)} < 360^\circ,\ i = 1, 3, 5$ $\alpha_{ab} + \alpha_{ac} + \alpha_{bc} = 180^\circ,\ 0 < \alpha_{ab}, \alpha_{ac}, \alpha_{bc} < 180^\circ$
QVP	$\alpha_{\mathrm{P}i} = \alpha_{\mathrm{P}ii} + \alpha_{\mathrm{P}i(i+1)},\ i = 1, 3, 4, 6$ $\alpha_{\mathrm{P}12} + \alpha_{\mathrm{P}2} + \alpha_{\mathrm{P}33} + \alpha_{ef} = 360^\circ,\ \alpha_{\mathrm{P}45} + \alpha_{\mathrm{P}5} + \alpha_{\mathrm{P}66} + \alpha_{gh} = 360^\circ$ $\alpha_{\mathrm{P}11} + \alpha_{he} + \alpha_{\mathrm{P}61} = 360^\circ,\ \alpha_{\mathrm{P}34} + \alpha_{fg} + \alpha_{\mathrm{P}44} = 360^\circ$ $0 < \alpha_{\mathrm{P}i} < 360^\circ,\ i = 2, 5;\ \ 0 < \alpha_{\mathrm{P}ii}, \alpha_{\mathrm{P}i(i+1)} < 360^\circ,\ i = 1, 3, 4,$ $\alpha_{ef} + \alpha_{fg} + \alpha_{gh} + \alpha_{he} = 360^\circ, 0 < \alpha_{ef}, \alpha_{fg}, \alpha_{gh}, \alpha_{he} < 180^\circ$

by two side angles of the panel, $\alpha_{\mathrm{P}ii}$ and $\alpha_{\mathrm{P}i(i+1)}$. For instance, the SSP in Fig. 3.1(b) gives $\alpha_{\mathrm{P}2} = \alpha_{\mathrm{P}22} + \alpha_{\mathrm{P}23} - 180^\circ$.

Mathematically, all sector angles must satisfy

$$\sum_{i=1}^{6} \alpha_{\mathrm{P}i} = 360^\circ \tag{3.2}$$

where the associated angles are further restricted by constraints in Table 3.1.

In addition, the TVP and QVP have an additional constraint coming from the void, i.e., the side lengths of each void must be positive and compatible with its interior angles.

By observation, the four bases and their derived units exhibit a few kinematic features as follows. With the aforementioned geometric constraints, these features are subsequently used to evaluate whether a unit is mobile.

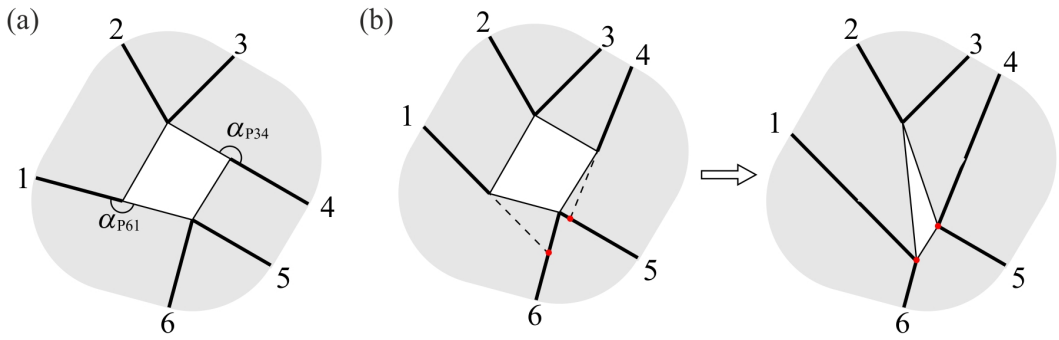


Figure 3.2: Special cases of the QVP. **(a)** The QVP is equivalent to the SSP. **(b)** The QVP is equivalent to the TVP.

- When certain geometric conditions are satisfied, the four bases are kinematically equivalent and repeated cases are thus not discussed. For example,
  - the SVP is a special case of the SSP when the slit length d reduces to zero;
  - the QVP becomes an SSP when $\alpha_{P34} = \alpha_{P61} = 180^\circ$ as shown in Fig. 3.2(a); and
  - the QVP is equivalent to a TVP when the intersecting points between folds 1 and 6, folds 4 and 5, as well as folds 2 and 3, can form a triangle, as shown in Fig. 3.2(b).
- Generally, the link length between folds i and $i+1$ is either h or zero, depending on the fold arrangement. All possibilities are enumerated in Fig. 3.3, where equivalent ones are removed.
- The link twist between folds i and $i+1$ is

$$\alpha_{i(i+1)} = \alpha_{Pi} \text{ or } \alpha_{i(i+1)} = 360^\circ - \alpha_{Pi} \tag{3.3}$$

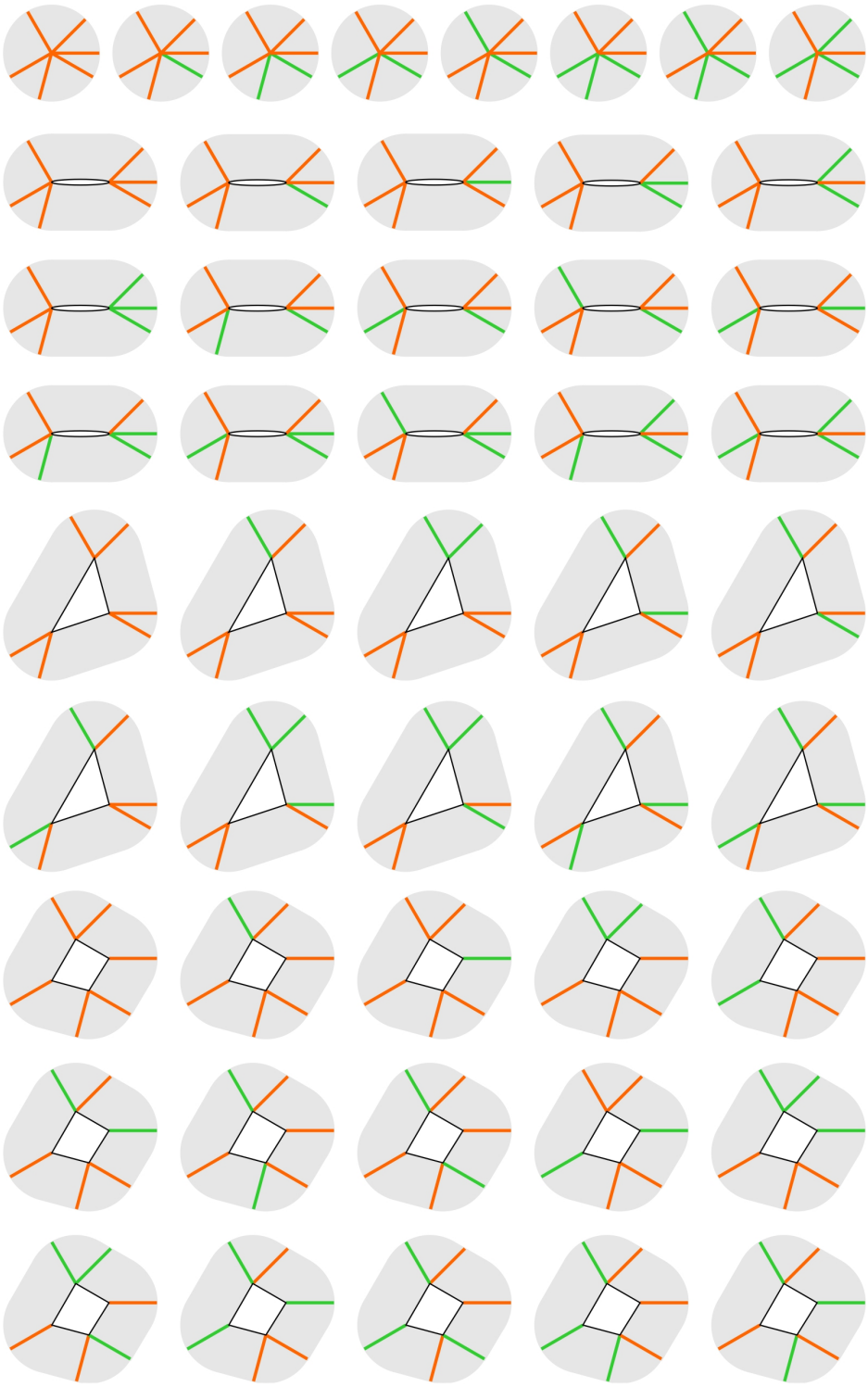


Figure 3.3: All possible fold arrangements on the origami bases.

which also depends on the arrangement of folds i and $i+1$, assuming that the z direction of each fold points outwards from the centre.

- All folds on the SVP as well as folds 1 and 4 on the SSP have zero joint offsets. To create zero offset for any other fold i, either case below must be satisfied.
  - Folds $i-1$, i, and $i+1$ intersect at the same point on the 2D base. For instance, the TVP shown in Fig. 3.4(a) has $R_1 = R_3 = R_5 = 0$ when $\alpha_{\mathrm{P12}} = \alpha_{\mathrm{P34}} = \alpha_{\mathrm{P56}} = 180°$ while the QVP in Fig. 3.4 has $R_2 = R_3 = 0$ when $\alpha_{\mathrm{P11}} = \alpha_{\mathrm{P34}} = 180°$.
  - Fold i is parallel to fold $i+1$. For instance, as shown in Fig. 3.4(c), $\alpha_{\mathrm{P22}} + \alpha_{\mathrm{P23}} = 180°$, giving zero joint offset for fold 2 or 3. When $\alpha_{\mathrm{P22}} = \alpha_{\mathrm{P23}} = 90°$ as shown in Fig. 3.4(d), both R_2 and R_3 are zero. Note that in such cases, the link length between folds i and $i+1$ need to be recalculated and the link twist $\alpha_{i(i+1)} = 0$.
- The quadrilateral void in the QVP can be modified without changing the joint offsets of its equivalent linkage. The only thing that matters with regard to its kinematics is where adjacent folds meet on the 2D base.

3.1.2 Evaluation process and selection criteria

To explore the possibility of single-DoF morphing units, each pattern in Fig. 3.3 is examined to see if it meets the requirement of a 6R spatial overconstrained linkage given in Tables 2.4 - 2.6. The geometric features listed in Subsection 3.1.1 are used to simplify the evaluation. The selection criteria for morphing units are as follows.

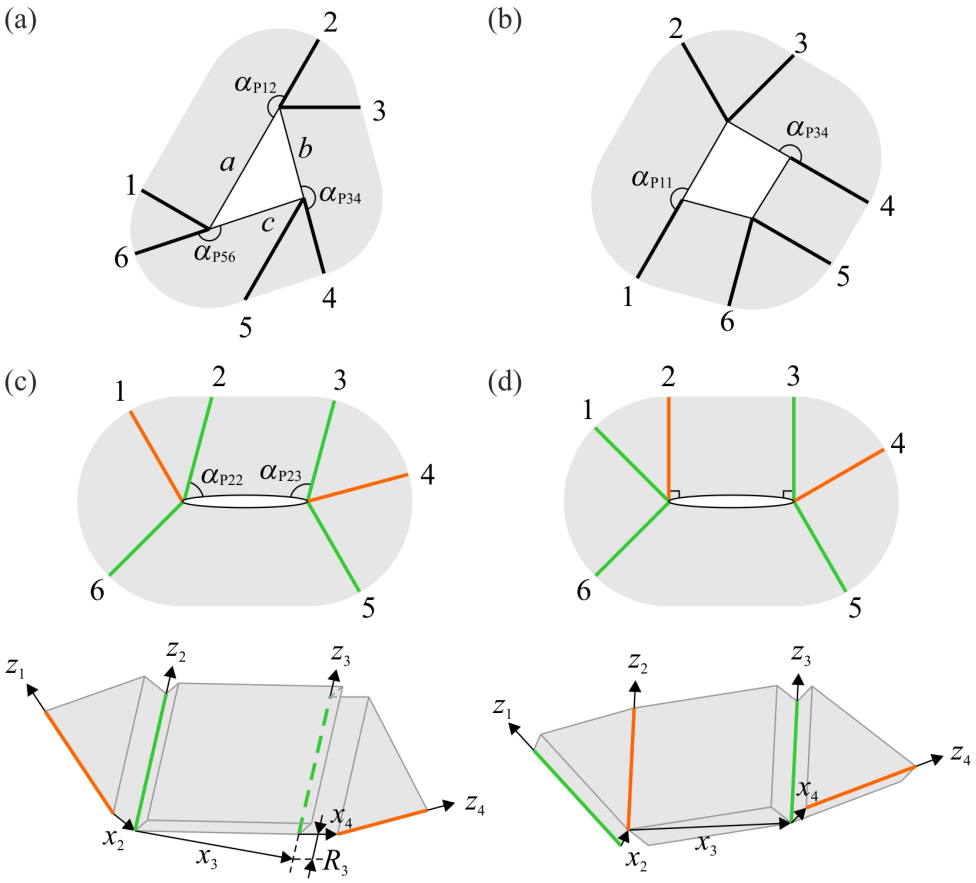


Figure 3.4: Special fold arrangement. **(a)** and **(b)** Examples of intersecting folds to create zero joint offsets. **(c)** and **(d)** Examples of parallel folds to create zero joint offsets.

- A unit must be able to move with all folds. Units with hinge motion only caused by collinear folds are excluded.

- A morphing unit may satisfy the geometric conditions of more than one 6R linkage. It is only counted once if this situation happens.

- Whilst a reference linkage is overconstrained, the unit could have more than one DoF under certain conditions. Such cases are listed in Appendix A.

- For some mobile units, physical interference between two disconnected but

adjacent panels, such as P_2 and P_5 on the SSP in Fig. 3.1(b), may occur but it can be eliminated the removal of some of the panels. Such cases are not the focus of this thesis but will also be summarised in Appendix A.

- Bifurcations that cause instantaneous mobility increase are not considered as multiple DoFs.

- Bifurcations of a reference linkage do not mean that they also exist on the unit. Some motion paths of a linkage may not satisfy the geometric constraints in Subsection 3.1.1. For instance, they might be physically blocked.

The entire evaluation process is tedious as there are 48 patterns in Fig. 3.3 and 17 linkages from Tables 2.4 - 2.6. Instead of providing mathematical derivations for all cases, only a few linkages and patterns are presented. All mobile units are categorised in Section 3.2. Some immobile cases are given in Section 3.3 as examples to illustrate the general selection process.

3.2 Morphing units

After evaluation, the mobile units are categorised into four types based on their reference linkages. This section details their design bases and kinematic behaviours.

3.2.1 Units based on the plane-symmetric Bricard linkage: type 1

As shown in Fig. 3.5, Units a_1, a_2, and a_3 are based on the plane-symmetric Bricard linkage. Two bottom folds are aligned, giving $\gamma = \alpha + \beta - 180°$. The top

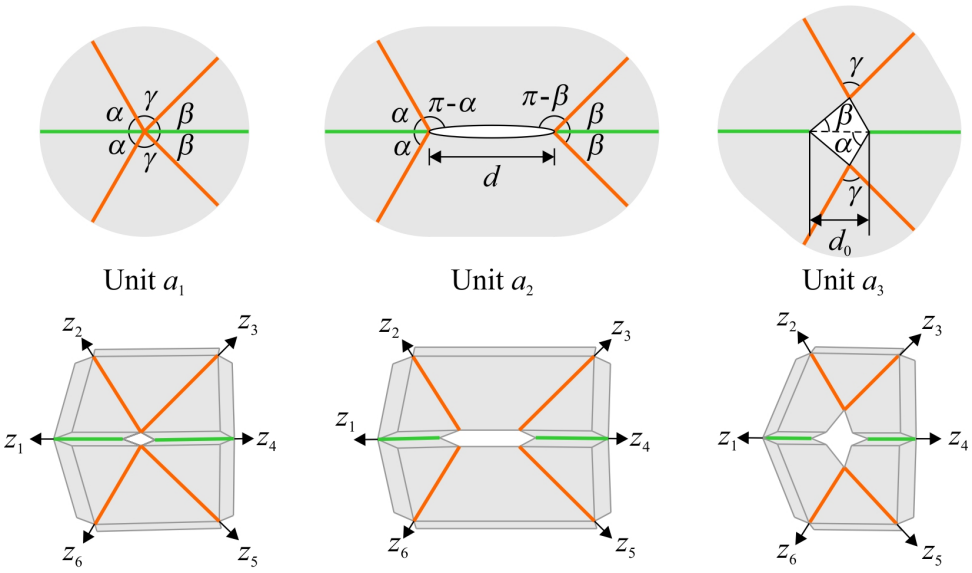


Figure 3.5: The origami bases of Units a_1 - a_3 based on the plane-symmetric Bricard linkage and their 3D models.

folds of Unit a_3 are also collinear with respective sides of the void. Each pattern is symmetric about its bottom folds. The geometric conditions under DH notations are given as follows.

$$\begin{gathered} a_{12} = a_{34} = a_{45} = a_{61} = h,\ a_{23} = a_{56} = 0 \\ \alpha_{12} = 360^\circ - \alpha_{61} = -\alpha \\ \alpha_{23} = 360^\circ - \alpha_{56} = 180^\circ - \alpha - \beta \\ \alpha_{34} = 360^\circ - \alpha_{45} = \beta \\ R_1 = R_4 = 0,\ R_2 = -R_6 = -\frac{\sin\beta}{\sin(\alpha+\beta)}d,\ R_3 = -R_5 = \frac{\sin\alpha}{\sin(\alpha+\beta)}d \end{gathered} \tag{3.4}$$

where d is the equivalent slit length. For Unit a_1, $d = 0$. For Unit a_3, $d = -d_0$ where d_0 is the horizontal width of the void as shown in Fig. 3.5.

The geometric conditions are then substituted into the closure equation in Eq. 2.5 to analyse the kinematic behaviours of each unit. To better understand

Table 3.2: Relationship between the revolute variable θ_i and dihedral angle ω_i of morphing units

θ_i	Unit a_1 - a_3	Unit b_1 - b_3, m_1	Unit c_1 - c_3	Unit m_2
θ_1	$180^\circ + \omega_1$	$180^\circ + \omega_1$	$180^\circ + \omega_1$	$180^\circ + \omega_1 + \arctan \frac{a \sin \delta_1}{h}$
θ_2	$180^\circ - \omega_2$	$180^\circ - \omega_2$	$180^\circ - \omega_2$	$180^\circ - \omega_2 - \arctan \frac{a \sin \delta_1}{h}$
θ_3	$-\omega_3$	$180^\circ + \omega_3$	$-\omega_3$	$-\omega_3 - \arctan \frac{b \sin \delta_2}{h}$
θ_4	$180^\circ + \omega_4$	$180^\circ - \omega_4$	$180^\circ + \omega_4$	$180^\circ + \omega_4 + \arctan \frac{b \sin \delta_2}{h}$
θ_5	$-\omega_5$	$180^\circ + \omega_5$	$180^\circ - \omega_5$	ω_5
θ_6	$180^\circ - \omega_6$	$180^\circ - \omega_6$	$-\omega_6$	$180^\circ + \omega_6$

the physical representation of these units, revolute variables of each fold θ_i are converted to dihedral angles according to Table 3.2 and the same process applies to all morphing units to be discussed in this thesis. As such, the closure equations of Units a_1 - a_3 as a general plane-symmetric Bricard linkage are

$$\begin{gathered} \omega_1 = \omega_4,\ \omega_2 = \omega_6,\ \omega_3 = \omega_5 \\ \tan \frac{\omega_2}{2} = \frac{1}{\cos \alpha} \tan \frac{\omega_1}{2},\ \tan \frac{\omega_3}{2} = \frac{1}{\cos \beta} \tan \frac{\omega_1}{2} \end{gathered} \tag{3.5}$$

which is defined as path 1 of these units.

The panel thickness h and equivalent slit length d do not influence the closure equations of Units a_1 - a_3. Taking $\alpha = 60^\circ$ and $\beta = 45^\circ$, path 1 is plotted in Fig. 3.6 along with simulated models in SOLIDWORKS.

Feng et al. (2017) has proven two general motion paths of the plane-symmetric Bricard linkage. It should be noted that only one exists here and the other is blocked. Regardless, it is still worth exploring whether these units have kinematic

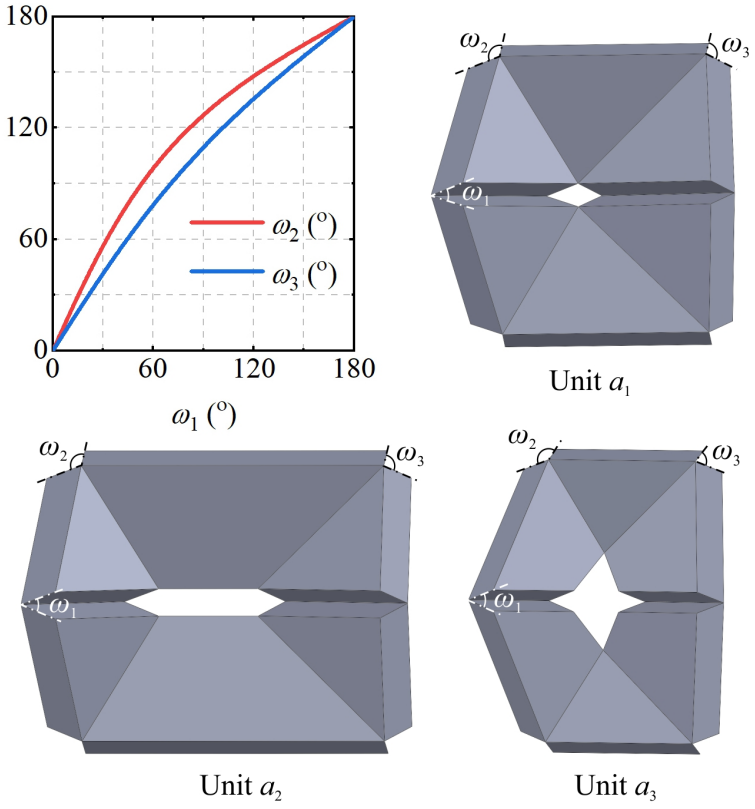


Figure 3.6: Path 1 of Units a_1 - a_3 and associated 3D models.

bifurcations that could lead to other configurations. Instead of revisiting the original closure equations in Eq. 2.5, the strategy is to evaluate whether the derived 6R linkage of each unit can meet one of the following requirements.

- The 6R spatial linkage can degenerate planar linkages with parallel folds. The simplest case could be two aligned folds.
- The 6R spatial linkage can degenerate 4R/5R spherical linkages, where at least four folds intersect at the same point.
- The 6R spatial linkage can degenerate 4R/5R spatial linkages, i.e., the Bennett linkage, the Myard linkage, and the Goldberg 5R linkage.

Likewise, the same strategy will be applied for all morphing units to be discussed in this section, thus identifying all of their bifurcations.

By observation, Units a_1 - a_3 have aligned bottom folds, producing path 2 as

$$\omega_1 = \omega_4,\ \omega_2 = \omega_3 = \omega_5 = \omega_6 = 0 \tag{3.6}$$

which is a hinge-like motion. The bifurcation point exists at the unfolded flat state of each unit, i.e., the origin in Fig. 3.6, which is its kinematic bifurcation.

It is also found that Unit a_2 can bifurcate into a 4R spherical linkage as its path 3 when folds 2, 3, 5, and 6 intersect at the same point and the dihedral angles of folds 1 and 4 are hence locked. The geometric conditions for such a situation are

$$\tan\frac{\omega_1}{2} = \tan\frac{\omega_4}{2} = \frac{d\sin\alpha\sin\beta}{h\sin(\alpha+\beta)} \tag{3.7}$$

after which other dihedral angles can be derived from the 4R spherical linkage.

To further illustrate where the third path happens, a special case when $\alpha = \beta$ is taken for Unit a_2. The corresponding dihedral angles in path 3 are

$$\begin{gathered} \omega_1 = \omega_4,\ \omega_2 = \omega_5,\ \omega_3 = \omega_6 \\ \tan\frac{\omega_1}{2} = \frac{d\tan\alpha}{2h} \\ \tan\frac{\omega_3}{2} = \frac{d\sin\alpha\tan\frac{\omega_2}{2}}{4h\cos^2\alpha\tan\frac{\omega_2}{2} - d\sin\alpha} \end{gathered} \tag{3.8}$$

Taking $\alpha = 60°$, the plots of path 1 and path 3 of Unit a_2 is given in Fig. 3.7. The new bifurcation point exists where two paths intersect, i.e., the unit is semi-folded. The point also varies along the ratio of slit length and panel thickness d/h. A simulated model is illustrated by the side.

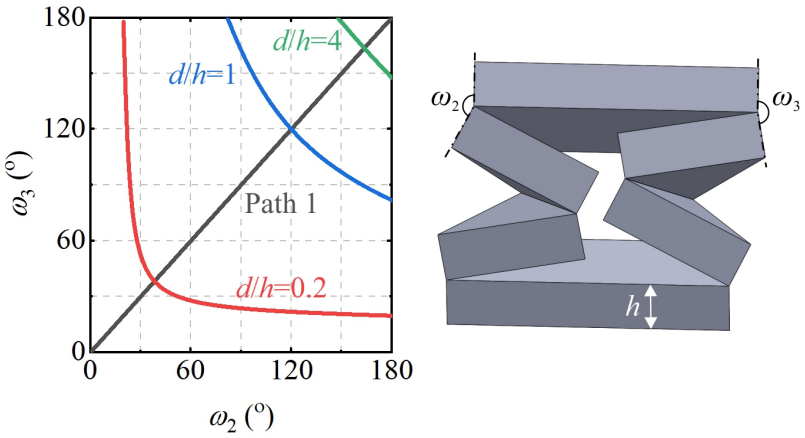


Figure 3.7: Path 1 (black) and path 3 (coloured) of Unit a_2 when $\alpha = \beta = 60°$. The 3D models depict the configurations along path 3.

3.2.2 Units based on the plane-symmetric Bricard linkage: type 2

Units b_1 - b_3 in Fig. 3.8 are also modelled as the plane-symmetric Bricard linkage, sharing exactly the same panels as Units a_1 - a_3, respectively. Their fold arrangements have been changed, altering the geometric conditions as follows.

$$\begin{gathered} a_{12} = a_{23} = a_{34} = a_{45} = a_{56} = a_{61} = h \\ \alpha_{12} = 360° - \alpha_{61} = -\alpha \\ \alpha_{23} = 360° - \alpha_{56} = 180° - \alpha - \beta \\ \alpha_{34} = 360° - \alpha_{45} = -\beta \\ R_1 = R_4 = 0,\ R_2 = -R_6 = -\frac{\sin\beta}{\sin(\alpha+\beta)}d,\ R_3 = -R_5 = \frac{\sin\alpha}{\sin(\alpha+\beta)}d \end{gathered} \tag{3.9}$$

where the joint offsets remain the same as those in Eq. 3.4.

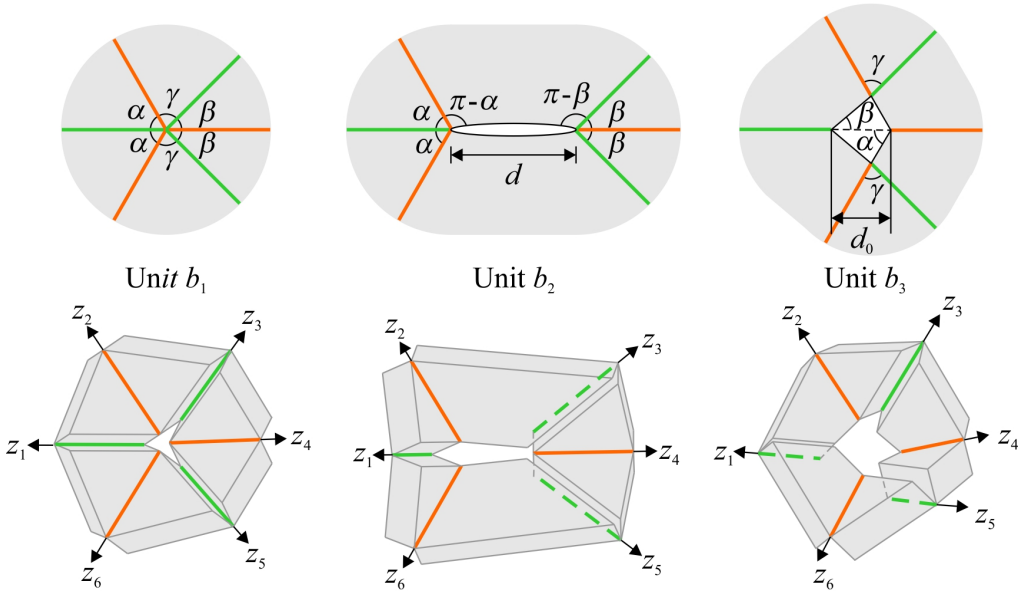


Figure 3.8: The origami bases of Units b_1 - b_3 based on the plane-symmetric Bricard linkage and their 3D models.

The closure equation of Units b_1 - b_3 as a plane-symmetric Bricard linkage is

$$\omega_2 = \omega_6,\ \omega_3 = \omega_5 \tag{3.10}$$

$$\tan\frac{\omega_1}{2} = -\frac{KI+L}{HI+J},\ \tan\frac{\omega_3}{2} = -\frac{2A_b}{I},\ \tan\frac{\omega_4}{2} = -\frac{OI+P}{MI+N} \tag{3.11}$$

for path 1,

$$I = -B_b - \sqrt{B_b^2 - 4A_bC_b} \tag{3.12}$$

for path 2,

$$I = -B_b + \sqrt{B_b^2 - 4A_bC_b} \tag{3.13}$$

where

$$A_b = h\sin(2\alpha)$$

$$B_b = 2d\sin(2\alpha)\sin\beta + 4h\sin(\alpha+\beta)\cot\frac{\omega_2}{2}$$

$$C_b = 3h\sin(2\alpha+2\beta) + \sin(2\beta)(h\cot\frac{\omega_2}{2} + 2d\sin\alpha)\cot\frac{\omega_2}{2}$$

$$H = -8h\sin^2\alpha\cos\beta\cot^2\frac{\omega_2}{2} - 2\sin(2\alpha)\sin\beta(h + d\sin\alpha\sin\omega_2)\csc^2\frac{\omega_2}{2}$$

$$\begin{aligned} J = -8h^2\sin\alpha\sin(2\alpha)\sin(2\alpha+2\beta)\cot\frac{\omega_2}{2} \\ - 4h^2\sin\alpha\sin(2\alpha)\sin(2\beta)\cos\omega_2\csc^2\frac{\omega_2}{2}\cot\frac{\omega_2}{2} \\ - 8hd\sin^2\alpha\sin(2\alpha)\sin(2\beta)\cot^2\frac{\omega_2}{2} \end{aligned}$$

$$K = 4\sin\alpha\sin(2\alpha)(h\cos\beta\cot\frac{\omega_2}{2} + d\cos\alpha\sin\beta)$$

$$L = 4h^2\sin^2\alpha\sin(2\alpha+2\beta) + 4h\sin^2\alpha\sin(2\beta)(h\cot\frac{\omega_2}{2} + d\sin\alpha)\cot\frac{\omega_2}{2}$$

$$\begin{aligned} M = 2h\sin(2\alpha)\sin(2\alpha+\beta) - 2\sin(2\alpha)\sin\beta(h\cot\frac{\omega_2}{2} + 2d\sin\alpha)\cot\frac{\omega_2}{2} \\ - 8h\sin^2\alpha\cos\beta\cot^2\frac{\omega_2}{2} \end{aligned}$$

$$\begin{aligned} N = -4h^2\sin\alpha\sin^2(2\alpha)\cot\frac{\omega_2}{2} - 12h^2\sin\alpha\sin(2\alpha)\sin(2\alpha+2\beta)\cot\frac{\omega_2}{2} \\ - 4h\sin\alpha\sin(2\alpha)\sin(2\beta)(h\cot\frac{\omega_2}{2} + 2d\sin\alpha)\sin^2(2\alpha) \end{aligned}$$

$$O = -8h\sin\alpha\sin(2\alpha)\cos\beta\cot\frac{\omega_2}{2} - 4\sin(2\alpha)\cos\alpha\sin\beta(h\cot\frac{\omega_2}{2} + d\sin\alpha)$$

$$P = -8h^2\sin^2(2\alpha)\sin(2\alpha+2\beta) - 4h\sin^2(2\alpha)\sin(2\beta)(h\cot\frac{\omega_2}{2} + d\sin\alpha)\cot\frac{\omega_2}{2}$$

For Unit b_1 where the slit length $d = 0$, Eqs. 3.11 - 3.13 can be simplified.

For path 1,

$$\tan\frac{\omega_3}{2} = \frac{\sin(2\alpha)\tan\frac{\omega_2}{2}}{2\sin(\alpha+\beta) + \sqrt{Q}\tan\frac{\omega_2}{2}} \tag{3.14}$$

for path 2,

$$\tan\frac{\omega_3}{2} = \frac{\sin(2\alpha)\tan\frac{\omega_2}{2}}{2\sin(\alpha+\beta) - \sqrt{Q}\tan\frac{\omega_2}{2}} \tag{3.15}$$

where

$$Q = \frac{4\sin^2(\alpha+\beta) - \sin(2\beta)}{\tan^2\frac{\omega_2}{2}} - 3\sin(2\alpha)\sin(2\alpha+2\beta)$$

and

$$\begin{aligned}\tan\frac{\omega_1}{2} = {} & \frac{\sin\alpha\sin(\alpha+\beta)\sin\omega_3}{1-\cos\omega_2(1-\cos\omega_3)-\cos(\alpha+\beta)\sin\omega_2\sin\omega_3} \\ & - \frac{-\cos\alpha(\sin\omega_2(1-\cos\omega_3)-\cos(\alpha+\beta)\cos\omega_2\sin\omega_3)}{1-\cos\omega_2(1-\cos\omega_3)-\cos(\alpha+\beta)\sin\omega_2\sin\omega_3}\end{aligned} \tag{3.16}$$

$$\begin{aligned}\tan\frac{\omega_4}{2} = {} & \frac{\sin\omega_3+\sin(\alpha+\beta)(\cot\alpha\csc\omega_2\cos\omega_3-\tan\beta\cot\omega_2)}{\sec\beta(\cos\omega_3+(\cos(\alpha+\beta)\cot\omega_2-\cot\alpha\sin(\alpha+\beta)\csc\omega_2)\sin\omega_3)} \\ & - \frac{\cos(\alpha+\beta)(\cot\omega_2\cos\omega_3+\cot\alpha\tan\beta\csc\omega_2)}{\sec\beta(\cos\omega_3+(\cos(\alpha+\beta)\cot\omega_2-\cot\alpha\sin(\alpha+\beta)\csc\omega_2)\sin\omega_3)}\end{aligned} \tag{3.17}$$

According to Eqs. 3.10 - 3.17, the motions of Unit b_1 is independent from its panel thickness while those of Units b_2 and b_3 rely on the ratio d/h.

The same strategy for Units a_1 - a_3 is employed to examine additional bifurcations, it is found that paths 1 and 2 are the only two motions of Units b_1 - b_3, which are switchable at the unfolded state of each unit. Taking $\alpha = 60°$, $\beta = 45°$, $d = 2h$ and $d_0 = 1.2h$, the kinematic behaviours of Units b_1 - b_3 are plotted in Fig. 3.9, respectively.

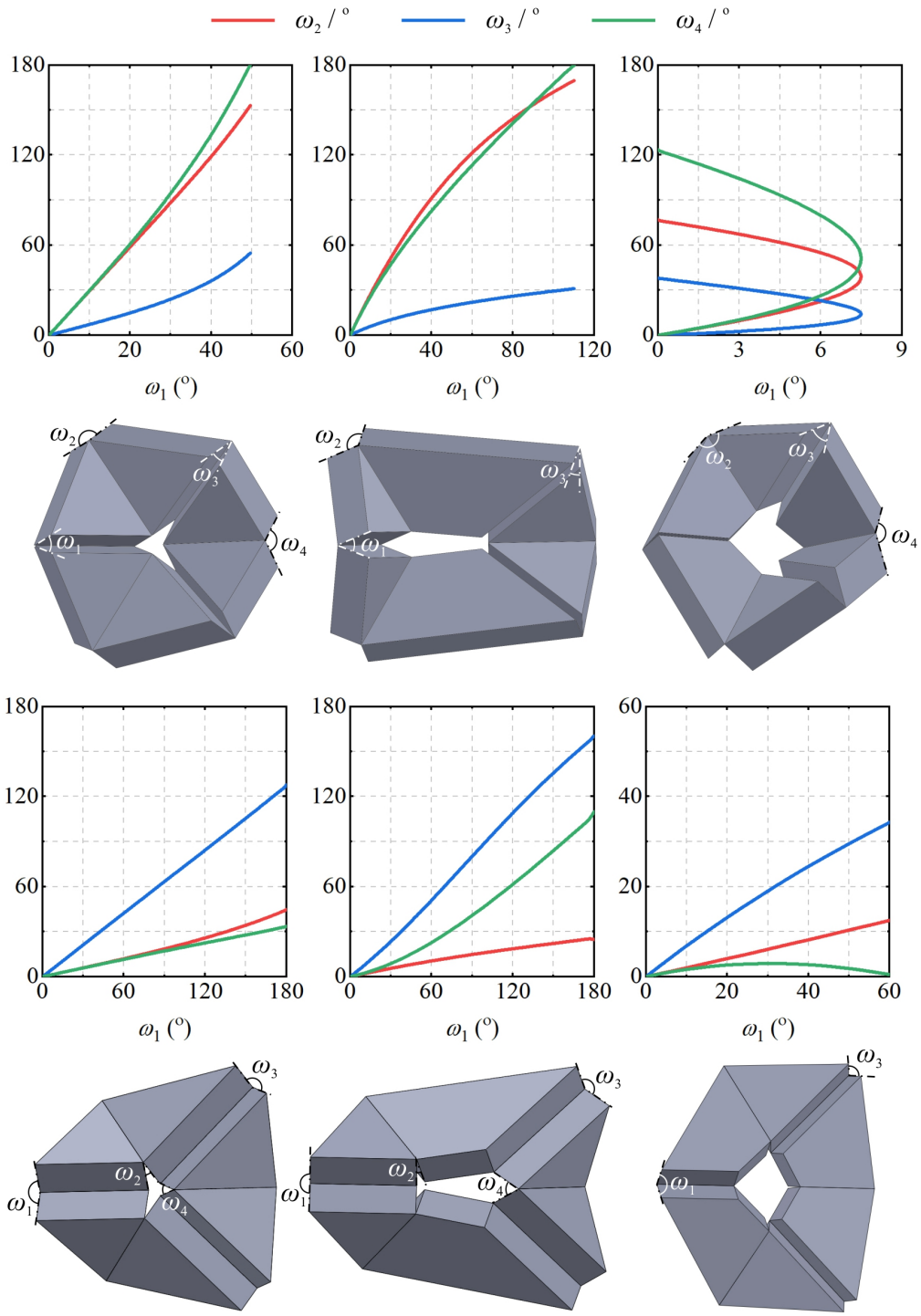


Figure 3.9: Kinematic behaviour of Units b_1 - b_3 and associated 3D models. Path 1 of each unit is given at the top while path 2 is at the bottom.

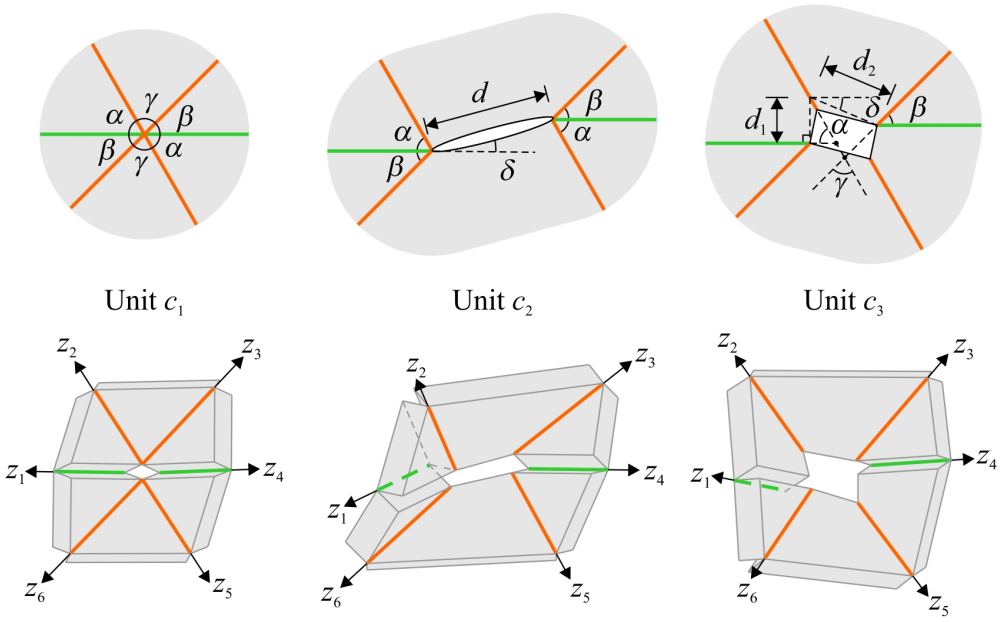


Figure 3.10: The origami bases of Units c_1 - c_3 based on the line-symmetric Bricard linkage and their 3D models.

3.2.3 Units based on the line-symmetric Bricard linkage

In addition to the plane-symmetric Bricard linkage, the line-symmetric one can also be used to design morphing units as shown in Fig. 3.10. In Unit c_1, three pairs of aligned folds exist, giving $\gamma = \alpha+\beta-180°$. Without changing the direction of these folds, a tilted slit and a parallelogram are introduced in Units c_2 and c_3 to maintain the line symmetry. Their geometric conditions are

$$\begin{gathered} a_{12} = a_{34} = a_{45} = a_{61} = h,\ a_{23} = a_{56} = 0 \\ \alpha_{12} = \alpha_{45} = -\alpha,\ \alpha_{23} = \alpha_{56} = 180° - \alpha - \beta,\ \alpha_{34} = \alpha_{61} = \beta \\ R_1 = R_4,\ R_2 = R_5,\ R_3 = R_6 \end{gathered} \tag{3.18}$$

The joint offsets of each unit are detailed as follows.

For Unit c_1,

$$R_1 = R_2 = R_3 = 0 \tag{3.19}$$

for Unit c_2,

$$R_1 = 0,\ R_2 = -\frac{\sin(\beta-\delta)}{\sin(\alpha+\beta)}d,\ R_3 = \frac{\sin(\alpha+\delta)}{\sin(\alpha+\beta)}d \tag{3.20}$$

and for Unit c_3,

$$R_1 \neq 0,\ R_2 \neq 0,\ R_3 \neq 0 \tag{3.21}$$

which means no three consecutive folds intersect at the same point on the 2D plane as depicted in Fig. 3.10.

The closure equations of Units c_1 - c_3 as a line-symmetric Bricard linkage are

$$\omega_1 = \omega_4,\ \omega_2 = \omega_5,\ \omega_3 = \omega_6 \tag{3.22}$$

$$\tan\frac{\omega_2}{2} = \frac{-B_{c1} - \sqrt{B_{c1}^2 - 4A_{c1}C_{c1}}}{2A_{c1}},\ \tan\frac{\omega_3}{2} = \frac{-B_{c2} + \sqrt{B_{c2}^2 - 4A_{c2}C_{c2}}}{2A_{c2}} \tag{3.23}$$

where

$$A_{c1} = 2R_1\sin\alpha\sin(\alpha+\beta) + R_2\sin\alpha\sin\beta(1+\cos\theta_1)$$
$$+ R_3(1-\cos\beta\cos(2\alpha+\beta)+\sin\beta\sin(2\alpha+\beta)\cos\theta_1) + 2h\cos\alpha\sin(\alpha+\beta)\sin\theta_1$$

$$B_{c1} = 2\sin(\alpha+\beta)(h(1+\cos\theta_1) + R_3\sin\beta\sin\theta_1)$$

$$C_{c1} = (1+\cos\theta_1)\sin\beta(R_2\sin\alpha + R_3\sin\beta)$$

$$A_{c2} = 2R_1\sin\alpha\sin(\alpha+\beta) + R_3\sin\alpha\sin\beta(1+\cos\theta_1)$$
$$+ R_2(1-\cos\alpha\cos(\alpha+2\beta)+\sin\alpha\sin(\alpha+2\beta)\cos\theta_1) - 2h\cos\beta\sin(\alpha+\beta)\sin\theta_1$$

$$B_{c2} = -2\sin(\alpha+\beta)(h(1+\cos\theta_1) - R_2\sin\alpha\sin\theta_1)$$

$$C_{c2} = (1+\cos\theta_1)\sin\alpha(R_2\sin\alpha + R_3\sin\beta)$$

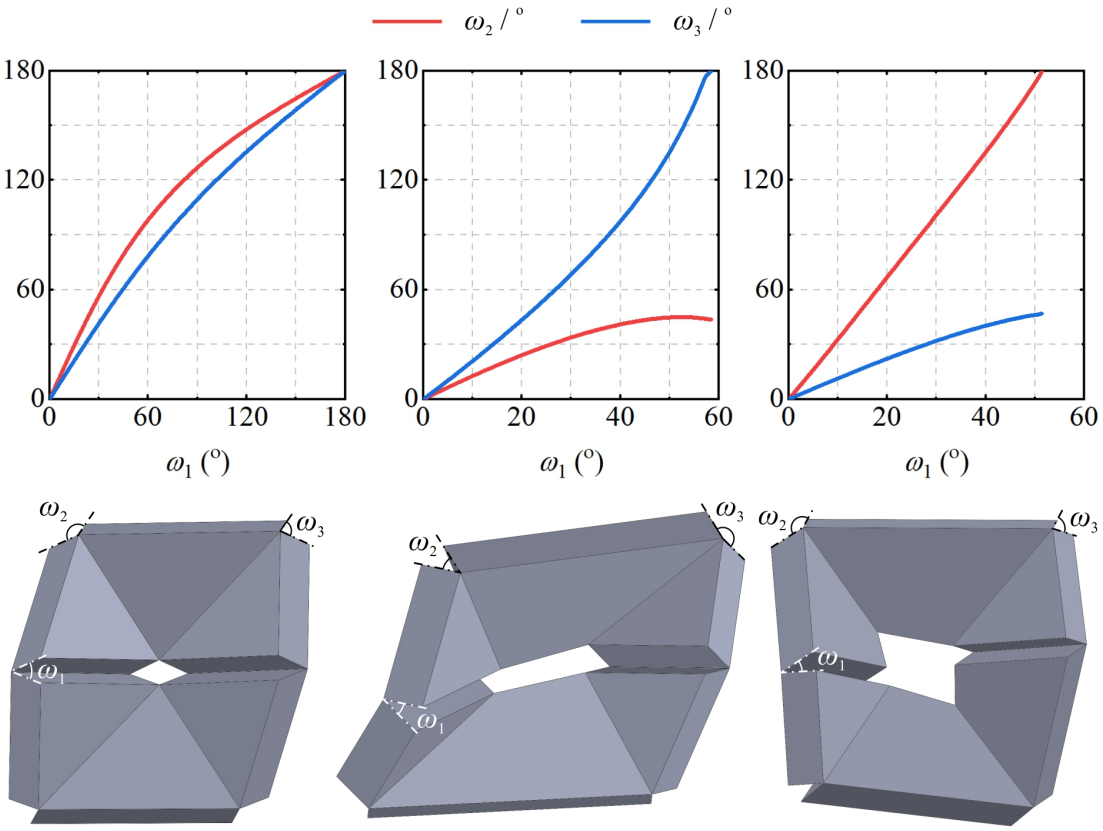


Figure 3.11: Path 1 of Units c_1 - c_3 and associated 3D models.

According to Song et al. (2013), a general line-symmetric Bricard linkage would normally have two motion paths, However, when it comes to Units c_1 - c_3, one path is blocked and the remaining one in Eqs. 3.22 - 3.23 is defined as path 1. Assign the following geometric parameters to Units c_1 - c_3 as $\alpha = 60°$, $\beta = 45°$, $\delta = 15°$, $d = 2h$, $R_1 = -0.75h$, $R_2 = -1.6h$, and $R_3 = 1.32h$. The kinematic behaviour of each unit in path 1 is plotted in Fig. 3.11.

The three units are also examined regarding their kinematic bifurcations. Unit c_1 has three pairs of aligned folds. Considering its zero joint offsets, its motion paths are rewritten as

$$\omega_1 = \omega_4, \ \omega_2 = \omega_5, \ \omega_3 = \omega_6 \tag{3.24}$$

for path 1 of Unit c_1,

$$\tan\frac{\omega_2}{2} = \frac{1}{\cos\alpha}\tan\frac{\omega_1}{2},\ \tan\frac{\omega_3}{2} = \frac{1}{\cos\beta}\tan\frac{\omega_1}{2} \tag{3.25}$$

for path 2 of Unit c_1,

$$\omega_1 = \omega_2 = 0 \tag{3.26}$$

for path 3 of Unit c_1:

$$\omega_1 = \omega_3 = 0 \tag{3.27}$$

for path 4 of Unit c_1:

$$\omega_2 = \omega_3 = 0 \tag{3.28}$$

Units c_2 and c_3 usually come with path 1 without bifurcations, whilst special geometric conditions could lead to additional motion paths. For instance, $\delta = 0$ or $\delta = \beta$ on Unit c_2 will lead to hinge-like motions as a result of aligned folds. Both units can also degenerate into 4R spherical linkages as detailed below.

For Unit c_2, if

$$\alpha = \beta,\ \delta = 0, \tag{3.29}$$

then

$$\tan\frac{\omega_1}{2} = \tan\frac{\omega_4}{2} = \frac{d\tan\alpha}{2h} \tag{3.30}$$

where the unit becomes the special case of Unit a_2 as discussed before. Folds 2, 3, 5, and 6 intersect at the same point while folds 1 and 4 are locked.

For Unit c_3, if

$$\begin{aligned} \tan\delta &= \frac{\sin(\alpha-\beta)}{2\cos\alpha\cos\beta} \\ \frac{d_1}{d_2} &= \frac{\sin(\alpha-\beta)\sin(\alpha-\delta)}{\sin(\alpha+\beta)\cos\alpha} \end{aligned} \tag{3.31}$$

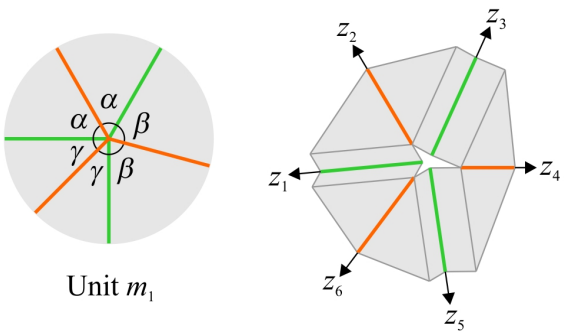


Figure 3.12: The origami base of Unit m_1 based on the Wohlhart 6R linkage and its 3D model.

then

$$\tan\frac{\omega_1}{2} = \tan\frac{\omega_4}{2} = \frac{d_1 \tan\beta}{h(\tan\alpha - \tan\beta)} \tag{3.32}$$

where folds 1 and 4 are locked again into the values above.

3.2.4 Units based on other 6R overconstrained linkages

Two more types of morphing units are found, which are based on the Wolhart 6R linkage and the Sarrus linkage, respectively.

As shown in Fig. 3.12 where $\alpha + \beta + \gamma = 180°$, Unit m_1 is modelled as the Wohlhart 6R linkage. Its geometric conditions are

$$\begin{gathered} a_{12} = a_{23} = a_{34} = a_{45} = a_{56} = a_{61} = h \\ \alpha_{12} = 360° - \alpha_{23} = -\alpha,\ \alpha_{34} = 360° - \alpha_{45} = -\beta,\ \alpha_{56} = 360° - \alpha_{61} = -\gamma \\ R_i = 0,\ i = 1, 2, ..., 6 \end{gathered} \tag{3.33}$$

When the geometric conditions in Eq. 3.33 are substituted into the closure equation in Eq. 2.5, no symmetry is found among the dihedral angles and solving the equation can be challenging. So far, no analytical solutions of a general

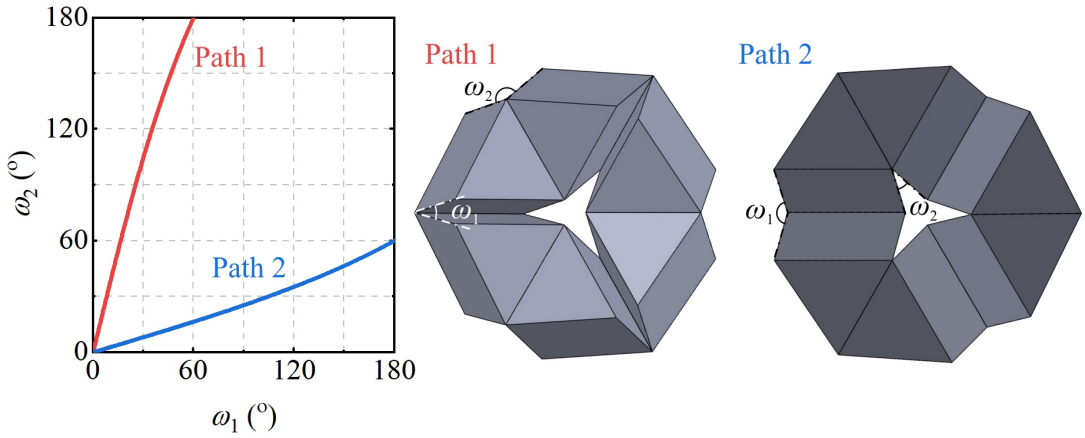


Figure 3.13: Kinematic behaviours of Unit m_1 when all sector angels are 60°. 3D configurations of the two motion paths are also displayed.

Wohlhart 6R linkage have been reported either. Nonetheless, when additional symmetry is added, i.e., $\alpha = \beta$ or $\alpha = \gamma$, Unit m_1 becomes a special case of Unit b_1, which is based on the plane-symmetric Bricard linkage. Its kinematic behaviours can thus be analysed from Eqs. 3.10 and 3.16 - 3.15.

Assigning $\alpha = \beta = \gamma = 60°$ to Unit m_1, its closure equation becomes

$$\omega_1 = \omega_3 = \omega_5, \ \omega_2 = \omega_4 = \omega_6 \tag{3.34}$$

for path 1,

$$\tan\frac{\omega_2}{2} = \frac{\sin\frac{\omega_1}{2}}{2\cos\frac{\omega_1}{2} - \sqrt{3}} \tag{3.35}$$

for path 2,

$$\tan\frac{\omega_2}{2} = \frac{\sin\frac{\omega_1}{2}}{2\cos\frac{\omega_1}{2} + \sqrt{3}} \tag{3.36}$$

which are plotted in Fig. 3.13 along with simulated models. The kinematic bifurcation is at the unfolded state of the unit.

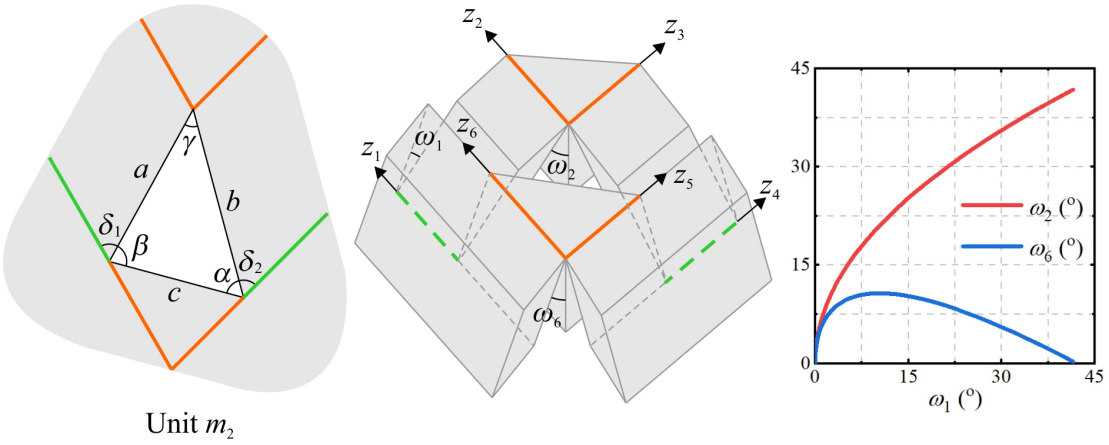


Figure 3.14: The origami base of Unit m_2 based on the Sarrus linkage and its 3D model. Its kinematic motion paths when $\alpha = \beta = \gamma = \delta_1 = \delta_2 = 60°$ and $a = 3h$ are plotted by the side.

Unit m_2 shown in Fig. 3.14 is based on the Sarrus linkage, whose geometric conditions are

$$a_{12} = \sqrt{h^2 + a^2 \sin^2 \delta_1},\ a_{23} = a_{56} = 0$$

$$a_{34} = \sqrt{h^2 + b^2 \sin^2 \delta_2},\ a_{45} = a_{61} = h$$

$$\alpha_{12} = \alpha_{34} = \alpha_{45} = \alpha_{61} = 0,\ \alpha_{23} = \alpha_{56} = \alpha + \beta + \delta_1 + \delta_2 - 180° \tag{3.37}$$

$$R_1 = a\cos\delta_1,\ R_2 = R_3 = 0,\ R_4 = -b\cos\delta_2$$

$$R_5 = -\frac{c\sin(\beta + \delta_1)}{\sin(\delta_1 + \delta_2 - \gamma)},\ R_6 = \frac{c\sin(\alpha + \delta_2)}{\sin(\delta_1 + \delta_2 - \gamma)}$$

where $\dfrac{a}{\sin\alpha} = \dfrac{b}{\sin\beta} = \dfrac{c}{\sin\gamma}$ and $\alpha + \beta + \gamma = 180°$ must hold.

The closure equation of Unit m_2 gives

$$\sin\omega_6 = \sin\omega_2 - (1 - \cos\omega_2)\frac{h_1}{h} \tag{3.38}$$

$$\tan\frac{\omega_3}{2} = \frac{-B_{m2} + \sqrt{B_{m2}^2 - 4A_{m2}C_{m2}}}{2A_{m2}} \tag{3.39}$$

$$\sin\omega_5 = \sin\omega_3 - (1-\cos\omega_3)\frac{h_2}{h} \tag{3.40}$$

$$\omega_1 = \omega_2 - \omega_6,\ \omega_4 = \omega_3 - \omega_5 \tag{3.41}$$

where

$$h_1 = a\sin\delta_1,\ h_2 = b\sin\delta_2$$

$$A_{m2} = -4h_2^2 - (2h + h\cos\omega_2 - h\cos\omega_6 - h_1\sin\omega_2)(h\cos\omega_2 - h\cos\omega_6 - h_1\sin\omega_2)$$

$$B_{m2} = 4h_2(h - h\cos\omega_2 + h\cos\omega_6 + h_1\sin\omega_2)$$

$$C_{m2} = -(h\cos\omega_2 - h\cos\omega_6 - h_1\sin\omega_2)(h\cos\omega_2 - h\cos\omega_6 - h_1\sin\omega_2 - 2h)$$

Unit m_2 has only one motion path. By letting $a = b$ and $\delta_1 = \delta_2 = \delta$, Eqs. 3.38 - 3.41 are simplified as

$$\begin{gathered}\omega_4 = \omega_1,\ \omega_3 = \omega_2,\ \omega_5 = \omega_6,\ \omega_2 = \omega_1 + \omega_6 \\ \sin\omega_6 = \sin\omega_2 - \frac{a\sin\delta}{h}(1-\cos\omega_2)\end{gathered} \tag{3.42}$$

Taking $\alpha = \delta = 60°$ and $a = 3h$, the kinematic behaviour of Unit m_2 is plotted in Fig. 3.14. The unit's movement is blocked when ω_6 returns to zero.

3.3 Immobile cases

The design methodology specified in Section 3.1 not only yields a series of morphing units, but also concludes which linkages or which bases cannot be transformed into a mobile unit with uniform thickness. This section illustrates the evaluation steps

on selected linkages and bases. Some immobile cases are found and the evaluation process is transferable to other overconstrained linkages and origami bases.

3.3.1 Extended Myard 6R linkage

According to Table 2.4, the extended Myard 6R linkage requires all joint offsets to be zero. It is hence examined on all bases in Fig. 3.1 as follows.

- If the linkage is transformed to an SVP and can still be mobile, the fold arrangement has to be either of the two cases shown in Fig. 3.15(a). This is because the linkage requires $a_{23} = a_{56} = 0$ and $\alpha_{23} + \alpha_{56} = 360°$.
  - Case 1 would not work as the link length condition $a_{12} = a_{34} = a_{45} = a_{51}$ cannot be satisfied, no matter how folds 1 and 4 are arranged.
  - Case 2 has two sub-cases satisfying the link length requirement, as shown in Fig. 3.15(b).
    - Case 2.1 gives $\alpha_{12} = 360° - \alpha_{P1}$ and $\alpha_{34} = \alpha_{P3}$. If they satisfy the link twist condition $\alpha_{12} = \alpha_{34}$, we can get $\alpha_{P1} + \alpha_{P3} = 360°$, conflicting the constraints in Eq. 3.1 and Table 3.2.
    - Case 2.2 meets the link twist condition with all folds on the same surface. The unit thus becomes a 6R spherical linkage and the only valid motions are caused by aligned folds.
- If the unit is not based on the SVP, only the patterns in Figs. 3.15(c) and 3.15(d) have zero offsets. However, the link twist conditions are unsatisfied.

Given the analysis above, it is concluded that the extended Myard 6R linkage cannot be used to design morphing units from any base in Fig. 3.1.

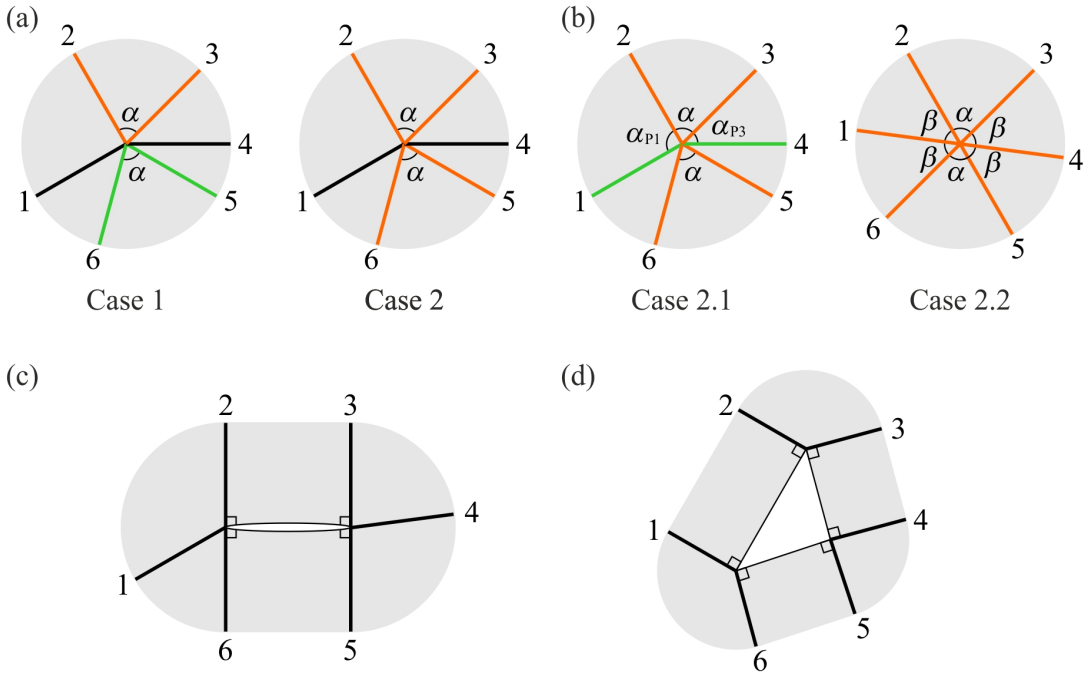


Figure 3.15: Evaluation of the extended Myard 6R linkage on a morphing unit. **(a)** and **(b)** Possible cases to meet certain geometric conditions on the SVP. **(c)** and **(d)** Possible cases to meet the zero joint offsets on the SSP and TVP.

3.3.2 Altmann linkage and Schatz linkage

The second example looks at the Altmann linkage and the Schatz linkage on the SVP. The former linkage requires $\alpha_{12} = \alpha_{23} = \alpha_{45} = \alpha_{56} = 90°$, which yields $\alpha_{P1} + \alpha_{P2} + \alpha_{P4} + \alpha_{P5} \geq 360°$ according to Eq. 3.3. The result conflicts with constraints in Eq. 3.1 and Table 3.2. Similarly, the Schatz linkage requires $\alpha_{12} = \alpha_{23} = \alpha_{34} = \alpha_{45} = \alpha_{56} = 90°$, leading to the same geometric conflict.

3.3.3 Bennett 6R hybrid linkage

The Bennett 6R hybrid linkage is evaluated on the SSP. The pattern in Fig. 3.16(a) satisfies the linkage condition and it has a single mobility. Only when $\alpha_{P1} + \alpha_{P6} >$

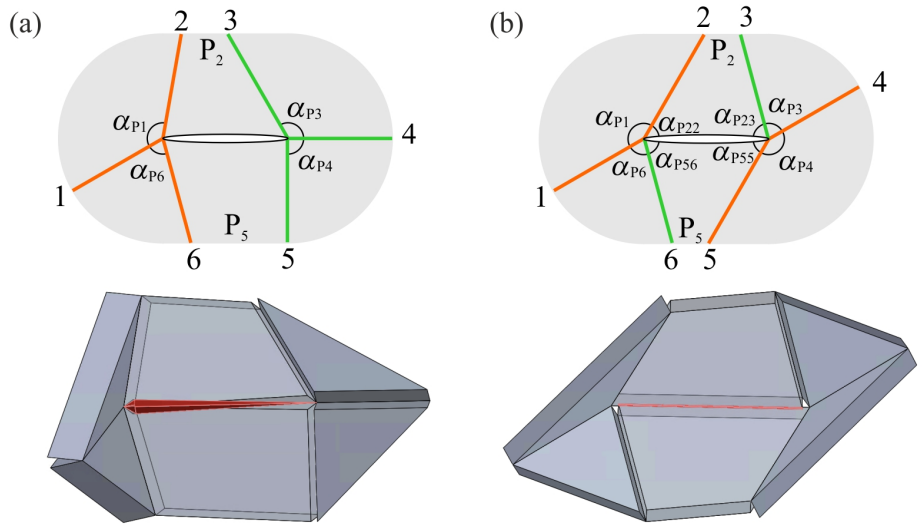


Figure 3.16: Patterns that satisfy **(a)** the Bennet 6R hybrid linkage and **(b)** the line-symmetric Bricard linkage. The physical inference exists between P_2 and P_5.

180° and $\alpha_{P3} + \alpha_{P4} > 180°$, the dihedral angle range in Eq. 3.1 could be satisfied. However, the corresponding 3D model simulated in SOLIDWORKS indicates that the lower edge of P_2 interferes with the upper edge of P_5 when the unit is folded from flat. The overlapping areas are highlighted in red as shown in Fig. 3.16(a). Due to the physical interference, such cases are not counted as mobile units.

The physical collision may also occur to linkages that are already feasible to design morphing units. Notably, Unit c_2 discussed before is based on the line-symmetric Bricard linkage. It could have an alternative fold arrangement as shown in Fig. 3.16(b), where $\alpha_{P1} = \alpha_{P4}$, $\alpha_{P22} = \alpha_{P55}$, $\alpha_{P23} = \alpha_{P56}$, and $\alpha_{P3} = \alpha_{P6}$. If the dihedral angle range in Eq. 3.1 is met, the sum of α_{P1} and α_{P22} should exceed 180°. Nonetheless, a collision between adjacent panels is detected in SOLIDWORKS, as shown in Fig. 3.16(b). Hence, the case was excluded from the categorisation of morphing units in Section 3.2.

3.3.4 Wohlhart 6R linkage

The Wohlhart 6R linkage has found a mobile counterpart on the SSP as Unit m_1. When it comes to the TVP, the situation turns out to be different.

The linkage requires joint offsets R_1, R_3, and R_5 to be all zero as detailed in Table 2.6, which is normally not the case of a TVP. To create zero joint offsets, one strategy is to introduce parallel folds as detailed in Section 3.1. However, it will result in at least three zero link twists, making it impossible to meet the linkage's link twist condition such as $\alpha_{12} + \alpha_{23} = 360°$. The pattern in Fig. 3.4(a) is also explored since it naturally meets the requirement of R_1, R_3, and R_5. Unfortunately, the offsets of other folds become $R_2 = a$, $R_4 = b$, and $R_6 = c$, where a, b, and c are the side lengths of the triangular void. Another geometric condition of the linkage $R_2 + R_4 + R_6 = 0$ cannot be satisfied.

3.4 Summary and discussions

Using a systematic design approach, a complete library of morphing units is uncovered and summarised in Table 3.3. Each unit is made from uniform-thickness panels and possesses single mobility. Among all the units, Units a_1 and c_1, Units a_2 and c_2, and Units b_1 and m_1 are interchangeable with each other under certain geometric conditions. Some units are bifurcation-free with only one path, whilst the rest have at least two sets of motions. In addition to the general 6R overconstrained linkage motion, other paths are caused by either aligned folds to produce hinge-like motions, or the intersection of four folds to create a spherical linkage. The units are ready to be assembled to create large-scale morphing surfaces.

It should also be noted that some units or their special cases have already been

Table 3.3: Summary of morphing units and their kinematic properties

Unit	Base	Linkage	Number of motion paths	Bifurcation point
a_1	SVP	Plane-symmetric Bricard linkage	2*	Flat
a_2	SSP		3	Flat, semi-folded
a_3	QVP		2	Flat
b_1	SVP		2	Flat
b_2	SSP		2	Flat
b_3	QVP		2	Flat
c_1	SVP	Line-symmetric Bricard linkage	4	Flat
c_2	SSP		1**	Flat, semi-folded
c_3	QVP		1***	Semi-folded
m_1	SVP	Wolhart 6R linkage	2	Flat
m_2	TVP	Sarrus linkage	1	None

* The number of motion paths rises to 4 when Unit a_1 has line and plane symmetry, i.e., $\alpha = \beta$.
** The number of motion paths in Unit c_2 rises to 2 when $\delta = 0$ or $\delta = \beta$, and rises to 3 when $\delta = 0$ and $\alpha = \beta$. Both cases have aligned folds and the latter is a special case of Unit a_2.
*** The number of motion paths rises to 2 when Unit c_3 meets the condition set in Eq. 3.31.

reported in the literature. In particular, as mentioned in Fig. 2.7, the constituent units of the uniform-thickness Diamond pattern can be regarded as Unit a_1. In addition, the units from a kirigami tessellation based on the Waldron hybrid linkage shown in Fig. 2.9 are equivalent to Unit a_2. Wang et al. (2023) later reported each unit's kinematic bifurcations using the predictor-corrector numerical method (Kumar and Pellegrino, 2000; Gan and Pellegrino, 2006), to which the analytical solutions in this Chapter are complementary. A special case of Unit m_1 was taken as a three-fold symmetric Bricard linkage (Yang, 2020).

Chapter 4

Construction of Morphing Surfaces from Individual Units

The morphing units obtained in Chapter 3 can be combined with shared folds to produce versatile motions. Regardless of the infinite connection possibilities, this chapter only focuses on tessellations to mimic soft material behaviours as well as assemblies that will be used for the development of robots. Together with Chapter 3, the chapter is modified from a manuscript under review by Liu et al. (2024a).

4.1 Tessellations of morphing units

A tessellation is the covering of a surface using one or more geometric shapes. This section details how the tessellation of origami bases and associated morphing units can produce bending-, expanding-, and twisting-like motions similar to those found in soft materials but with a single mobility.

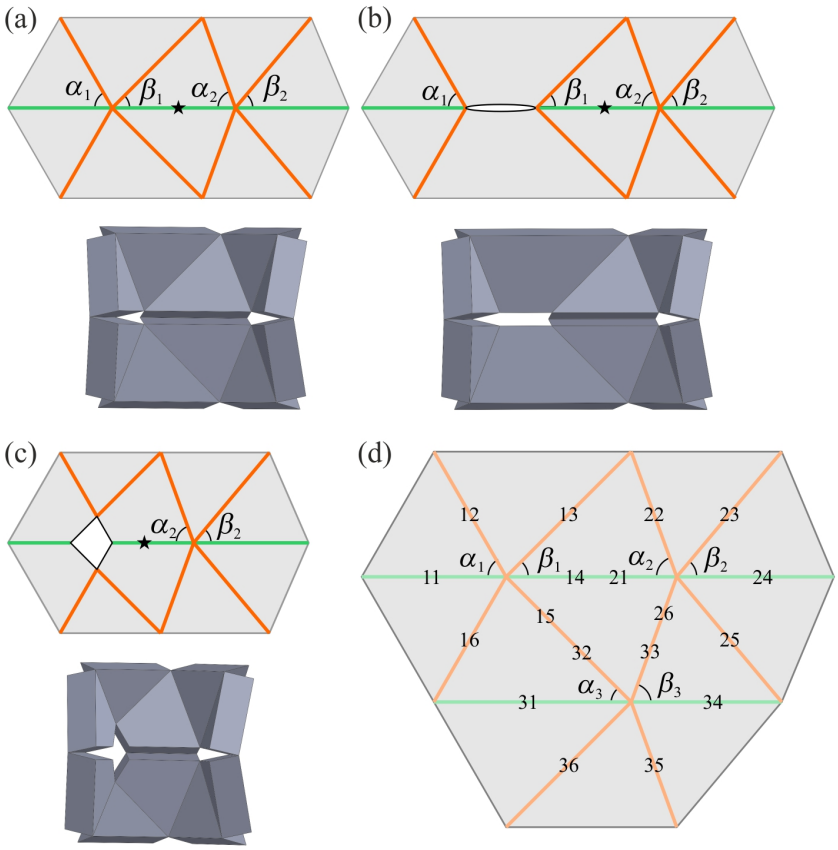


Figure 4.1: Tessellations of Units a_1 - a_3 from Fig. 3.5 and their 3D models. **(a)**, **(b)**, and **(c)** Horizontal strips based on the connection of Units a_1 - a_3. **(d)** Vertical extension of a strip.

4.1.1 Bending behaviours

Bending motions can be achieved by tessellating Units a_1 - a_3 as follows.

Figure 4.1(a) illustrates a strip where two Units a_1 are connected. They are assigned with different geometric parameters, i.e., α_1, β_1, α_2, and β_2. The upper and bottom edges of the strip are parallel to the bottom folds. The shared fold, denoted by a star in the middle, passes the motion from one unit to the other. As such, the strip remains single mobility. According to Eq. 3.5, the use of slit or void does not influence the kinematic behaviours of these units as a Bricard

linkage. The strip can thus be lengthened or shortened by changing one of Units a_1 to Unit a_2 or a_3, as shown in Figs. 4.1(b) and 4.1(c), respectively.

The strip in Fig. 4.1(a) can be extended vertically by adding an extra Unit a_1 with parameters α_3 and β_3 as shown in Fig. 4.1(d). The numbering of each fold is given, thereby representing the associated dihedral angles. The two units from the original strip give two angle inputs to the bottom unit with α_3 and β_3 via the shared folds, i.e., folds 15 and 32, folds 26 and 33. If the tessellation is mobile, the two angles must be compatible with the motion of the bottom unit, which is

$$\tan\frac{\omega_{33}}{2} = \frac{\cos\alpha_3}{\cos\beta_3}\tan\frac{\omega_{32}}{2} \tag{4.1}$$

where $\omega_{32} = \omega_{15}$ and $\omega_{33} = \omega_{26}$, as given by the shared folds.

The mathematical demonstration is as follows. Geometrically, we know

$$\alpha_3 = \beta_1,\ \beta_3 = \alpha_2,\ \omega_{14} = \omega_{21} \tag{4.2}$$

According to Eq. 3.5, we can obtain

$$\tan\frac{\omega_{i1}}{2} = \cos\alpha_i\tan\frac{\omega_{i2}}{2} = \cos\beta_i\tan\frac{\omega_{i3}}{2},\ i = 1,\ 2 \tag{4.3}$$

$$\omega_{i1} = \omega_{i4},\ \omega_{i2} = \omega_{i6},\ \omega_{i3} = \omega_{i5},\ i = 1,\ 2 \tag{4.4}$$

Equations 4.2 - 4.4 yields Eq. 4.1, making the motion of all units kinematically compatible. Thus, the tessellation is foldable and remains single-DoF.

Using such methods, various Units a_1 - a_3 can be tessellated to form large-scale surfaces with single mobility. Figure 4.2 illustrates a general tessellation

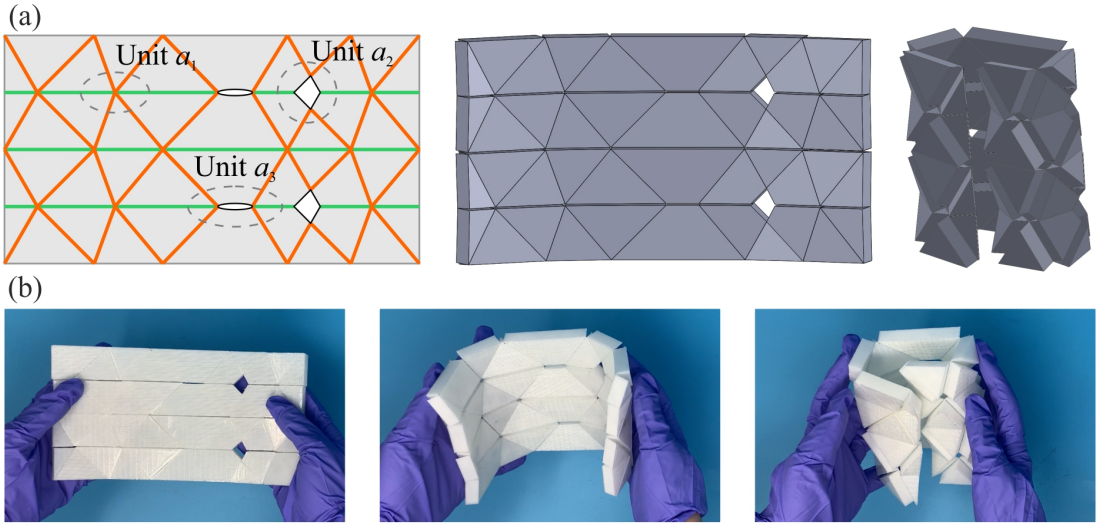


Figure 4.2: The general tessellation of Units a_1 - a_3 and its bending motion. **(a)** The fold pattern and its simulated model in the flat unfolded and semi-folded states. **(b)** The bending motion on a physical prototype made from 3D-printed prisms (serving as rigid panels) and glass fibre tapes (serving as folds).

surface bending into an ellipse shape. The previously discovered origami and kirigami structures (Zhang and Chen, 2018b; Wang et al., 2018b, 2022), which are composed of uniform-thickness panels as shown in Figs. 2.7 and 2.9, belong to a subset of the tessellation given here. In addition to the bending behaviour where each unit has a general Bricard linkage motion, the surface also has bifurcation paths caused by the alignment of bottom folds.

The bending curvature of such tessellations can be altered by tuning the geometric parameters of their constituent units. To obtain a regular-shaped curvature, identical panels are used to form the units. Figure 4.3(a) depicts the tessellation of a triangle with interior angles α, β, and γ, which can roughly bend into a circular shape. When $\alpha = \beta$, the tessellation becomes Fig. 4.3(b), which is the thick-panel version of the Diamond pattern or the Yoshimura origami.

Identical trapezoids can also be used to create a tessellation of Units a_2 with

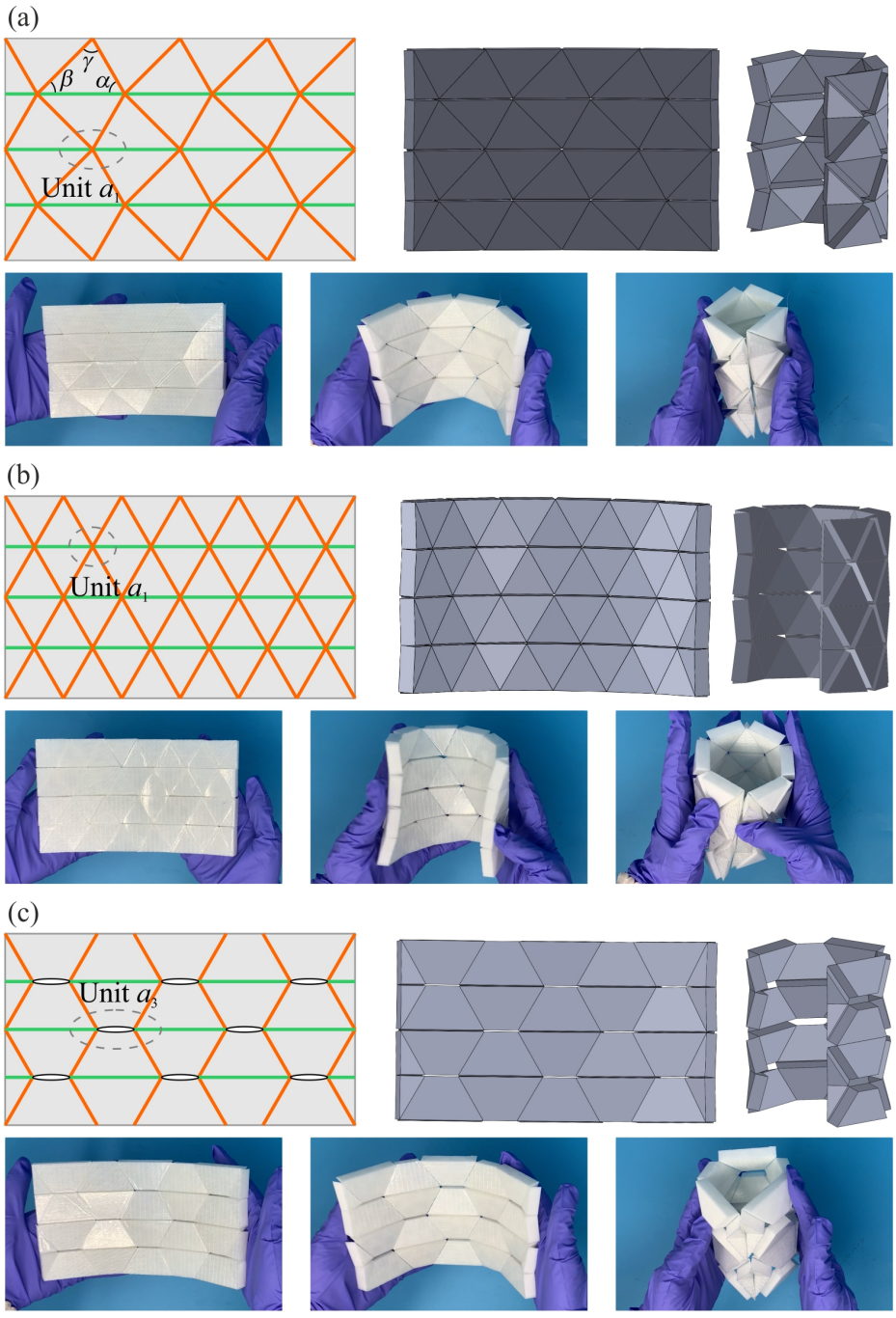


Figure 4.3: Tessellations of identical panels to achieve regular bending shapes. The panels' bases include **(a)** general triangles, **(b)** isosceles triangles, and **(c)** isosceles trapezoids. Repeated individual units of each tessellation are highlighted.

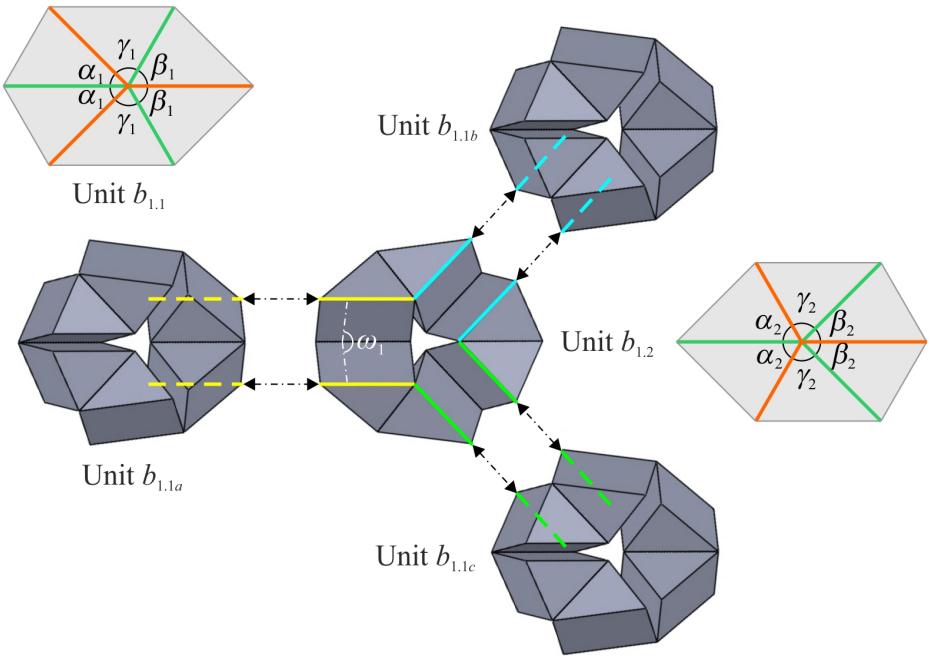


Figure 4.4: Assemblies of Units b_1 from Fig. 3.8 for expanding behaviours. ω_1 of Unit $b_{1.2}$ is taken as input.

slits. A special case is illustrated in Fig.4.3(c), where the trapezoid is isosceles. The surfaces have single DoF when all units undergo the general motion of a Bricard linkage but could also move into other configurations due to the aligned folds. Theoretically, the surface can also shift from bending to twisting when each unit degenerates into a 4R spherical linkage at the semi-folded state, as detailed in Eq. 3.8. However, this turns out physically impossible due to panel collisions.

4.1.2 Expanding behaviours

Identical Units b_1 - b_3 can be connected into a two-layered surface capable of expanding. Taking Unit b_1 as an example, the tessellation method is as follows.

The patterns of Units $b_{1.1}$ and $b_{1.2}$, composed of identical triangular prisms, are given in Fig. 4.4. Their geometric parameters have the following relationship: $\alpha_1 =$

$\beta_2 = \alpha$, $\alpha_2 = \beta_1 = \beta$, and $\gamma_1 = \gamma_2 = \gamma$. Hence, the two units are kinematically equivalent but positioned upside down. When Units $b_{1.1a}$ and $b_{1.2}$ are in their paths 1 and 2 respectively, their finished configurations are the same. This enables three Units $b_{1.1}$ to be connected with Unit $b_{1.2}$ by three pairs of edges highlighted in Fig. 4.4. Each pair of connections plus folds between the pairs form a planar 4R linkage. The connection also blocks the bifurcation paths as a result of physical inference. Hence, these connected units remain single-DoF and become bifurcation-free.

More Units b_1 can be joined to form a two-layered tessellation as shown in Fig. 4.5. The constituent units in Fig. 4.5(a) are derived from a general triangle base. The tessellation in Fig. 4.5(b) is based on equilateral triangles, making the individual unit also a special case of Unit m_1. The input angle ω_1, marked in Fig. 4.4, increases from 0 to 180° to illustrate the expanding motions.

The tessellations originating from Unit b_1 are possible as a result of the plane symmetry among dihedral angles and the alternative top and bottom fold arrangements on each unit. Therefore, Unit b_2 or Unit b_3, which has similar properties, can be connected in the same way. Their examples are not detailed here.

4.1.3 Twisting behaviours

Units c_1 - c_2 exhibit line (or rotational) symmetry in the folding process, which is commonly observed in twisting structures. Identical units are connected to form large-scale tessellations as shown in Figs. 4.6 - 4.8, some of which clearly show twisting behaviours. The tessellation process is detailed below.

Figure 4.6 is a tessellation of Unit c_1, where each unit based on triangles with α, β and γ as the internal angles. The kinematic motion is passed from one unit to

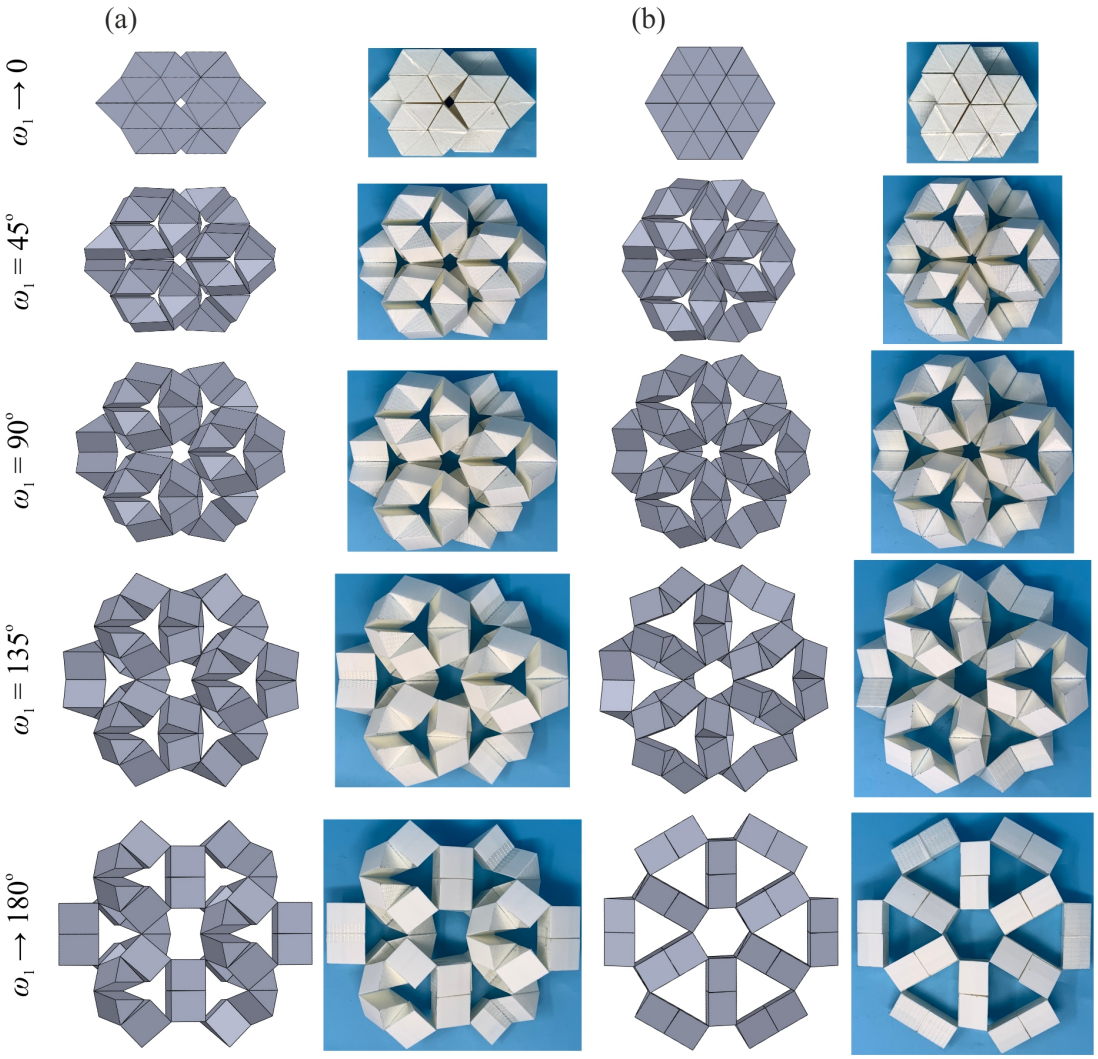


Figure 4.5: Expanding behaviours on the tessellations of Units b_1 where the two-layered surfaces are based on **(a)** general triangles with interior angles as 45°, 75°, and 60°, and **(b)** equilateral triangles. The latter has a more uniform expansion.

another via the shared folds, and thus the mechanism remains single mobility when all units are in the general motion path of a Bricard linkage. In the meantime, the mechanism also has multiple DoFs at the flat state due to aligned folds.

Unit c_2 or Unit c_3 can also be arranged similarly. The tilted slits or voids will destroy aligned folds, thereby eliminating hinge-like motion paths on such

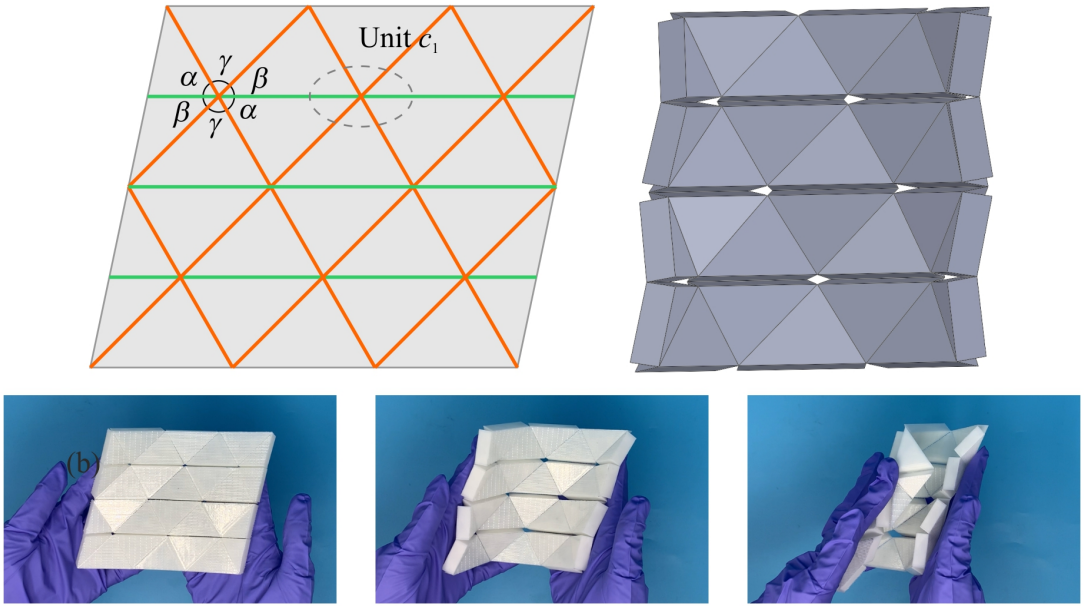


Figure 4.6: Tessellation of repeated Units c_1 from Fig. 3.10. The surface is based on identical triangle panels, where $\alpha = 60°$, $\beta = 45°$, and $\gamma = 75°$. The fold pattern, simulated model, and physical prototypes are all displayed.

tessellations. For instance, Fig. 4.7 illustrates an example of Unit c_2 tessellation. The bases consist of identical quadrilaterals. A more evident twisting behaviour is observed and the motion is bifurcation-free.

Unit c_3 with a parallelogram void can also be tessellated as depicted in Fig. 4.8. Before assembling, the unit's central void shape is modified into a hexagon, which would not change the unit's kinematic behaviours, as depicted in Fig. 4.8(a). The hexagon's sides are parallel to the respective folds of the unit. The opposite sides of the hexagon are also equal. Then each panel of the unit is replaced by the same hexagon as the central void, making the unit ready to be tessellated into a surface shown in Fig. 4.8(b). Note that none of the folds on Unit c_3 are aligned, and thus, the bifurcation paths caused by colinear folds are removed. The physical prototype of the tessellation and its folding process are illustrated in Fig. 4.8(c).

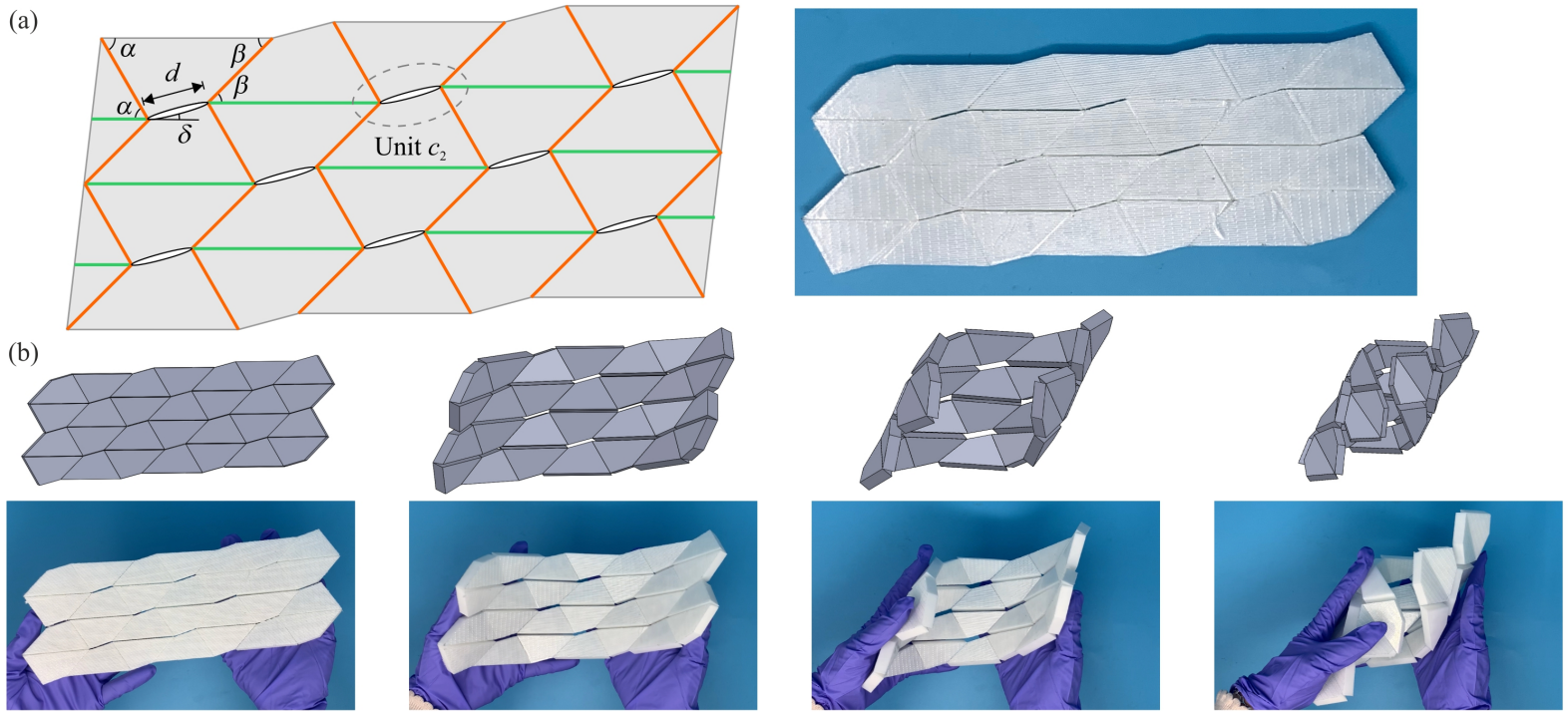


Figure 4.7: Tessellation of repeated Units c_2 from Fig. 3.10. The surface is based on identical quadrilateral panels. Fold pattern where $\alpha = 60°$, $\beta = 45°$, $\gamma = 75°$, and $\delta = 15°$. The slit length d is set twice as the panel thickness h. **(b)** and **(c)** Physical prototype and its twisting process.

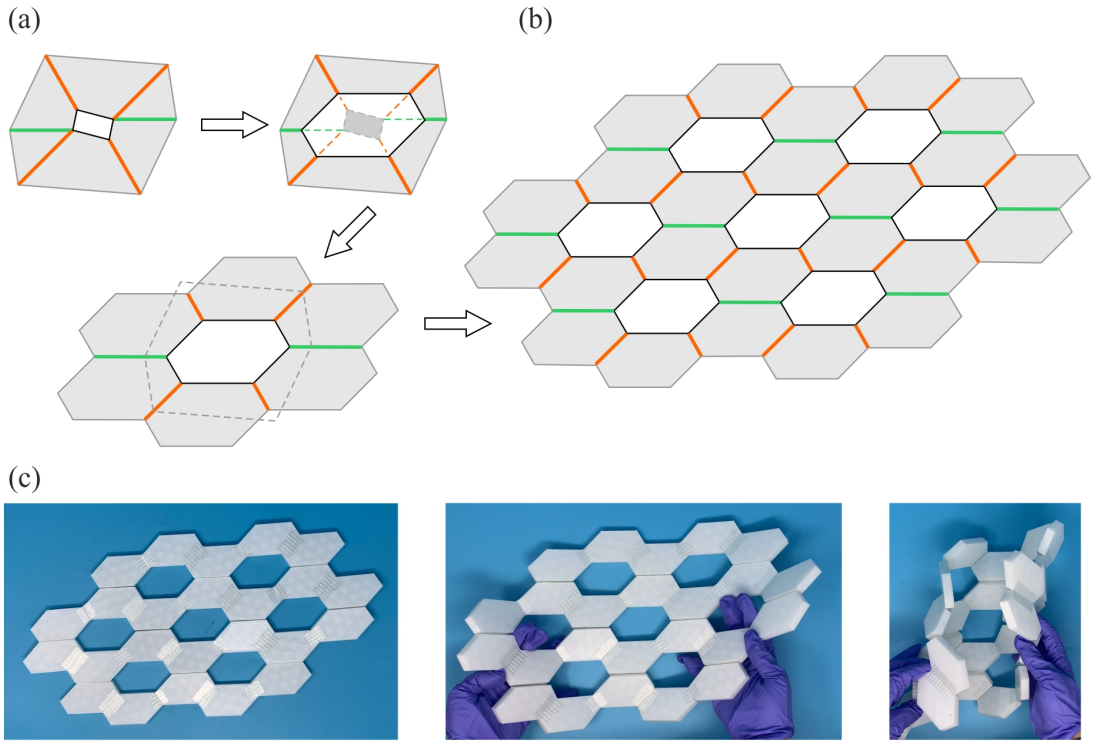


Figure 4.8: Tessellation of repeated Units c_3 from Fig. 3.10 and their modifications into an assembly of identical hexagon panels. **(a)** and **(b)** Single unit modification process and its tessellation pattern. **(c)** Folding process of the physical prototype.

4.1.4 Summary and discussions

In this section, soft-material-like behaviours such as bending, expanding, and twisting are realised by tessellating some units into morphing surfaces. In real-world applications, identical panels are often desired for fabrication simplicity. Given this fact, a new categorisation of identical basic shapes, i.e., triangles, quadrilaterals, and hexagons, is given in Table 4.1, to form versatile morphing surfaces.

Compared to the properties of morphing units in Table 3.2, it is found that some surfaces, i.e., the ones capable of expanding, have a smaller number of bifurcations than their constituent units. This is because new physical inferences are introduced

Table 4.1: Basic shapes and their tessellation properties

Shape	Requirement	Unit	Motion of tessellated surface	Number of motion paths
Triangle	General	a_1	Bending	>1
		b_1	Expanding	1
		c_1	Twisting (imperceptible)	>1
	Equilateral	a_1/c_1	Bending	>1
		b_1/m_1	Expanding (isotropic)	1
Quadrilateral	General	c_2	Twisting (obvious)	1
	Trapezoid	a_2	Bending	>1
		b_2	Expanding	1
Hexagon	Equal and parallel opposite sides	c_3	Twisting (imperceptible)	1

to remove one of the original motion paths. Some twisting surfaces have only one DoF as a result of their bifurcation-free units.

Note that QVP-based morphing units, i.e., Units a_3, b_3, and m_2, are not well included in Table 4.1 except for Unit c_3. However, this does not mean that those units cannot be used for surface tessellations as this section only aims to give a few examples to achieve bending, expanding, and twisting motions. It should be emphasised again that the possibilities are unlimited and all units in Table 3.3 can be explored according to the specific needs.

4.2 Assemblies of morphing units

In addition to tessellations capable of basic motions, the morphing units can be assembled to produce complex behaviours as another type of morphing surface. Regardless of the infinite permutations, this section only presents surfaces capable of wrapping or curling. They are specially developed to achieve functions such as grasping, manipulation, and reconfiguration in Chapters 5, 6, and 7, respectively.

4.2.1 Wrapping surface

Wrapping behaviours can be achieved on a circular assembly of Units a_1 or Units c_1 when they have both line and plane symmetry.

Three-unit, four-unit, and five-unit assemblies are illustrated in Fig. 4.9. The corner panels of each assembly can wrap around the central base when the units are in their respective path 1. The single-DoF feature is preserved due to shared common folds. Take the central base as a palm and the corner panels as fingers. Thus, the wrapping motion can be regarded as an imitation of human hand grasping, which will be demonstrated as a gripper in Chapter 5.

In addition to the wrapping motion, these assemblies have other motion paths due to the aligned folds. Its specific kinematic performance is to be analysed in Chapter 6. These bifurcations have equipped each assembly with motion possibilities beyond grasping. They will be exploited for object manipulation with a limited number of control inputs.

4.2.2 Curling surface

The chain-like assembly shown in Fig. 4.10 can generate curling motions.

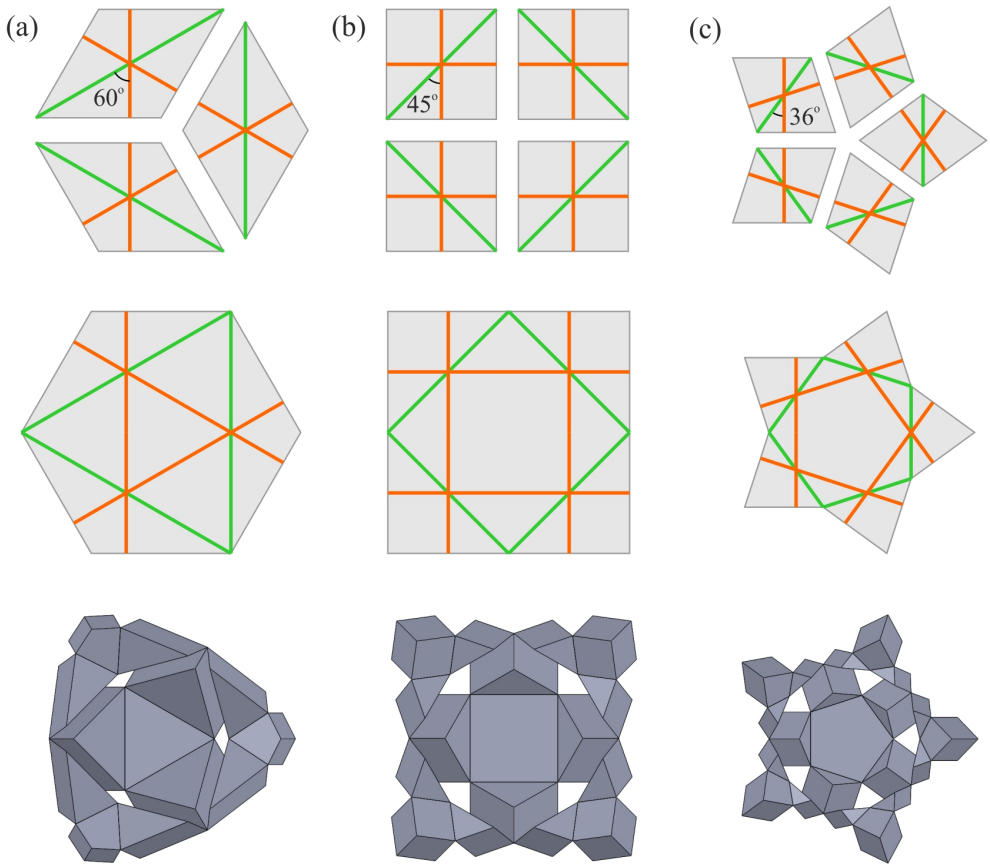


Figure 4.9: Wrapping motions of **(a)** three-unit, **(b)** four-unit, and **(c)** five-unit assemblies.

The surface is composed of two types of morphing units, i.e., Units a_2 and b_1. The pattern is symmetric about its central axis, as denoted by the dashed line. The units repeat one after another along the chain.

When all Units a_2 and b_1 are in their respective motion path 1, a curling behaviour of the chain is produced, whose cross-sectional view is illustrated in Fig. 4.10(b). When Units a_1 remain in the same path and all Units b_1 switch to their motion path 2, another curling motion is generated in Fig. 4.10(c). The two configurations make it natural for the surface to mimic a millipede's curling behaviour when it senses danger.

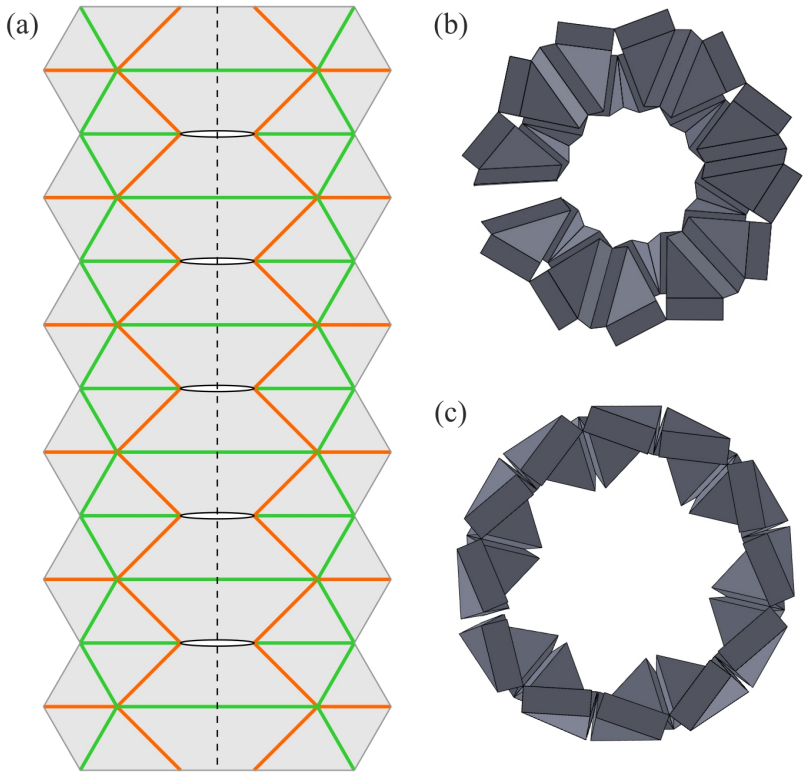


Figure 4.10: Design of a curling surface. **(a)** Top view of the origami pattern. **(b)** and **(c)** Cross-sectional views of two curling configurations.

It is also anticipated that with permutations of paths 1 and 2 on different Units b_2 along the surface, the chain can reconfigure itself into other profiles, which are also observed on the millipede. The exact kinematic bifurcations and associated configurations of the surface are detailed in Chapter 7. With actuation and control components integrated, the surface will be developed into a reconfigurable robot to imitate the millipede's morphologies.

Chapter 5

Wrapping Surface: a Robotic Gripper Enabled by a Single Motor

A robotic gripper is developed from a surface that can wrap. This chapter reports the design, modelling, and fabrication of the gripper, whose grasping performance is also experimentally characterised. The contents in this chapter are modified from publications by Liu et al. (2020b, 2021c).

5.1 Gripper design from the wrapping surface

This section recaps the motivation of the gripper and gives its conceptual design from the wrapping surface. The grasping motion is kinematically analysed. The associated actuation method, fingertip trajectory, and grasping range are also presented in detail.

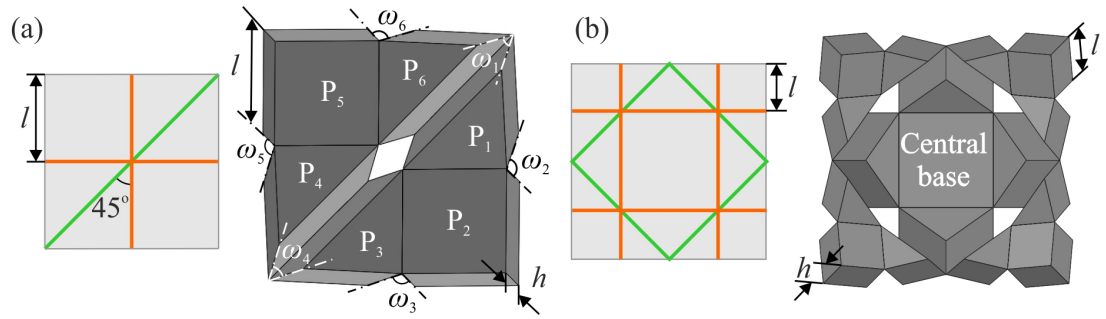


Figure 5.1: Origami pattern and corresponding 3D kinematic models of **(a)** a morphing unit and **(b)** its assembly that forms the gripper backbone.

5.1.1 Motivation statement

As detailed in Subsection 2.3.1, grasping and manipulation are two basic functions of end effectors, which always strive to balance the motion dexterity and control intricacy. Whilst grasping cannot guarantee manipulation, the former is often a prerequisite for the latter. Hence, a basic gripper design will be presented first, which aims at grasping with minimal actuators. This lays the foundation to carry out manipulation tasks in Chapter 6.

5.1.2 Kinematic modelling of the wrapping surface

The four-unit wrapping surface in Fig. 4.9(b) is intended as the gripper backbone. To model its kinematic behaviour, the assembly and its constituent units are reproduced in Fig. 5.1, where the side length is l and panel thickness is h. For each unit, the dihedral angles are obtained as follows according to Eq. 3.5.

$$\begin{gathered} \omega_1 = \omega_4,\ \omega_2 = \omega_3 = \omega_5 = \omega_6,\ 0 \leq \omega_i \leq \pi \\ \tan\frac{\omega_2}{2} = \sqrt{2}\tan\frac{\omega_1}{2} \end{gathered} \tag{5.1}$$

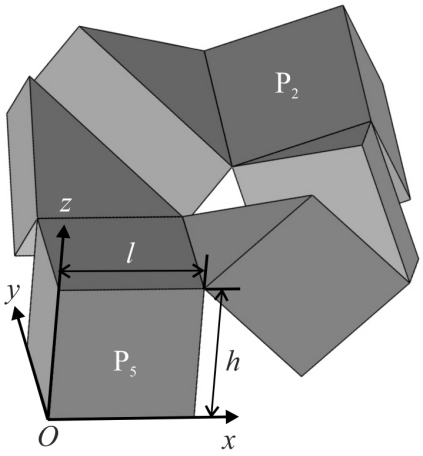


Figure 5.2: The Cartesian coordinate system for the morphing unit.

To investigate the exact motion behaviour of the unit, a Cartesian coordinate system is set up as shown in Fig. 5.2 where P_5 is taken as the ground. The centre of P_2 is used to represent the unit's motion trajectory, whose coordinates are

$$x_{P2} = y_{P2} = \frac{6h\sin\omega_2 + 5l\cos\omega_2 + 7l}{2l(3+\cos\omega_2)},\ z_{P2} = \frac{4l\sin\omega_2 - 5h\cos\omega_2 + 9h}{2l(3+\cos\omega_2)} \tag{5.2}$$

Merging three items in Eq. 5.2 yields

$$(x_{P2} - l)^2 + (y_{P2} - l)^2 + (z_{P2} - 2h)^2 = \frac{9h^2 + 2l^2}{4l^2} \tag{5.3}$$

which is a sphere with its centre at $(l, l, 2h)$. Considering that $x_{P2} = y_{P2}$, it can be concluded that the motion trajectory of P_2 is part of a circle relative to P_5.

Four units are put together to form an assembly shown in Fig. 5.1(b). Mechanical coupling is achieved via shared folds and merged panels. As such, it is not difficult to find that each unit retains its ability to perform the single-DoF circular movement. The trajectories of four corner panels lead to a wrapping motion,

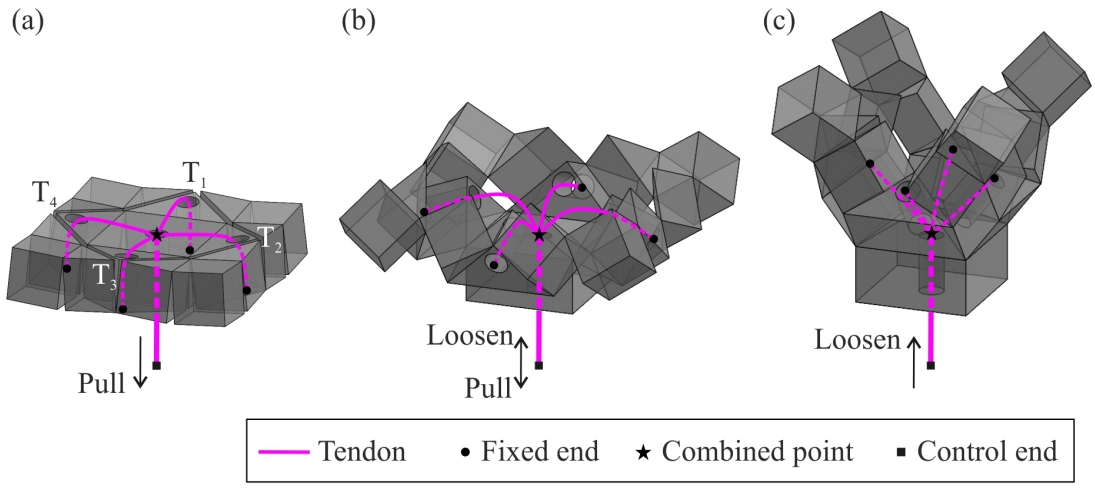


Figure 5.3: Pulling the tendons enables the assembly to start from **(a)** the nearly unfolded state, pass through **(b)** the semi-folded state, and end up at **(c)** the near fully folded state. The process is reversible by loosening the tendons.

similar to four fingers bending towards a central palm, which forms the foundation to grasp objects. The assembly also has other motions due to the aligned folds, which will be discussed in Chapter 6 for manipulation tasks.

5.1.3 Actuation of the wrapping motion

The active wrapping behaviour is achieved through a tendon-based system. As shown in Fig. 5.3(a), four through-hole channels are made on the surrounding panels, where tendons T_1 - T_4 are fixed. Then the tendons pass through the channels respectively and meet at the centre. The assembly's bifurcation point is at its unfolded state, and hence, pulling a single tendon cannot reliably activate the wrapping motion. Instead, all tendons are combined to form a single end, whose position is to be controlled by the actuator, e.g., a motor.

When the control end is pulled at the assembly's flat configuration, it subsequently passes through different folded states shown in Figs. 5.3(b) and 5.3(c),

the process of which is the closing motion. The folds are designed elastic and only strain-free at the unfolded state, i.e., the flat configuration. Therefore, the assembly will return to the flat state to release strain energy in those folds, once the control end is loosened. This process is the opening motion. The grasping behaviour is repeatable by pulling and releasing the tendons.

5.1.4 Gripper design and modelling

The corner panels of the assembly exhibit circular motion trajectories and are taken as the backbone of four fingers. To enhance their grasping capability, the panels are replaced by lengthened fingers with hemispheres mounted as fingertips, yielding the gripper design in Fig. 5.4(a). A cross-sectional view of the gripper at two poses is illustrated in Fig. 5.4(b), where only finger 1, i.e., F_1 is presented and others are omitted due to symmetry. Pose 1 is the initial state of the gripper and F_1 can rotate about point O_1 according to Eq. 5.3. Note that the Cartesian coordinate system in Fig. 5.4 has been rotated about the z axis compared to the one set up in Fig. 5.2 and the origin has also been moved along the z axis. Pulling the tendons activates all fingers synchronously to Pose 2 and even further until the fingertips collide. The rotation angle θ is used to represent the finger's state. Its value is given by

$$\tan\frac{\theta}{2} = \tan\frac{\omega_1}{2} = \frac{\sqrt{2}}{2}\tan\frac{\omega_2}{2} \tag{5.4}$$

The top point A_1 of F_1 is used to represent its trajectory, whose coordinates

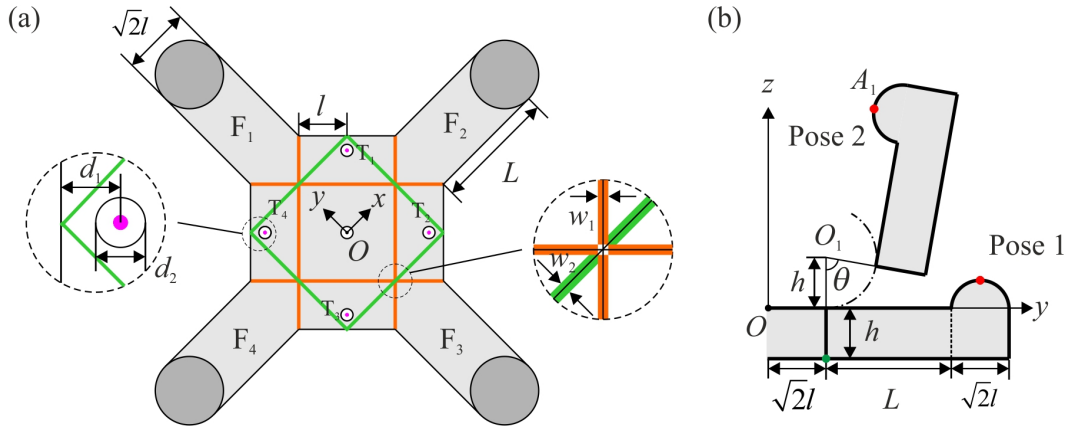


Figure 5.4: Kinematic model of the gripper and its fingers. **(a)** Proposed design of the origami gripper from its top view, where lengthened fingers, hemisphere fingertips, tendon channels, and folds' widths are all denoted. **(b)** Cross-sectional view of F_1 at two poses. Its rotation angle is represented by θ. The central top point of the fingertip is marked in red.

are given by

$$\begin{aligned} x_{\mathrm{A1}} &= 0 \\ y_{\mathrm{A1}} &= \sqrt{2}l + R\sin\left(\theta + \arctan\frac{\sqrt{2}L + l}{\sqrt{2}h - l}\right) \\ z_{\mathrm{A1}} &= h - R\cos\left(\theta + \arctan\frac{\sqrt{2}L + l}{\sqrt{2}h - l}\right) \end{aligned} \tag{5.5}$$

where R is the distance between points A_1 and O_1 obtained as below.

$$R^2 = (L + \frac{\sqrt{2}}{2}l)^2 + (h - \frac{\sqrt{2}}{2}l)^2$$

The above analysis is based on the assumption that all folds are perfect revolute joints and their widths are regarded as zero. In practice, the widths may not be negligible due to the actual fabrication parameters. Two types of folds exist in the gripper backbone, whose widths are w_1 and w_2 as illustrated in Fig. 5.4(a). The middle lines of these folds are marked in black and used as the new folding

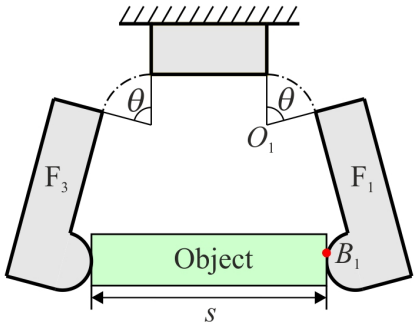


Figure 5.5: Cross-sectional view of the gripper holding an object.

creases. In this case, Eq. 5.5 should be rewritten as

$$
\begin{aligned}
x'_{\mathrm{A1}} &= 0 \\
y'_{\mathrm{A1}} &= \sqrt{2}l + R' \sin\left(\theta + \arctan\frac{\sqrt{2}L + l + w_1 + \frac{\sqrt{2}}{2}w_2}{\sqrt{2}h - l}\right) \\
z'_{\mathrm{A1}} &= h - R' \cos\left(\theta + \arctan\frac{\sqrt{2}L + l + w_1 + \frac{\sqrt{2}}{2}w_2}{\sqrt{2}h - l}\right)
\end{aligned}
\tag{5.6}
$$

where the new distance between points A_1 and O_1 is R', given by

$$
R'^2 = (L + \frac{\sqrt{2}}{2}l + \frac{\sqrt{2}}{2}w_1 + \frac{1}{2}w_)^2 + (h - \frac{\sqrt{2}}{2}l)^2
$$

5.1.5 Calculation of grasping range

When grasping, the cross-sectional view of the gripper along the x axis is shown in Fig. 5.5. The object is assumed as a cuboid whose base has equal side lengths of s. The contact point between the fingertip and the object keeps changing depending on the gripper's closing state. Given this, the relationship between the object's size s and the finger's rotation angle θ is depicted as

$$
s = \sqrt{2}(l + w_1) + w_2 + 2r \sin\left(\theta + \arctan\frac{\sqrt{2}L + l + w_1 + \frac{\sqrt{2}}{2}w_2}{\sqrt{2}h}\right) \tag{5.7}
$$

where r is the distance between points B_1 and O_1 marked in Fig. 5.5, given by

$$r^2 = (L + \frac{\sqrt{2}}{2}l + \frac{\sqrt{2}}{2}w_1 + \frac{1}{2}w_2)^2 + h^2$$

According to Eq. 5.7, the maximum grasping size is $\sqrt{2}(l + w_1) + w_2 + 2r$. The minimum grasping size is $(2 - \sqrt{2})l$ when adjacent fingers touch each other.

5.2 Experimental procedure

This section details how a gripper was fabricated. Experiments were then carried out to characterise the gripper's behaviours, including its motion trajectories, the contact force generated on objects, and its grasping performance.

5.2.1 Gripper prototype fabrication

3D printing was used for the ease and repeatability of fabrication. Figure 5.6 illustrates the computer-aided-design (CAD) model of the gripper backbone, which was fabricated using thermoplastic polyurethane (TPU) material. The material has a shore hardness of 95A. It is flexible and elastic as thin layers, serving as the origami folds or hinges to complete repeatable grasping motions. When the thickness of TPU increases to around 10 mm, the material is almost rigid, making it a suitable candidate for thick panels. Thus, the entire gripper backbone was fabricated with TPU material in a single print on a desktop 3D printer (Ultimaker 3 extended). The actual design and fabrication parameters in Figs. 5.4 and 5.6 are specified in Table 5.1.

The soft fingertip coat, also shown in Fig. 5.6, has an inner diameter of 9.2

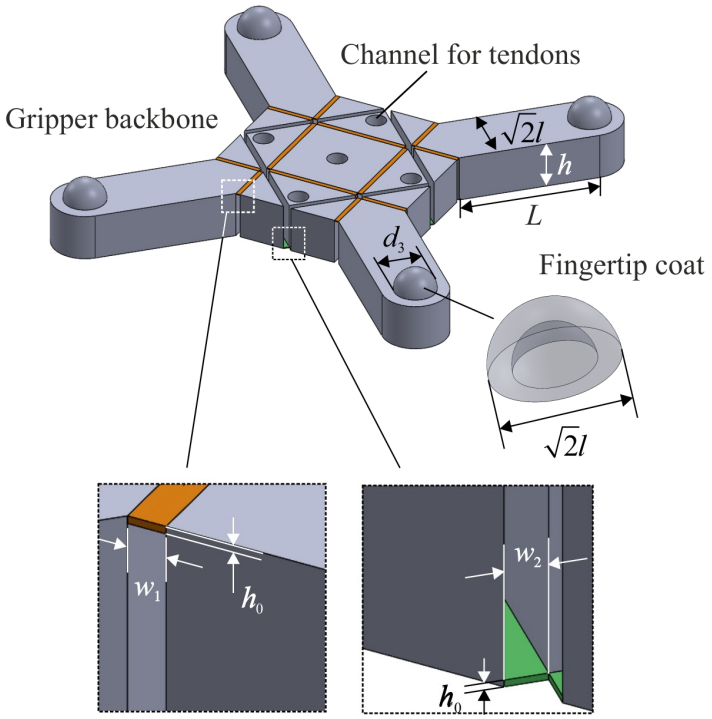


Figure 5.6: CAD model of the gripper backbone and fingertip coat for 3D printing.

Table 5.1: Fabrication parameters of the gripper prototype (unit: mm)

L	l	h	w_1	w_2	d_1	d_2	d_3	h_0
30	10	10	1	1.2	2.8	4.3	9	0.2 - 0.3

mm so that it can be glued to the protruding part of the gripper backbone. For better grasping performance, tiny points with a radius of 0.1 mm were evenly embossed on the coat's outer surface to increase friction. Such fingertip coats were 3D-printed on a Polyjet printer (Stratasys-j735) using Agilus30$^{\text{TM}}$ material, which comes with a shore hardness of 30A. Then the coats were securely attached to the gripper fingers. Clear nylon fishing lines were used as tendons and fixed to the end of each tendon channel on the triangular prisms.

To evaluate the gripper's performance, it was mounted on an adapter with a

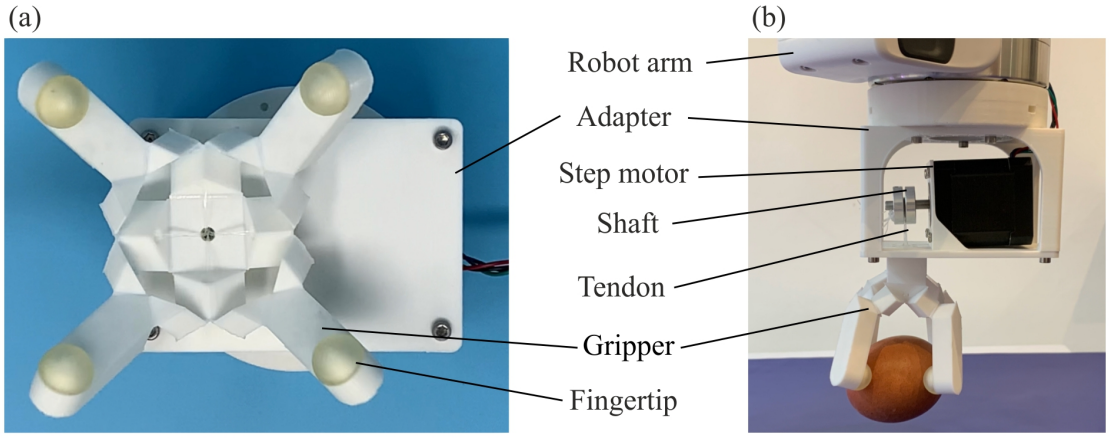


Figure 5.7: The gripper prototype. **(a)** Top view of the gripper with four fingers semi-closed. **(b)** Side view of the gripper holding an egg.

step motor (NEMA 17), as shown in Fig. 5.7. The control end of the tendons was tied to the motor's shaft. Under the open-loop control of a microcontroller (Arduino UNO), the gripper can achieve closing and opening motions via clockwise and anticlockwise rotations of the shaft. The adapter was then bolted to a robot arm (PANDA, Franka Emika) for grasping evaluation as shown in Fig. 5.7(b).

The entire fabrication process was completed within six hours and is relatively straightforward without much human intervention.

5.2.2 Characterization of the gripper's performance

Experiments were carried out on the prototype to characterise its behaviours.

To validate the gripper's motion trajectories, markers with a size of 2 mm were placed at the top centre of the fingertips. Their positions were recorded by a desktop 3D scanner (EinScan Pro+) with a resolution of 0.24 mm. The gripper was opened from the completely closed configuration until it turned into the flat state. Then the gripper was closed until all the fingertips touched. A full cycle of

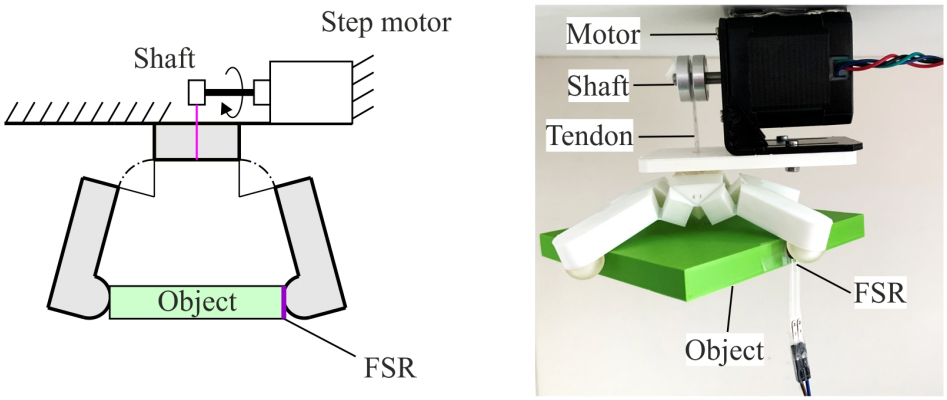


Figure 5.8: Experimental setup to measure the maximum contact force that the gripper is able to generate on objects of different sizes.

the gripper's motion was thus obtained. Still positions were provided by the step motor which rotated at a 10.8° interval, six times its minimum step. Each position was acquired by the 3D scanner and one cycle included 22 sets of coordinates in the opening process and 21 in the closing process. The cycle was repeated five times and all the position data were used to assess the gripper's motion.

Secondly, as shown in Fig. 5.8, the gripper prototype was used to grasp a set of cuboids. Each has a square base with a side length ranging from 10 to 100 mm at a step of 10 mm. A calibrated force resistive sensor (FSR) was attached to one side of each cuboid. A thin plastic pad was placed between the FSR and the object to evenly distribute the contact force. The gripper was closed to grasp each cuboid until the motor reached its maximum torque. 100 continuous readings were taken from the FSR for further analysis.

Lastly, the gripper's grasping capability was evaluated on 20 daily objects, whose specifics will be given in Section 5.3. The experimental setup is shown in Fig. 5.7(b) where the robot arm is employed. The test on each object under open-loop control was conducted as follows. Twelve trials were performed on each

object. The number of successful grasps was counted.

- Lower the robot arm to approach an object placed on a flat surface.
- Close the gripper to the object until the motor reaches its maximum torque.
- Lift the arm and hold the object for around 10 seconds.

5.3 Results and discussions

5.3.1 Motion trajectories of the gripper

Figure 5.9(a) illustrates each fingertip's position in the opening and closing motions. Theoretical trajectories are also plotted with the marker size taken into account. The data used here are the average of each position from the five repeated experiments. The standard error of the mean was calculated for each position, ranging from 0.03 to 1.38 mm, which is considered insignificant compared to the range of the finger movements. Therefore, the averaged positions are used for subsequent discussions. To quantify the difference between experimental results and theoretical predictions, the trajectories are analysed in the 2D planes.

First of all, the experimental positions are compared with the theoretical lines. The opening motion of fingertip 2 is taken as an example. Its 2D trajectories in the xOy and xOz planes are plotted, as shown in Figs. 5.9(b) and 5.9(c), respectively. The measure of error at each position is indicated, i.e., d_{i-xOy} and d_{j-xOz}. The detailed 2D trajectories of all fingers are given in Fig. 5.10 and the maximum position error (MPE) of each finger is summarised in Table 5.2.

As for the position error in the xOy plane, fingertip 1 has the best performance in both closing and opening motions. In the vertical plane, i.e., the xOz or yOz

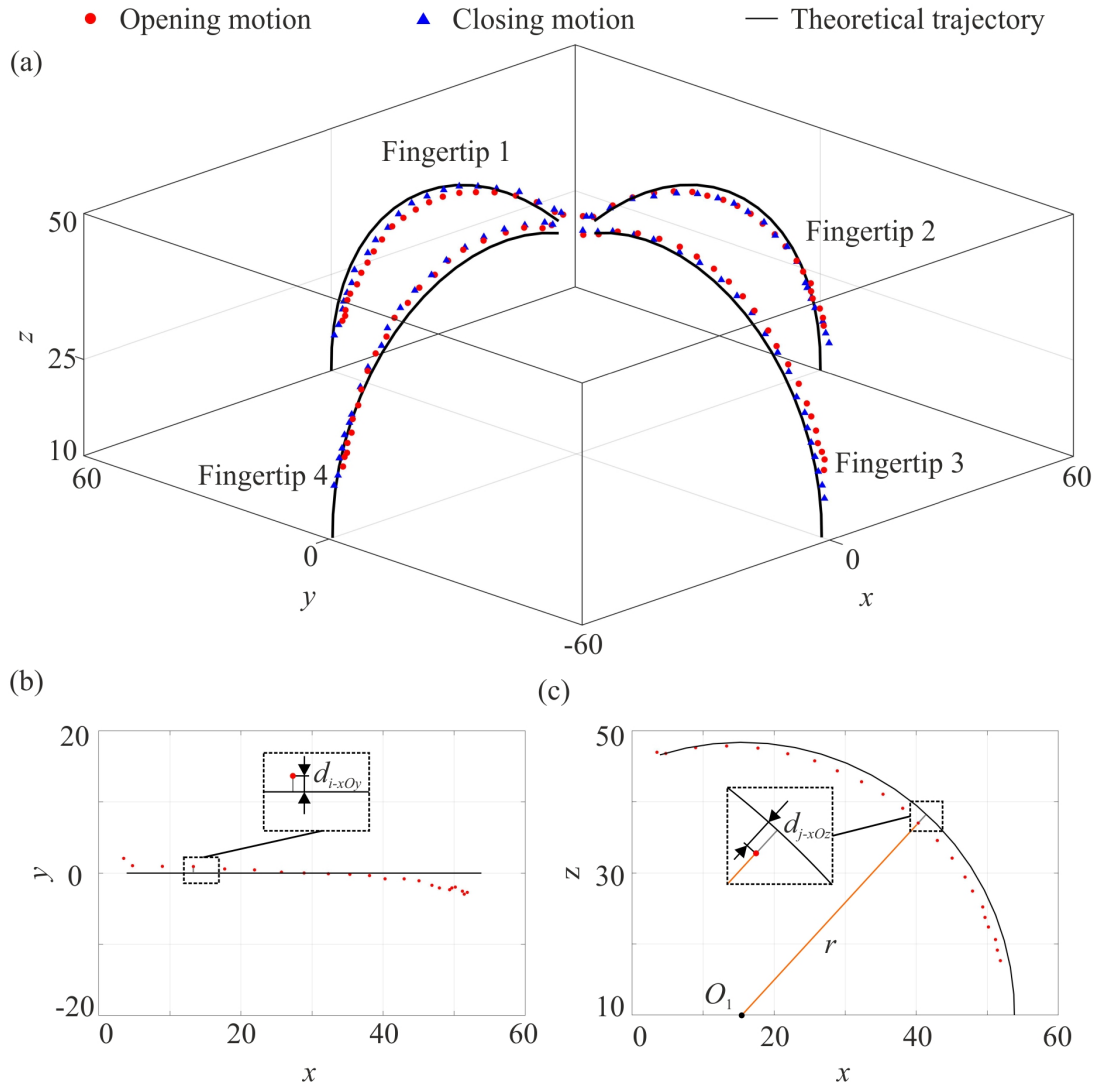


Figure 5.9: Motion trajectories and position errors of the gripper. **(a)** Experimental results of 3D fingertip positions in comparison with theoretical predictaions. Calculation of position error in **(b)** the xOy plane and **(c)** the xOz plane are illustrated by taking a random position of fingertip 2 in its opening motion. The unit is in mm.

plane, fingertip 4 has the highest accuracy. The maximum position error within all four fingers is 3 mm, indicating good alignment with theoretical predictions. Slight differences are visible when comparing four fingers, whose trajectories are

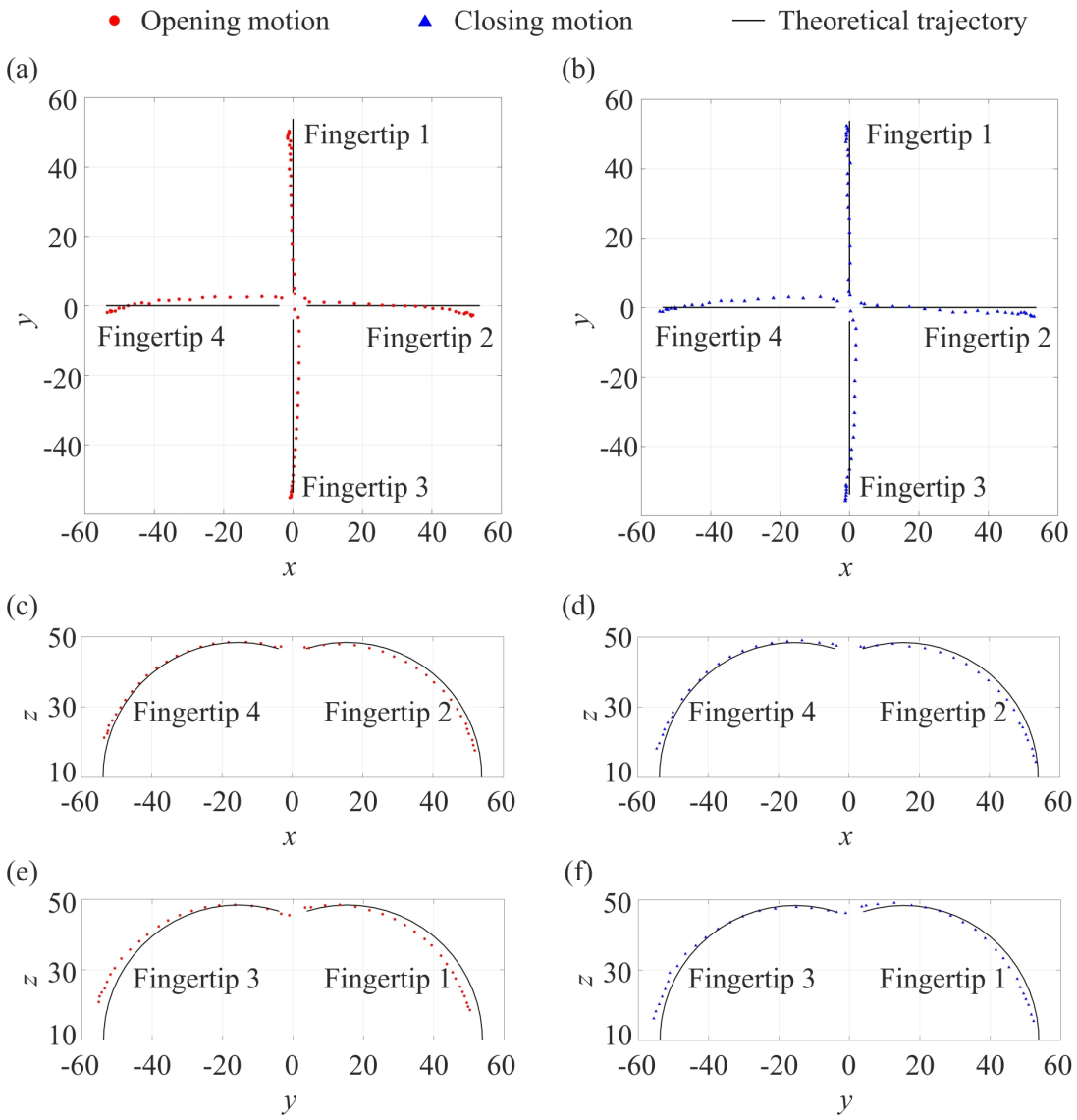


Figure 5.10: Experimental 2D trajectories of all fingertips in the closing and opening motions. **(a)** and **(b)** Fingertip trajectories in the xOy plane. **(c)** and **(d)** Fingertip trajectories in the xOz plane. **(e)** and **(f)** Fingertip trajectories in the yOz plane. The unit is in mm.

supposed to be symmetric around the origin. The small asymmetry might be attributed to differences among elastic folds made by 3D printing.

The experimental opening and closing motions of each finger are also compared

Table 5.2: MPE of fingertips in the 2D planes (unit: mm)

Finger	**MPE in the opening motion**		**MPE in the closing motion**	
	xOy **plane**	$x(y)Oz$ **plane**	xOy **plane**	$x(y)Oz$ **plane**
1	1.55	3.00	1.03	1.99
2	2.96	1.70	2.60	1.89
3	1.80	3.03	1.89	2.56
4	2.60	1.29	3.00	1.66

Table 5.3: Displacement between the opening and closing motions (unit: mm)

Finger	xOy **plane**	$x(y)Oz$ **plane**	
		Fitted opening motion	**Fitted closing motion**
1	0.52	1.33	1.67
2	0.36	0.38	1.54
3	0.09	1.27	1.37
4	0.40	0.78	0.69

to understand the two-way difference. In the xOy plane, the trajectory displacement is calculated as the difference of their maximum position errors with the theoretical line. For the displacement in the xOz or yOz plane, positions in the experimental opening (or closing) motion for each fingertip are fitted into a circle using the least square method. Then the positions in the experimental closing (or opening) motion are used to calculate their displacements from the fitted circle, using similar methods in Fig. 5.10(c). The maximum displacement among all positions is taken as the trajectory displacement. All data are given in Table 5.3. The alignment between the two-way motions indicates almost no hysteresis.

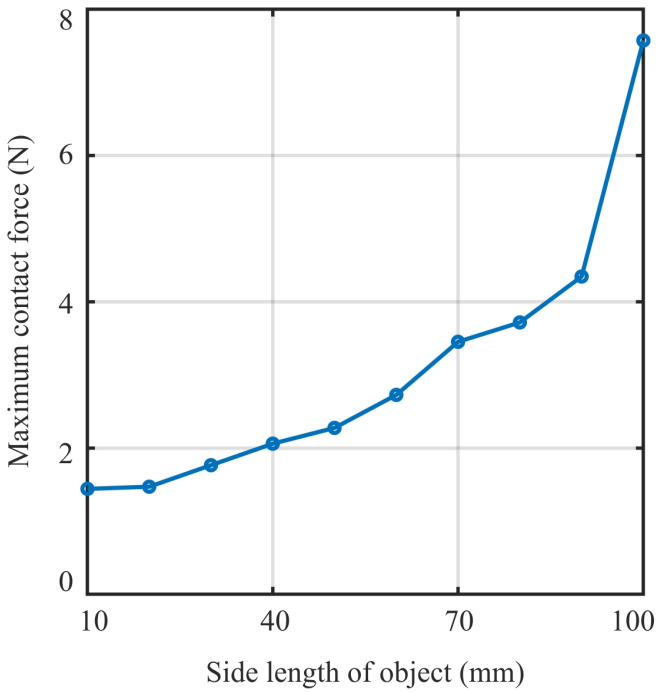


Figure 5.11: The contact forces generated on objects of different side lengths, ranging from 10 to 100 mm at a step of 10 mm.

5.3.2 Contact force generated on objects

The contact force generated on objects of different sizes is plotted in Fig. 5.11. The bigger the size of an object, the higher the contact force generated. According to Eq. 5.7 and the fabrication parameters in Table 5.1, the maximum size the gripper can hold is 97 mm, which is lower than the actual successful grasp of 100 mm. The difference can be attributed to the elastic TPU folds and indicates a certain level of compliance within the gripper fingers.

If a grasp is successful, the contact force on the object can be broken down into two components, normal force and static friction. The sum of friction on each finger should equal the object's weight. Assuming that the maximum value of static friction is proportional to the normal force, the results in Fig. 5.11 suggest that

Table 5.4: Daily objects for grasping evaluation and the successful grasping rate

Object	**Weight (g)**	**Successful rate**
Toilet roll	160	12/12
Snack bag	28	10/12
Dice	31	12/12
Hand sanitizer	60	9/12
Sponge	8	12/12
Mini iron	258	8/12
Mug	524	10/12
Orange	86	11/12
Egg	60	12/12
Socket	46	8/12
Data line	27	7/12
Toy	87	12/12
Glue bottle	232	12/12
Marker pen	14	6/12
Force scale	143	11/12
Luck knot	78	12/12
Lunchbox bag	171	8/12
Towel	122	12/12
USB stick	20	12/12
Pulley	41	12/12

within grasping range, the gripper tends to have a better grasping performance, i.e., higher maximum grasping weight (MGW), on objects with a larger size.

5.3.3 Grasping performance

The specifics and the successful grasping rates on the 20 objects are summarised in Table 5.4. Selected grasping images of the gripper are displayed in Fig. 5.12 and a video of the grasping process is available in Appendix B.

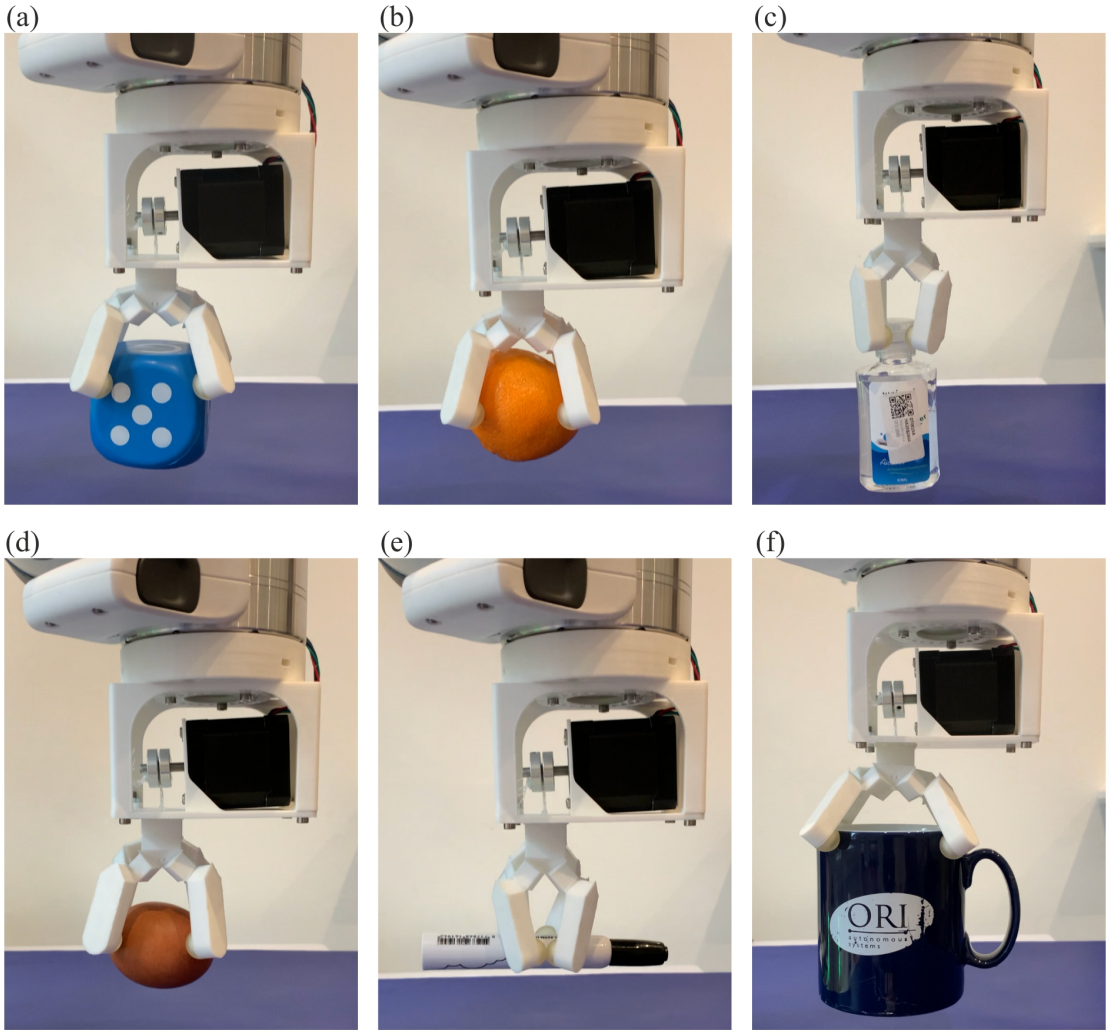


Figure 5.12: Grasping daily objects, which include **(a)** a dice, **(b)** an orange, **(c)** a hand sanitiser, **(d)** an egg, **(e)** a marker pen, and **(f)** a mug with water.

Although the gripper shows relatively stable grasping on the selected 20 objects, its performance varies significantly in terms of object size, shape, and texture. For instance, its MGW was achieved on the mug with water inside, even though it has a rather low coefficient of friction on the ceramic surface. The mug's diameter is around 90 mm, close to the maximum grasping size of 97 mm. As discussed in Fig. 5.11, the gripper can exert a relatively higher contact force on objects of a

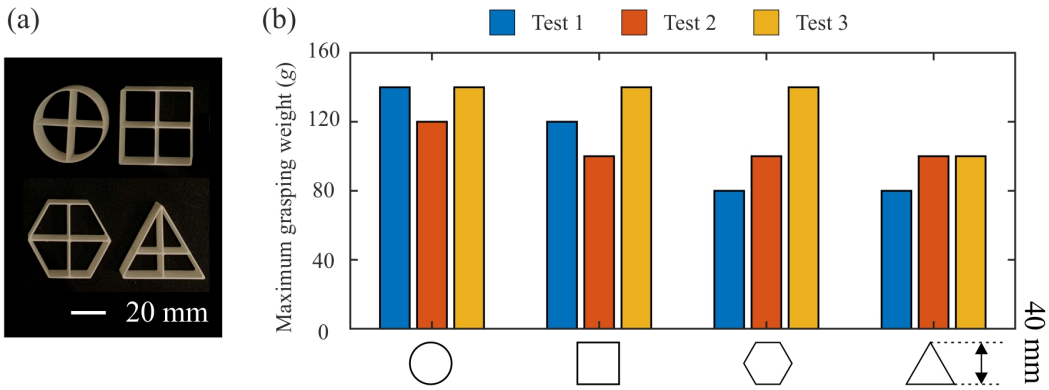


Figure 5.13: Grasping capability evaluation. **(a)** Objects used for grasping whose bases are circle, square, hexagon, and triangle. **(b)** MGW of each object.

larger size, which helps to improve the grasping performance. The gripper also performs well on objects with a relatively rough surface, such as the sponge, the orange, and the egg.

One interesting fact in the grasping evaluation is that the gripper can grasp objects of both regular and irregular shapes, although its symmetric design only allows for the former in theory. The shape adaptability indicates compliance of the gripper, which is likely due to the elastic folds made from the TPU material. This feature enables the gripper to conform to irregular-shaped objects with a relatively simple design and actuation scheme. However, the gripper seems to still perform better on regular-shaped objects due to its innate symmetry among fingers, as evidenced by the mug grasping where the object has a circular base.

To further explore the gripper's capability against object shape, a new set of grasping experiments was carried out on four same-sized objects, whose bases are circle, square, hexagon, and triangle, as shown in Fig. 5.13(a). The objects are ranked by their symmetry to the finger arrangement. The grasp on each object was repeated three times. The MGW is used to reflect the gripper's grasping

capability. Experimentally, MGW was measured by gradually adding weights to the object until it fell off. The results are shown in Fig. 5.13(b). The object with a circle base has the highest MGW while the triangular one leads to the lowest. The square-based object has a similar MGW to the circular one while the performance on the hexagonal object varies in each grasp. The results conclude that the gripper performs better on an object whose shape is more symmetric to the finger arrangement.

5.4 Summary

A robotic gripper, derived from the wrapping surface, has been presented in this chapter. The prototype can generate synchronous grasping motions on its four fingers. With an appropriate tendon-based design, only one motor is required to achieve repeatable grasping motions, making the control much simpler. Aided by 3D printing technique, the fabrication complexity is also reduced. The gripper's motion aligns well with the theoretical models and it can grasp a variety of objects.

Notably, although designed to be symmetric, the gripper is able to handle objects with less symmetry. A certain level of compliance exists in the gripper, which is desirable to achieve versatile functions with a relatively simple design. The innate compliance and bifurcations of the gripper are further exploited in Chapter 6, which aims to achieve object manipulation on the same design.

Chapter 6

A Two-Motor-Controlled Gripper for Object Manipulation

The gripper in Chapter 5 is further developed to achieve object manipulation, for which the kinematic bifurcations and gripper compliance are the focus. The newly developed gripper can attain eight motion modes and various transition paths with only two motors, thereby enabling manipulation under a rather simple control strategy. This chapter is modified from a previous publication by Liu et al. (2024b).

6.1 Gripper platform design and analysis

This section again recaps the motivation of a further-developed gripper for object manipulation, after which the bifurcation paths of the gripper and the associated motion modes are presented in detail. Compliance observed in Chapter 5 is also analysed kinematically. Given the bifurcations and innate compliance, a differen-

tial mechanism is finally proposed to enable the two-motor-control strategy.

6.1.1 Motivation statement

As discussed in Subsection 2.3.1, in-hand manipulation is quite challenging and often requires complex actuation and control strategies on a sophisticated mechanical design. As for the gripper based on the wrapping surface, one interesting fact is that its kinematic bifurcations have the potential to generate multiple motion modes without increasing the overall DoFs of the system. The observed compliance in Chapter 5 can enable the fingers to finely tune their positions even if their motions are blocked. Hence, in this chapter, a further-developed gripper platform will be presented to exploit the bifurcation and compliance for manipulation tasks, targeting relatively simple design, actuation, and control.

6.1.2 Motion paths of a single finger

The CAD model of the gripper backbone is reproduced in Fig. 6.1, where red dashed lines highlight finger 1 (F_1). The finger's kinematic path given in Eq. 5.1 contributes to the grasping behaviour. In addition, as analysed for Units a_1 and c_1 from Chapter 3, the finger has three hinge-like motions due to the aligned folds. For further analysis, all the motion paths of the finger are rewritten as follows, with 3D configurations illustrated in Fig. 6.2.

For path 1 of F_1,

$$\omega_1 = \omega_4,\ \omega_2 = \omega_3 = \omega_5 = \omega_6 = \omega,\ 0 \leq \omega_i \leq 180^\circ;\ \tan\frac{\omega_2}{2} = \sqrt{2}\tan\frac{\omega_1}{2} \qquad (6.1)$$

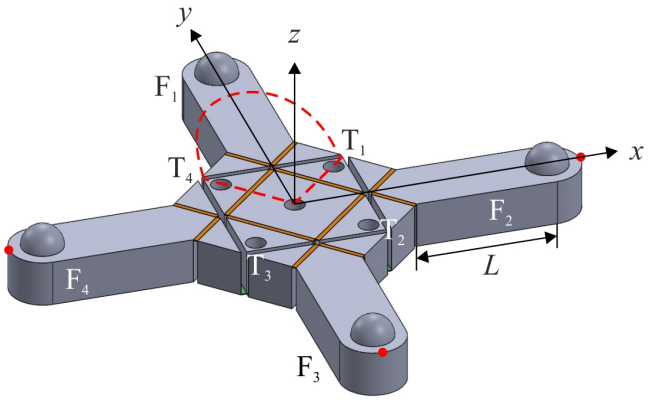


Figure 6.1: CAD model of the gripper reproduced from Fig. 5.6. The endpoints of each finger are marked in red for trajectory analysis.

for path 2 of F_1,

$$\omega_1 = \omega_2 = \omega_4 = \omega_5 = 0,\ 0 \leq \omega_3 = \omega_6 = \omega \leq 180^\circ \tag{6.2}$$

for path 3 of F_1,

$$\omega_1 = \omega_3 = \omega_4 = \omega_6 = 0,\ 0 \leq \omega_2 = \omega_5 = \omega \leq 180^\circ \tag{6.3}$$

for path 4 of F_1,

$$\omega_2 = \omega_3 = \omega_5 = \omega_6 = 0,\ 0 \leq \omega_1 = \omega_4 = \omega \leq 180^\circ \tag{6.4}$$

where all dihedral angles are marked in Fig. 6.2 and ω is taken as an input.

The finger has a single mobility, with a sudden increase in the DoFs at its bifurcation point, i.e., the unfolded state. This characteristic not only enables the finger to be controlled in each motion path with ease but also allows for the possibility to transit between multiple configurations. With the tendon channel

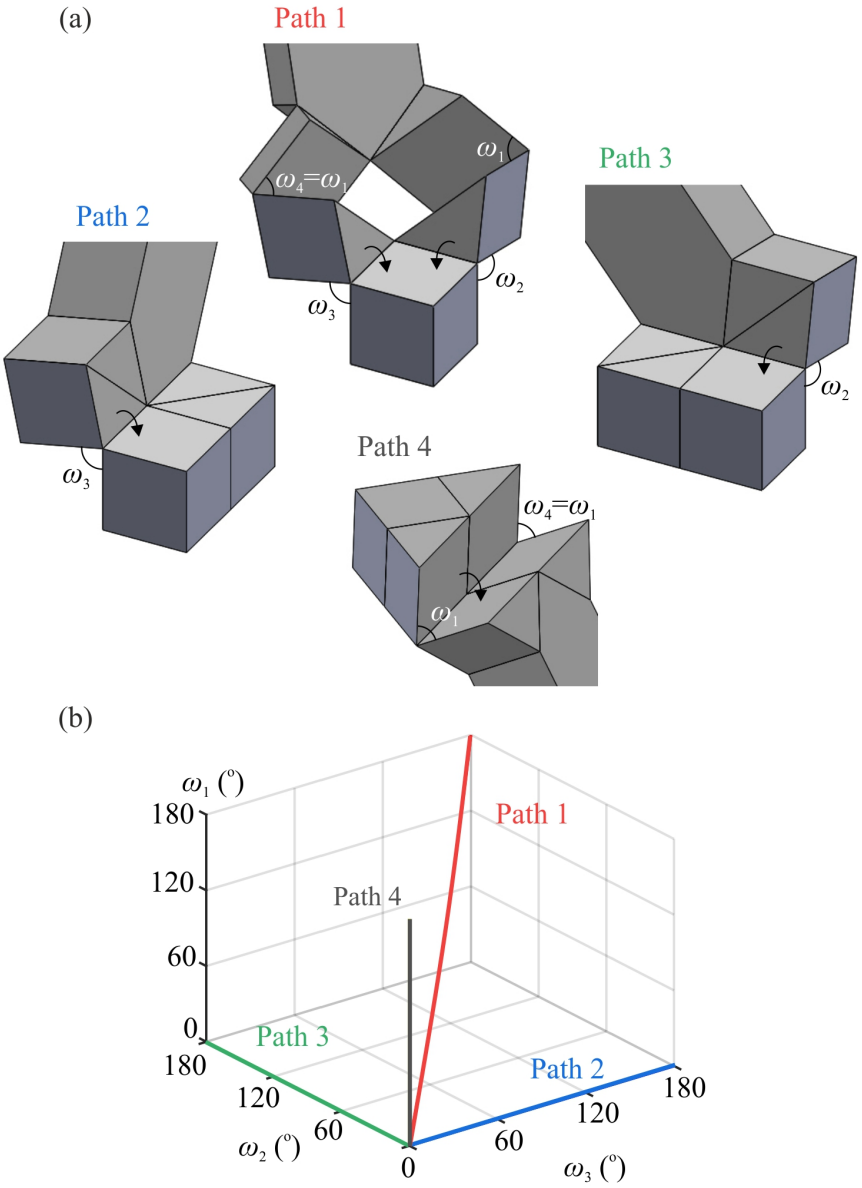


Figure 6.2: Motion paths of a single finger. **(a)** 3D models that illustrate each motion path, where path 1 is a Bricard linkage motion. Paths 2 and 3 are symmetric to each other. **(b)** Plots of kinematic behaviours in each path.

design for the gripper in Chapter 5, paths 1 - 3 of a finger can be achieved by pulling tendons separately or in combination. As shown in Fig. 6.3(a), pulling T_4 or T_1 will lead F_1 into its path 2 or path 3 depicted in Fig. 6.2, respectively.

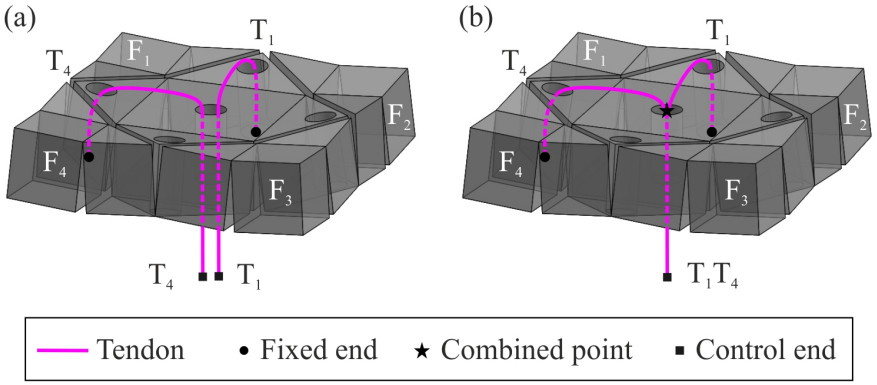


Figure 6.3: Actuation scheme where the tendons can be pulled **(a)** individually or **(b)** in combination. F_1 and its associated tendon channels are taken as an example. For simplicity, lengthened fingers and fingertips are omitted in the assembly.

When it comes to the setup in Fig. 6.3(b) to pull T_1 and T_4 together at the flat state, the finger switches to its path 1, which previously contributes to grasping. Path 4 is disabled, as the current tendon arrangement cannot achieve it.

It should be noted that pulling T_1 or T_4 will also cause movements in fingers that are adjacent to F_1, as they share common folds and blocks. For instance, simply pulling T_4 will also activate F_4 in the corresponding motion path. Whilst only F_1 and its associated two tendon channels are taken as an example to illustrate the actuation principle, the whole scheme can be extended to the entire gripper backbone assembly by symmetry.

6.1.3 Motion mode analysis of the gripper

Each tendon channel can have multiple tendon outputs. There are four tendon channels in total on the griper backbone, and hence, their output tendon combinations can generate diverse modes on the gripper. With an exhaustive permutation of all possible tendon combinations, it is found that the gripper's modes can be

categorised into five types as shown in Table 6.1, where symmetric motions are omitted. The endpoint of each finger, highlighted in red in Fig. 6.1, is used to represent its motion trajectory.

Table 6.1: Gripper motion type, relevant tendon arrangements, and kinematic behaviours

Type	**Active tendon**	**Active finger**	**Finger motion**	**Mobility**	**Alternatives**
1	T_1	Finger 1	$x_{11},\ y_{11},\ z_{11}$	1 DoF	T_2 or T_3 or T_4
		Finger 2	$x_{12} = y_{11},\ y_{12} = x_{11},\ z_{12} = z_{11}$		
2	T_1T_4	Finger 1	$x_{21},\ y_{21},\ z_{21}$	1 DoF	T_1T_2 or T_2T_3 or T_3T_4
		Finger 2	$x_{22} = y_{11},\ y_{22} = x_{11},\ z_{22} = z_{11}$		
		Finger 4	$x_{24} = -y_{11},\ y_{24} = x_{11},\ z_{24} = z_{11}$		
3	T_1T_3	Finger 1	$x_{31} = x_{11},\ y_{31} = y_{11},\ z_{31} = z_{11}$	2 DoFs	T_2T_4
		Finger 2	$x_{32} = y_{11},\ y_{32} = x_{11},\ z_{32} = z_{11}$		
		Finger 3	$x_{33} = -x_{11},\ y_{33} = -y_{11},\ z_{33} = z_{11}$		
		Finger 4	$x_{34} = -y_{11},\ y_{34} = -x_{11},\ z_{34} = z_{11}$		
4	$T_1T_3T_4$	Finger 1	$x_{41} = x_{21},\ y_{41} = y_{21},\ z_{41} = z_{21}$	1 DoF	$T_1T_2T_3$ or $T_1T_2T_4$ or $T_2T_3T_4$
		Finger 2	$x_{42} = y_{11},\ y_{42} = x_{11},\ z_{42} = z_{11}$		
		Finger 3	$x_{43} = -x_{11},\ y_{43} = -y_{11},\ z_{43} = z_{11}$		
		Finger 4	$x_{44} = -y_{21},\ y_{44} = x_{21},\ z_{44} = z_{21}$		
5	$T_1T_2T_3T_4$	Finger 1	$x_{51} = x_{21},\ y_{51} = y_{21},\ z_{51} = z_{21}$	1 DoF	None
		Finger 2	$x_{52} = y_{21},\ y_{52} = x_{21},\ z_{52} = z_{21}$		
		Finger 3	$x_{53} = x_{21},\ y_{53} = -y_{21},\ z_{53} = z_{21}$		
		Finger 4	$x_{54} = -y_{21},\ y_{54} = x_{21},\ z_{54} = z_{21}$		

In Table 6.1, $(x_{ij},\ y_{ij},\ z_{ij})$ represents the coordinates of finger j under motion type i. According to the finger kinematics in Eqs. 6.1 - 6.3, the unknown coordinates, $(x_{11},\ y_{11},\ z_{11})$ and $(x_{21},\ y_{21},\ z_{21})$ from Table 6.1 are given as

$$\begin{aligned} x_{11} &= -(\frac{1}{2}L + \frac{\sqrt{2}}{2}l + \frac{\sqrt{2}}{4}w_1 + \frac{1}{2}w_2)(1-\cos\omega) \\ y_{11} &= \sqrt{2} + \frac{\sqrt{2}}{2}w_1 + (\frac{1}{2}L + \frac{\sqrt{2}}{2}l + \frac{\sqrt{2}}{4}w_1 + \frac{1}{2}w_2)(1+\cos\omega) \\ z_{11} &= (\frac{\sqrt{2}}{2}L + l + \frac{1}{2}w_1 + \frac{\sqrt{2}}{2}w_2)\sin\omega \end{aligned} \tag{6.5}$$

$$\begin{aligned} x_{21} &= 0 \\ y_{21} &= \sqrt{2}l + \frac{\sqrt{2}}{2}w_1 + \frac{1}{2}w_2 + h\sin\omega_1 + (L + \sqrt{2}l + \frac{\sqrt{2}}{2}w_1 + \frac{1}{2}w_2)\cos\omega_1 \\ z_{21} &= h(1-\cos\omega_1) + (L + \sqrt{2}l + \frac{\sqrt{2}}{2}w_1 + \frac{1}{2}w_2)\sin\omega_1 \end{aligned} \tag{6.6}$$

where the hinge widths have been taken into account, and for $(x_{21},\ y_{21},\ z_{21})$, the relationship between ω and ω_1 is obtained from Eq. 6.1.

The range of ω in Eqs. 6.5 - 6.6 varies under different motion types. For motion types 1, 2, and 3, ω ranges from 0 to 180°. For motion types 4 and 5, the range changes to [0, 95°] and [0, 125°], respectively. Motion type 3 performs motion type 1 on opposite sides of the gripper, making it the only 2-DoF movement of the gripper. All these motions are switchable at the bifurcation point, i.e., the gripper is unfolded. To have a clearer picture of how the gripper behaves, the five motion types are also illustrated in Fig. 6.4.

6.1.4 A differential mechanism for minimal actuators

Whilst most motion types are of single mobility, the bifurcation feature still necessitates the need for a proper actuation system for the gripper to switch among

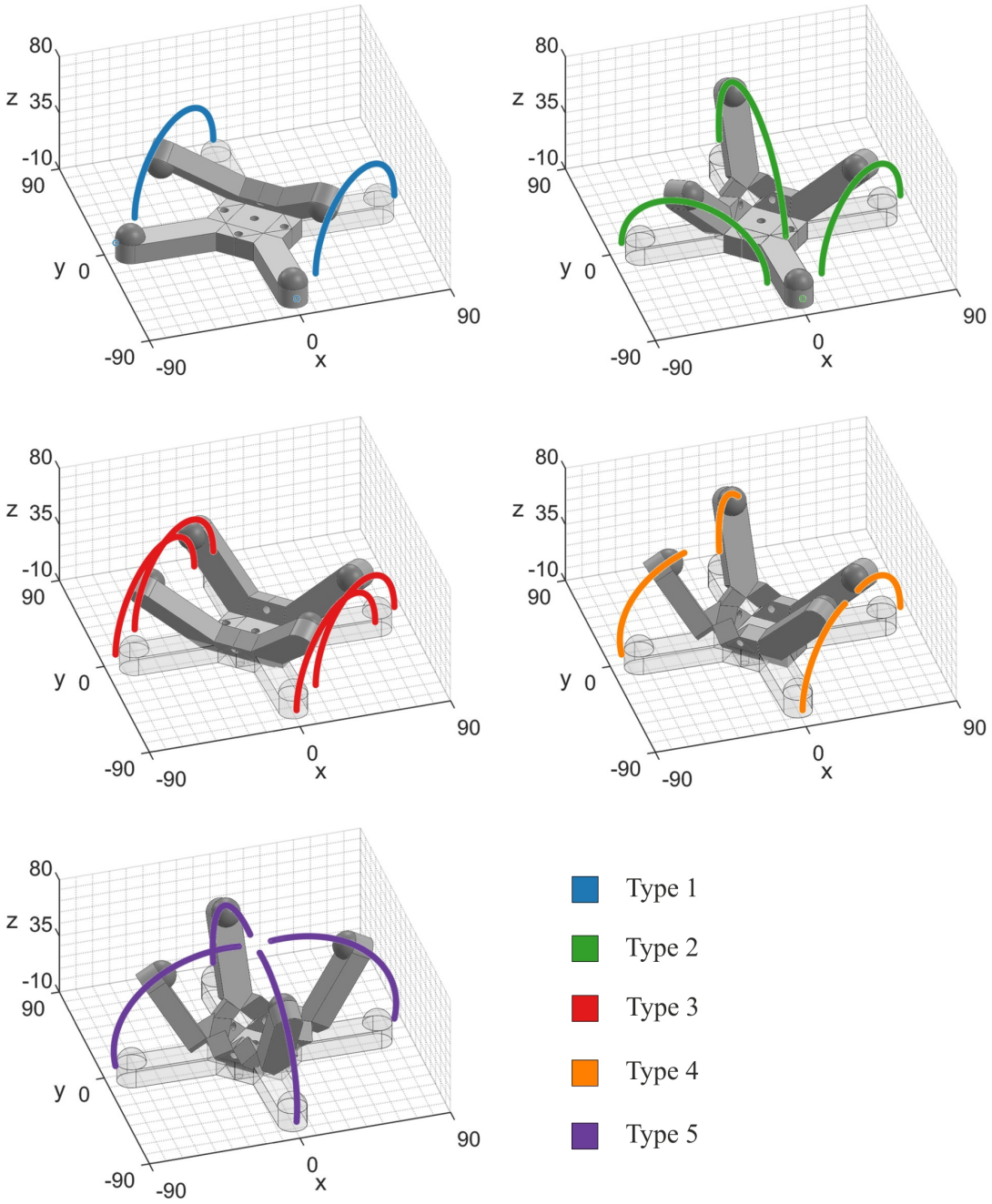


Figure 6.4: Five motion types of the gripper. The unit is in mm under actual fabrication parameters. They are the same as Table 5.1, except that the finger length L has increased to 45 mm for a wider motion range. In particular, motion type 5 is the grasping motion in Chapter 5.

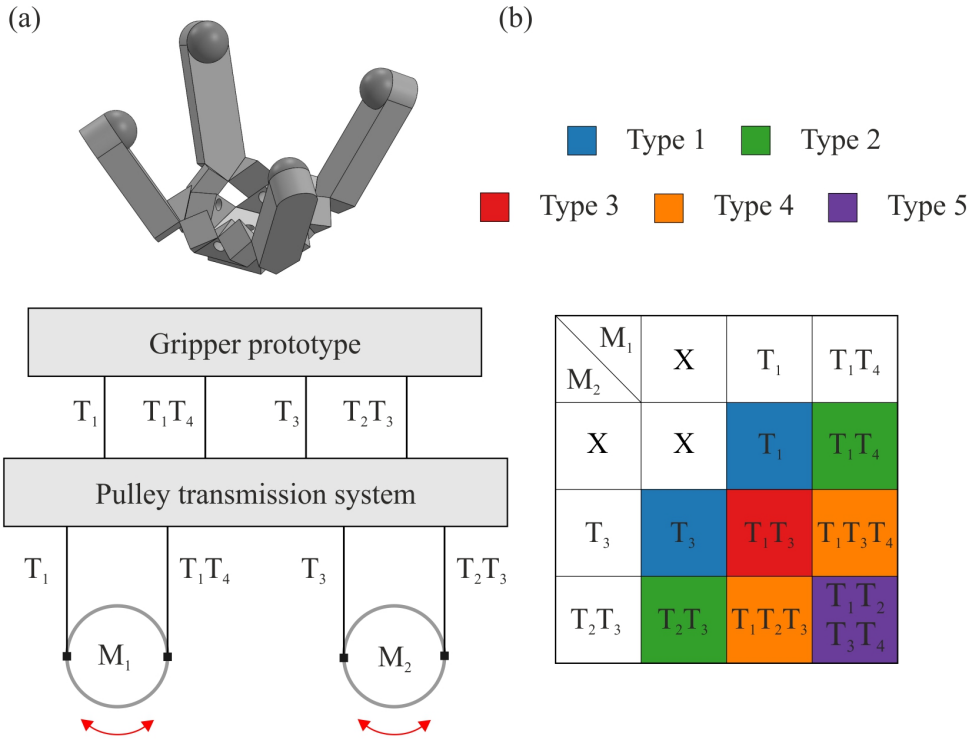


Figure 6.5: Design of a tendon-pulley-based differential mechanism where **(a)** four sets of tendons are controlled by two motors to achieve **(b)** eight motion modes. X indicates that the motor is immobile rather than pulling any tendons.

different motion paths. To realise all five motion types in Table 6.1 with minimal actuators, a tendon-pulley-based differential mechanism is proposed.

As shown in Fig. 6.5(a), two motors, M_1 and M_2, are connected with four sets of tendons. The two motors can be activated independently or in combination, with either clockwise (CW) or anticlockwise (ACW) rotation. Each motor's rotation leads to the pulling of one tendon set and the loosening of the other simultaneously. The pulled tendon set contributes to the gripper's motion. Thus, the permutation of motor combinations gives eight motion modes of the gripper as shown in Fig. 6.5(b), where the pulled tendon sets are indicated. The design has covered all five motion types with only two motors.

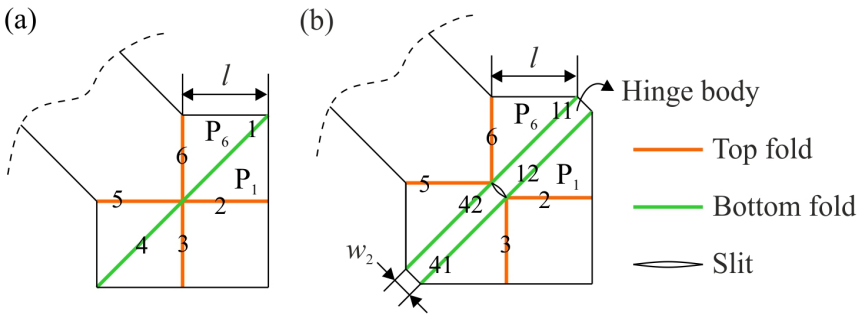


Figure 6.6: Origami pattern for a finger in its (a) original form and (b) new version with hinge width taken into account. The hinge body has zero thickness.

6.1.5 Analysis of gripper compliance via a kinematic model

To achieve in-hand manipulation on various objects, eight kinematic motion modes are not sufficient. The shape adaptability observed in Chapter 5 indicates a certain level of compliance, which is further exploited to improve the dexterity of the gripper.

It was deduced that the elastic hinges contribute to the compliance of the gripper. Instead of simulating the material behaviour with complex finite element modelling, a new kinematic model is proposed to analyse the gripper's compliance.

Figure 6.6 presents the new origami pattern for a single finger in comparison with its original version. Hinge widths are taken into account to build up the kinematic model. As shown in Fig. 6.6(b), the bottom folds are replaced by two rigid hinge bodies with width w_2 and thickness of zero. Instead of placing a single axle in its centre, each hinge body has two revolute connections with its adjacent thick panels. The top folds retain the previous assumption as perfect rotary joints for the simplicity of modelling. Consequently, the original 6R Bricard linkage model derived from the pattern in Fig. 6.6(a) is changed to an 8R spatial linkage,

Table 6.2: New conversion between revolute variable and dihedral angle

θ_1	θ_2	θ_3	θ_4
$\omega_{11} + 180°$	$\omega_{12} + 180°$	$-\omega_2 + 180°$	$-\omega_3$
θ_5	θ_6	θ_7	θ_8
$\omega_{41} + 180°$	$\omega_{42} + 180°$	$-\omega_5 + 180°$	$-\omega_6$

whose geometric conditions are

$$\begin{gathered} a_{12} = a_{56} = w_2,\ a_{23} = a_{45} = a_{67} = a_{81} = h,\ a_{34} = a_{78} = 0 \\ \alpha_{12} = \alpha_{56} = 0,\ \alpha_{23} = \alpha_{67} = -45°,\ \alpha_{34} = \alpha_{78} = 90°,\ \alpha_{45} = \alpha_{81} = 45° \\ R_i = 0,\ i = 1, 2, ..., 8 \end{gathered} \tag{6.7}$$

which can be substituted into the closure equation Eq. 2.6 in Chapter 2.

To better represent the physical meanings and compare with the original model, the revolute variable θ_i $(i = 1, 2, ..., 8)$ of the revised model is converted to dihedral angles in Table 6.2. The numbering of dihedral angles has been changed in the new pattern as shown in Fig. 6.6(b), matching the original pattern for comparison.

The detailed steps to solve the closure equation are given in Appendix C. It is found that the new model still has the line-symmetric property as

$$\omega_{11} = \omega_{41},\ \omega_{12} = \omega_{42},\ \omega_2 = \omega_5,\ \omega_3 = \omega_6 \tag{6.8}$$

Considering the line symmetry, the following discussion will be centred on ω_{11}, ω_{12}, ω_2, and ω_3. Specifically, ω_{11} and ω_{12} are the dihedral angles between side walls of P_1, P_6 and the bottom hinge as illustrated in Fig. 6.7(a). The angle for comparison with the original model is the one between side walls of P_1 and P_6,

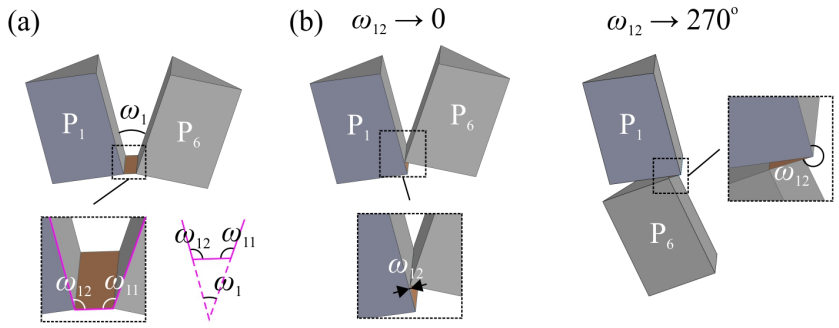


Figure 6.7: Dihedral angles among P_1 , P_6, and the hinge body.

i.e., ω_1. By observation, we know

$$\omega_1 = \omega_{11} + \omega_{12} - 180^{\circ} \tag{6.9}$$

The bottom hinges are modelled as rigid bodies. Hence, to avoid inference, ω_{11} and ω_{12} must satisfy

$$0 \leq \omega_{11},\ \omega_{12} \leq 270^{\circ} \tag{6.10}$$

whose extreme positions are illustrated in Fig. 6.7(b).

According to the Kutzbach criterion, an 8R closed-loop spatial linkage has two DoFs. The mobility increases if the linkage is overconstrained. Assigning different geometric constraints to the closure equation will lead to a variety of motion paths. Path 1, path 2, and a transition path between both are identified as follows.

The condition for path 1 is

$$\omega_2 = \omega_3 \tag{6.11}$$

which gives the closure equation as

$$\tan\omega_{11} = \tan\omega_{12} = -\sqrt{2}\cot\frac{\omega_2}{2},\ \tan\frac{\omega_1}{2} = \frac{\sqrt{2}}{2}\tan\frac{\omega_2}{2} \tag{6.12}$$

The condition for path 2 is

$$\omega_2 = 0 \tag{6.13}$$

which gives the closure equation as

$$\tan\omega_{12} = \sqrt{2}\cot\frac{\omega_3}{2},\ \omega_{11} = 180^\circ - \omega_{12},\ \omega_1 = 0 \tag{6.14}$$

ω_1, ω_2, and ω_3 from Eqs. 6.11 - 6.14 are compared with the corresponding values in the original model, whose kinematic behaviours are given by Eqs. 6.1 - 6.2. The two paths of the new and old models are found to be the same.

The condition for the transition path is that ω_3 is fixed at a certain value, defined as the transition angle. In practice, it refers to a state when the finger is semi-folded in its path 2. The revised relationship among ω_1, ω_2, and ω_3 are

$$\tan\omega_1 = \frac{\sqrt{2}(\sin\omega_2 + \sin\omega_3 - \sin(\omega_2+\omega_3))}{\cos\omega_2 + \cos\omega_3 - 2\cos\omega_2\cos\omega_3 + \sin\omega_2\sin\omega_3} \tag{6.15}$$

The kinematic behaviours of paths 1 and 2 are plotted in Fig. 6.8 along with the transition path. Corresponding 3D configurations of the finger are also illustrated. The finger starts from position 1, the unfolded state, and passes along position 2 and position 3 along path 2 until ω_3 reaches 60°. Keep ω_3 fixed and let ω_2 increase from 0. The finger subsequently passes position 4 in the transition path and then reaches position 5 where $\omega_2 = \omega_3$. The finger is now in path 1, where ω_2 and ω_3 can increase synchronously to get to position 6.

According to Fig. 6.8, it seems that the finger can transit from path 1 to 2 without passing the bifurcation point as long as the bottom hinge width is considered and the value would not matter. However, it is also important to

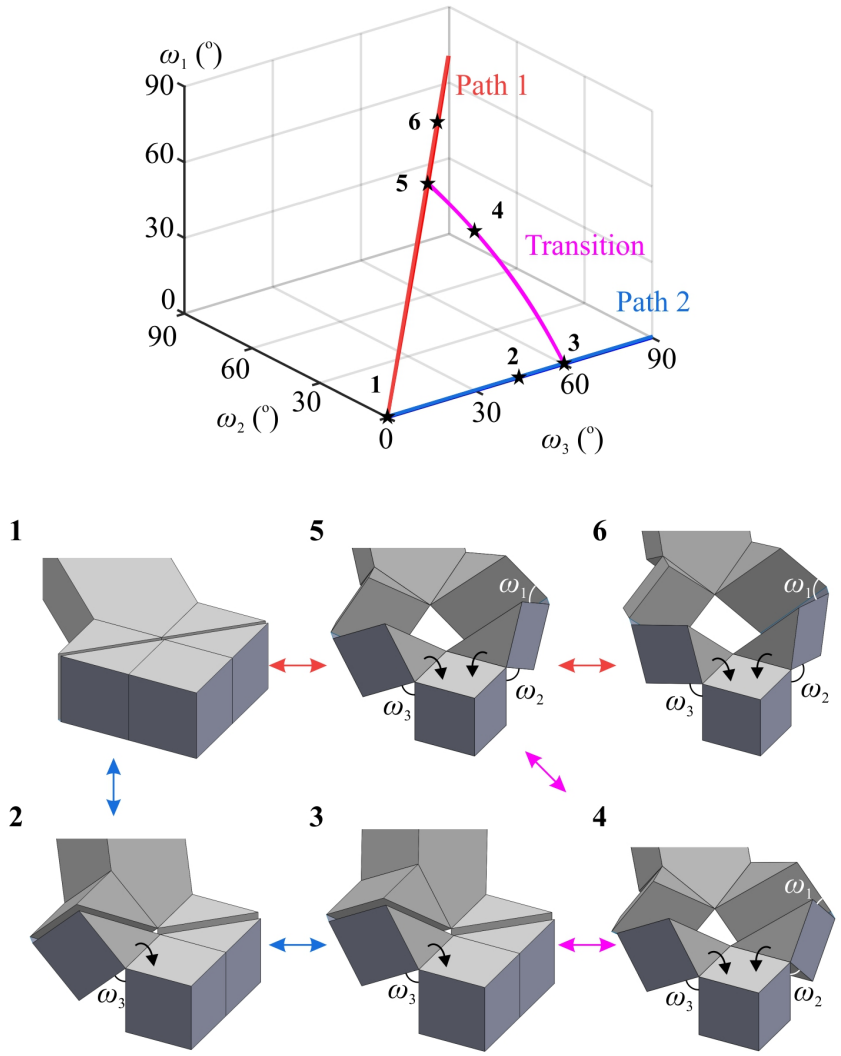


Figure 6.8: Path 1, path 2, and their transition. Note that ω_2 and ω_3 can increase to 180° in paths 1 and 2 but only half of their motion range is indicated.

examine whether the actual dihedral angles ω_{11} and ω_{12} satisfy the condition in Eq. 6.10, so that physical interference is prevented in the transition process.

Given the analysis in Appendix C, the values of ω_{11} and ω_{12} are

$$\tan\frac{\omega_{11}}{2} = \frac{-B_{11} + \sqrt{B_{11}^2 - 4A_{11}C_{11}}}{2A_{11}},\ \omega_{12} = \omega_1 + 180^\circ - \omega_{11} \tag{6.16}$$

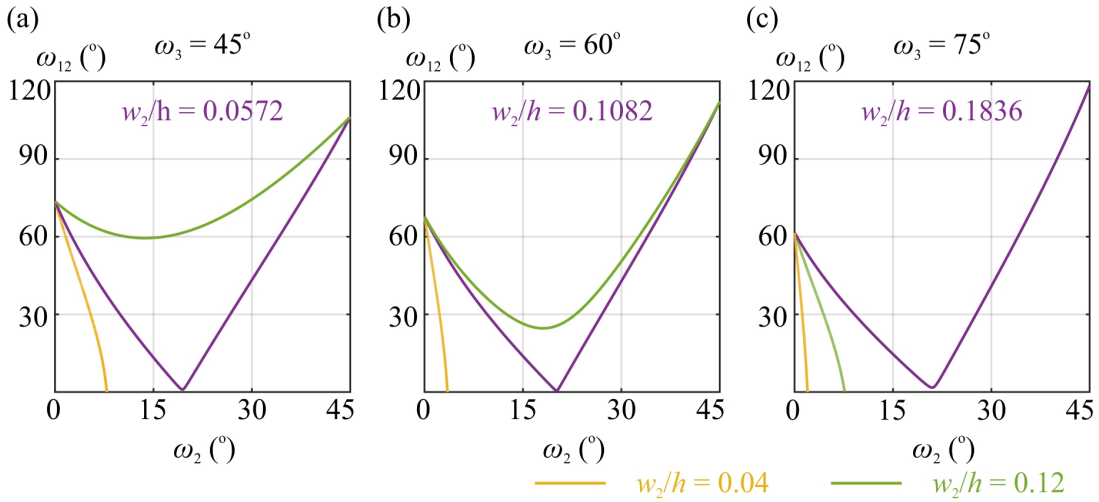


Figure 6.9: The relationship between ω_{12} and ω_2 when the transition angle ω_3 is fixed at **(a)** 45°, **(b)** 60°, and **(c)** 75°. The threshold value of w_2/h is indicated.

where

$$A_{11} = -(1 + \frac{w_2}{h})(\sin\omega_3 + \sin\omega_2 \cos\omega_3) + \sin\omega_2 + \cos\omega_2 \sin\omega_3$$

$$B_{11} = \sqrt{2}\frac{w_2}{h}(\sin\omega_2 \sin\omega_3 + \cos\omega_2 - \cos\omega_3)$$

$$C_{11} = -(1 - \frac{w_2}{h})(\sin\omega_3 + \sin\omega_2 \cos\omega_3) + \sin\omega_2 + \cos\omega_2 \sin\omega_3$$

It is found that when w_2/h varies, ω_{12} is the key constraint. Figure 6.9 illustrates the relationship between ω_{12} and ω_2 in the transition path at multiple values of w_2/h and ω_3. Taking Fig. 6.9(b) as an example where $w_2/h = 0.04$ and $\omega_3 = 60°$, ω_{12} drops to 0 when ω_2 is no more than 7.5°. The result indicates that in Fig. 6.8, the finger cannot move from position 3 to 5 along the transition path, as ω_2 cannot reach the same value as ω_3. When w_2/h increases gradually and passes a threshold value of 0.1082, ω_{12} would increase before dropping to zero and ω_2 is then able to reach 60°, the same value as the transition angle ω_3. Hence, a wider

hinge means higher compliance, as the gripper can more easily switch from one path to the other in the semi-folded configuration. However, the hinge cannot be too wide, as it will be too soft for the original kinematic motions to hold.

Comparing all three graphs in Fig. 6.9, it is also noticed that the threshold value increases with the transition angle. This means when the gripper is closer to its bifurcation point, the transition is easier to take place.

The new model presented only considers the widths of the bottom folds, whilst the top ones can add extra compliance. Whichever the case, it is expected that with the design of small TPU-printed hinges, the gripper will possess enough compliance to carry out motion switches outside of bifurcations. The finding would add to the current motion modes given in Fig. 6.5(b). Infinite transition paths, due to the varying transition angle, will exist between types 2 and 4 as well as types 2 and 5. They can be achieved by activating M_1 first and then M_2, or vice versa.

6.2 Experimental procedure

This section depicts the gripper platform fabrication. Experimental setups are subsequently detailed to characterise the gripper's behaviours.

6.2.1 Gripper platform fabrication

The gripper prototype is made in the same way as detailed in Chapter 5. The fabrication parameters are based on Table 5.1. The only difference is that the finger length L increases to 45 mm, thereby expanding the gripper's motion range.

Figure 6.10 shows the final platform. The gripper is mounted on a frame with the tendon-pulley-based differential mechanism. Tendons coming out from the

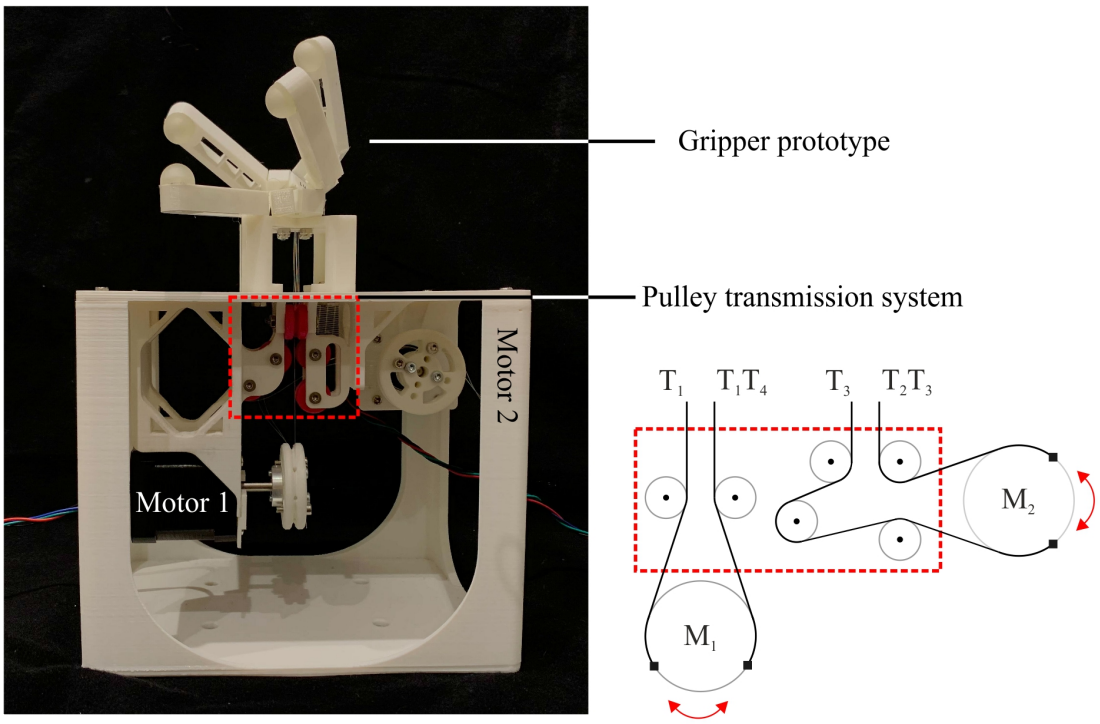


Figure 6.10: The gripper platform for object manipulation. Some small pulleys are used to guide the tendon sets so that they do not intertwine.

gripper are guided by the pulley transmission system to avoid intertwining. The ends of tendon sets are tied to the motor shafts. Two steppers (NEMA 17) are used to pull or loosen the tendons under the open-loop control of Arduino UNO.

6.2.2 Characterisation of the gripper

The intended experiments will validate the gripper's kinematic paths and compliant transitions. Finally, in-hand manipulation of objects will be explored.

First of all, to validate the eight motion modes shown in Figs. 6.4 and 6.5, the gripper platform was placed under a motion capture system (OptiTrack) to record the finger movements. Markers were attached at the finger ends. After calibration, the gripper was actuated to reach all possible motion paths. Closing and opening

motions of the gripper were achieved by pulling and loosening relevant tendons. Each cycle was repeated five times, with an interval period of five seconds. The position data were recorded on software (Motive).

Secondly, according to the compliance analysis, the gripper can complete transitions, i.e. motion type 2 to 4 or 5 at non-bifurcations. Hence, the gripper was examined for this hypothesis. The motor control strategy for types 2 to 4 is as follows. Each trial was repeated five times, at an interval of five seconds.

- When the gripper is unfolded, M_1 rotates CW. The gripper moves to motion type 2.
- Keep M_1 still. M_2 rotates ACW to see whether the gripper can move to motion type 4.
- Return M_1 and M_2 to their original states. Wait until the gripper is flat.

The motor control to switch motion type 2 to 5 is the same, except that in the second step, M_2 needs to rotate CW to see whether the gripper can move to motion type 5. In each motion switch, the fingers' positions were recorded.

Lastly, the gripper's capability for object manipulation was evaluated. Cuboids, balls, and cones were used to explore the gripper's function. The motor control strategy to manipulate each object is described as follows, the process of which is also illustrated in Fig. 6.11 taking the ball as an example. Each trial was repeated five times and the interval time between each repetition was five seconds. The movements of objects were recorded.

- Ball manipulation 1 as shown in Fig. 6.11(a)
  - M_1 and M_2 rotate CW synchronously.

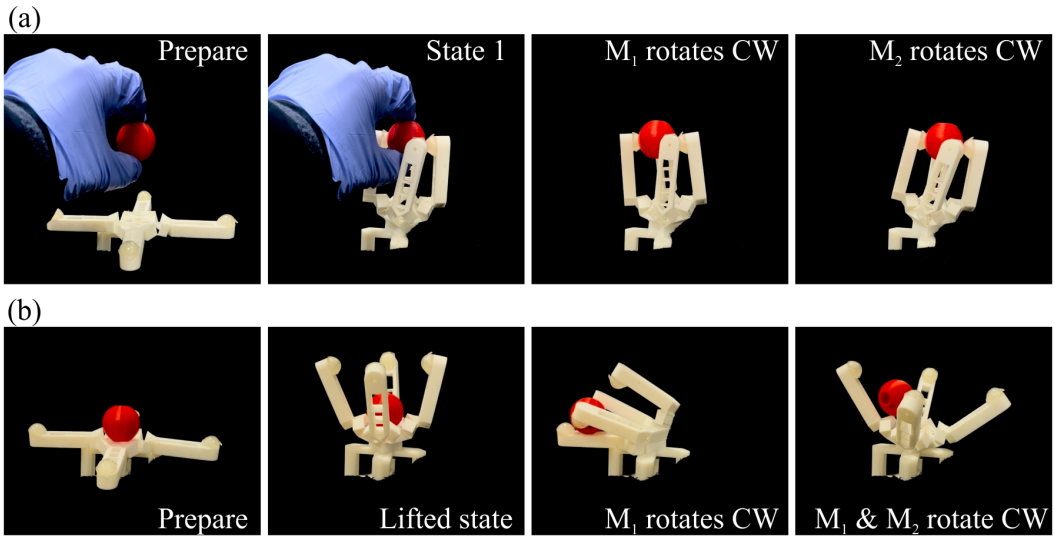


Figure 6.11: Key steps for ball manipulation by exploiting **(a)** motion type 5 and **(b)** a combination of motion types 2 and 5. Innate compliance is also required.

  - The gripper moves into motion type 5 to grab a ball (state 1).
  - M_2 stays still. M_1 continues CW rotation until it reaches the maximum output torque.
  - Return M_1 to state 1 and keep it still. Likewise, M_2 rotates CW until it reaches the maximum output torque.

- Ball manipulation 2 as shown in Fig. 6.11(b)
  - Place a ball at the gripper centre when it is unfolded.
  - M_1 and M_2 rotate CW synchronously.
  - The gripper moves into motion type 5 to lift the ball (lifted state).
  - Release M_2. M_1 continues CW rotation to change the ball's position.
  - Release M_1 until the gripper is flat. M_2 rotates CW.
  - When the gripper is semi-folded, M_1 is also activated to rotates CW.

  - Track the object and check whether it can return to the lifted state.

- Cuboid manipulation (similar to ball manipulation 1)
  - M_1 and M_2 rotate ACW synchronously.
  - The gripper moves into motion type 3 to grab a cuboid (state 2).
  - M_2 stays still. M_1 continues ACW rotation until it reaches the maximum output torque.
  - Return M_1 to state 2 and keep it still. Likewise, M_2 rotates ACW until it reaches the maximum output torque.

- Cone manipulation (also similar to ball manipulation 1)
  - M_1 rotates CW and M_2 rotates ACW synchronously.
  - The gripper moves into motion type 4 to grab a cone (state 3).
  - M_2 stays still. M_1 continues CW rotation until it reaches the maximum output torque.
  - Return M_1 to the grasped state 3 and keep it still. Likewise, M_2 rotates ACW until it reaches the maximum output torque.

6.3 Results and discussions

6.3.1 Basic motion paths

Figure 6.12 depicts fingers' experimental positions against the theoretical models of the eight paths, where the marker size is taken into account to adjust Eqs. 6.5 - 6.6. Associated motor states are also indicated.

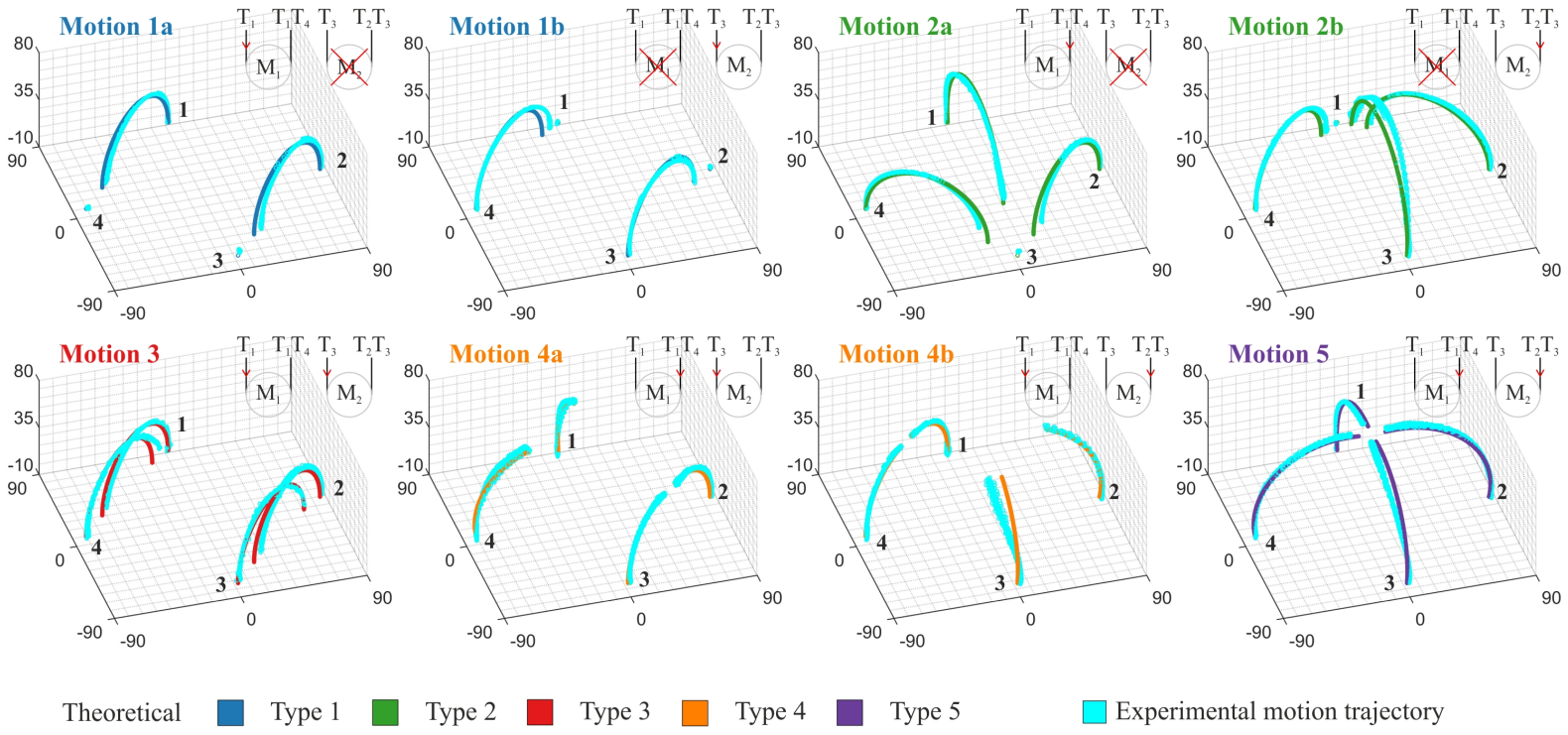


Figure 6.12: Experimental motions against theoretical models. Fingers are numbered for clarity. The unit is in mm.

Table 6.3: RMSE and ME of experimental motion paths (unit: mm)

Motion	Finger 1		Finger 2		Finger 3		Finger 4	
	RMSE	ME	RMSE	ME	RMSE	ME	RMSE	ME
1a	1.68	4.34	2.60	6.46	3.32	5.18	1.44	2.87
1b	1.36	1.92	1.57	2.74	1.92	5.71	2.56	6.87
2a	1.86	5.29	2.44	6.56	3.24	4.24	1.62	4.77
2b	1.51	2.25	1.34	3.05	2.26	7.80	2.06	5.01
3	1.50	3.78	2.18	6.54	1.37	4.49	1.71	6.77
4a	1.70	6.67	1.70	4.06	1.35	2.75	0.94	8.72
4b	1.20	5.28	1.43	3.66	2.26	12.32	1.21	3.24
5	2.35	4.87	1.33	5.29	1.80	6.71	1.18	4.49

A video of all motion modes is available in Appendix B. Their displacements from the theoretical lines are quantified. Specifically, for a finger at a certain position, the error is calculated as the shortest distance between the measured position and the theoretical line. The root-mean-square error (RMSE) is the standard deviation of all the errors. ME represents the maximum error in the path. The RMSE and ME of each finger under different modes are summarised in Table 6.3.

The RMSE in all motion modes ranges from 0.5 mm to 3.5 mm, indicating relatively good alignment with the theoretical models. The ME varies, with a minimum of 1.92 mm for finger 1 under motion 1b and a maximum of 12.32 mm for finger 3 under motion 4b. This suggests that under some motion types, a finger's actual motion can have a quite big discrepancy from its theoretical trajectory. The difference could be attributed to the gripper compliance and uneven force distribution on tendons, the latter of which is not currently under control.

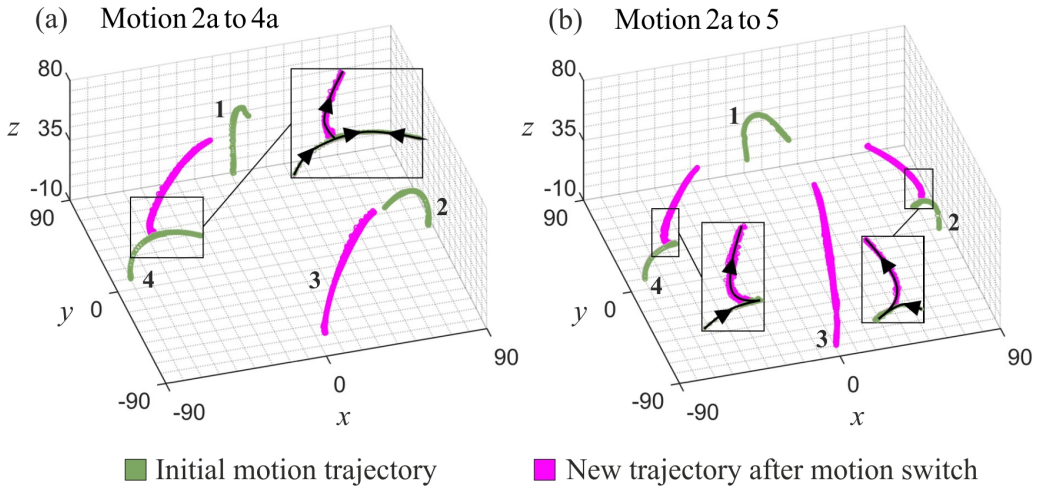


Figure 6.13: Compliant motion switch from **(a)** motion 2a to motion 4a and **(b)** motion 2a to motion 5. The switch process occurs outside of the gripper's bifurcation. The unit is in mm.

6.3.2 Motion switch at non-bifurcations

Figure 6.13 shows the experimental transitions from one path, i.e., motion type 2, to the other, i.e., motion type 4 or 5 at a semi-folded position. A video of the switching processes is given in Appendix B. Such phenomena are deduced from the compliance analysis of the gripper and the hypothesis is thus validated.

Compliance is beneficial to the manipulation of objects in many ways. For instance, most of the gripper's motion types are single-DoF. In theory, their movements will be blocked when touching an object. Compliance could allow the fingers to finely tune their positions to move the object without damaging it. In addition, compliance would also allow the fingers to switch from one motion path to another at non-bifurcation points, i.e., different semi-folded states. Hence, even with a small hinge width design of 1 - 1.2 mm, the introduced compliance would add more varieties of motions on top of the eight basic ones. Note that the two motors need to be activated in sequence rather than simultaneously.

6.3.3 Object manipulation

Given the eight motion modes and their compliant transitions, the gripper has demonstrated its capability for object manipulation as shown in Figs. 6.14 - 6.16. The unit is in mm. A video of all manipulation tasks is available in Appendix B.

The manipulation is attributed to the eight motion modes of the gripper as well as its innate compliance. For instance, card manipulation, ball manipulation 1, and cone manipulation exploit a certain motion type which best suits the object shape. Thus constant fingertip contact is realised and forces can be exerted on the object to change its position. On the other hand, ball manipulation 2 used a variety of motion modes to interact with the object, which include motion type 2 and motion type 5. The transition paths at non-bifurcations also play a role.

It is observed that the object motion trajectories vary, depending on the gripper's motion mode as well as the object shape. For instance, as shown in Fig. 6.14, under motion type 3, the trajectories of both cuboids are approximately an arch, while in Fig. 6.15, the balls have a more translational movement under motion type 5. The object size also matters, as the curvatures of these trajectories differ. In addition to translational and rotational movements, complex trajectories can be achieved, as shown in Fig. 6.16(a), where a cone is manipulated under motion type 4.

In most manipulation tasks listed here, constant contact between fingertips and the object is a prerequisite. However, it is not essential, as demonstrated in Fig. 6.16(b) where the gripper can manipulate the ball without continuous fingertip contact. The ball has reached a relatively wide motion range of up to 71 mm, roughly the distance between the gripper centre and one of its finger ends.

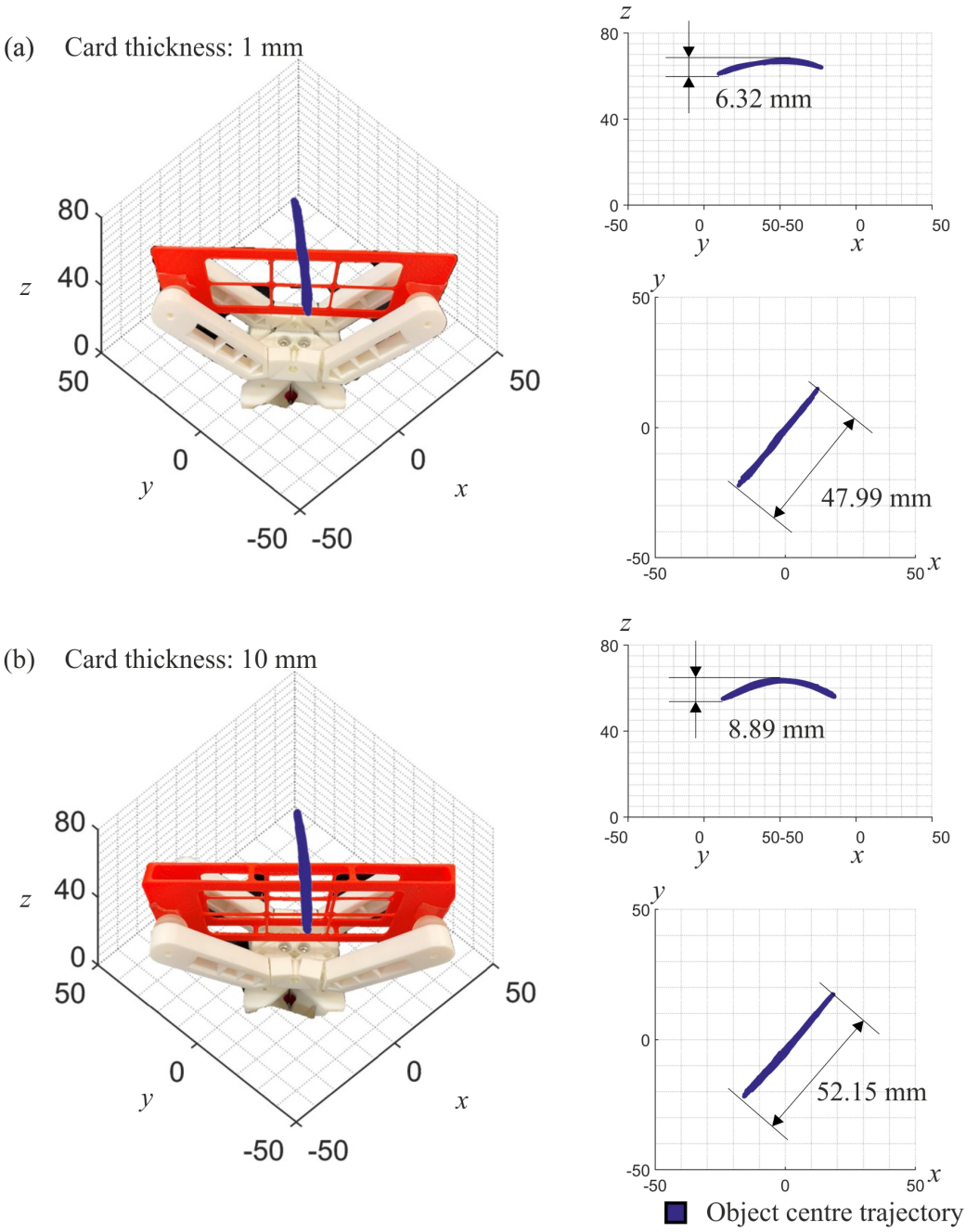


Figure 6.14: Manipulation of cuboids under motion type 3. Each object's trajectory is roughly an arch whose size varies along with the cuboid thickness. The unit is in mm. The widest motion range is up to 52 mm.

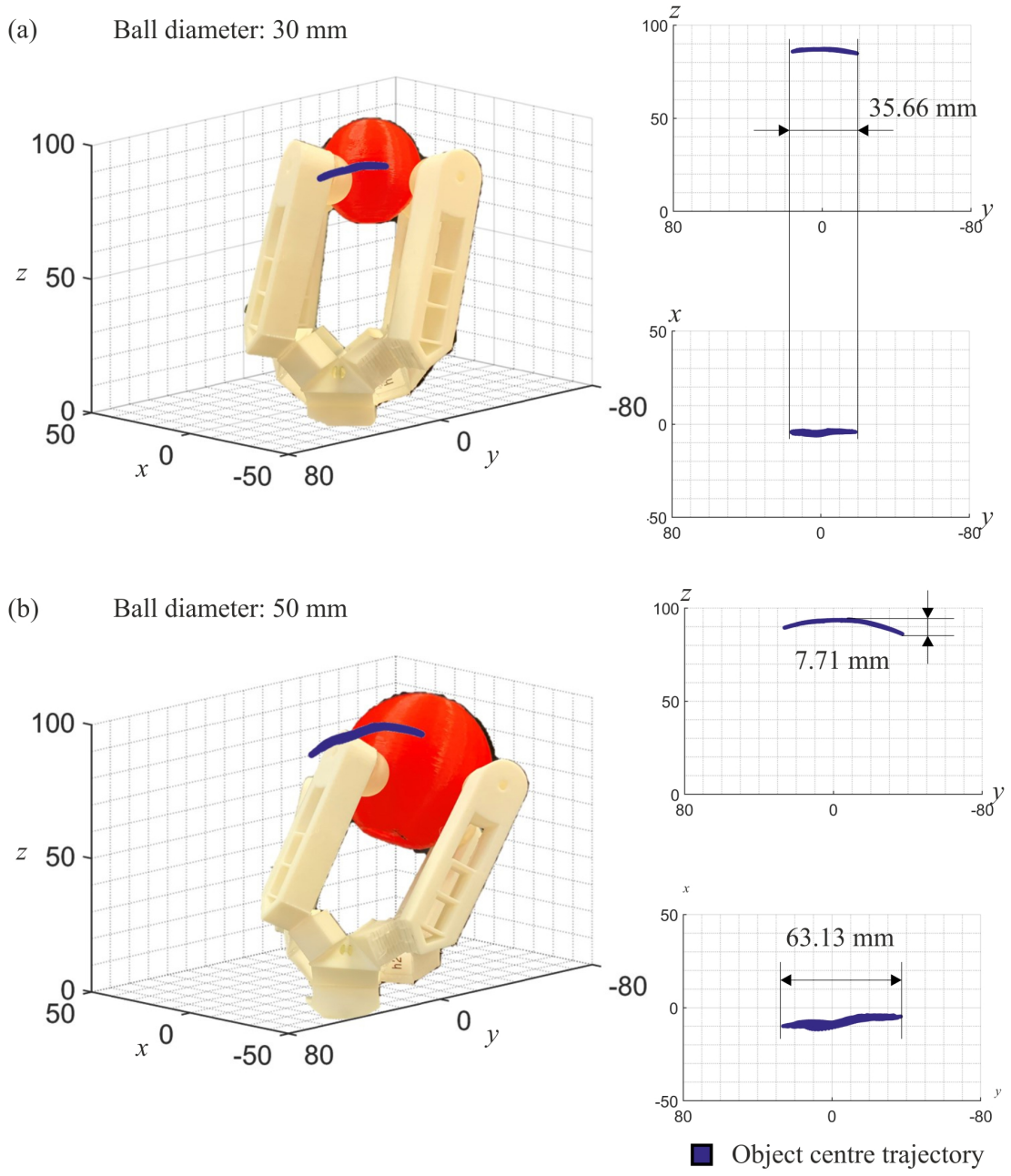


Figure 6.15: Manipulation of balls under motion type 5. The smaller ball's trajectory is roughly a line while the bigger one still has a curvature. The unit is in mm. The widest motion range is up to 63 mm.

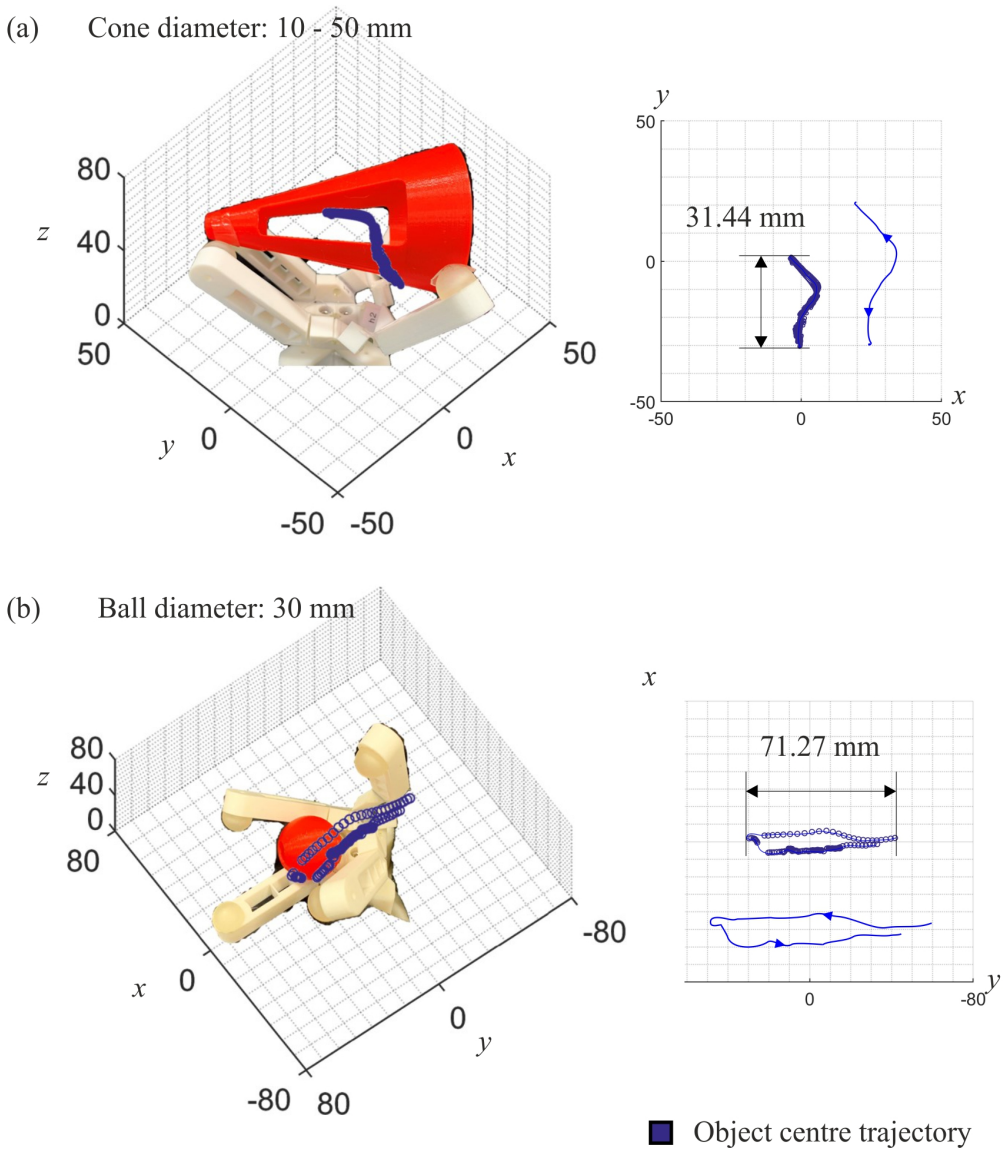


Figure 6.16: Manipulation of **(a)** a cone under motion type 4 and **(b)** a ball using a variety of motion modes. The cone has a complex motion trajectory. The unit is in mm. The ball has the widest motion range of up to around 71 mm.

6.4 Summary

In this chapter, an origami-based gripper has been encoded with manipulation functions, with a simple design, actuation, and control strategy. The completion

challenges the common views in robotics. More specifically, a single-DoF design is normally thought to have very limited capability but was chosen to be the theme of this thesis. However, the design has now demonstrated its potential to complete challenging tasks without an intricate control scheme.

The results are naturally linked to two terms, embodied intelligence and morphological computation. The former refers to intelligence that requires and leverages the properties of a physical body to produce desired behaviours in robots (Mengaldo et al., 2022). The latter exploits morphological features to develop intelligent bodies to obtain better-performing robots (Hauser et al., 2014).

With regards to the gripper, many morphological features have contributed to its 'intelligence', i.e., the diverse motion modes for object manipulation with only two motors. In particular, the single-DoF motion paths, the kinematic bifurcations, and the compliance of hinges are truly fundamental. Any of these features can be extended to other robotic applications, especially those that require dexterous motions and simplified control. The next chapter will thus focus on improving another aspect of the robot's intelligence, i.e., reconfigurability, by leveraging kinematic bifurcations of the morphing surfaces.

Chapter 7

Curling Surface: a Millipede-Like Reconfigurable Robot

This chapter further explores the kinematic bifurcations of morphing surfaces to develop reconfigurable robots. As a proof-of-concept study, the curling surface in Chapter 4 is developed into a millipede-like robot that can morph into a coil and other configurations. This chapter is modified from a previous publication by Liu et al. (2022) and a manuscript under review by Liu et al. (2024c).

7.1 Design and analysis of a curling surface

This section starts with a brief recap of reconfigurable robots. Then a case study is conducted on a millipede, which can curl up and also exhibit other morphologies. A curling surface is subsequently presented to mimic the millipede's configurations. The kinematic behaviours of the surface are analysed in detail, along with its segmentation, bifurcations, and curling profiles.

7.1.1 Motivation statement

As discussed in Subsection 2.3.2, reconfigurability allows robots to create new morphologies to adapt to the environment or perform specific tasks (Støy, 2015). Many reconfigurable robots employ a modular design. These modules can disassemble and reassemble themselves to create new shapes (Seo et al., 2019). To make the system more robust, it would be desirable to reduce the number of module reconnections while still achieving the desired configurations (Yao et al., 2019). Hence, different approaches have been attempted, including morphable origami (Belke and Paik, 2017), multi-DoF mechanisms (Liu et al., 2022b), and soft materials (Gu et al., 2020). However, it is still challenging to strike a balance between reconfigurability and controllability of the robotic system.

The kinematic bifurcations enable a morphing surface to move into different motion paths and only lead to an instantaneous mobility increase at a certain configuration. They have already demonstrated the possibility for dexterous motions with a small number of actuation inputs, which were used for manipulation tasks as detailed in Chapter 6. It is thus feasible to exploit the bifurcated paths to improve the reconfigurability of a robot, without adding excessive DoFs or sacrificing the system robustness. The design renders the potential to achieve desired configurations with a simplified control strategy.

Locomotion is one of the basic tasks of reconfigurable robots (Støy, 2015). To validate the above hypothesis, a millipede, a worm-like arthropod capable of curling and crawling, is hence taken as an example. A robotic prototype is developed from the curling surface presented in Chapter 4. Its bifurcations are used to produce multiple configurations mimicking the millipede's morphologies.

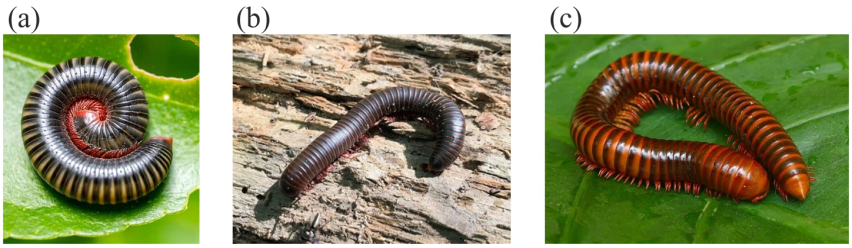


Figure 7.1: Morphologies of a millipede, including **(a)** coil, **(b)** wave-like, and **(c)** triangular shapes. Photos are adapted from Northwest Pest Control (2020); Innovative Pest Control (2020); Native Pest Management (2023).

7.1.2 Millipede and its morphologies

From a biological perspective, while a millipede resembles worms in many ways, it is not a worm but an arthropod. The millipede's body segments are covered by stiff outer skins (Hopkin et al., 1992), suitable to be mimicked with rigid origami.

In response to danger, the millipede curls into a coil shape as shown in Fig. 7.2(a). This is a self-defensive mechanism to protect the millipede against predators (VandenSpiegel and Golovatch, 2012). The millipede can also exhibit wave-like and triangular configurations, as shown in Figs. 7.2(b) and 7.2(c), respectively. Since the crawling motion of a millipede has been systematically studied (Garcia et al., 2020), this chapter focuses specifically on curling and other configurations to design a reconfigurable robot imitating the millipede.

As said, a millipede has rigid exoskeletons, and thus, material deformation is not the primary cause of curling. However, the millipede is too small to be thoroughly investigated. Instead, the movements of a lobster and a toy version of a pill bug, shown in Fig. 7.2, are analysed. They are larger in size while sharing similar curling motions and biological features to those of the millipede (Thorp, 2009). All these animals belong to the arthropod family (Regier et al., 2010).

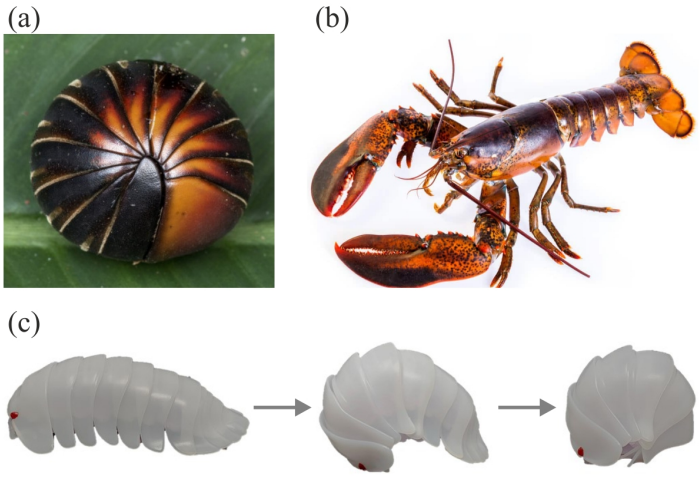


Figure 7.2: Animals similar to the millipede. **(a)** A pill bug, **(a)** a lobster, and **(c)** the curling process of a pill bug toy, which is made by a Japanese company named Bandai Co., Ltd. The photos are adapted from Lanier (2017); Alois (2021).

As illustrated in Fig. 7.2, the pill bug can curl up into a compact volume. Its toy version has seven body segments connected by simple rotational joints, enabling the curling mechanism. Similarly, the lobster bends its abdomen through two symmetric spherical joints on each side of its body (Chen et al., 2017). Due to physical constraints, a pair of spherical joints is kinematically equivalent to a rotational joint. A flexible but almost inextensible film bonds the shells of the lobster, sealing its inner body and also restricting its curling angle. The curling mechanisms of the toy and the lobster are essentially the same. Both have multiple DoFs, which might also account for the wave-like configurations of the millipede.

7.1.3 The curling surface and its constituent units

The aim of this chapter is to achieve the curling, wave-like, and triangular configurations of a millipede. However, the multi-DoF mechanisms are not desirable for control simplicity. Thus, the curling surface introduced in Chapter 4 Fig. 4.10 is

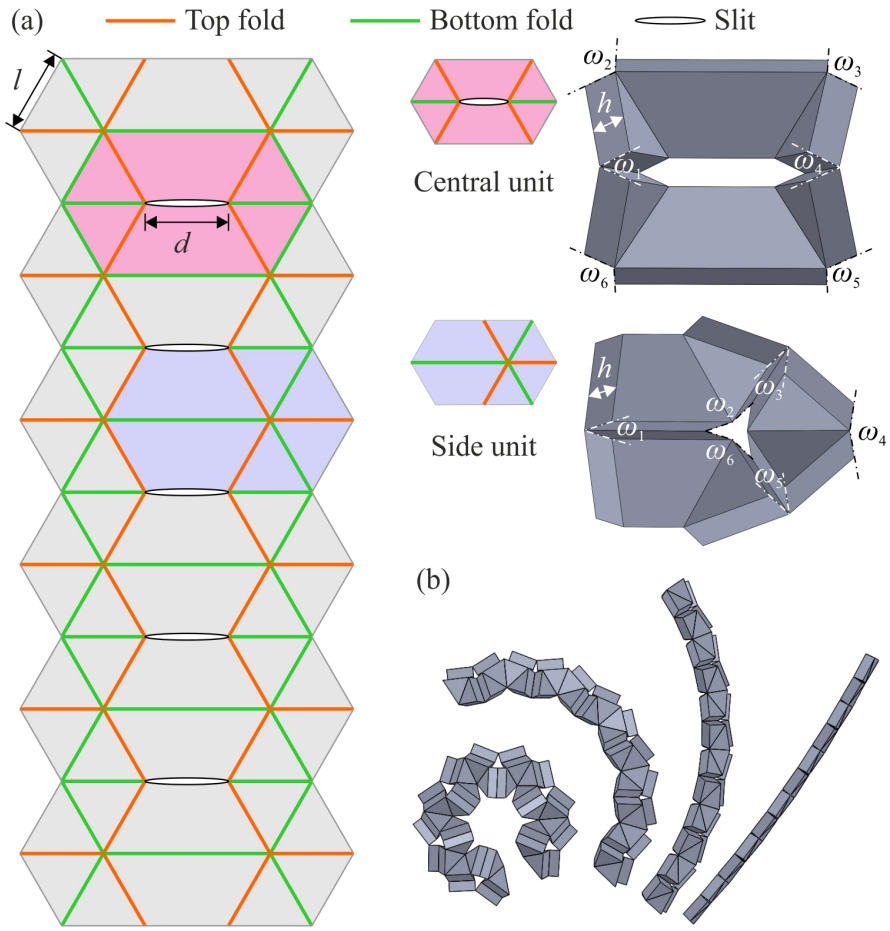


Figure 7.3: (a) Origami pattern of the curling surface and its constituent units. The pattern is composed of identical equilateral triangles and isosceles trapezoids. (b) The curling process in SOLIDWORKS when all central and side units are in their respective path 1.

used to replace the multiple rotational joints. It naturally has a curling motion, and its bifurcation paths are exploited for other configurations.

A special case of the surface is produced in Fig. 7.3, where design parameters are also illustrated. The surface is composed of identical equilateral triangles and isosceles trapezoids, forming interlinked segments to mimic the feature of a millipede. The connection of these panels yields two types of units identified in

Chapter 3, i.e., Unit a_2 with line- and plane-symmetry and Unit b_1. The latter also belongs to Unit m_1. For simplicity, they are renamed as the central unit and side unit in this chapter. Their kinematic behaviours are rewritten as follows.

For the central unit, it has three motion paths.

$$\omega_1 = \omega_4,\ \omega_2 = \omega_5,\ \omega_3 = \omega_6 \tag{7.1}$$

for path 1,

$$\begin{aligned} \omega_2 &= \omega_3 \\ \tan\frac{\omega_2}{2} &= 2\tan\frac{\omega_1}{2} \end{aligned} \tag{7.2}$$

for path 2,

$$\omega_2 = \omega_3 = 0 \tag{7.3}$$

for path 3,

$$\begin{aligned} \tan\frac{\omega_1}{2} &= \frac{\sqrt{3}d}{2h} \\ \tan\frac{\omega_3}{2} &= \frac{\sqrt{3}d\tan\frac{\omega_2}{2}}{2h\tan\frac{\omega_2}{2} - \sqrt{3}d} \end{aligned} \tag{7.4}$$

The side unit has two motion paths as

$$\omega_1 = \omega_3 = \omega_5;\ \omega_2 = \omega_4 = \omega_6 \tag{7.5}$$

for path 1,

$$\tan\frac{\omega_2}{2} = \frac{\sin\frac{\omega_1}{2}}{2\cos\frac{\omega_1}{2} - \sqrt{3}} \tag{7.6}$$

for path 2,

$$\tan\frac{\omega_2}{2} = \frac{\sin\frac{\omega_1}{2}}{2\cos\frac{\omega_1}{2} + \sqrt{3}} \tag{7.7}$$

When all central units and side units are in their respective path 1, the surface can curl up into a coil shape. The process is illustrated in Fig. 7.3(b).

7.1.4 Combined kinematics, segmentation, and bifurcation

Each unit of the curling surface is single-DoF with multiple motion paths. However, it is unclear whether the entire surface remains single mobility and how many bifurcation paths it has. This part analyses the surface's overall mobility and kinematic bifurcations.

In Fig. 7.3. a pair of side units refer to the ones symmetric to each other with two overlapping panels. They also share a bottom fold. A central unit is then connected with the pair, leading to two top shared folds. Units are repeatedly combined to form the entire surface. A single combination is reproduced in Fig. 7.4, along with its topological diagram. The three units share three folds, resulting in three dihedral angles, namely φ_1, φ_2, and φ_{12} as marked in Fig. 7.4.

Considering the shared folds and motion paths of each unit given in Eqs. 7.1 - 7.7, the combination exhibits single mobility as the shared folds pass the motion from one to the other and all the movements are kinematically compatible. Three motion possibilities exist as follows.

- The central unit is in its path 1 while two side units are in its path 1, as shown in Fig. 7.4(c).
- The central unit is in its path 1 while two side units are in its path 2, as shown in Fig. 7.4(d).
- The central unit is in its path 3 while two side units stay immobile. This is purely a hinge-like motion.

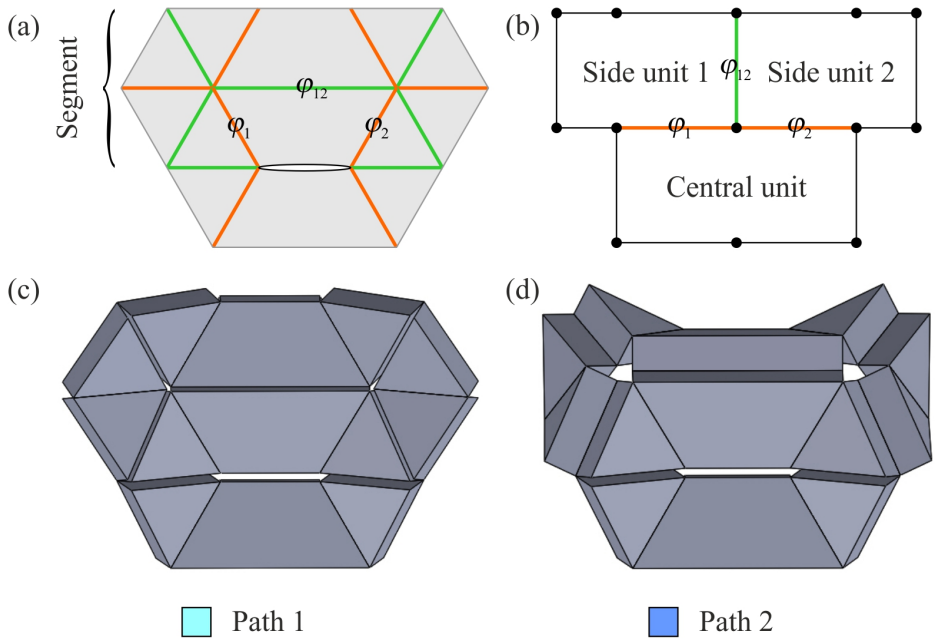


Figure 7.4: Unit combination and bifurcation. **(a)** Origami pattern of a central unit and a pair of side units, along with **(b)** its topological diagram. Two bifurcation paths are displayed, where the central unit is in path 1. The side units are in **(c)** path 1 and **(d)** path 2, respectively.

The last case is less interesting as it will generate more than one DoF on a longer surface. Considering that this motion path can be easily eliminated by actuating any side unit, it is hence excluded from following the analysis.

For two cases where the side units are mobile, the relationship among φ_1, φ_2, and φ_{12} are

$$\varphi_1 = \varphi_2 \tag{7.8}$$

for case 1 when the side units are in path 1,

$$\tan\frac{\varphi_{12}}{2} = \frac{\sin\frac{\varphi_1}{2}}{2\cos\frac{\varphi_1}{2} - \sqrt{3}} \tag{7.9}$$

for case 2 when the side units are in path 2,

$$\tan\frac{\varphi_{12}}{2} = \frac{\sin\frac{\varphi_1}{2}}{2\cos\frac{\varphi_1}{2} + \sqrt{3}} \tag{7.10}$$

More units can be added to create a long surface. Due to the shared folds, the surface maintains single mobility regardless of how many units are added. Noticeably, all panels of a central unit are also part of the side units. To simplify the representation, a pair of side units is defined as a segment with path 1 (marked in light blue) and path 2 (marked in dark blue).

The number of bifurcations on an n-segment surface is obtained by motion path permutation. Specifically, when n is odd, the number of motion paths is $2^{n-1}+2^{(n-1)/2}$. It becomes $2^{n-1}+2^{(n-2)/2}$ when n is even. Symmetric configurations are omitted. The six-segment surface shown in Fig. 7.3 can produce 32 distinct configurations, some of which are illustrated in Fig. 7.5. The associated motion path of each segment is also given.

Given the kinematic bifurcations, the surface can not only curl up like the millipede's defensive mechanism, but also produce wave-like or triangular configurations. In each bifurcated path, the surface's motion is of a single DoF.

7.1.5 Analysis of curling profile

There are two curling configurations in Fig. 7.5, where segments are all in either path 1 or path 2. Their profiles are approximately an arch. The profiles of other configurations can be regarded as a combination of the two curvatures, depending on the motion path arrangement. Hence, the curling configurations are taken as the basis to quantify different morphologies of the surface. They are reproduced in

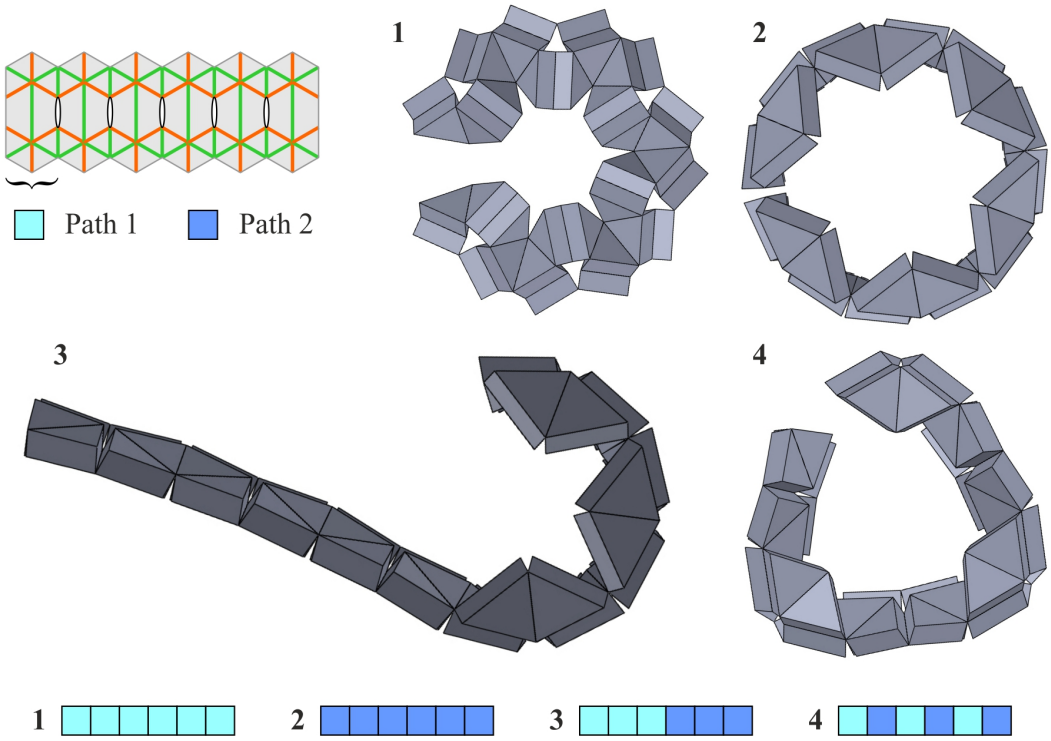


Figure 7.5: Cross-sectional view of selected surface configurations. Curling, wave-like, and triangular morphologies can be obtained from the kinematic bifurcations. Note that segments can look different even if they are in the same path as they may have different curvatures. This is exemplified by configurations 1 and 3 where path 1 of each looks distinctive.

Fig. 7.6 in a larger size. For each configuration, the cross-sections of the trapezoid panels are highlighted in light green. The outer vertices form an arc as part of a circle, denoted by a dashed curve. The radius r of each circle is calculated geometrically as follows.

For curling motion 1 illustrated in Fig. 7.6(a),

$$\begin{aligned} r^2 &= l_0^2 + r_1^2 + 2l_0 r_1 \sin\frac{\varphi_{12}}{2} \\ \alpha &= 90^\circ - \beta - \frac{\varphi_{12}}{2} \end{aligned} \tag{7.11}$$

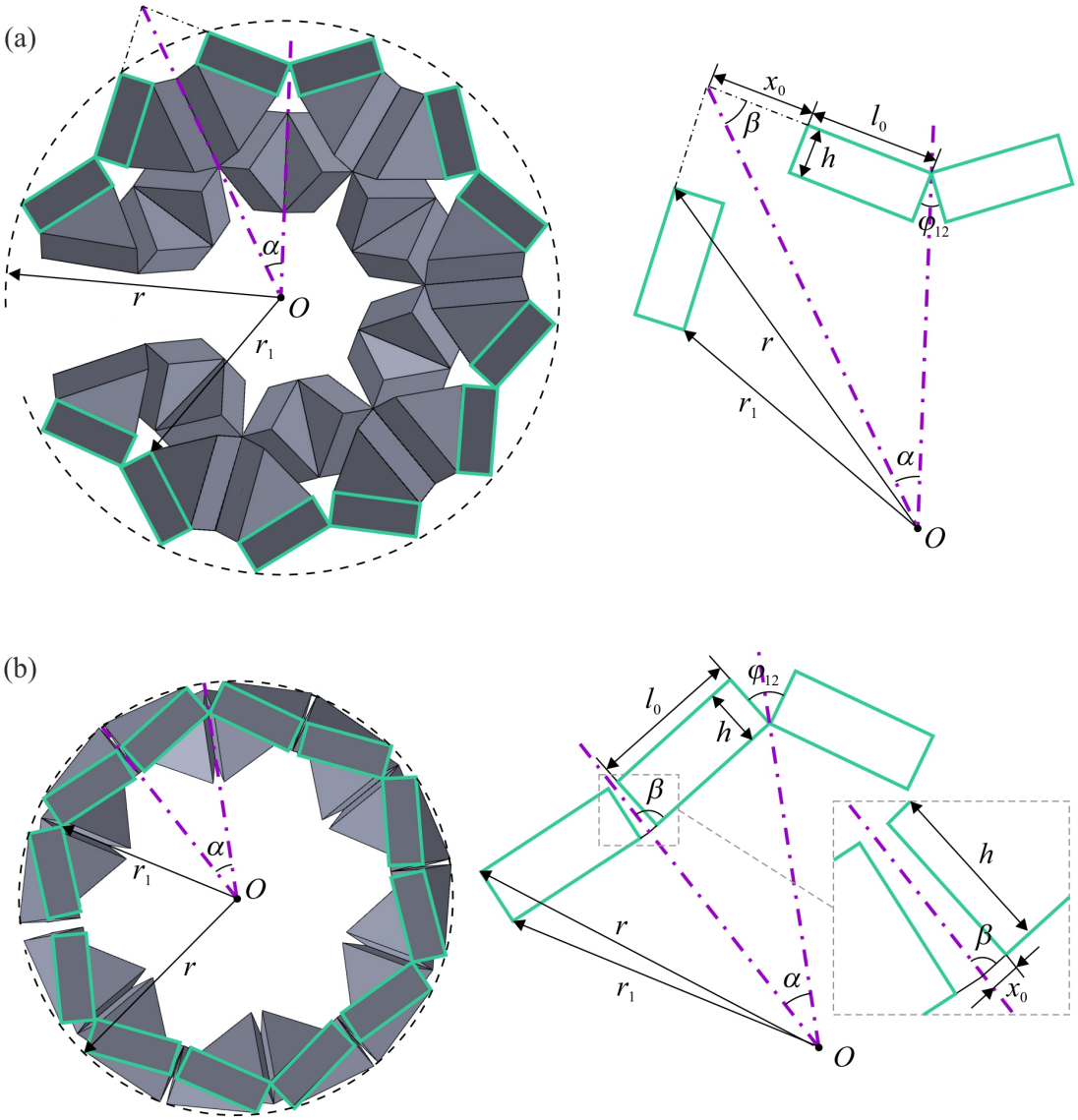


Figure 7.6: Cross-sectional views of the curling configurations when all segments are in **(a)** path 1 and **(b)** path 2. Parameters for geometric analysis are denoted.

For curling motion 2 illustrated in Fig. 7.6(b),

$$\begin{aligned} r^2 &= h_0^2 + r_1^2 + 2hr_1 \cos\frac{\varphi_{12}}{2} \\ \alpha &= -90^\circ + \beta + \frac{\varphi_{12}}{2} \end{aligned} \tag{7.12}$$

where all variables are denoted in Fig. 7.6 and can be obtained as

$$\tan\beta = 2\cot\frac{\varphi_1}{2},\ x_0 = \frac{h\sin\frac{\varphi_1}{2}}{\sqrt{1+\cos^2\frac{\varphi_1}{2}}},\ l_0 = \frac{\sqrt{3}}{2}l,\ r_1 = \frac{l_0\sin\beta + x_0\cos\beta + h}{\sin\alpha}$$

It is worth noting that φ_1 and φ_{12} in geometric analysis should follow Eqs. 7.9 - 7.10 for the respective curling motion. For the six-segment surface, a circle is completed when $\alpha = 60°$, at which point two ends of the surface will collide.

7.2 Experimental procedure

The curling surface is taken as the backbone of a millipede robot. This section depicts its actuation components and associated fabrication trials. Experiments are subsequently carried out on actuated prototypes of a single segment, double segments, and a six-segment robot.

7.2.1 Actuation of the curling surface

Due to friction and energy loss, it is not practical to actuate the entire surface using only one actuator, although it is theoretically single-DoF. Instead, three segments are chosen to be actuated by a tendon-based system, with the other three left passively. Even though multiple actuators are employed, their input signals remain identical without increasing control complexity.

The design of an actuated segment is illustrated in Fig. 7.7. Porous structures have been adopted on all panels to reduce self-weight. A rotating axle is added to one trapezoid panel, which will be driven by a pair of motors on both sides. Tendon channels are left in some panels. Specifically, four sets of tendons are

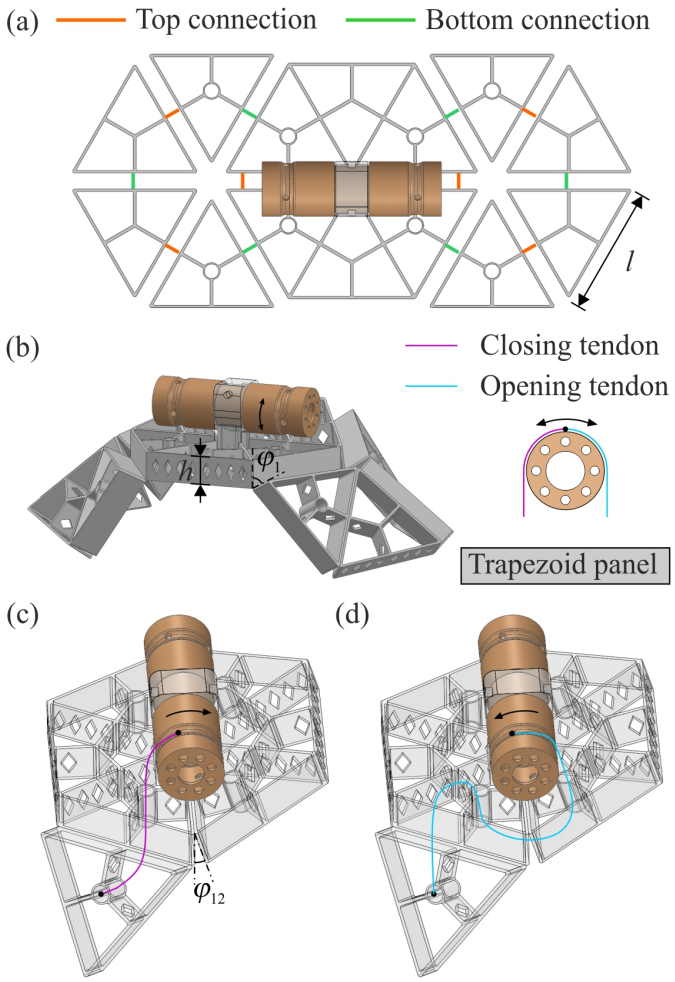


Figure 7.7: Actuation design of a single segment. **(a)** Top view of the segment with a rotating axle. Note that the panel connections are upside-down from the original one in Fig. 7.3. **(b)** Side view of the segment in a semi-closed state. The arrangements of closing and opening tendons are given in **(c)** and **(d)**, respectively.

used to activate the segment from the flat unfolded state, which is defined as the closing motion. Another four tendons are used to reverse the process and return the segment to the flat state, which is defined as the opening motion.

To illustrate the working principle, one closing tendon and one opening set are presented in Figs. 7.7(c) and 7.7(d), respectively, with the rest symmetric with them. One end of each tendon is fixed to the triangular panel. The tendon

then passes through the closing or opening routes with the other end connected to the axle. When the axle rotates clockwise, the closing tendon is pulled and the opening tendon is released. The segment is thus closed. When the axle rotates anticlockwise, the closing tendon is loosened and the opening tendon is pulled, causing the segment to open. The approximate tendon length changes, i.e., δL_1 for the closing motion and δL_2 for the opening motion, are given as follows. Each tendon is assumed inextensible.

$$\delta L_1 = \frac{\sqrt{3}}{3} l(\cos\frac{\varphi_1}{2} - 1),\ \delta L_2 = 2h(\sin\frac{\varphi_1}{2} + \sin\frac{\varphi_{12}}{2}) \tag{7.13}$$

where φ_1, φ_{12}, h, and l are marked in Fig. 7.7.

Since the closing and opening tendons are tied to the same axle, the sum of their length changes, $\delta L_1 + \delta L_2$, should be zero. However, a discrepancy always exists according to Eq. 7.13. It is thus deduced that the assumption of inextensible tendons does not hold. Instead, they must have been stretched to match the difference. The phenomenon will also be reflected in the experimental results.

Additionally, for the actuated segment, the axle has physically blocked its path 2, leading to a decrease in the surface's possible configurations. The relationship between φ_1 and φ_{12} in Eq. 7.13 would only follow motion path 1 given in Eq. 7.6.

7.2.2 Fabrication trials

The key mechanical components to actuate a segment are illustrated in Fig. 7.8(a). The axle and rigid panels were 3D printed using polylactic acid (PLA) material on a desktop 3D printer (Creality Ender 3). The side length of panels l and the slit length d were taken as 40 mm. The panel thickness h was set as 10 mm.

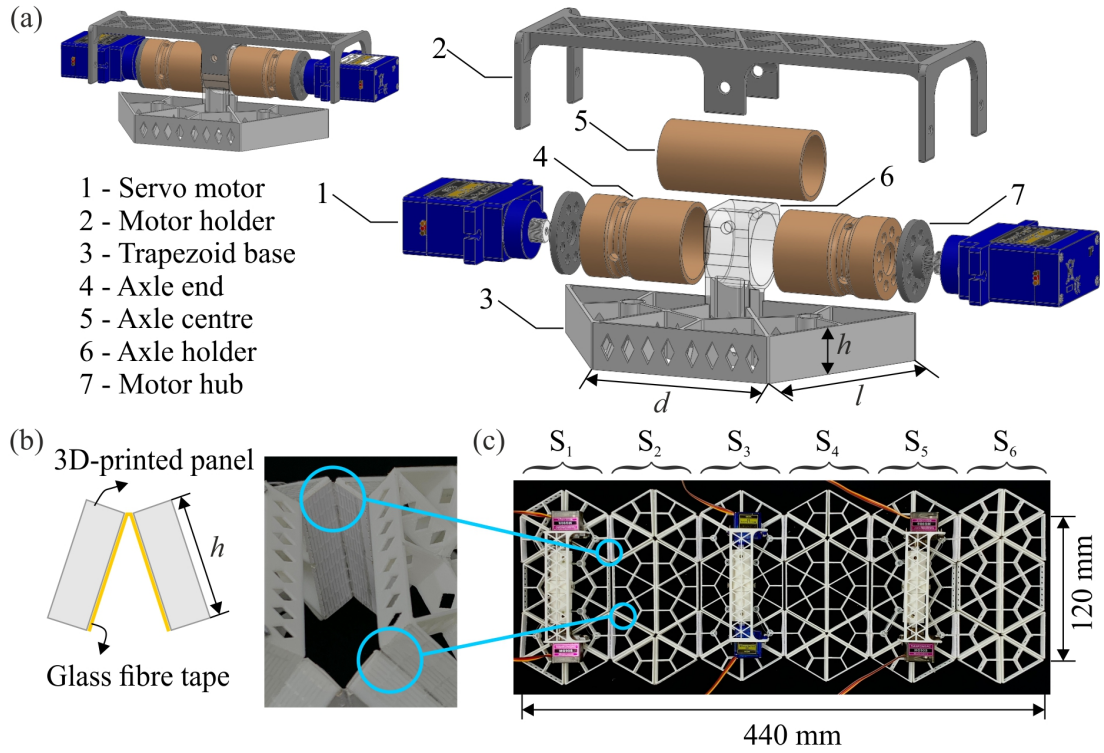


Figure 7.8: Fabrication of an actuated surface. **(a)** Schematic design of the driving axle. **(b)** Fabrication of fold connections between panels. **(c)** Completed prototype of a six-segment millipede-like robot.

Individual panels were manually connected to form a segment. Each fold was made by glueing glass-fibre tapes on the side walls of adjacent panels, as shown in Fig. 7.8(b). Clear nylon fishing lines were used as tendons for the actuated segments. Two servo motor sets (SG90s) were fixed symmetrically to provide the driving force for axle rotation. Each actuated segment was then connected to a passive one until a six-segment robot was finished as shown in Fig. 7.8(c).

In the robotic prototype, the actuated segments are S_1, S_3, and S_5. S_2, S_4, and S_6 are left with passive motions, which can be either in path 1 or path 2. A microcontroller (Arduino UNO) was employed to synchronously control the motors. Due to the blockage caused by the axles, the robot has only eight configurations.

7.2.3 Characterisation of the actuated prototypes

Single and double segments were actuated to evaluate their kinematic behaviours. The entire robotic prototype was used to characterise the curling, wave-like, and triangular configurations. The experimental setup is as follows.

In the segment-level experiments, two basic cases were used: (a) a single actuated segment, and (b) double segments where one is actuated and one is passive. Markers were affixed to multiple panels as illustrated in Fig. 7.9. Each marker is highlighted in red and numbered by the side. The single segment was only examined for its path 1, as shown in 7.9(a). For the double segments, path 1 of the passive segment was evaluated using the marker arrangement in Fig. 7.9(b). Path 2 was assessed according to Fig. 7.9(c). The different marker arrangements ensure that each path is achievable and the markers's positions can be recorded by the motion capture system (OptiTrack) without occlusion.

Markers with a yellow background were used to calculate the dihedral angles between adjacent trapezoid panels, i.e., $\varphi_{12-\text{actuated}}$, $\varphi_{12-\text{passive}}$, and $\varphi_{\text{actuated-passive}}$. Their relationship is

$$\varphi_{12-\text{actuated}} = \varphi_{12-\text{passive}} = \varphi_{12},\ \tan\frac{\varphi_{\text{actuated-passive}}}{2} = 2\cot\frac{\varphi_1}{2} \tag{7.14}$$

where φ_1 and φ_{12} are marked in Fig. 7.4 and obtained from Eqs. 7.9 - 7.10.

The distance between marker i and marker j is named $d_{i,\,j}$. Their theoretical values are given as follows with the marker's diameter d_0 taken into account.

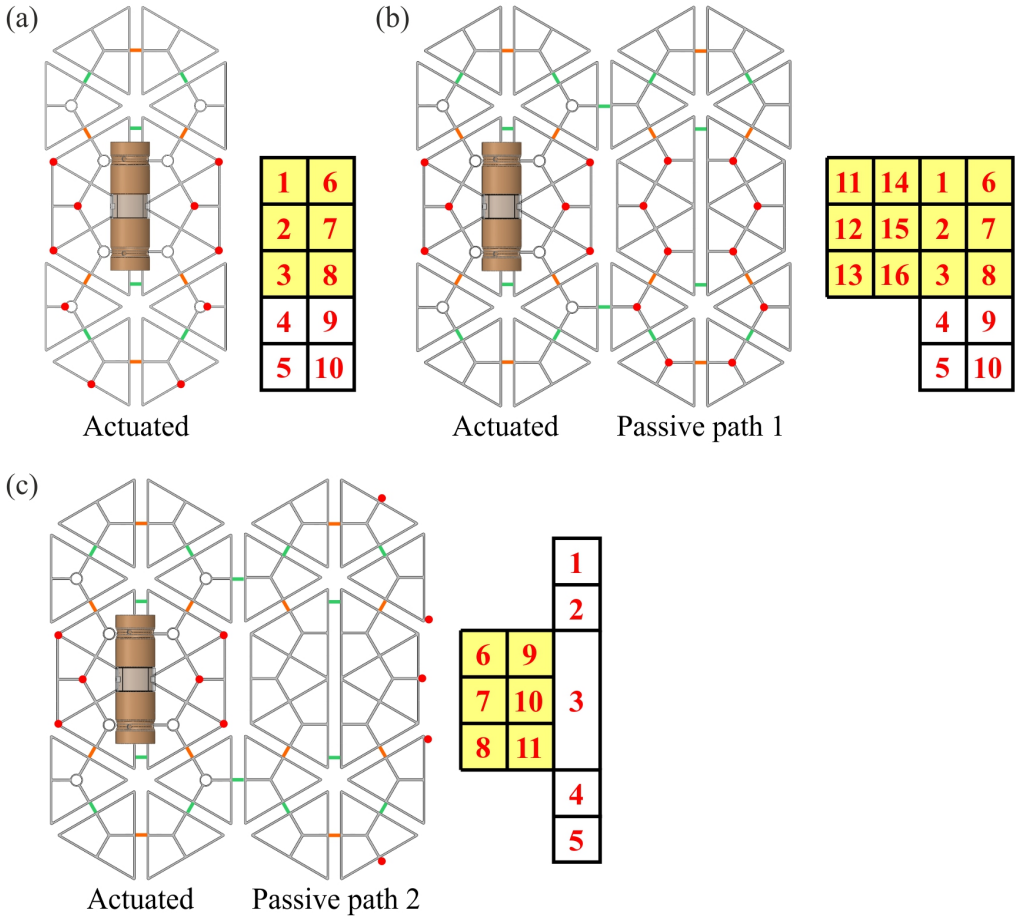


Figure 7.9: Marker placement for (a) an actuated single segment which only has path 1, (b) an actuated segment with a passive one in path 1, and (c) an actuated segment with a passive one in path 2.

For the single segment in Fig. 7.9(a),

$$d_{2,\,7} = \sqrt{2(\frac{l^2}{3} + d_0^2)(1 + \cos\left(\varphi_{12} + 2\arctan\frac{\sqrt{3}d_0}{l}\right))} \tag{7.15}$$

$$d_{3,\,4} = d_{8,\,9} = \sqrt{\begin{array}{r}\frac{l^2}{3} + 2(h + d_0)^2 - 2\sqrt{(h + d_0)^2 + \frac{d^2}{12}}(h + d_0) \\ \cos\left(\varphi_{12} + \arctan\frac{\sqrt{3}l}{6h + 6d_0}\right)\end{array}} \tag{7.16}$$

$$d_{4,\,5} = d_{9,\,10} = \sqrt{\begin{array}{r}\frac{l^2}{3} + 2d_0^2 + 2\sqrt{(\frac{l^2}{16} + s_0^2)(\frac{l^2}{12} + d_0^2)} \\ \cos\left(\varphi_{12} + \arctan\frac{4\sqrt{3}d_0}{3l} + \arctan\frac{2\sqrt{3}d_0}{l}\right)\end{array}} \tag{7.17}$$

$$d_{5,\,10} = \sqrt{2((h+d_0)^2 + \frac{3l^2}{16})(1 - \cos\left(\varphi_{12} + 2\arctan\sqrt{\frac{\sqrt{3}l}{4h+4d_0}}\right))} \tag{7.18}$$

For the double segments in Fig. 7.9(b),

$$d_{2,\,7} = \sqrt{2(\frac{l^2}{3} + d_0^2)(1 + \cos\left(\varphi_{12} + 2\arctan\frac{\sqrt{3}d_0}{l}\right))} \tag{7.19}$$

$$d_{3,\,4} = d_{8,\,9} = d_{5,\,10} = \sqrt{\begin{array}{r}2(\frac{l^2}{12} + (h+d_0)^2) \\ (1 - \cos\left(\varphi_{12} + 2\arctan\frac{\sqrt{3}l}{6h+6d_0}\right))\end{array}} \tag{7.20}$$

$$d_{4,\,5} = d_{3,\,8} = d_{9,\,10} = \sqrt{2(\frac{l^2}{12} + d_0^2)(1 + \cos\left(\varphi_{12} + 2\arctan\frac{2\sqrt{3}d_0}{l}\right))} \tag{7.21}$$

$$d_{2,\,15} = \frac{2((2h+d_0)\sin\frac{\varphi_1}{2} + \frac{\sqrt{3}}{3}l\cos\frac{\varphi_1}{2})}{\sqrt{1 + \cos^2\frac{\varphi_1}{2}}} \tag{7.22}$$

For the double segments in Fig. 7.9(c),

$$d_{7,\,10} = \sqrt{2(\frac{l^2}{3} + d_0^2)(1 + \cos\left(\varphi_{12} + 2\arctan\frac{\sqrt{3}d_0}{l}\right))} \tag{7.23}$$

$$d_{1,\,2} = d_{4,\,5} = \sqrt{\begin{array}{r}(\frac{3d_0}{2} - \frac{l}{4})^2 + (\frac{h}{2}\sin\delta_1 + (\frac{\sqrt{3}l}{4} + d_0)\cos\delta_1 + \frac{\sqrt{3}l}{2} - d_0)^2 \\ + (\frac{h}{2}\cos\delta_1 + (\frac{\sqrt{3}l}{4} + d_0)\sin\delta_1 - d_0)^2\end{array}} \tag{7.24}$$

$$d_{2,\,3} = d_{3,\,4} = \sqrt{\begin{array}{r}(d_0 + \frac{h}{2}\sin\delta_2 + \frac{\sqrt{3}l}{4}\cos\delta_2)^2 + (\frac{l}{4} + \frac{\sqrt{3}d_0}{6})^2 \\ + (h - d_0 - \frac{h}{2}\cos\delta_2 + \frac{\sqrt{3}l}{4}\sin\delta_2)^2\end{array}} \tag{7.25}$$

where

$$\tan\frac{\delta_1}{2} = \frac{\sin\frac{\delta_2}{2}}{2\cos\frac{\delta_2}{2} - \sqrt{3}},\ \tan\frac{\delta_2}{2} = \frac{\sin\frac{\varphi_{12}}{2}}{2\cos\frac{\varphi_{12}}{2} - \sqrt{3}}$$

The robotic prototype in Fig. 7.8(c) was used to validate its eight configurations. Motors were controlled synchronously for actuation. No switching mechanism has been developed for the passive segments, and hence, they had to be manually configured into path 1 or path 2.

In addition to the planned experiments listed above, the segments and the robotic prototype were also explored for locomotion strategies such as crawling and rolling. They were tested on a flat surface and a slope.

7.3 Results and discussions

7.3.1 Single segment behaviour

Experimental results of the single segment are given in Fig. 7.10. Theoretical predictions are also plotted for comparison. The segment's configurations from flat to folded states are also illustrated.

In general, the motions match the kinematic model, albeit with some degree of deviation. On top of system errors in the motion capture system, the manual fabrication of folds and placement of markers may cause the discrepancy.

Hysteresis is also observed between the closing and opening motions, which is likely due to the mismatch of tendon length changes, as analysed before. The nylon tendons must have been stretched or slacked to compensate for the mismatch.

7.3.2 Double segment behaviour

Experimental results for the double segments are given in Figs. 7.11 and 7.12 when the passive segment is in path 1 and path 2, respectively.

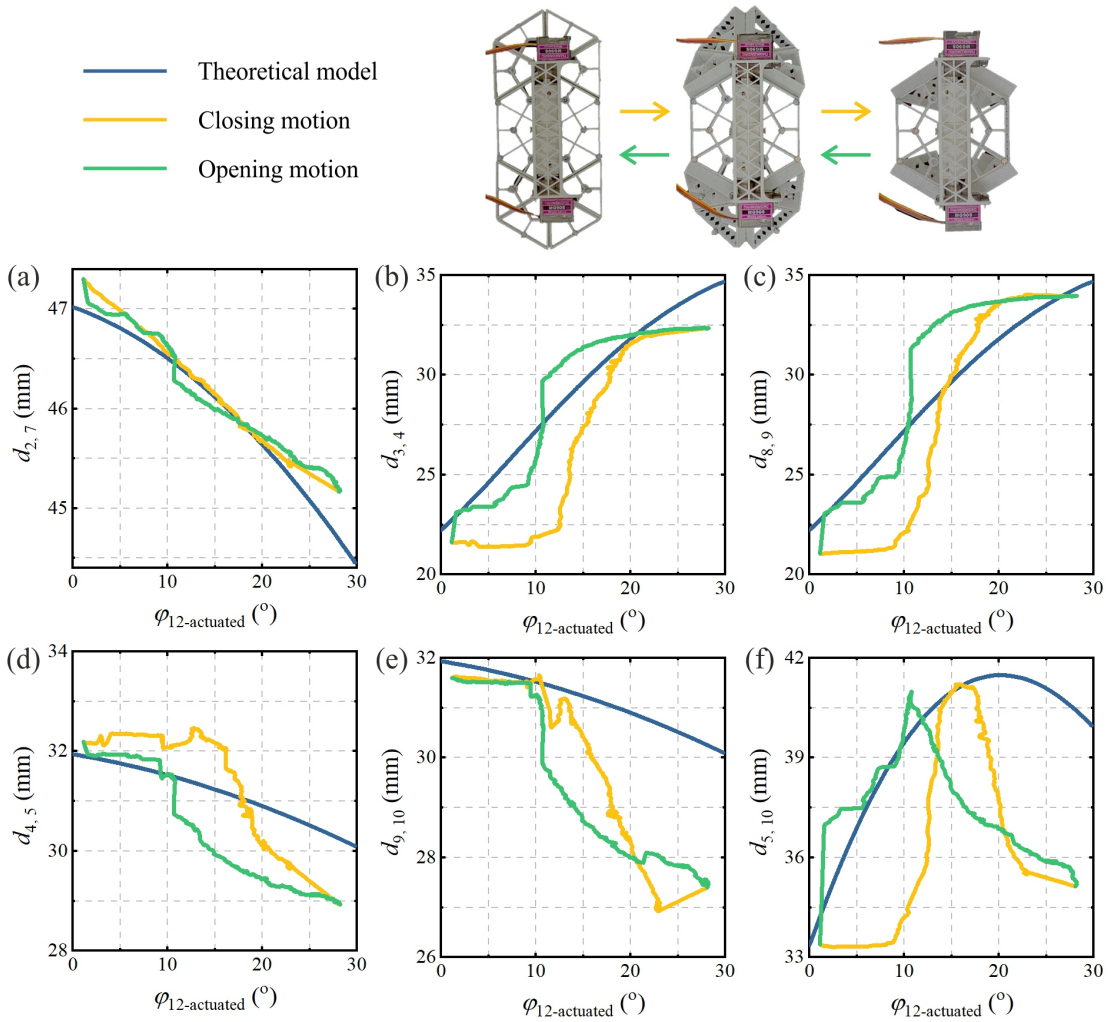


Figure 7.10: Experimental results of the single segment in path 1 compared with the theoretical model. Note that the range of the vertical axis differs for each distance, making some of the errors seemingly bigger than others but actually not. The same applies to Figures 7.11 and 7.12.

When in path 1, the experimental results of the passive segment align well with the theoretical model, as shown in Figs. 7.11(a) - 7.11(f). Little hysteresis exists, as no tendons are connected to the passive segment. The phenomenon further confirms that hysteresis is due to the mismatch of tendon length changes. When it comes to the relationship with the actuated segment, the angle change matches

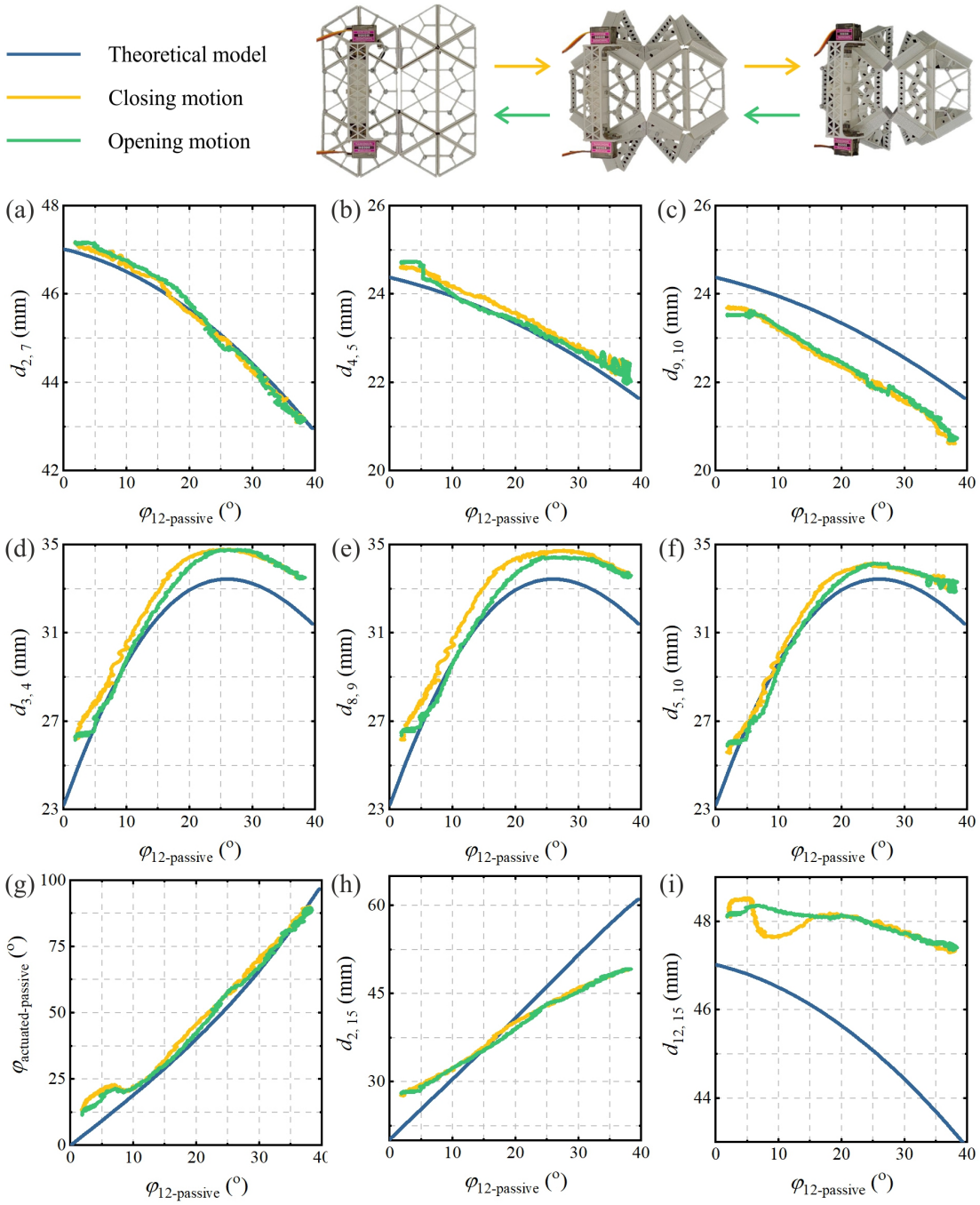


Figure 7.11: Experimental results of double segments compared with the theoretical model. The passive segment is in path 1.

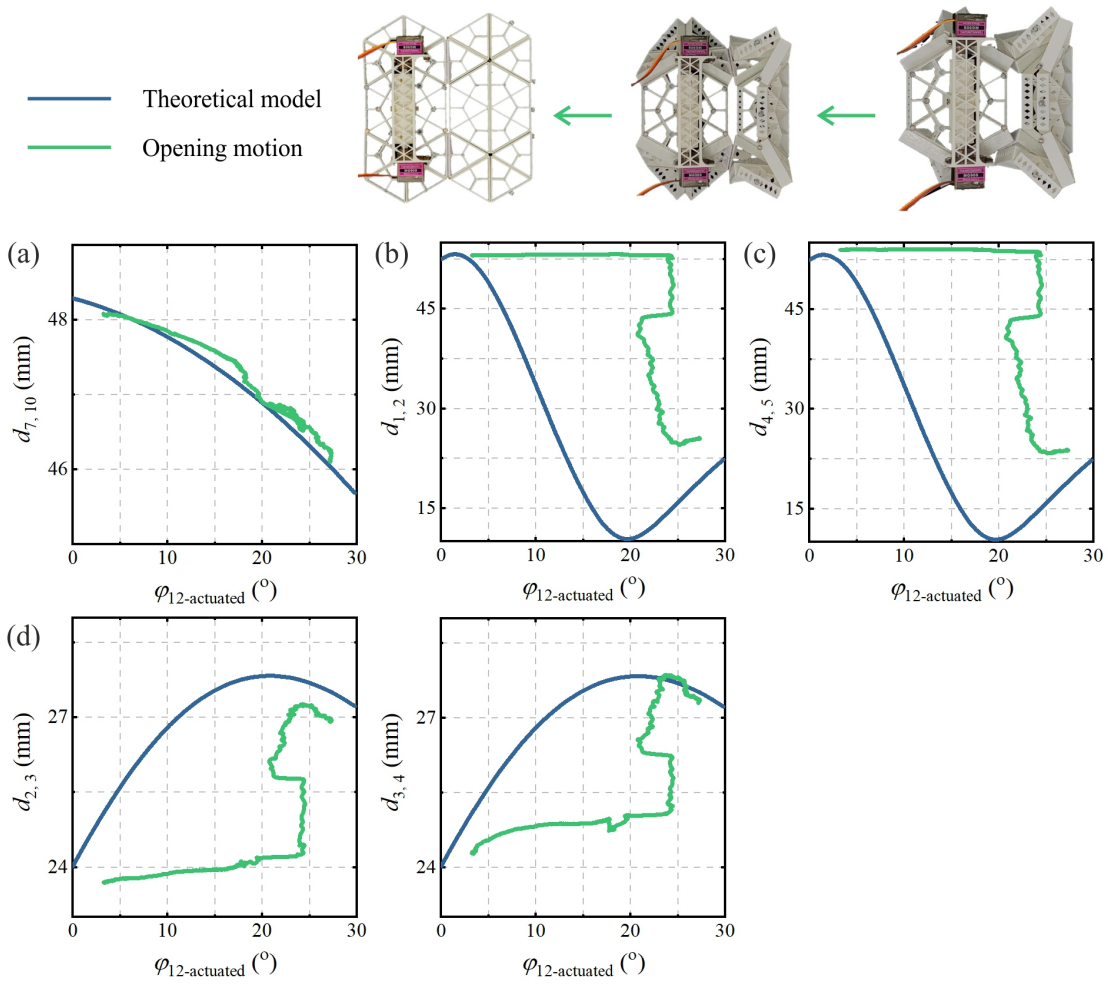


Figure 7.12: Experimental results of double segments compared with the theoretical model. The passive segment is in path 2.

with the prediction as shown in Fig. 7.11(g). However, the marker distances have a much larger discrepancy, as evidenced by Figs. 7.11(h) and 7.11(i).

When the passive segment is in path 2, only opening motions were tested as a manual switch was required to access the path. As shown in Fig. 7.12(a), the panel distance on the actuated segment matches well with the associated dihedral angle. A substantial discrepancy from the prediction is observed in Figs. 7.12(b) - 7.12(e), where only the starting and ending points are close to the model.

In addition to the same error analysis for the single segment, compliance, caused by the glass-fibre tapes, may also account for the discrepancy. Such compliant behaviour is further influenced by the segments' self-weight and stretchable tendons.

7.3.3 Configurations of the six-segment robot

The six-segment robot has demonstrated its configurations as shown in Fig. 7.13. Simulated models from SOLIDWORKS are also displayed for comparison, with the motion path of each segment indicated.

The curling motion is achieved in Fig. 7.13(a), replicating the behaviour of a millipede when disturbed. A variety of wave-like configurations are realised in Figs. 7.13(b) - 7.13(g), similar to the morphology of a crawling millipede. Fig. 7.13(h) gives a closed-loop configuration which can be approximated to a triangle.

The diverse morphologies make the robot reconfigurable. They are purely achieved from bifurcations without disassembling or reassembling a single module.

7.3.4 Potential of the robotic prototype and its segments

Although this chapter focuses on realising a reconfigurable robot to mimic the millipede, its potential for locomotion is also briefly explored.

The curling and triangular configurations of the robot can facilitate rolling, as illustrated in Figs. 7.14(a) and 7.14(b). The alternation among different morphologies is also useful to generate different locomotion gaits, in which case the manual motion path switch should be replaced by a more automatic system.

Crawling-like motion is also possible on individual segments, as shown in Figs. 7.14(c) - 7.14(e). By controlling the motors to repeatedly rotate clockwise and

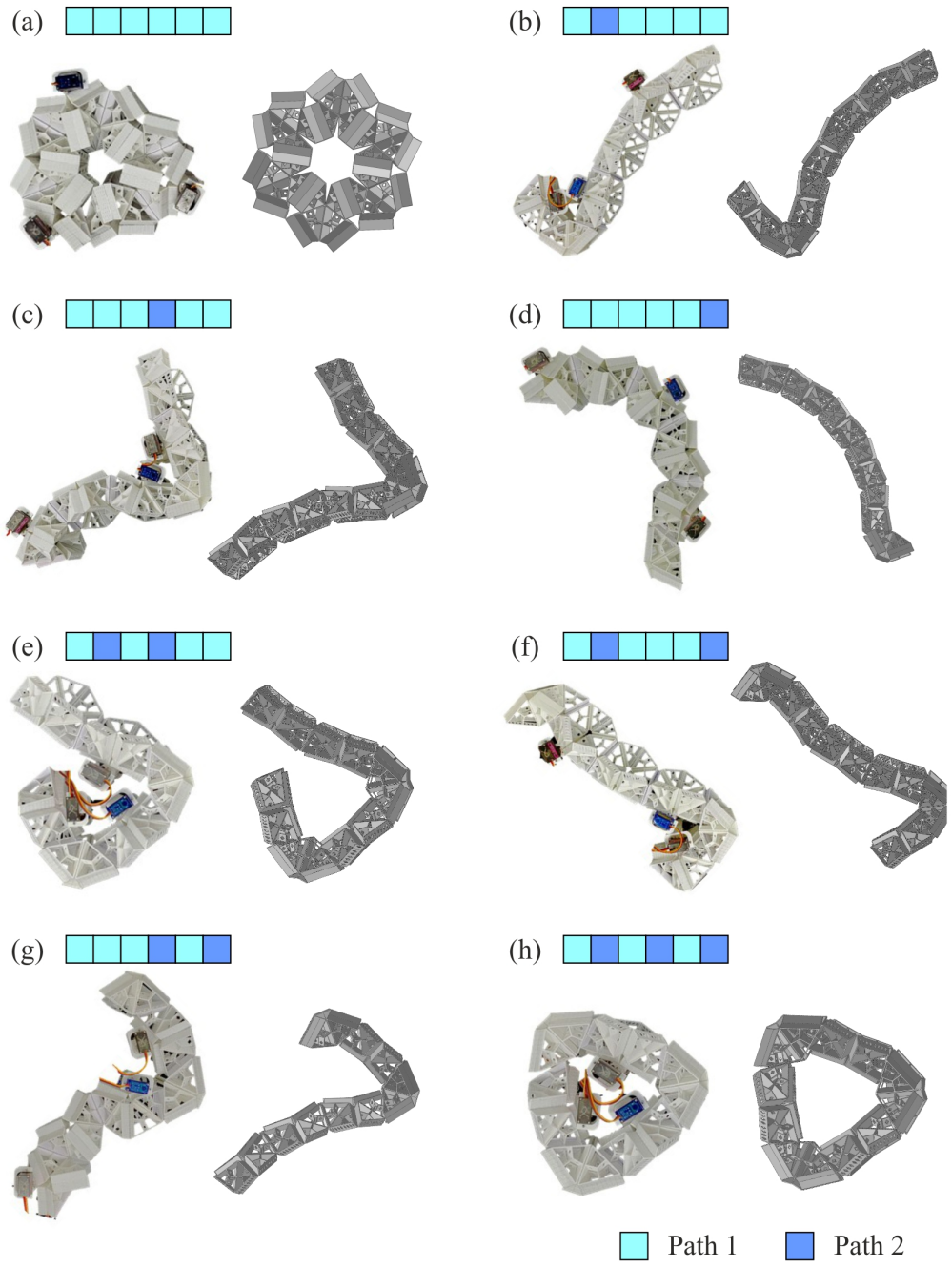


Figure 7.13: Eight configurations of the robot in comparison with simulations.

anticlockwise, the single, double, and four segments can rise from the flat state and crawl forward, a video of which is available in Appendix B. Hysteresis may

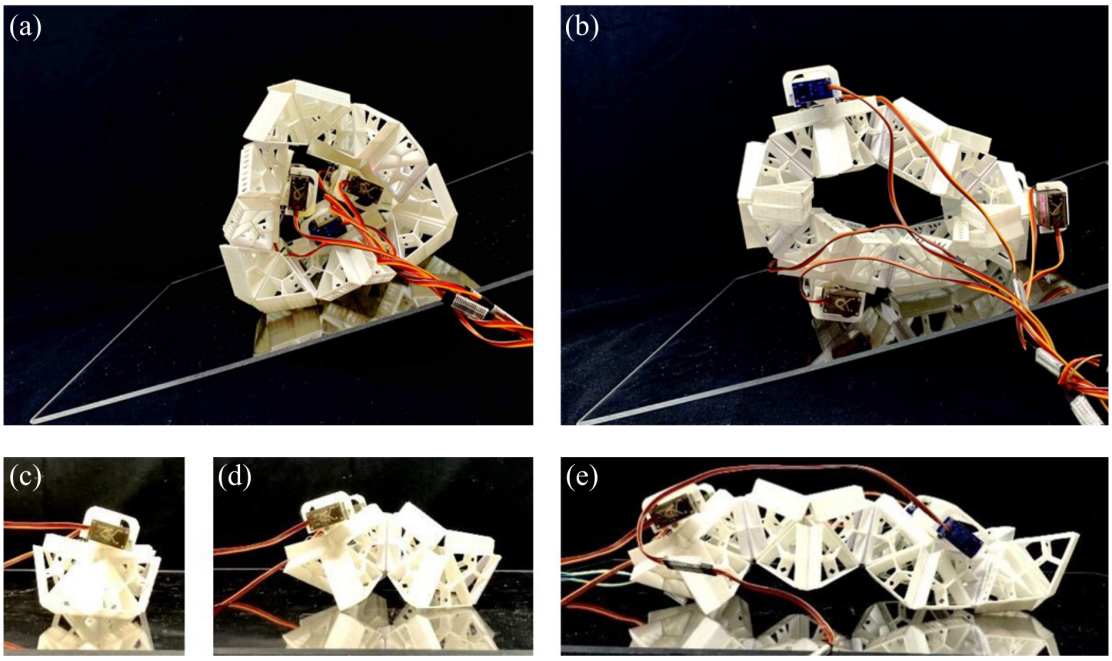


Figure 7.14: Potential of the robotic prototype and its segments. **(a)** The curling and **(b)** triangular configurations roll down a slope. Crawling behaviours have been achieved on **(c)** a single segment, **(d)** double segments, and **(e)** four segments.

have played a role in such a motion. Besides, friction feet between the segments and the ground should be studied to improve the crawling efficiency.

Another interesting phenomenon is that in the single and double segments, all motions are naturally in path 1. However, in four connected segments, one end automatically switches to path 2 without additional controllers. The switching mechanism needs to be fully understood, which can be further exploited as a viable approach to morphological computation.

7.4 Summary

To further explore the reconfigurability of morphing surfaces, the conceptual design of a curling surface and its realisation as an actuated robot is presented. The robot can generate a variety of configurations akin to those observed in millipedes. Such reconfiguration is achieved through the incorporation of kinematic bifurcations, rather than disconnecting and reconnecting individual modules or utilising a multi-DoF mechanism. Hence, the robot is more robust and can be extended to any desired length without excessive DoFs.

The robotic prototype and its segments are characterised. Hysteresis is observed on actuated segments. Locomotion strategies such as rolling and crawling are explored, which reveals a promising future application avenue. The current prototype is limited by the requirement of a manual switch to access different configurations. To make the robot fully functional, it is necessary to design a proper mechanism to achieve machine-aided or even automatic motion switches.

Chapter 8

Final Remarks

This thesis is concerned with two aspects. The first is the design methodology of morphing surfaces, which systematically maps thick-panel origami and 6R spatial overconstrained linkages to produce a variety of motion behaviours. The second is to exploit the unique features of morphing surfaces, e.g., single mobility and bifurcations, to improve the physical intelligence of robots, for which grasping, manipulation, and reconfiguration are the intended functions. The achievements are summarised in this chapter, followed by a list of exciting topics for future work.

8.1 Summary of achievements

8.1.1 Design of morphing units and surfaces

Roboticists have vastly used origami structures as skeletons for desirable motions. Origami engineers also make efforts to design novel structures for shape-changing. Despite the substantial progress, limitations exist in both fields as summarised in Chapter 2, preventing new origami structures from being used for better robots.

To address the research gaps, Chapter 3 proposes a systematic approach to designing kinematic morphing units. They all have single mobility and uniform thickness, some of which also exhibit kinematic bifurcations. The library of morphing units is achieved by an exhaustive mapping between thick-panel origami and 6R spatial overconstrained linkages. The obtained units are capable of versatile motions, whose kinematic behaviours are analysed in detail.

To make the results more accessible to the roboticists, Chapter 4 combines the units into tessellations or assemblies, yielding morphable surfaces that can bend, expand, twist, wrap, or curl. With a proper selection and combination of morphing units from the library, the surfaces' shape-changing possibilities are unlimited. Notably, all the morphing surfaces retain single mobility as their constituent units, whilst bifurcations may accumulate or be eliminated.

8.1.2 Wrapping surface: grasping and manipulation with limited control inputs

Given the unique kinematic properties, the morphing surfaces can be encoded with complex robotic functions with simplified control. For instance, it is difficult to achieve adaptable grasping and dexterous manipulation with simple mechanical design and actuation. To solve the challenge, the wrapping surface devised in Chapter 4 is selected as a gripper backbone.

Chapter 5 presents the gripper design and characterises its grasping behaviour. The gripper can be fully 3D-printed without much human intervention. Given the single mobility in the wrapping motion, only one motor is required to activate the gripper via tendon sets. Regardless of a relatively symmetric design, the gripper

can adapt to objects of various shapes and sizes. The results also indicate a certain level of compliance in the gripper backbone.

The wrapping surface also has other motions due to its kinematic bifurcations. Hence, Chapter 6 further develops the gripper into a platform for object manipulation, by exploiting its bifurcations and compliance.

More specifically, the bifurcation yields an instantaneous mobility increase at the gripper's unfolded state. Driven by a differential mechanism, the gripper can bifurcate into eight motion paths with only two motors. On top of the basic motion modes, compliance allows the gripper to transit from one path to the other outside of the bifurcation state, thereby adding more motion possibilities. In-hand manipulation of balls, cuboids, and cones is thus achieved on the griper platform, under the control of only two motors.

The robotic study on the wrapping surface has proven the possibility of balancing motion dexterity and control complexity with a simple mechanical design.

8.1.3 Curling surface: a low-DoF reconfigurable robot free from module reconnection

Besides object manipulation, bifurcations can also be used to improve the robot's reconfigurability without adding excessive DoFs. In addition, the system's robustness and reliability will not be sacrificed, as no disconnection or reconnection of modules is required for reconfiguration. The curling surface presented in Chapter 4 is taken as an example towards reconfigurable robots.

Chapter 7 further analyses the curling surface composed of interlinked segments. The surface can morph into a coil and also demonstrates other configura-

tions via bifurcated paths. By adding more segments to the surface, the overall DoF remains one while the number of bifurcation paths increases, facilitating the surface's potential for reconfiguration.

With tendon-based actuation, a robotic prototype is fabricated from a six-segment surface. The robot can curl up into a coil and reconfigure into wave-like or triangular shapes, mimicking a millipede's morphologies. On top of reconfigurability, crawling motions are observed, which is likely due to hysteresis on actuated segments. The robot's potential for other locomotion strategies such as rolling is also revealed. Limitations of the prototype are identified, necessitating the need for an automatic motion switch system to replace the manually configured one.

8.2 Future work

The findings lay the ground for leveraging morphing surfaces to design intelligent robots. Potential benefits include improved motion dexterity and reconfigurability, reduced control complexity, as well as simplified mechanical design. The research also ends with a list of exciting topics for future exploration.

From the design perspective of morphing surfaces, further work can be attempted as listed below.

- The current design only permits top and bottom folds parallel to the surfaces. It would also be interesting to move some folds perpendicular.

- In the kinematic model, some folds can be replaced by a rigid hinge body with widths taken into account. The result is similar to the 8R linkage model in Chapter 6 and adds extra compliance that is desired in robots.

- The current morphing surface is obtained from a forward design paradigm. An inverse design algorithm can be developed to suit target applications.
- A general kinematic solution to the unit based on the Wohlhart 6R linkage should be derived, as the current one is only a special case.

From the perspective of robots, more work can be done with both existing and newly developed prototypes. Some promising avenues are as follows.

- Tactile sensors can be added to the gripper, thereby enabling closed-loop control. It is also worth exploring whether the simple design can achieve object recognition via grasping at different motion modes. This would further enhance the gripper's embodied intelligence.
- An automatic motion switch system is needed for the curling surface. It can be extended to other morphing surfaces for versatile reconfigurable robots.
- The multi-stability of morphing surfaces can be explored by prototyping them at a semi-folded configuration. It is thus possible to transit from one stable pose to another, the property of which can be used on a robotic system for morphological computation without digital controllers.
- Environmentally responsive materials such as SMAs can be used to achieve fully untethered robots for autonomous shape changes.

Appendix A

Additional Morphing Units

This appendix is a brief summary of uniform-thickness morphing units that do not satisfy the selection criteria detailed in Chapter 3.

Figure A.1(a) is a unit based on the Waldron hybrid linkage, where $\alpha_{P1} = \alpha_{P22} = \alpha_{P23} = \alpha_{P3}$ and $\alpha_{P4} = \alpha_{P55} = \alpha_{P56} = \alpha_{P6}$. The case was also reported by Wang et al. (2018b). Figure A.1(b) is a special case Unit c_2 derived from the line-symmetric Bricard linkage, where $\alpha_{P1} = \alpha_{P22} = \alpha_{P4} = \alpha_{P55}$ and $\alpha_{P23} = \alpha_{P3} = \alpha_{P56} = \alpha_{P6}$. Both units have two DoFs at the flat state due to the aligned folds, i.e., folds 2 and 6 as well as folds 3 and 5. When these folds are fully folded, each unit can move into a single-DoF path via the newly aligned folds 1 and 4.

Figures A.1(c) - A.1(g) illustrate single-DoF units with physical collisions. These units are based on the Bennett 6R hybrid linkage, the Bricard linkage, and the Sarrus linkage and should satisfy the relevant geometric conditions. For instance, the unit in Fig. A.1(e) is derived from the plane-symmetric Bricard linkage. Hence, $\alpha_{P1} = \alpha_{P6}$, $\alpha_{P22} = \alpha_{P56}$, $\alpha_{P23} = \alpha_{P55}$, and $\alpha_{P3} = \alpha_{P4}$. The overlapping areas of these units are marked in red.

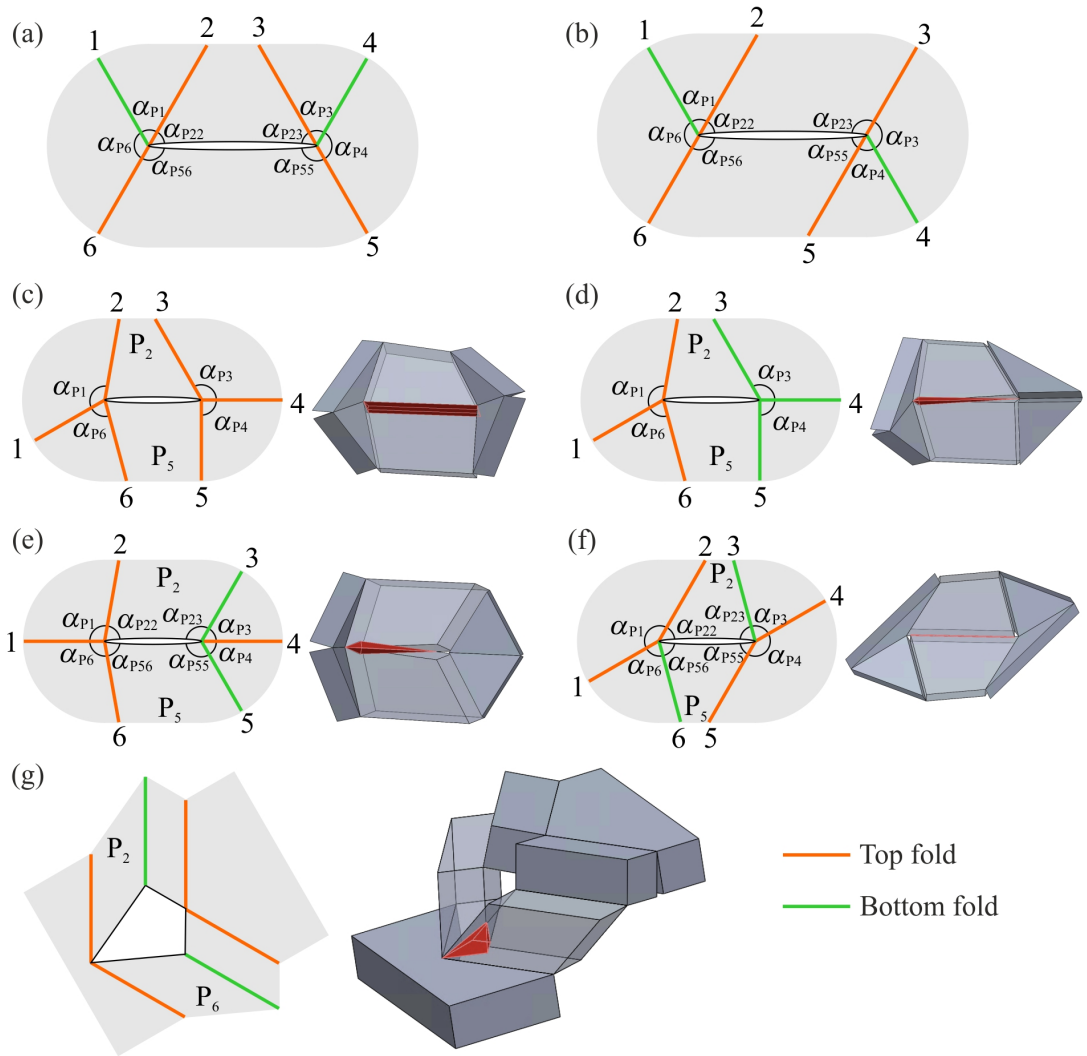


Figure A.1: Morphing units with more than one DoF or physical collisions. **(a)** Unit based on the Waldron hybrid linkage. **(b)** Unit based on the line-symmetric Bricard linkage. Both start with two DoFs and then reduce to a single mobility. **(c)** and **(d)** Units based on Bennett 6R hybrid linkage. **(e)** and **(f)** Units based on the plane-symmetric and line-symmetric Bricard linkages, respectively. The collision occurs between P_2 and P_5 on these four units. **(e)** Unit based on the Sarrus linkage and the interference exists between P_2 and P_6. The interfered area of each unit is identified by the SOLIDWORKS simulation and marked in red.

Appendix B

Supplementary Videos

This appendix gives supplementary videos of this thesis as follows.

- Chapter 5 - Wrapping Surface: a Robotic Gripper Enabled by a Single Motor
  - A video summarising the motion of the gripper and its object grasping performance can be found at: https://youtu.be/duQv6t03GOk.
  - The process to measure the maximum grasping weight can be found at: https://youtube.com/shorts/mgsRxzwGVng?feature=share.
- Chapter 6 - A Two-Motor-Controlled Gripper for Object Manipulation
  - A video summarising the gripper's motion modes, compliant motion switch, and manipulation can be found at: https://youtu.be/eHl7J3I2UUc.
- Chapter 7 - Curling Surface: a Millipede-Like Reconfigurable Robot
  - Individual segments of the millipede-like robot are explored for locomotion purposes. A video summarising their crawling motions can be found at: https://youtu.be/dnUU755oeXY.

Appendix C

Kinematic Model for Compliance Analysis

This appendix details how to solve the kinematic model for compliance analysis, which was presented in Chapter 6.

According to the geometric condition of the 8R-linkage-based kinematic model in Eq. 6.7 as well as the revised dihedral angle conversion in Table 6.2, the loop closure equation specified in Eq. 2.6 is simplified as follows.

$$\begin{aligned} E(1,1) = &-\cos(\omega_{11}+\omega_{12})\cos\omega_2\cos\omega_3 + \cos(\omega_{41}+\omega_{42})\cos\omega_5\cos\omega_6 \\ &- \frac{\sin(\omega_{11}+\omega_{12})(\cos\omega_3\sin\omega_2 - \sin\omega_3)}{\sqrt{2}} \\ &+ \frac{\sin(\omega_{41}+\omega_{42})(\cos\omega_6\sin\omega_5 - \sin\omega_6)}{\sqrt{2}} \end{aligned} \tag{C.1}$$

$$E(1,2) = \frac{\cos(\omega_{11}+\omega_{12})(\sin\omega_2 - \cos\omega_2\sin\omega_3)}{\sqrt{2}} - \frac{\sin(\omega_{11}+\omega_{12})(\cos\omega_2+\cos\omega_3+\sin\omega_2\sin\omega_3)}{2} + \sin(\omega_{41}+\omega_{42})\cos\omega_5\cos\omega_6 + \frac{\cos(\omega_{41}+\omega_{42})(\sin\omega_6-\cos\omega_6\sin\omega_5)}{\sqrt{2}} \quad \text{(C.2)}$$

$$E(1,3) = \frac{\sin(\omega_{11}+\omega_{12})(\sin\omega_2\sin\omega_3-\cos\omega_2+\cos\omega_3)}{2} + \frac{\cos(\omega_{11}+\omega_{12})(\cos\omega_2\sin\omega_3+\sin\omega_2)+\cos\omega_6\sin\omega_5+\sin\omega_6}{\sqrt{2}} \quad \text{(C.3)}$$

$$E(1,4) = h - w_2\cos\omega_{11} + h\cos(\omega_{11}+\omega_{12})(1-\cos\omega_2\cos\omega_3) - (h-w_2\cos\omega_{42})\cos\omega_5\cos\omega_6 + \frac{h\cos(\omega_{11}+\omega_{12})(\sin\omega_3-\cos\omega_3\sin\omega_2)}{\sqrt{2}} - \frac{w_2\sin\omega_{42}(\sin\omega_6-\cos\omega_6\sin\omega_5)}{\sqrt{2}} \quad \text{(C.4)}$$

$$E(2,1) = -\frac{\cos(\omega_{41}+\omega_{42})(\sin\omega_5-\cos\omega_5\sin\omega_6)}{\sqrt{2}} + \frac{\sin(\omega_{41}+\omega_{42})(\cos\omega_5+\cos\omega_6+\sin\omega_5\sin\omega_6)}{2} - \sin(\omega_{11}+\omega_{12})\cos\omega_2\cos\omega_3 - \frac{\cos(\omega_{11}+\omega_{12})(\sin\omega_3-\cos\omega_3\sin\omega_2)}{\sqrt{2}} \quad \text{(C.5)}$$

$$E(2,2) = \frac{\cos(\omega_{11}+\omega_{12})(\cos\omega_2+\cos\omega_3+\sin\omega_2\sin\omega_3)}{2} - \frac{\cos(\omega_{41}+\omega_{42})(\cos\omega_5+\cos\omega_6+\sin\omega_5\sin\omega_6)}{2} + \frac{\sin(\omega_{11}+\omega_{12})(\sin\omega_2-\cos\omega_2\sin\omega_3)}{\sqrt{2}} - \frac{\sin(\omega_{41}+\omega_{42})(\sin\omega_5-\cos\omega_5\sin\omega_6)}{\sqrt{2}} \quad \text{(C.6)}$$

$$E(2,3) = \frac{\sin(\omega_{11}+\omega_{12})(\sin\omega_2+\cos\omega_2\sin\omega_3)}{\sqrt{2}} + \frac{\cos\omega_5-\cos\omega_6+\sin\omega_5\sin\omega_6}{2} + \frac{\cos(\omega_{11}+\omega_{12})(\cos\omega_2-\cos\omega_3-\sin\omega_2\sin\omega_3)}{\sqrt{2}} \quad \text{(C.7)}$$

$$E(2,4) = \frac{h\cos(\omega_{11}+\omega_{12})(\cos\omega_3\sin\omega_2-\sin\omega_3)}{\sqrt{2}} - \frac{-(h-w_2\cos\omega_{42})(\cos\omega_5\sin\omega_6-\sin\omega_5)}{\sqrt{2}} + h\sin(\omega_{11}+\omega_{12})(1-\cos\omega_2\cos\omega_3) - w_2\sin\omega_{11} + \frac{w_2\sin\omega_{42}(\cos\omega_5+\cos\omega_6+\sin\omega_5\sin\omega_6)}{2} \quad \text{(C.8)}$$

$$E(3,1) = -\frac{\sin(\omega_{41}+\omega_{42})(\sin\omega_5\sin\omega_6-\cos\omega_5+\cos\omega_6)}{2} - \frac{\sin\omega_3+\cos\omega_3\sin\omega_2+\cos(\omega_{41}+\omega_{42})(\sin\omega_5+\cos\omega_5\sin\omega_6)}{\sqrt{2}} \quad \text{(C.9)}$$

$$E(3,2) = -\frac{\sin(\omega_{41}+\omega_{42})(\sin\omega_5+\cos\omega_5\sin\omega_6)}{\sqrt{2}} - \frac{\cos\omega_2-\cos\omega_3+\sin\omega_2\sin\omega_3}{2} - \frac{\cos(\omega_{41}+\omega_{42})(\cos\omega_5-\cos\omega_6-\sin\omega_5\sin\omega_6)}{\sqrt{2}} \quad \text{(C.10)}$$

$$E(3,3) = \frac{\sin\omega_2\sin\omega_3-\cos\omega_2-\cos\omega_3-\sin\omega_5\sin\omega_6+\cos\omega_5+\cos\omega_6}{2} \quad \text{(C.11)}$$

$$E(3,4) = -\frac{h(\cos\omega_3\sin\omega_2+\sin\omega_3-cos\omega_5\sin\omega_6-\sin\omega_2)}{\sqrt{2}} + \frac{w_2\sin\omega_{42}(\cos\omega_5-\cos\omega_6-\sin\omega_5\sin\omega_6)}{2} - \frac{w_2\cos\omega_{42}(\sin\omega_5+\cos\omega_5\sin\omega_6)}{\sqrt{2}} \quad \text{(C.12)}$$

$$E(4,i) = 0,\ i = 1,2,3,4 \quad \text{(C.13)}$$

According to Eq. 2.6, each $E(i,j)$ must be zero. By inspection, assign the

following angle symmetry into Eqs. C.1 - C.12 for further simplification.

$$\omega_{11} = \omega_{41},\ \omega_{12} = \omega_{42},\ \omega_2 = \omega_5,\ \omega_3 = \omega_6 \tag{C.14}$$

It is thus found that

$$E(1,1) = E(2,2) = E(3,3) = 0 \tag{C.15}$$

$$E(1,2) + E(2,1) = E(1,3) + E(3,1) = E(2,3) + E(3,2) = 0 \tag{C.16}$$

Given this, only $E(1,2)$, $E(1,3)$, $E(1,4)$, $E(2,3)$, $E(2,4)$, and $E(3,4)$, i.e., Eqs. C.2 - C.4, C.7 - C.8, and C.12, are the independent to solve the four dihedral angles ω_{11}, ω_{12}, ω_2, and ω_3. According to Chapter 6,

$$\omega_1 = \omega_{11} + \omega_{12} - 180^\circ \tag{C.17}$$

Substituting Eq.C.17 into Eq.C.2 yields

$$E(1,2) = \frac{\sin\omega_1(\cos\omega_2 + \cos\omega_3 - 2\cos\omega_2\cos\omega_3 + \sin\omega_2\sin\omega_3)}{2} - \frac{\cos\omega_1(\sin\omega_2 + \sin\omega_3 - \sin(\omega_2+\omega_3))}{\sqrt{2}} \tag{C.18}$$

which gives

$$\tan\omega_1 = \frac{\sqrt{2}(\sin\omega_2 + \sin\omega_3 - \sin(\omega_2+\omega_3))}{\cos\omega_2 + \cos\omega_3 - 2\cos\omega_2\cos\omega_3 + \sin\omega_2\sin\omega_3} \tag{C.19}$$

where conditions of path 1, path 2, and the transition path are: (1) $\omega_2 = \omega_3$, (2) $\omega_2 = 0$, and (3) ω_3 at a fixed value, respectively.

The exact values of ω_{11} and ω_{12} can be solved via Eqs. C.4 and C.17 using the different inputs of ω_1, ω_2, and ω_3. Note that all the results need to be substituted into other matrix elements for validation.

Bibliography

Alois, J. (2021), 'Discover the world's oldest lobster (140 years old!)'.
URL: *https://a-z-animals.com/blog/discover-the-worlds-oldest-lobster-140-years-old/*

Amend, J., Cheng, N., Fakhouri, S. and Culley, B. (2016), 'Soft robotics commercialization: Jamming grippers from research to product', *Soft robotics* **3**(4), 213–222.

Andrychowicz, O. M., Baker, B., Chociej, M., Jozefowicz, R., McGrew, B., Pachocki, J., Petron, A., Plappert, M., Powell, G., Ray, A. et al. (2020), 'Learning dexterous in-hand manipulation', *The International Journal of Robotics Research* **39**(1), 3–20.

Arnold, T. and Scheutz, M. (2017), 'The tactile ethics of soft robotics: Designing wisely for human–robot interaction', *Soft robotics* **4**(2), 81–87.

Baines, R., Patiballa, S. K., Booth, J., Ramirez, L., Sipple, T., Garcia, A., Fish, F. and Kramer-Bottiglio, R. (2022), 'Multi-environment robotic transitions through adaptive morphogenesis', *Nature* **610**(7931), 283–289.

Baker, J. E. (1980), 'An analysis of the bricard linkages', *Mechanism and machine Theory* **15**(4), 267–286.

Baker, J. E. (1993), 'A geometrico-algebraic exploration of altmann's linkage', *Mechanism and machine theory* **28**(2), 249–260.

Baker, J. E. (2002), 'Displacement–closure equations of the unspecialised double-hooke's-joint linkage', *Mechanism and Machine Theory* **37**(10), 1127–1144.

Bansal, R., Hauser, H. and Rossiter, J. (2023), Self-reconfiguring soft modular cellbots, *in* '2023 IEEE International Conference on Soft Robotics (RoboSoft)', IEEE, pp. 1–6.

Bauer, S., Bauer-Gogonea, S., Graz, I., Kaltenbrunner, M., Keplinger, C. and Schwödiauer, R. (2014), '25th anniversary article: a soft future: from robots and sensor skin to energy harvesters', *Advanced Materials* **26**(1), 149–162.

Belke, C. H., Holdcroft, K., Sigrist, A. and Paik, J. (2023), 'Morphological flexibility in robotic systems through physical polygon meshing', *Nature Machine Intelligence* pp. 1–7.

Belke, C. H. and Paik, J. (2017), 'Mori: a modular origami robot', *IEEE/ASME Transactions on Mechatronics* **22**(5), 2153–2164.

Bennett, G. T. (1903), 'A new mechanism', *Engineering* **76**, 777.

Bennett, G. T. (1905), 'Lxxvii. the parallel motion of sarrut and some allied mechanisms', *The London, Edinburgh, and Dublin Philosophical Magazine and Journal of Science* **9**(54), 803–810.

Bhovad, P., Kaufmann, J. and Li, S. (2019), 'Peristaltic locomotion without digital controllers: Exploiting multi-stability in origami to coordinate robotic motion', *Extreme Mechanics Letters* **32**, 100552.

Boley, J. W., Van Rees, W. M., Lissandrello, C., Horenstein, M. N., Truby, R. L., Kotikian, A., Lewis, J. A. and Mahadevan, L. (2019), 'Shape-shifting structured lattices via multimaterial 4d printing', *Proceedings of the National Academy of Sciences* **116**(42), 20856–20862.

Bricard, R. (1926), *Leçons de cinématique*, Vol. 1, Gauthier-Villars.

Brunete, A., Ranganath, A., Segovia, S., De Frutos, J. P., Hernando, M. and Gambao, E. (2017), 'Current trends in reconfigurable modular robots design', *International Journal of Advanced Robotic Systems* **14**(3), 1729881417710457.

Calisti, M., Picardi, G. and Laschi, C. (2017), 'Fundamentals of soft robot locomotion', *Journal of The Royal Society Interface* **14**(130), 20170101.

Cappello, L., Galloway, K. C., Sanan, S., Wagner, D. A., Granberry, R., Engelhardt, S., Haufe, F. L., Peisner, J. D. and Walsh, C. J. (2018), 'Exploiting textile mechanical anisotropy for fabric-based pneumatic actuators', *Soft robotics* **5**(5), 662–674.

Castano, A., Behar, A. and Will, P. M. (2002), 'The conro modules for reconfigurable robots', *IEEE/ASME transactions on mechatronics* **7**(4), 403–409.

Chai, X. and Dai, J. S. (2019), 'Three novel symmetric waldron–bricard metamorphic and reconfigurable mechanisms and their isomerization', *Journal of Mechanisms and Robotics* **11**(5), 051011.

Chen, T., Bilal, O. R., Shea, K. and Daraio, C. (2018), 'Harnessing bistability for directional propulsion of soft, untethered robots', *Proceedings of the National Academy of Sciences* **115**(22), 5698–5702.

Chen, Y. and Chen, Y. (2003), Design of structural mechanisms, PhD thesis, Oxford University, UK.

Chen, Y., Feng, H., Ma, J., Peng, R. and You, Z. (2016), 'Symmetric waterbomb origami', *Proceedings of the Royal Society A: Mathematical, Physical and Engineering Sciences* **472**(2190), 20150846.

Chen, Y., Peng, R. and You, Z. (2015), 'Origami of thick panels', *Science* **349**(6246), 396–400.

Chen, Y., Wan, F., Wu, T. and Song, C. (2017), 'Soft-rigid interaction mechanism towards a lobster-inspired hybrid actuator', *Journal of Micromechanics and Microengineering* **28**(1), 014007.

Chen, Y. and You, Z. (2007), 'Spatial 6r linkages based on the combination of two goldberg 5r linkages', *Mechanism and Machine Theory* **42**(11), 1484–1498.

Chen, Y. and You, Z. (2008), 'An extended myard linkage and its derived 6r linkage', *Journal of Mechanical Design* **130**, 052301–1.

Cobos, S., Ferre, M., Uran, M. S., Ortego, J. and Pena, C. (2008), Efficient human hand kinematics for manipulation tasks, *in* '2008 IEEE/RSJ International Conference on Intelligent Robots and Systems', IEEE, pp. 2246–2251.

Coevoet, E., Morales-Bieze, T., Largilliere, F., Zhang, Z., Thieffry, M., Sanz-Lopez, M., Carrez, B., Marchal, D., Goury, O., Dequidt, J. et al. (2017), 'Soft-

ware toolkit for modeling, simulation, and control of soft robots', *Advanced Robotics* **31**(22), 1208–1224.

Connolly, F., Walsh, C. J. and Bertoldi, K. (2017), 'Automatic design of fiber-reinforced soft actuators for trajectory matching', *Proceedings of the National Academy of Sciences* **114**(1), 51–56.

Dai, J. S. and Rees Jones, J. (1999), 'Mobility in metamorphic mechanisms of foldable/erectable kinds'.

Della Santina, C., Grioli, G., Catalano, M., Brando, A. and Bicchi, A. (2015), Dexterity augmentation on a synergistic hand: The pisa/iit softhand+, *in* '2015 IEEE-RAS 15th International Conference on Humanoid Robots (Humanoids)', IEEE, pp. 497–503.

Denavit, J. and Hartenberg, R. S. (1955), 'A kinematic notation for lower-pair mechanisms based on matrices'.

Dietmaier, P. (1995), A new 6r space mechanism, *in* 'Proceeding 9th World Congress IFToMM, Milano', Vol. 1, pp. 52–56.

Digumarti, K. M., Conn, A. T. and Rossiter, J. (2019), 'Pellicular morphing surfaces for soft robots', *IEEE Robotics and Automation Letters* **4**(3), 2304–2309.

Dollar, A. M. and Howe, R. D. (2010), 'The highly adaptive sdm hand: Design and performance evaluation', *The international journal of robotics research* **29**(5), 585–597.

Doumit, M., Fahim, A. and Munro, M. (2009), 'Analytical modeling and ex-

perimental validation of the braided pneumatic muscle', *IEEE transactions on robotics* **25**(6), 1282–1291.

Drotman, D., Jadhav, S., Sharp, D., Chan, C. and Tolley, M. T. (2021), 'Electronics-free pneumatic circuits for controlling soft-legged robots', *Science Robotics* **6**(51), eaay2627.

Dudte, L. H., Choi, G. P., Becker, K. P. and Mahadevan, L. (2023), 'An additive framework for kirigami design', *Nature Computational Science* **3**(5), 443–454.

Evans, T. A., Lang, R. J., Magleby, S. P. and Howell, L. L. (2015), 'Rigidly foldable origami gadgets and tessellations', *Royal Society open science* **2**(9), 150067.

Fang, G., Matte, C.-D., Scharff, R. B., Kwok, T.-H. and Wang, C. C. (2020), 'Kinematics of soft robots by geometric computing', *IEEE Transactions on Robotics* **36**(4), 1272–1286.

Feng, H., Chen, Y., Dai, J. S. and Gogu, G. (2017), 'Kinematic study of the general plane-symmetric bricard linkage and its bifurcation variations', *Mechanism and Machine Theory* **116**, 89–104.

Feng, H., Ma, J., Chen, Y. and You, Z. (2018), 'Twist of tubular mechanical metamaterials based on waterbomb origami', *Scientific reports* **8**(1), 9522.

Galloway, K. C., Polygerinos, P., Walsh, C. J. and Wood, R. J. (2013), Mechanically programmable bend radius for fiber-reinforced soft actuators, *in* '2013 16th International Conference on Advanced Robotics (ICAR)', IEEE, pp. 1–6.

Gan, W. W. and Pellegrino, S. (2006), 'Numerical approach to the kinematic analysis of deployable structures forming a closed loop', *Proceedings of the in-*

stitution of mechanical engineers, Part C: Journal of Mechanical Engineering Science **220**(7), 1045–1056.

Garcia, A., Krummel, G. and Priya, S. (2020), 'Fundamental understanding of millipede morphology and locomotion dynamics', *Bioinspiration & Biomimetics* **16**(2), 026003.

Gariya, N. and Kumar, P. (2021), 'A review on soft materials utilized for the manufacturing of soft robots', *Materials Today: Proceedings* **46**, 11177–11181.

Georgakopoulos, S. V., Zekios, C. L., Sattar-Kaddour, A., Hamza, M., Biswas, A., Clark, B., Ynchausti, C., Howell, L. L., Magleby, S. P. and Lang, R. J. (2021), 'Origami antennas', *IEEE Open Journal of Antennas and Propagation* **2**, 1020–1043.

Goldberg, M. (1943), 'New five-bar and six-bar linkages in three dimensions', *Transactions of the American Society of Mechanical Engineers* **65**(6), 649–656.

Gorissen, B., Melancon, D., Vasios, N., Torbati, M. and Bertoldi, K. (2020), 'Inflatable soft jumper inspired by shell snapping', *Science Robotics* **5**(42), eabb1967.

Grodzinski, P. and M'Ewen, E. (1954), 'Link mechanisms in modern kinematics', *Proceedings of the Institution of Mechanical Engineers* **168**(1), 877–896.

Grünbaum, B., Grünbaum, Z. and Shephard, G. (1986), Symmetry in moorish and other ornaments, *in* 'Symmetry', Elsevier, pp. 641–653.

Grünbaum, B. and Shephard, G. C. (1987), *Tilings and patterns*, Courier Dover Publications.

Gu, H., Boehler, Q., Cui, H., Secchi, E., Savorana, G., De Marco, C., Gervasoni, S., Peyron, Q., Huang, T.-Y., Pane, S. et al. (2020), 'Magnetic cilia carpets with programmable metachronal waves', *Nature communications* **11**(1), 2637.

Gu, Y., Wei, G. and Chen, Y. (2021), 'Thick-panel origami cube', *Mechanism and Machine Theory* **164**, 104411.

Guseinov, R., McMahan, C., Pérez, J., Daraio, C. and Bickel, B. (2020), 'Programming temporal morphing of self-actuated shells', *Nature communications* **11**(1), 237.

Han, M.-W. and Ahn, S.-H. (2017), 'Blooming knit flowers: Loop-linked soft morphing structures for soft robotics', *Advanced materials* **29**(13), 1606580.

Hauser, H., Füchslin, R. M. and Pfeifer, R. (2014), 'Opinions and outlooks on morphological computation'.

Hon-Cheung, Y. and Baker, J. E. (1981), 'On the generation of new linkages from bennett loops', *Mechanism and Machine Theory* **16**(5), 473–485.

Hopkin, S. P., Read, H. J. et al. (1992), *The biology of millipedes*.

Hughes, J., Culha, U., Giardina, F., Guenther, F., Rosendo, A. and Iida, F. (2016), 'Soft manipulators and grippers: A review', *Frontiers in Robotics and AI* **3**, 69.

Hull, T. (1994), 'On the mathematics of flat origamis', *Congressus numerantium* pp. 215–224.

Hull, T. C. and Tachi, T. (2018), 'Self-foldability of monohedral quadrilateral origami tessellations', *arXiv preprint arXiv:1809.04243* .

Hussain, I., Al-Ketan, O., Renda, F., Malvezzi, M., Prattichizzo, D., Seneviratne, L., Abu Al-Rub, R. K. and Gan, D. (2020), 'Design and prototyping soft–rigid tendon-driven modular grippers using interpenetrating phase composites materials', *The International Journal of Robotics Research* **39**(14), 1635–1646.

Iida, F. and Laschi, C. (2011), 'Soft robotics: Challenges and perspectives', *Procedia Computer Science* **7**, 99–102.

Ilievski, F., Mazzeo, A. D., Shepherd, R. F., Chen, X. and Whitesides, G. M. (2011), 'Soft robotics for chemists', *Angewandte Chemie* **123**(8), 1930–1935.

Innovative Pest Control, O. (2020), 'The secret to effective centipede & millipede control for your home'.
URL: *https://www.ipcpest.com/blog/2020/october/the-secret-to-effective-centipede-millipede-cont/*

Jeong, D. and Lee, K. (2018), 'Design and analysis of an origami-based three-finger manipulator', *Robotica* **36**(2), 261–274.

Jeong, U., Kim, K., Kim, S.-H., Choi, H., Youn, B. D. and Cho, K.-J. (2021), 'Reliability analysis of a tendon-driven actuation for soft robots', *The International Journal of Robotics Research* **40**(1), 494–511.

Jiao, Z., Zhang, C., Ruan, J., Tang, W., Lin, Y., Zhu, P., Wang, J., Wang, W., Yang, H. and Zou, J. (2021), 'Re-foldable origami-inspired bidirectional twisting of artificial muscles reproduces biological motion', *Cell Reports Physical Science* **2**(5).

Kan, Z., Zhang, Y., Pang, C. and Wang, M. Y. (2020), Origami-based shape

morphing fingertip to enhance grasping stability and dexterity, *in* '2020 IEEE 16th International Conference on Automation Science and Engineering (CASE)', IEEE, pp. 1070–1077.

Kan, Z., Zhang, Y., Yang, Y., Tse, Y. A. and Wang, M. Y. (2019), An origami-inspired monolithic soft gripper based on geometric design method, *in* '2019 2nd IEEE International Conference on Soft Robotics (RoboSoft)', IEEE, pp. 470–476.

Kaufmann, J., Bhovad, P. and Li, S. (2022), 'Harnessing the multistability of kresling origami for reconfigurable articulation in soft robotic arms', *Soft Robotics* **9**(2), 212–223.

Khosravi, H., Iannucci, S. M. and Li, S. (2021), 'Pneumatic soft actuators with kirigami skins', *Frontiers in Robotics and AI* **8**, 749051.

Kotikian, A., McMahan, C., Davidson, E. C., Muhammad, J. M., Weeks, R. D., Daraio, C. and Lewis, J. A. (2019), 'Untethered soft robotic matter with passive control of shape morphing and propulsion', *Science robotics* **4**(33), eaax7044.

Kresling, B. (2020), 'The fifth fold: complex symmetries in kresling-origami patterns', *Symmetry Cult. Sci* **31**, 403–416.

Kumar, P. and Pellegrino, S. (2000), 'Computation of kinematic paths and bifurcation points', *International Journal of Solids and Structures* **37**(46-47), 7003–7027.

Kuribayashi, K., Tsuchiya, K., You, Z., Tomus, D., Umemoto, M., Ito, T. and Sasaki, M. (2006), 'Self-deployable origami stent grafts as a biomedical applica-

tion of ni-rich tini shape memory alloy foil', *Materials Science and Engineering: A* **419**(1-2), 131–137.

Lang, R. J. (2007), 'The science of origami', *Physics world* **20**(2), 30.

Lanier, K. (2017), 'Meet the roly poly (aka pill bug) and learn its roles in the garden'.
URL: *https://www.hobbyfarms.com/roly-poly-pill-bug-garden-roles/*

Laschi, C., Mazzolai, B. and Cianchetti, M. (2016), 'Soft robotics: Technologies and systems pushing the boundaries of robot abilities', *Science robotics* **1**(1), eaah3690.

Lee, C. and Dai, J. (2003), 'Configuration analysis of the schatz linkage', *Proceedings of the Institution of Mechanical Engineers, Part C: Journal of Mechanical Engineering Science* **217**(7), 779–786.

Lee, D.-Y., Kim, S.-R., Kim, J.-S., Park, J.-J. and Cho, K.-J. (2017), 'Origami wheel transformer: A variable-diameter wheel drive robot using an origami structure', *Soft robotics* **4**(2), 163–180.

Lee, H., Kim, H., Ha, I., Jung, J., Won, P., Cho, H., Yeo, J., Hong, S., Han, S., Kwon, J. et al. (2019), 'Directional shape morphing transparent walking soft robot', *Soft Robotics* **6**(6), 760–767.

Lee, K., Wang, Y. and Zheng, C. (2020), 'Twister hand: Underactuated robotic gripper inspired by origami twisted tower', *IEEE Transactions on Robotics* **36**(2), 488–500.

Li, G., Chen, X., Zhou, F., Liang, Y., Xiao, Y., Cao, X., Zhang, Z., Zhang, M., Wu, B., Yin, S. et al. (2021), 'Self-powered soft robot in the mariana trench', *Nature* **591**(7848), 66–71.

Li, J., Zhang, X., An, S., Zhu, Z., Deng, Z. and You, Z. (2022), 'Kirigami-inspired foldable 3d cellular structures with a single degree of freedom', *International Journal of Solids and Structures* **244**, 111587.

Li, S., Stampfli, J. J., Xu, H. J., Malkin, E., Diaz, E. V., Rus, D. and Wood, R. J. (2019), A vacuum-driven origami "magic-ball" soft gripper, *in* '2019 International Conference on Robotics and Automation (ICRA)', IEEE, pp. 7401–7408.

Li, S., Vogt, D. M., Rus, D. and Wood, R. J. (2017), 'Fluid-driven origami-inspired artificial muscles', *Proceedings of the National academy of Sciences* **114**(50), 13132–13137.

Li, S. and Wang, K. (2015), 'Fluidic origami: a plant-inspired adaptive structure with shape morphing and stiffness tuning', *Smart Materials and Structures* **24**(10), 105031.

Liang, H., Hao, G., Olszewski, O. Z., Jiang, Z. and Zhang, K. (2023), 'Design of a foldable origami mechanism with helical motion inspired by the resch triangular tessellation', *Mechanism and Machine Theory* **179**, 105101.

Liu, C., Edwards, O., Althoefer, K., Zhang, K. and Godaba, H. (2022b), An electro-pneumatic shape morphing rolling robot with variable locomotion modes, *in* '2022 IEEE 5th International Conference on Soft Robotics (RoboSoft)', IEEE, pp. 715–721.

Liu, C., He, L., Wang, S., Williams, A., You, Z. and Maiolino, P. (2024b), 'Exploring kinematic bifurcations and hinge compliance for in-hand manipulation: How could thick-panel origami contribute?', *Advanced Intelligent Systems* p. 2300691.

Liu, C., He, L., Williams, A., You, Z. and Maiolino, P. (2024c), Towards mechanical intelligence: Exploiting origami bifurcations for robot reconfiguration.

Liu, C., Maiolino, P., Yang, Y. and You, Z. (2020b), Hybrid soft-rigid deployable structure inspired by thick-panel origami, *in* 'International Design Engineering Technical Conferences and Computers and Information in Engineering Conference', Vol. 83990, American Society of Mechanical Engineers, p. V010T10A080.

Liu, C., Maiolino, P. and You, Z. (2021c), 'A 3d-printable robotic gripper based on thick panel origami', *Frontiers in Robotics and AI* **8**, 730227.

Liu, C., Wohlever, S. J., Ou, M. B., Padir, T. and Felton, S. M. (2021b), 'Shake and take: Fast transformation of an origami gripper', *IEEE Transactions on Robotics* **38**(1), 491–506.

Liu, C., Yang, F., Maiolino, P. and You, Z. (2024a), Morphing surfaces inspired by thick-panel origami.

Liu, C., You, Z. and Maiolino, P. (2022), Kinematics of an origami inspired millipede robot, *in* 'International Design Engineering Technical Conferences and Computers and Information in Engineering Conference', Vol. 86281, American Society of Mechanical Engineers, p. V007T07A062.

Liu, K., Chen, W., Yang, W., Jiao, Z. and Yu, Y. (2022a), 'Review of the research progress in soft robots', *Applied Sciences* **13**(1), 120.

Liu, K., Hacker, F. and Daraio, C. (2021a), 'Robotic surfaces with reversible, spatiotemporal control for shape morphing and object manipulation', *Science Robotics* **6**(53), eabf5116.

Liu, S., Wu, H., Yang, Y. and Wang, M. Y. (2020a), Parallel-motion thick origami structure for robotic design, *in* '2020 IEEE International Conference on Robotics and Automation (ICRA)', IEEE, pp. 934–939.

Liu, T., Wang, Y. and Lee, K. (2017), 'Three-dimensional printable origami twisted tower: Design, fabrication, and robot embodiment', *IEEE Robotics and Automation Letters* **3**(1), 116–123.

Lu, H., Zhang, M., Yang, Y., Huang, Q., Fukuda, T., Wang, Z. and Shen, Y. (2018), 'A bioinspired multilegged soft millirobot that functions in both dry and wet conditions', *Nature communications* **9**(1), 3944.

Lu, Q., Baron, N., Clark, A. B. and Rojas, N. (2021), 'Systematic object-invariant in-hand manipulation via reconfigurable underactuation: Introducing the ruth gripper', *The International Journal of Robotics Research* **40**(12-14), 1402–1418.

Lynch, K. M. and Park, F. C. (2017), *Modern robotics*, Cambridge University Press.

Majidi, C. (2019), 'Soft-matter engineering for soft robotics', *Advanced Materials Technologies* **4**(2), 1800477.

Mason, M. T. (2018), 'Toward robotic manipulation', *Annual Review of Control, Robotics, and Autonomous Systems* **1**, 1–28.

Mavroidis, C. and Roth, B. (1994), Analysis and synthesis of overconstrained mechanism, *in* 'International Design Engineering Technical Conferences and Computers and Information in Engineering Conference', Vol. 12846, American Society of Mechanical Engineers, pp. 115–133.

Mavroidis, C. and Roth, B. (1995), 'New and revised overconstrained mechanisms', *Journal of Mechanical Design* **117**(1), 75–82.

Medynski, C. and Rattray, B. (2011), Bebionic prosthetic design, Myoelectric Symposium.

Mengaldo, G., Renda, F., Brunton, S. L., Bächer, M., Calisti, M., Duriez, C., Chirikjian, G. S. and Laschi, C. (2022), 'A concise guide to modelling the physics of embodied intelligence in soft robotics', *Nature Reviews Physics* **4**(9), 595–610.

Mishra, A. K., Del Dottore, E., Sadeghi, A., Mondini, A. and Mazzolai, B. (2017), 'Simba: Tendon-driven modular continuum arm with soft reconfigurable gripper', *Frontiers in Robotics and AI* **4**, 4.

Miyashita, S., Guitron, S., Ludersdorfer, M., Sung, C. R. and Rus, D. (2015), An untethered miniature origami robot that self-folds, walks, swims, and degrades, *in* '2015 IEEE international conference on robotics and automation (ICRA)', IEEE, pp. 1490–1496.

Mosadegh, B., Polygerinos, P., Keplinger, C., Wennstedt, S., Shepherd, R. F., Gupta, U., Shim, J., Bertoldi, K., Walsh, C. J. and Whitesides, G. M. (2014), 'Pneumatic networks for soft robotics that actuate rapidly', *Advanced functional materials* **24**(15), 2163–2170.

Native Pest Management, O. (2023), 'Centipede & millipede identification in florida'.

URL: *https://www.nativepestmanagement.com/pest-library/centipedes-and-millipedes*

Northwest Pest Control, O. (2020), 'What you need to know about millipede control: Millipede prevention'.

URL: *https://www.callnorthwest.com/2020/07/what-you-need-to-know-about-millipede-control/*

Onal, C. D., Tolley, M. T., Wood, R. J. and Rus, D. (2014), 'Origami-inspired printed robots', *IEEE/ASME transactions on mechatronics* **20**(5), 2214–2221.

Onal, C. D., Wood, R. J. and Rus, D. (2012), 'An origami-inspired approach to worm robots', *IEEE/ASME Transactions on Mechatronics* **18**(2), 430–438.

Ou, J., Ma, Z., Peters, J., Dai, S., Vlavianos, N. and Ishii, H. (2018), 'Kinetix-designing auxetic-inspired deformable material structures', *Computers & Graphics* **75**, 72–81.

O'Rourke, J. (2011), *How to fold it: the mathematics of linkages, origami, and polyhedra*, Cambridge University Press.

Pagoli, A., Chapelle, F., Corrales, J. A., Mezouar, Y. and Lapusta, Y. (2021b), 'A soft robotic gripper with an active palm and reconfigurable fingers for fully dexterous in-hand manipulation', *IEEE Robotics and Automation Letters* **6**(4), 7706–7713.

Pagoli, A., Chapelle, F., Corrales-Ramon, J.-A., Mezouar, Y. and Lapusta, Y.

(2021a), 'Review of soft fluidic actuators: Classification and materials modeling analysis', *Smart Materials and Structures* **31**(1), 013001.

Peng, R. and Chirikjian, G. S. (2023), 'A methodology for thick-panel origami pattern design', *Mechanism and Machine Theory* **189**, 105423.

Peng, R. and Chirikjian, G. S. (2024), 'Morphable thick-panel origami', *Mechanism and Machine Theory* **192**, 105528.

Phillips, J. (1984), *Freedom in machinery: Introducing screw theory*, Vol. 1, Cambridge University Press.

Pratapa, P. P. and Bellamkonda, A. (2022), 'Thick panel origami for load-bearing deployable structures', *Mechanics Research Communications* **124**, 103937.

Puhlmann, S., Harris, J. and Brock, O. (2022), 'Rbo hand 3: A platform for soft dexterous manipulation', *IEEE Transactions on Robotics* **38**(6), 3434–3449.

Regier, J. C., Shultz, J. W., Zwick, A., Hussey, A., Ball, B., Wetzer, R., Martin, J. W. and Cunningham, C. W. (2010), 'Arthropod relationships revealed by phylogenomic analysis of nuclear protein-coding sequences', *Nature* **463**(7284), 1079–1083.

Robertson, M. A., Kara, O. C. and Paik, J. (2021), 'Soft pneumatic actuator-driven origami-inspired modular robotic "pneumagami"', *The International Journal of Robotics Research* **40**(1), 72–85.

Rojas, N., Ma, R. R. and Dollar, A. M. (2016), 'The gr2 gripper: An underactuated hand for open-loop in-hand planar manipulation', *IEEE Transactions on Robotics* **32**(3), 763–770.

Rossiter, J. M. and Hauser, H. (2016), 'Soft robotics-the next industrial revolution?', *IEEE Robotics and Automation Magazine* **23**(3), 17–20.

Rus, D. and Sung, C. (2018), 'Spotlight on origami robots', *Science Robotics* **3**(15), eaat0938.

Rus, D. and Tolley, M. T. (2015), 'Design, fabrication and control of soft robots', *Nature* **521**(7553), 467–475.

Rus, D. and Tolley, M. T. (2018), 'Design, fabrication and control of origami robots', *Nature Reviews Materials* **3**(6), 101–112.

Sareh, S. and Rossiter, J. (2012), 'Kirigami artificial muscles with complex biologically inspired morphologies', *Smart Materials and Structures* **22**(1), 014004.

Sarraf, N., Rodriguez, K. R. and Qian, L. (2023), 'Modular reconfiguration of dna origami assemblies using tile displacement', *Science Robotics* **8**(77), eadf1511.

Sarrus, P. (1853), 'Note sur la transformation des mouvements rectilignes alternatifs, en mouvements circulaires, et reciproquement', *Comptes. Rendus, Acad. Sci., Paris* **36**, 1036–1038.

Seo, J., Paik, J. and Yim, M. (2019), 'Modular reconfigurable robotics', *Annual Review of Control, Robotics, and Autonomous Systems* **2**, 63–88.

Shah, D. S., Powers, J. P., Tilton, L. G., Kriegman, S., Bongard, J. and Kramer-Bottiglio, R. (2021), 'A soft robot that adapts to environments through shape change', *Nature Machine Intelligence* **3**(1), 51–59.

Shepherd, R. F., Ilievski, F., Choi, W., Morin, S. A., Stokes, A. A., Mazzeo, A. D., Chen, X., Wang, M. and Whitesides, G. M. (2011), 'Multigait soft robot', *Proceedings of the national academy of sciences* **108**(51), 20400–20403.

Shintake, J., Cacucciolo, V., Floreano, D. and Shea, H. (2018), 'Soft robotic grippers', *Advanced materials* **30**(29), 1707035.

Siebrecht, J., Corves, B., Paris, J., Dehn, S., Buffart, H., Jacobs, G., Weigel, C., Hoffmann, S. and Trautz, M. (2018), On using tessellation properties for the development of classifying criteria for foldable mechanisms, *in* 'The International Meeting on Origami Science, Mathematics, and Education, Oxford'.

Song, C., Chen, Y. and Chen, I.-M. (2013), 'A 6r linkage reconfigurable between the line-symmetric bricard linkage and the bennett linkage', *Mechanism and Machine Theory* **70**, 278–292.

Støy, K. (2015), 'Reconfigurable robots', *Springer Handbook of Computational Intelligence* pp. 1407–1421.

Tachi, T. (2009), 'Simulation of rigid origami', *Origami* **4**(08), 175–187.

Tang, Y., Li, Y., Hong, Y., Yang, S. and Yin, J. (2019), 'Programmable active kirigami metasheets with more freedom of actuation', *Proceedings of the National Academy of Sciences* **116**(52), 26407–26413.

Tao, J., Khosravi, H., Deshpande, V. and Li, S. (2023), 'Engineering by cuts: How kirigami principle enables unique mechanical properties and functionalities', *Advanced Science* **10**(1), 2204733.

Teeple, C. B., Louis, R. C. S., Graule, M. A. and Wood, R. J. (2021), The role of digit arrangement in soft robotic in-hand manipulation, *in* '2021 IEEE/RSJ International Conference on Intelligent Robots and Systems (IROS)', IEEE, pp. 7201–7208.

Thorp, J. H. (2009), Arthropoda and related groups, *in* 'Encyclopedia of insects', Elsevier, pp. 50–56.

Thrall, A. P. and Quaglia, C. (2014), 'Accordion shelters: A historical review of origami-like deployable shelters developed by the us military', *Engineering structures* **59**, 686–692.

Tondu, B. (2012), 'Modelling of the mckibben artificial muscle: A review', *Journal of Intelligent Material Systems and Structures* **23**(3), 225–253.

Treml, B., Gillman, A., Buskohl, P. and Vaia, R. (2018), 'Origami mechanologic', *Proceedings of the National Academy of Sciences* **115**(27), 6916–6921.

Truby, R. L., Wehner, M., Grosskopf, A. K., Vogt, D. M., Uzel, S. G., Wood, R. J. and Lewis, J. A. (2018), 'Soft somatosensitive actuators via embedded 3d printing', *Advanced Materials* **30**(15), 1706383.

VandenSpiegel, D. and Golovatch, S. (2012), 'The millipede family ammodesmidae (diplopoda, polydesmida) in western africa', *ZooKeys* (221), 1.

Verrill, H. (1998), Origami tessellations, *in* 'Bridges: Mathematical Connections in Art, Music, and Science', pp. 55–68.

Waldron, K. J. (1968), 'Hybrid overconstrained linkages', *Journal of Mechanisms* **3**(2), 73–78.

Wang, C., Li, J. and You, Z. (2018b), A kirigami-inspired foldable model for thick panels, *in* 'The 7th international meeting on origami in science, mathematics and education (7OSME), Oxford, United Kingdom', pp. 5–7.

Wang, C., Li, J. and Zhang, D. (2023), 'Motion singularity analysis of the thick-panel kirigami', *Mechanism and Machine Theory* **180**, 105162.

Wang, C., Zhang, D., Li, J. and You, Z. (2022), 'Kirigami-inspired thick-panel deployable structures', *International Journal of Solids and Structures* **251**, 111752.

Wang, T., Ge, L. and Gu, G. (2018a), 'Programmable design of soft pneu-net actuators with oblique chambers can generate coupled bending and twisting motions', *Sensors and Actuators A: Physical* **271**, 131–138.

Watanabe, N. and Kawaguchi, K.-i. (2009), 'The method for judging rigid foldability', *Origami* **4**, 165–174.

Wei, Y., Zou, Z., Qian, Z., Ren, L. and Wei, G. (2022), 'Biomechanical analysis of the effect of finger joint configuration on hand grasping performance: rigid vs flexible', *IEEE Transactions on Neural Systems and Rehabilitation Engineering* **31**, 606–619.

Wockenfuß, W. R., Brandt, V., Weisheit, L. and Drossel, W.-G. (2022), 'Design, modeling and validation of a tendon-driven soft continuum robot for planar motion based on variable stiffness structures', *IEEE Robotics and Automation Letters* **7**(2), 3985–3991.

Wohlhart, K. (1987), A new 6r space mechanism, *in* 'Proceedings of the seventh

world congress on the theory of machines and mechanisms, Sevilla, Spain', Vol. 1, pp. 193–198.

Wohlhart, K. (1991), 'Merging two general goldberg 5r linkages to obtain a new 6r space mechanism', *Mechanism and Machine Theory* **26**(7), 659–668.

Wu, S., Ze, Q., Dai, J., Udipi, N., Paulino, G. H. and Zhao, R. (2021), 'Stretchable origami robotic arm with omnidirectional bending and twisting', *Proceedings of the National Academy of Sciences* **118**(36), e2110023118.

Xavier, M. S., Tawk, C. D., Zolfagharian, A., Pinskier, J., Howard, D., Young, T., Lai, J., Harrison, S. M., Yong, Y. K., Bodaghi, M. et al. (2022), 'Soft pneumatic actuators: A review of design, fabrication, modeling, sensing, control and applications', *IEEE Access* **10**, 59442–59485.

Yang, F., Zhang, M., Ma, J., You, Z., Yu, Y., Chen, Y. and Paulino, G. H. (2022a), 'Design of single degree-of-freedom triangular resch patterns with thick-panel origami', *Mechanism and Machine Theory* **169**, 104650.

Yang, J. and You, Z. (2023), Cutting and folding thick-panel miura-ori with one dof, *in* 'International Design Engineering Technical Conferences and Computers and Information in Engineering Conference', Vol. 87363, American Society of Mechanical Engineers, p. V008T08A044.

Yang, J., Zhang, X., Chen, Y. and You, Z. (2022b), 'Folding arrays of uniform-thickness panels to compact bundles with a single degree of freedom', *Proceedings of the Royal Society A* **478**(2261), 20220043.

Yang, Y. (2020), Modular origami-inspired kinematic metamaterials, PhD thesis, University of Oxford.

Yang, Y., Vella, K. and Holmes, D. P. (2021), 'Grasping with kirigami shells', *Science Robotics* **6**(54), eabd6426.

Yao, M., Belke, C. H., Cui, H. and Paik, J. (2019), 'A reconfiguration strategy for modular robots using origami folding', *The International Journal of Robotics Research* **38**(1), 73–89.

Yasa, O., Toshimitsu, Y., Michelis, M. Y., Jones, L. S., Filippi, M., Buchner, T. and Katzschmann, R. K. (2023), 'An overview of soft robotics', *Annual Review of Control, Robotics, and Autonomous Systems* **6**, 1–29.

Ye, H., Liu, Q., Cheng, J., Li, H., Jian, B., Wang, R., Sun, Z., Lu, Y. and Ge, Q. (2023), 'Multimaterial 3d printed self-locking thick-panel origami metamaterials', *Nature Communications* **14**(1), 1607.

Yim, M., Duff, D. G. and Roufas, K. D. (2000), Polybot: a modular reconfigurable robot, *in* 'Proceedings 2000 ICRA. millennium conference. IEEE international conference on robotics and automation. Symposia proceedings (Cat. No. 00CH37065)', Vol. 1, IEEE, pp. 514–520.

Yim, M., Shen, W.-M., Salemi, B., Rus, D., Moll, M., Lipson, H., Klavins, E. and Chirikjian, G. S. (2007), 'Modular self-reconfigurable robot systems [grand challenges of robotics]', *IEEE Robotics & Automation Magazine* **14**(1), 43–52.

Yoon, S. J., Choi, M., Jeong, B. and Park, Y.-L. (2022), 'Elongatable gripper

fingers with integrated stretchable tactile sensors for underactuated grasping and dexterous manipulation', *IEEE Transactions on Robotics* **38**(4), 2179–2193.

You, Z. and Chen, Y. (2012), *Motion structures: deployable structural assemblies of mechanisms*, Taylor & Francis.

Zaidi, S., Maselli, M., Laschi, C. and Cianchetti, M. (2021), 'Actuation technologies for soft robot grippers and manipulators: A review', *Current Robotics Reports* **2**(3), 355–369.

Ze, Q., Wu, S., Nishikawa, J., Dai, J., Sun, Y., Leanza, S., Zemelka, C., Novelino, L. S., Paulino, G. H. and Zhao, R. R. (2022b), 'Soft robotic origami crawler', *Science advances* **8**(13), eabm7834.

Zhakypov, Z., Heremans, F., Billard, A. and Paik, J. (2018), 'An origami-inspired reconfigurable suction gripper for picking objects with variable shape and size', *IEEE Robotics and Automation Letters* **3**(4), 2894–2901.

Zhakypov, Z. and Okamura, A. M. (2022), Fingerprint: A 3-d printed soft monolithic 4-degree-of-freedom fingertip haptic device with embedded actuation, *in* '2022 IEEE 5th International Conference on Soft Robotics (RoboSoft)', IEEE, pp. 938–944.

Zhang, B., Xie, Y., Zhou, J., Wang, K. and Zhang, Z. (2020), 'State-of-the-art robotic grippers, grasping and control strategies, as well as their applications in agricultural robots: A review', *Computers and Electronics in Agriculture* **177**, 105694.

Zhang, K. and Dai, J. S. (2015), 'Screw-system-variation enabled reconfiguration of

the bennett plano-spherical hybrid linkage and its evolved parallel mechanism', *Journal of Mechanical Design* **137**(6), 062303.

Zhang, X. and Chen, W. (2023), 'Folding a flat rectangular plate of uniform-thickness panels using miura-ori', *International Journal of Mechanical Sciences* p. 108570.

Zhang, X. and Chen, Y. (2018a), 'Mobile assemblies of bennett linkages from four-crease origami patterns', *Proceedings of the Royal Society A: Mathematical, Physical and Engineering Sciences* **474**(2210), 20170621.

Zhang, X. and Chen, Y. (2018b), 'The diamond thick-panel origami and the corresponding mobile assemblies of plane-symmetric bricard linkages', *Mechanism and Machine Theory* **130**, 585–604.

Zhang, X. and Chen, Y. (2021), Mobile assemblies of bricard linkages inspired from waterbomb thick-panel origami, *in* 'IFToMM Asian conference on Mechanism and Machine Science', Springer, pp. 101–108.

Zhang, Z., Tang, S., Fan, W., Xun, Y., Wang, H. and Chen, G. (2022), 'Design and analysis of hybrid-driven origami continuum robots with extensible and stiffness-tunable sections', *Mechanism and Machine Theory* **169**, 104607.

Zhao, L., Wu, Y., Blanchet, J., Perroni-Scharf, M., Huang, X., Booth, J., Kramer-Bottiglio, R. and Balkcom, D. (2022b), 'Soft lattice modules that behave independently and collectively', *IEEE Robotics and Automation Letters* **7**(3), 5942–5949.

Zhao, L., Wu, Y., Yan, W., Zhan, W., Huang, X., Booth, J., Mehta, A., Bekris,

K., Kramer-Bottiglio, R. and Balkcom, D. (2023), 'Starblocks: Soft actuated self-connecting blocks for building deformable lattice structures', *IEEE Robotics and Automation Letters* .

Zhao, Y., Chi, Y., Hong, Y., Li, Y., Yang, S. and Yin, J. (2022a), 'Twisting for soft intelligent autonomous robot in unstructured environments', *Proceedings of the National Academy of Sciences* **119**(22), e2200265119.

Zirbel, S. A., Lang, R. J., Thomson, M. W., Sigel, D. A., Walkemeyer, P. E., Trease, B. P., Magleby, S. P. and Howell, L. L. (2013), 'Accommodating thickness in origami-based deployable arrays', *Journal of Mechanical Design* **135**(11), 111005.